Mineral inclusions in diamonds from Wawa metaconglomerate: Implications for thermal evolution of the lithospheric mantle

by

Christine Miller

BSc, Dickinson College, 2010

A THESIS SUBMITTED IN PARTIAL FULFILLMENT OF THE REQUIREMENTS FOR THE DEGREE OF MASTER OF SCIENCE

in

The Faculty of Graduate Studies
(Geological Sciences)

THE UNIVERSITY OF BRITISH COLUMBIA

(Vancouver)

August 2012

Abstract

Mineral inclusions in non-fibrous and fibrous diamonds from an Archean metaconglomerate deposit in Wawa, Ontario, Southern Superior craton were studied to characterize the compositional and thermal state of the lithospheric mantle from the Archean to present day. Electron microprobe analysis of Wawa non-fibrous diamonds shows large inclusions of Cr-pyrope, Mg-chromite, olivine, and enstatite indicating harzburgitic parent rock. Wawa fibrous diamonds host microinclusions of pyrope and olivine of predominantly lherzolitic assemblage. Thermobarometry calculations for non-fibrous diamonds yield temperatures and pressures consistent with formation in a cool, cratonic root reaching to a minimum depth of 190 km with a geotherm between 39-41 mW/m^2, located beneath the Southern Superior province during the Archean. Comparison to results from xenoliths in nearby post-Archean kimberlites, and to modern geophysics, indicates heating and thinning of the cratonic root. This effectively destroyed the diamondiferous portion of the lithospheric mantle, as early as 1.1 Ga in some areas of the Southern Superior, through tectonic erosion during amalgamation of terranes to the protocraton.

Diamond inclusion analysis for Wawa fibrous diamonds and datasets for non-fibrous and fibrous diamonds from Diavik, Ekati (Panda kimberlite), and Koffiefontein (South Africa) reveal metasomatic trends of mantle rock evolution due to the influx of K-rich hydrous carbonatitic fluid related to fibrous diamond precipitation. Thermometry for fibrous diamond inclusions yields temperatures of 580-1030 °C. Low formation temperatures, paired with the alkali-rich and hydrous nature of the metasomatic agent, result in subsolidus diamond growth in the absence of melting or thermal disturbance of the mantle. Fibrous diamond growth, previously linked to kimberlite generation, may be a temporally distinct and genetically independent event, as suggested by long mantle residence times for fibrous diamonds and contrasting chemistry of fibrous diamond fluid and kimberlites. This would make metasomatism associated with formation of fibrous diamonds a “cratonic root-friendly” process that would not have played any part in the destruction of the Southern Superior lithospheric root.

Preface

Part of the research contained in this thesis (Chapter 2) has been published in the form of the following manuscript:

Miller, C.E., Kopylova, M., Ryder, J. (2012) Vanished diamondiferous cratonic root beneath the Southern Superior province: evidence from diamond inclusions in the Wawa metaconglomerate. *Contrib Mineral Petrol*. doi: 10.1007/s00410-012-0773-1.

Changes were made to this chapter post-publication according to suggested edits from the examining committee after the oral defense of the thesis. The work presented in Chapter 3 of this thesis has been submitted for publication in July, 2012 under the title and authorship:

Miller, C.E., Kopylova, M., Smith, E., Fibrous diamond formation by "cold" metasomatism: new constraints on the timing and conditions involved in fibrous diamond growth.

Samples were contributed to this research by J. Ryder of Dianor Resources, Inc. I completed all polishing and cleaving of diamond samples, as well as collection of electron microprobe analyses for Wawa and Diavik samples analyzed in this study. Carbon isotope analysis of non-fibrous diamond samples was conducted at the Sobolev Institute of Geology and Mineralogy, Siberian Branch of RAS. Much of this manuscript was written with the assistance of Dr. Maya Kopylova, who also authored portions of the discussion sections, in addition to providing editorial comments and feedback throughout the manuscript. Evan Smith additionally authored and edited small amounts of Chapter 3 as a co-author on the submitted paper.

Table of Contents

Abstract ii
Preface iii
Table of Contents iv
List of Tables vi
List of Figures vii
Abbreviations viii
Acknowledgements ix
Dedication x
1. Introduction 1
1.1 Project motivation 1
1.2 Samples 2
1.3 Current models on diamond forming processes and environments 7
1.3.1 Diamond types 7
1.3.1.1 Diamond appearance and inclusions 7
1.3.1.2 Nitrogen aggregation 8
1.3.2 Inclusion paragenesis 9
1.3.3 Craton characteristics and stability 10
1.3.4 How diamonds form 11
2. Vanished diamondiferous cratonic root beneath the Southern Superior province: Evidence from diamond inclusions in the Wawa metaconglomerate 13
2.1 Summary 13
2.2 Introduction 13
2.3 Samples and analytical methods 16
2.4 Physical characteristics 17
2.5 Inclusion chemistry 18
2.5.1 Chromite 21
2.5.2 Olivine 25
2.5.3 Garnet 25
2.5.4 Orthopyroxene 25
2.6 Geothermobarometry 28
2.7 Discussion 34

2.7.1 Harzburgitic origin of metaconglomerate diamonds 34
2.7.2 Lithosphere and thermal regime of the Southern Superior in the Archean-Mesozoic 36
2.7.3 Present lithosphere and thermal regime of the Southern Superior 40
2.7.4 Destruction of the diamondiferous cratonic root in the Archean-Proterozoic 42
2.7.5 Mechanisms of root destruction 43
2.7.6 How was the Southern Superior diamondiferous root destroyed? 45
2.8 Concluding remarks 47
3. Fibrous diamond formation by "cold" metasomatism: new constraints on the timing and conditions involved in fibrous diamond growth 48
3.1 Summary 48
3.2 Introduction 48
3.3 Samples and methods 50
3.3.1 Samples 50
3.3.2 Analysis 52
3.3.3 Quantitative analysis of microinclusions: methodology and accuracy 53
3.4 Results 59
3.4.1 Mineral chemistry 59
3.4.2 Thermometry 63
3.5 Discussion 63
3.5.1 Evolution of mineral compositions during formation of fibrous diamonds 63
3.5.2 Evolution of the thermal regime accompanying formation of fibrous diamonds 68
3.5.3 Metasomatism accompanying fibrous diamond growth 69
3.5.4 Are fibrous diamonds older and not grown from proto-kimberlitic fluids? 73
4. Conclusions 78
References 81
Appendix A: Wawa non-fibrous diamond characteristics 94
Appendix B: Wawa non-fibrous diamond inclusion electron microprobe analyses 101
Appendix C: Wawa non-fibrous diamond carbon isotope analyses 118
Appendix D: Raw electron microprobe data for non-fibrous diamond mineral inclusions 119
Appendix E: Wawa non-fibrous diamond inclusion Zn-in-chromite analyses 128
Appendix F: Replicate analyses for olivine microinclusions in fibrous diamonds from Wawa 130
Appendix G: Raw electron microprobe data for fibrous diamond mineral inclusions 133

List of Tables

Table 2.1. Identified inclusions from Wawa conglomerate diamonds 20
Table 2.2. Select mineral inclusion compositions and thermobarometry results 22
Table 2.3. Iterative P-T point solving for sample Wsc13 33
Table 2.4. Approximate P-T intersections of garnet-olivine temperature calculations with the minimum and maximum geothermal gradients for the Archean Southern Superior 37
Table 3.1. Electron microprobe analyses for fibrous diamond inclusions from Wawa and Diavik. 54

List of Figures

Figure 1.1. Sample location map for this study 3
Figure 1.2. Photographs of fibrous diamond morphologies 4
Figure 1.3. Photographs of non-fibrous diamond morphologies 5
Figure 1.4. Photographs of mineral inclusions in Wawa non-fibrous diamonds. 6
Figure 2.1. Regional map of tectonic terranes in the Superior craton 15
Figure 2.2. Carbon isotopic range 19
Figure 2.3. Composition of the DI chromite 24
Figure 2.4. Histogram demonstrating the range of Mg# for olivine and orthopyroxene 26
Figure 2.5. Garnet inclusion analyses from the Wawa metaconglomerate 27
Figure 2.6. Pressure-temperature diagram illustrating thermobarometry calculations for metaconglomerate samples 30
Figure 2.7. Pressure-temperature diagram showing preferred pressure-temperature estimates for the metaconglomerate diamonds 31
Figure 2.8. Pressure-temperature diagram comparing thermobarometry estimates for Archean DIs and post-Archean kimberlites. 39
Figure 3.1. Comparison of fibrous and non-fibrous diamond samples and mineral inclusions .. 51
Figure 3.2. Plot of Si cations versus Mg# for Wawa olivine in fibrous and non-fibrous diamonds 57
Figure 3.3. Histogram of Mg# for olivine inclusions in Wawa fibrous and non-fibrous diamonds 60
Figure 3.4. Histograms of Mg# for olivine inclusions in fibrous and non-fibrous diamonds for Diavik, Panda and Koffiefontein kimberlites 61
Figure 3.5. Compositions of garnet in Wawa fibrous and non-fibrous diamonds 62
Figure 3.6. Pressure-temperature diagram of equilibrium conditions for Wawa diamonds. 64
Figure 3.7. Ternary plots of mineral inclusion compositions from fibrous and non-fibrous diamonds from Wawa, Panda, and Koffiefontein 66
Figure 3.8. Histogram of total FeO content for garnet inclusions in Wawa fibrous and non-fibrous diamonds. 67
Figure 3.9. Plot of Zr/Y ratios in non-fibrous and fibrous diamonds 72
Figure 3.10. A Ca-Na-K (wt%) ternary diagram of compositions of fluid inclusions in diamonds and the Udachnaya East serpentine-free kimberlite 76

Abbreviations

DI = Diamond inclusion

DRC = Democratic Republic of Congo

LIP = Large Igneous Province

MGB = Michipicoten Greenstone Belt

MCR = Midcontinent Rift

PBK90 = Brey and Kohler (1990) Al-in-orthopyroxene barometer

PNG85 = Nickel and Green (1985) Al-in-orthopyroxene barometer

TBK90Ca-in-opx = Brey and Kohler (1990) Ca-in-orthopyroxene thermometer

TBK90grt-opx = Brey and Kohler (1990) garnet-orthopyroxene thermometer

THA84 = Harley (1984) garnet-orthopyroxene thermometer

TNG10 = Nimis and Grutter (2010) garnet-orthopyroxene thermometer

TOW79 = O'Neill and Wood (1979) garnet-olivine thermometer

Acknowledgements

First and foremost, I would like to thank my advisor, Maya Kopylova, for all of her guidance, assistance, and encouragement throughout my studies. Her advice has been invaluable and I've gained more knowledge in two years working with her than I ever thought possible. I would also like to thank my other committee members, Kelly Russell and Jim Mortensen for their contributions and feedback.

Research compiled in this thesis was made possible thanks to funding from an NSERC Discovery grant to M. Kopylova, samples and support received from J. Ryder (Dianor Resources), and samples from Diavik Diamond Mines Inc. obtained with the assistance of H. McLean, C. Kinakin, and G. Villegas (collected by E. Smith; UBC Diamond Research Lab). M. Raudsepp and E. Czech are also acknowledged and greatly thanked for their assistance with data collection on the electron microprobe. I would also like to thank the reviewers that made publication of portions of this thesis possible, including H. Helmstaedt and the reviewers that remained anonymous.

Lastly, I want to thank my friends here at UBC, especially my lab mates Wren, Evan, and Yvette, and those elsewhere, especially Ashley, for their support and for providing me with a social outlet that was much needed during my time here. And of course, I must thank my parents, because without their encouragement, love, and support I would never have had the courage to not only pursue a higher degree in my education, but move to another country in order to do so.

Dedication

To my parents, Charles and Patricia Miller

1. Introduction

1.1 Project motivation

The primary goal of this research is to fully characterize the state of the lithospheric mantle beneath the Southern Superior province, including composition of the mantle host rock, thermal state of the mantle in the Archean, and implications for known tectonic activity in the area. To achieve this, diamonds containing mineral inclusions were chosen as the sample set for this study.

Mineral inclusions were analyzed because of their unique ability to provide a snapshot of mantle chemistry at the time of diamond formation. The diamond protects inclusions from alteration by outside influences during its residence in the mantle and transport to the surface by kimberlite magma or other host magma (Gurney et al., 2010). Isotopic dating of diamond reveals ages from ~0.99 to 3.50 Ga (Gurney et al., 2010, and references therein); thus diamonds become vessels providing our only direct source of information on the Archean mantle, whereas xenoliths are subject to alteration and generally reflect mantle conditions from the time of kimberlite eruption (e.g., Phanerozoic). Tracing changes in mantle composition then becomes possible using the older diamond inclusion data and younger mantle xenoliths or xenocrysts recovered from the same kimberlites as points for comparison.

In addition to determining the composition of the mantle host rocks, mineral inclusion chemistry makes possible estimations of temperatures and pressures in the mantle at the time of diamond formation through cation exchange reactions. Similar thermometers and barometers applied to polycrystalline xenoliths record conditions just prior to emplacement at the surface, again offering a way of tracing changing conditions in the mantle. The combination of temperature and mantle lithology in a known cratonic or orogenic tectonic setting of diamond formation help to elucidate the geologic history of an area.

Many studies of mineral inclusions in diamonds have been conducted for various places worldwide, resulting in a large database of compositional data for potential mantle host rocks and connections between mantle rocks and diamond potential for a deposit. By analyzing diamonds and their inclusions from the Southern Superior province, a new location is added to

the larger world dataset, and models for thermal and tectonic processes surrounding diamond formation and cratonic roots can be further developed in terms of local events that may have had an effect on the survival of the cratonic root.

An additional goal of this study is to further clarify processes of fibrous diamond formation. The fluid from which fibrous diamonds grow is well-characterized due to the trapping of thousands of fluid microinclusions during rapid growth (Navon et al., 1988); however, conditions of fibrous diamond growth, such as temperature, are not well-constrained. The further constraint of the temperature of fibrous diamond growth in the mantle achieved through fibrous diamond inclusion analysis allows for comparison to the thermal state of non-fibrous diamond growth, clarifying how the process of fibrous diamond formation affects the mantle.

1.2 Samples

Diamonds analyzed for this research are from a metaconglomerate deposit located in the Wawa subprovince of the Superior province (Figure 1.1). These samples were collected in 2004 and consist of diamonds that are hosted in one of the world's oldest detrital diamond deposits. The metaconglomerate, located 12 km northeast of the town of Wawa, is contained within the Michipicoten Greenstone Belt (MGB), with a complex geological history involving three cycles of bimodal volcanism. The conglomerate is Archean in age (2.695-2.700 Ga) and contains indicator minerals suggestive of an Archean kimberlite primary source in close proximity (i.e., the northern Wawa or Opatica subprovinces) that has now been completely eroded away (Kopylova et al., 2011).

The samples analyzed in this research consisted of a subset of both non-fibrous and fibrous diamonds from the Wawa metaconglomerate, which were extracted by commercial dense media separation. Samples from the Diavik mine were a subset of fibrous diamonds of two different sieve sizes, collected by Evan Smith (UBC) in 2011. Whereas fibrous samples displayed dominantly cuboid morphology (Figure 1.2), non-fibrous diamonds displayed a wider range of morphologies, dominated by whole and fragmented octahedral diamonds, but including cubo-octahedrons, dodecahedroids, macle, and polycrystalline aggregates (Figure 1.3). Non-fibrous samples for this study were selected based on their observable inclusion content (Figure 1.4), but are still considered to be a representative subset of the larger suite of metaconglomerate

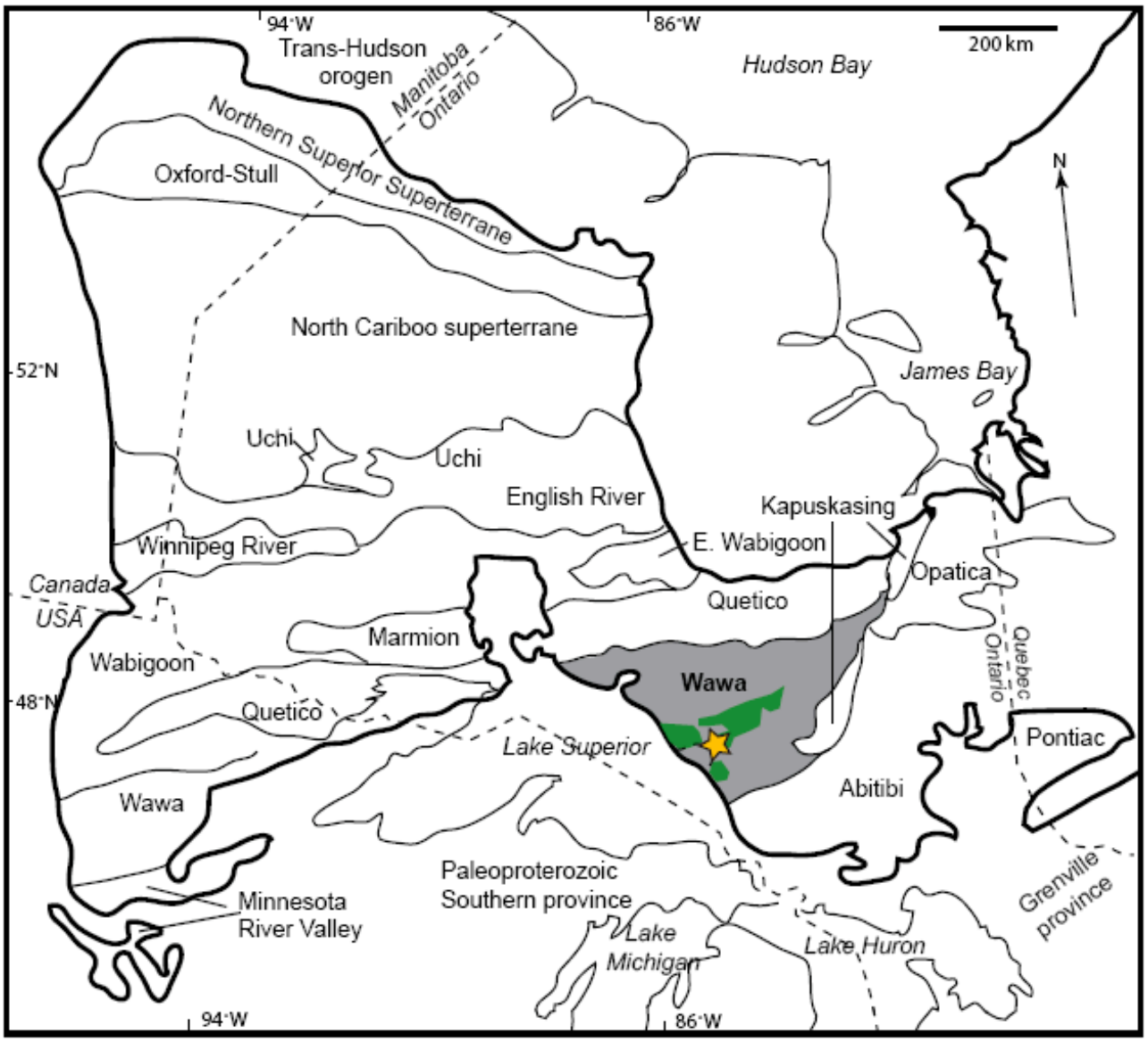

Figure 1.1. Sample location map for this study after Williams et al. (1991) and Percival et al. (2006). *Dark outline* corresponds to the Superior craton boundary, whereas thin lines represent geographical boundaries between tectonic domains. Diamonds analyzed are from a metaconglomerate (*star*) located within the MGB (*green area*) of the Wawa subprovince (*grey*).

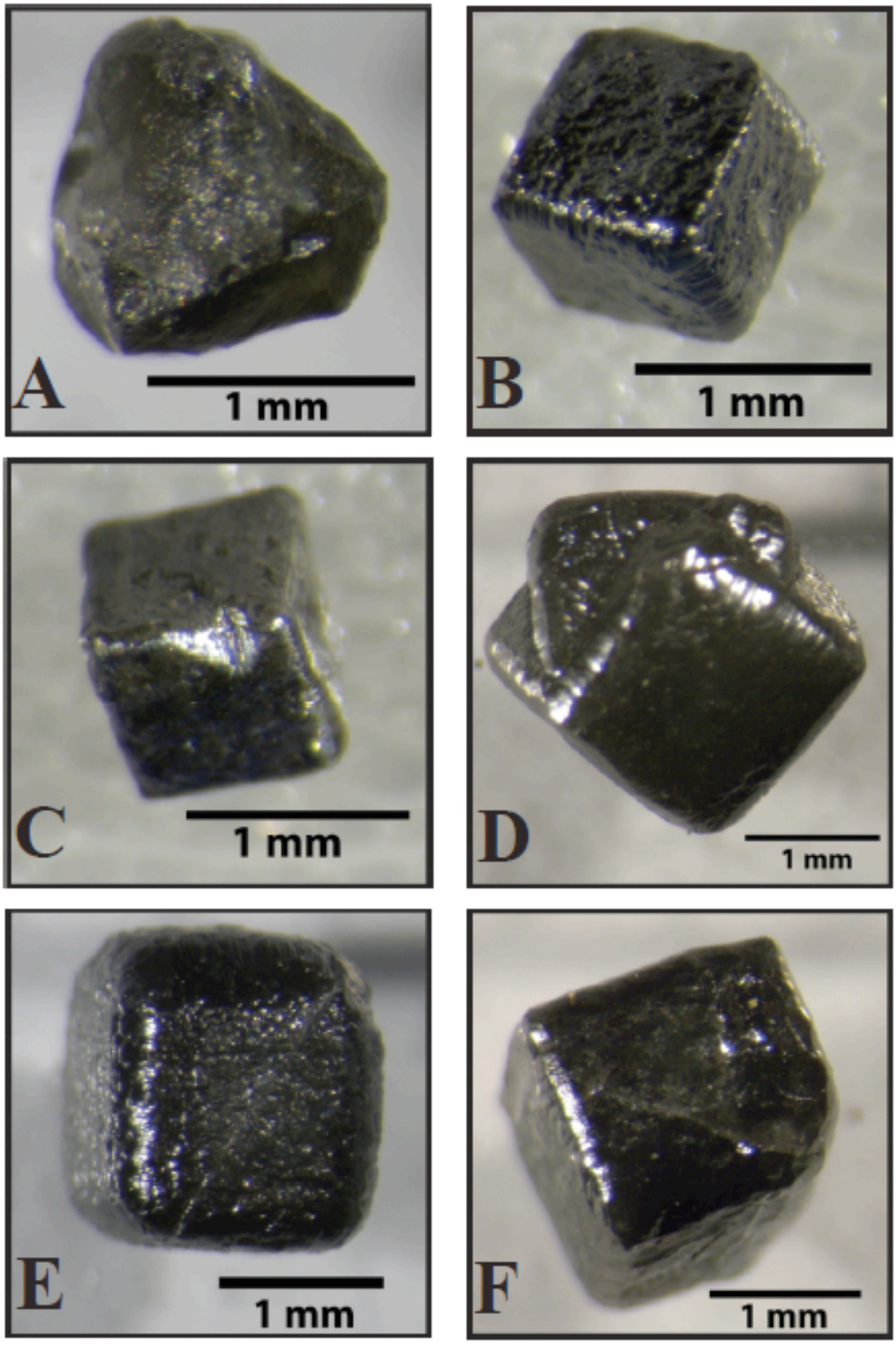

Figure 1.2. Photographs of fibrous diamond morphologies from the Wawa metaconglomerate (A-C) and the Diavik mine (D-F). Samples are dominated by cubic habit, with sample (D) exhibiting twinning.

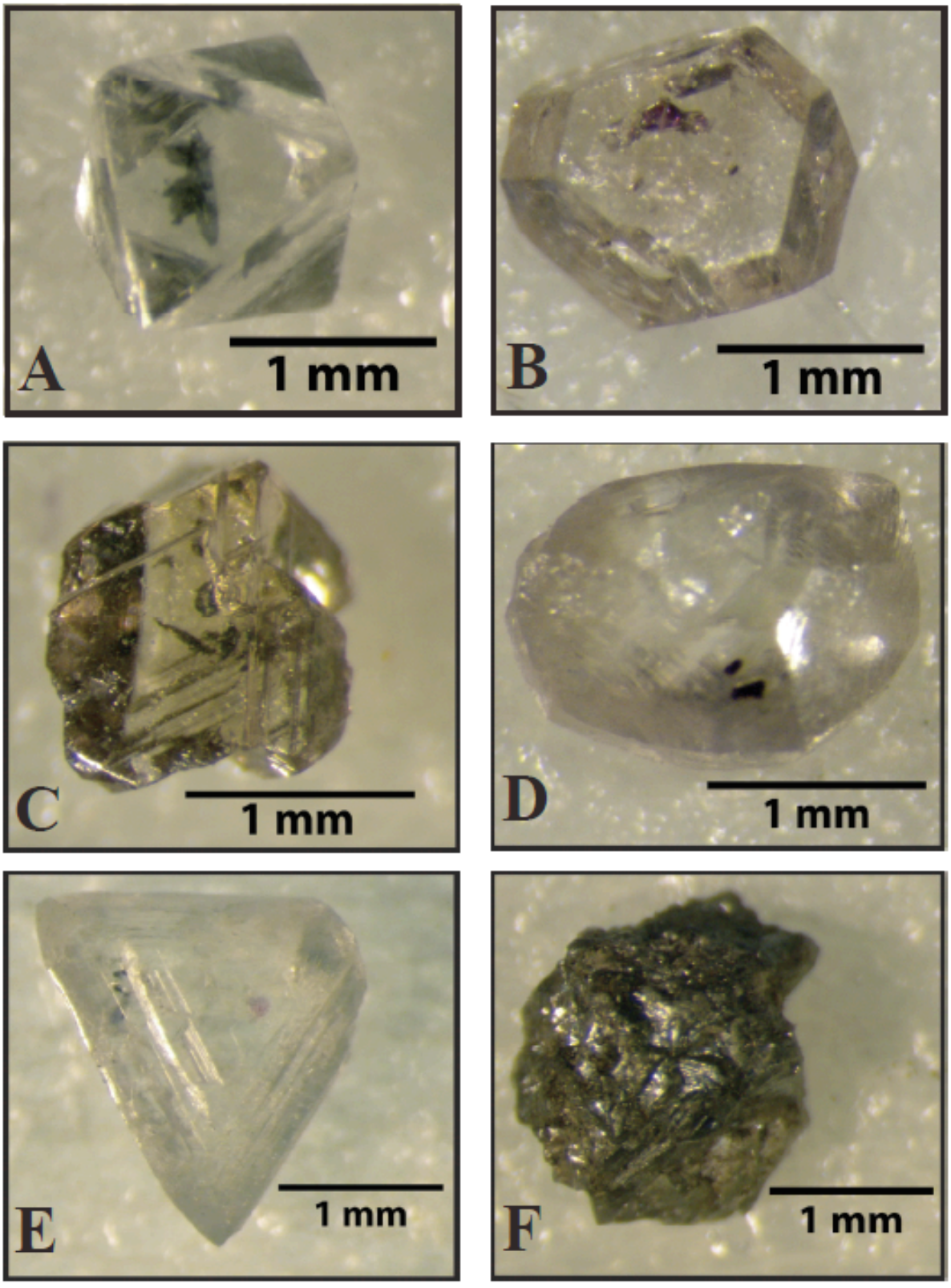

Figure 1.3. Photographs of non-fibrous diamond morphologies observed in metaconglomerate diamonds from this study. (A) octahedral; (B) cubo-octahedral; (C) octahedral fragment; (D) resorbed dodecahedroids; (E) macle; (F) polycrystalline aggregate.

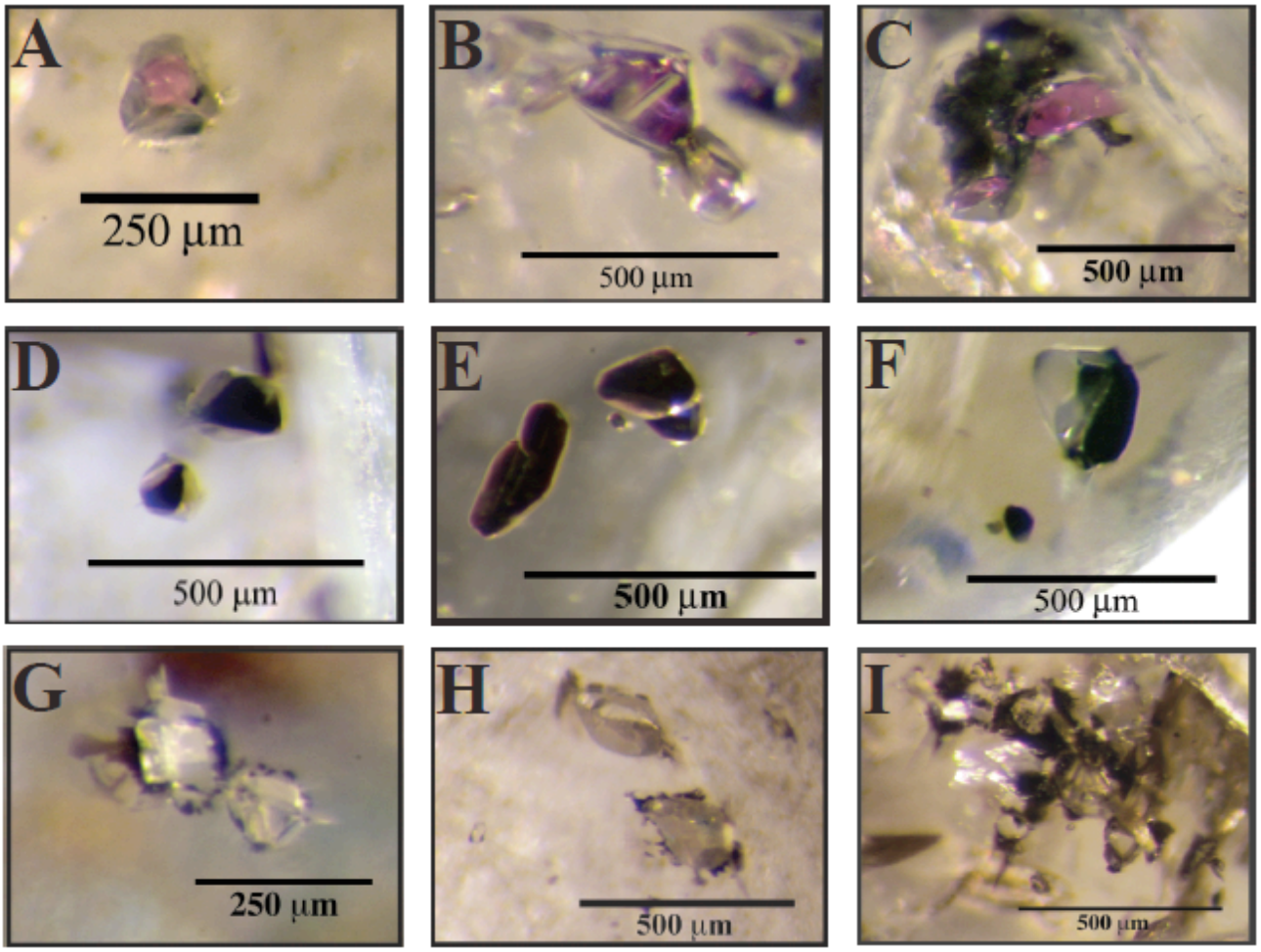

Figure 1.4. Photographs of mineral inclusions in Wawa non-fibrous diamonds. Observed inclusion types include Cr-pyrope (A-C), Mg-chromite (D-F), olivine (G-H *lower inclusion*), and orthopyroxene (H *upper inclusion*-I).

diamonds. Fibrous samples were chosen based on the general appearance and sample turbidity, with darker, more heavily included diamonds being preferentially selected in order to maximize the possibility of finding a larger abundance of inclusions for analysis.

1.3 Current models on diamond forming processes and environments

1.3.1 Diamond types

There are two main types of diamonds, which differ in terms of style of growth, appearance, and inclusion type and abundance. The more common and well-known type are the non-fibrous, or gem-quality diamonds, with the other being fibrous diamonds. Certain characteristics of these two types of diamond indicate that they form in separate, distinct events; the non-fibrous diamonds are older, and the fibrous diamonds a younger event. The most important of these characteristics is the diamonds' nitrogen aggregation state, which is used to determine how long a diamond has resided in the mantle prior to emplacement at the Earth's surface.

1.3.1.1 Diamond appearance and inclusions

Non-fibrous diamonds are dominated by an octahedral morphology, with varying levels of resorption, but can display a range of morphologies, including cubo-octahedral, cubic, dodecahedroids, macle, and irregular aggregates (Gurney et al., 2010). Diamonds crystallize smooth crystal faces in a step-like process forming transparent crystals, but these are commonly resorbed. Inclusions in non-fibrous diamonds are typically on the scale of tens to hundreds of microns in size, comprise mainly silicate or sulfide minerals, and are less abundant than in fibrous samples (Gurney et al., 2010). Inclusion morphology is generally diamond-controlled (e.g.., cubo-octahedral) consistent with syngenetic growth with the diamond, as opposed to protogenetic, with morphology governed by the mineral's crystal structure, or epigenetic, infiltrating along cracks after diamond growth (Stachel and Harris, 2008).

Fibrous diamonds are typically of a cubic habit, occurring as individual crystals or as coats on top of non-fibrous cores. The crystals are bound by rough surfaces formed due to rapid, dendritic diamond growth from a fluid, resulting in the trapping of thousands of microinclusions. The abundant microinclusions give fibrous stones a turbid appearance and grey to black coloring (Gurney et al., 2010, and references therein). The microinclusions are on the micron to sub-

micron scale and can include silicate minerals, similar to the non-fibrous diamonds, but are dominated by fluid inclusions containing variable amounts of carbonate, water, and brine (Izraeli et al., 2001; Klein-Ben David et al., 2009; Bureau et al., 2012). The fluid inclusions in these diamonds represent the diamond-forming fluid, and therefore provide direct samples of deep mantle fluids that we cannot get elsewhere (Navon et al., 1988).

1.3.1.2 Nitrogen aggregation

The timing of fibrous diamond growth and residence time within the mantle prior to eruption are best constrained by nitrogen impurity characteristics. Nitrogen aggregation state can be used to determine how long a diamond has spent in the mantle after formation, and is controlled by time, nitrogen content, and temperature (Taylor et al., 1996). Nitrogen initially substitutes as single atoms into the diamond structure as C-centers; these diamonds are called Type Ib. Single nitrogen quickly aggregates at mantle temperatures into nitrogen pairs, or A-centers, creating Type IaA diamonds. Depending on mantle temperatures, this aggregation can occur as quickly as a few thousand years and as long as 7 Myr (Taylor et al., 1996). The transition from nitrogen pairs to groups of four nitrogen atoms and a vacancy (B-center in Type IaB diamond), , is a longer process (Navon, 1999).

Both fibrous diamonds and fibrous coats typically have high nitrogen contents (800-1500 ppm) and all exhibit mild IaA aggregation states (Boyd et al, 1987; 1994). Very rarely, type Ib diamonds are found, and are always fibrous in nature (Taylor et al., 1996). The low aggregation state of nitrogen in fibrous diamonds is believed to represent short residence times in the mantle and formation in as little as ~5 Myr prior to kimberlite eruption (Navon, 1999; Gurney et al., 2010). Nitrogen aggregation rules out fibrous diamond formation from the kimberlite melt itself, however, because the time scale for even the quickest aggregation to IaA centers (days) is still longer than the time scale (hours) for kimberlite eruptions (Taylor et al., 1996). Studies comparing fibrous coats to non-fibrous cores also show a marked difference in nitrogen aggregation and content between the two, suggesting that the coat grew in a later event from a different fluid (Boyd et al., 1987; 1994).

In contrast, non-fibrous diamonds are typically of type IaA, IaB, or a transition between the two (IaAB). Aggregation from A- to B-centers is a much slower process than C- to A-center

aggregation, and operates on the scale of billions of years (Navon, 1999), indicating much longer residence times for non-fibrous diamonds than observed in fibrous samples. Long residence times based on nitrogen aggregation also match well with isotopic dating of non-fibrous diamonds, indicating Precambrian ages of formation (0.99-3.5 Ga), but Phanerozoic ages of kimberlite emplacement (Gurney et al., 2010, and references therein). This makes the non-fibrous diamond forming event older than the one responsible for fibrous diamond growth.

1.3.2 Inclusion paragenesis

Diamonds form in three different parent rock types in the lithospheric mantle, peridotitic, eclogitic, and websteritic, as well as in the lower mantle. A review of more than 5000 inclusion analyses by Stachel and Harris (2008) revealed links between mineral inclusion composition and diamond host rock in the mantle. Peridotitic diamonds are known to be the most common among upper mantle diamonds, with more than 60% of the world's diamonds falling into that category; this is followed by eclogitic diamonds comprising ~30% (Stachel and Harris, 2008). Inclusion assemblages within diamonds of the two main host rocks match the mineralogy of the mantle rocks, with peridotitic diamonds containing Cr-pyrope garnet, olivine, enstatite, Cr-diopside, Mg-chromite, and Ni-Fe sulfides, and eclogitic diamonds containing grossular-almandine-pyrope, omphacitic clinopyroxene, and Fe sulfides (Stachel and Harris, 2008). A further classification of diamond host rock is based on garnet chemistry. The Cr_2O_3 and CaO content of peridotitic garnet inclusions allows them to be divided into low-Ca harzburgitic, lherzolitic, and wehrlitic categories according to the classification developed by Gurney and Zweistra (1995) and later revised by Grutter et al. (2004). Eclogitic garnet is generally defined by <1 wt% Cr_2O_3 and websteritic garnets are similar to lherzolitic, but with Mg/(Mg+Fe) <0.7 (Grutter et al., 2004).

Determination of the parent diamond paragenesis can be useful in unraveling the thermal and tectonic conditions of diamond formation. Certain rock types are associated with different geological settings, some of which are known to yield higher diamond potential, i.e., depleted, harzburgitic cratonic roots beneath Archean cratons (Helmstaedt and Gurney, 1995). Pairing a mantle host rock for a diamond suite with the age of the diamonds is also useful for determinining the compositional evolution of the mantle.

1.3.3 Craton characteristics and stability

The majority of diamonds grow within the cratonic mantle. This portion of the mantle is dominated by peridotitic rocks and cool temperatures favorable for diamond growth. Therefore, it is important to understand craton dynamics when attempting to unravel the history of a particular diamond suite.

Cratons are defined as relatively flat, stable regions of crust that have remained undeformed since the Precambrian (King, 2005). Craton growth was substantial in the Archean producing old crust in the core of most continents. The oldest dated rocks currently on Earth are from the Acasta gneiss (4.0 Ga; Stern and Bleeker, 1998), however, U-Pb ages for detrital zircons imply that older crust existed as early as 4.4 Ga, and was subsequently destroyed by meteor impacts (Windley, 1998; Wilde et al., 2001). Accretion and amalgamation of crust occurred rapidly after this with large volumes of crust formed by 3.7 Ga.

The lithospheric mantle roots attached to the cratons have been shown through seismic and xenolithic studies to be cold, depleted areas, extending to depths of 200-250 km (James et al., 2004; King, 2005). Xenoliths also reveal that the formation of cratons and cratonic roots was roughly simultaneous, with roots cooling and stabilizing by the Late Archean (King, 2005). Heat was transported through cratonic roots by conduction, and depletion in heat producing elements (K, Th, U) resulted in significantly cooler roots when compared to the surrounding convecting mantle (Sleep, 2003). Typical geotherms for cratonic areas worldwide range from 36-42 mW/m^2 (Stachel and Harris, 2008), contrasting with areas such as flood basalt provinces (~90 mW/m^2; Pollack et al., 1993) or areas with significantly thinner crust and lithospheric mantle (70-80 km, 64 mW/m^2, Zhang, 2012). The extension of relatively cold temperatures into the deeper mantle affects the diamond stability field and creates ideal conditions for the formation of diamonds (Helmstaedt and Gurney, 1995).

Cratonic roots protrude into the mantle and disrupt lateral convection in the upper mantle (King, 2005). Diamondiferous roots must stay insulated against reheating, avoid tectonic reworking and mechanical erosion by the convecting mantle, and remain attached to the overlying craton during plate movement to remain stable (Helmstaedt and Gurney, 1994). To resist mechanical erosion for long periods of time, the roots must possess chemical buoyancy, high viscosity, and high

mechanical strength. It is the combination of all of these that is key in root survival (Sleep, 2003; King, 2005).

Helmstaedt and Gurney (1994) and Helmstaedt and Gurney (1995) first presented the idea of cratonic root "friendly" and "unfriendly" processes that can be active in the mantle. Friendly processes, such as lateral intrusions and thin-skinned deformation, would leave the root intact, whereas subduction, kimberlite propagation, and plume activity would erode and eventually destroy a root. The root-destructive processes involve reactivation and reworking of basement rock, something that occurred in the Superior Province until about 2.4 Ga (Helmstaedt and Gurney, 1994).

1.3.4 How diamonds form

Diamonds of both non-fibrous and fibrous types are known to be xenocrystic in relation to their host kimberlite, having formed within the mantle host rock before emplacement. Formation of non-fibrous and fibrous diamonds occurs in two separate events involving metasomatism (Stachel and Harris, 2008; Gurney et al., 2010).

Non-fibrous diamond can exhibit homogeneous growth, with no zoning, or heterogeneous zoned growth, as revealed through cathodoluminescence of diamonds (Bulanova, 1995). Zoning indicates growth in multiple stages, under changing mantle conditions, with the possibility of development of more than one morphology in a diamond's history (Bulanova, 1995). The medium of non-fibrous diamond growth is still a mystery as the growth is slow and does not result in the trapping of the diamond-forming medium. Temperatures and pressures of formation, however, indicate subsolidus crystallization for peridotitic and eclogitic diamonds, favoring growth from percolating metasomatic fluids rather than from melts (Stachel and Harris, 2008). This may have been achieved through the reduction of carbonate-bearing fluids, or oxidation of methane-bearing fluids (Frost and McCammon, 2008). Many experiments have been run using different growth environments and fluids, with the ultimate conclusions that alkaline carbonate, carbonate-silicate, and silicate melts containing H_2O and CO_2 were the most favorable for natural diamond growth, with increasing water content resulting in more favorable precipitation conditions (Pal'yanov et al., 1999; 2002; 2005; Pal'yanov and Sokol, 2009).

The source of the fluids responsible for diamond formation can be constrained through carbon isotope analysis. Non-fibrous diamond carbon isotopes display wide ranges in values, suggestive of heterogeneous sources (peridotitic +0.2 to -26.4 ‰; eclogitic +2.7 to -41 ‰; Cartigny, 2005; De Stefano et al., 2009). In contrast, the narrow range of carbon isotope values for fibrous diamonds (-4.1 to -12.8 ‰; Boyd et al., 1987; 1994; Gurney et al., 2010; Klein-Ben David et al., 2007; 2010) indicate a homogeneous, convecting source, such as the asthenosphere.

Fibrous diamond formation is better understood due to access to the diamond-forming fluid in the form of microinclusions. Three end-member fluids have been identified: 1) a silicic end-member rich in water, Si, Al, and K; 2) a saline end-member rich in water, Cl and K; and 3) a carbonatitic end-member rich in carbonate, Mg, Ca and K, which can be further split into a high-Mg (17-28 wt% MgO) and low-Mg (<14 wt% MgO) carbonatitic groups (Klein-Ben David et al., 2009). Continuous trends are observed between silica-carbonate and saline-carbonate end-members, but the carbonates associated with the silica-rich and saline fluids are different (Klein-Ben David et al., 2009). The abundance of carbonate inclusions in fibrous diamonds and experimental efforts to grow diamond in various media have shown that fibrous diamond precipitates from the reduction of carbonate, making this component essential in diamond-forming fluids (Pal'yanov et al., 1999; Arima et al., 2002; Frost and McCammon, 2008), similar to non-fibrous diamond growth. Compositions of fibrous diamond fluids resemble those of kimberlite melts in trace element patterns, high volatile content, and unradiogenic Sr-isotope signatures, suggesting a sublithospheric source (Akagi and Masuda, 1988; Klein-Ben David et al., 2010). This, paired with low degrees of nitrogen aggregation (IaA) in fibrous diamond, has linked fibrous diamond growth genetically and temporally to kimberlite melt propagation and associated precursor fluids, assuming rapid growth and short mantle residence times of 5-7 Myr prior to kimberlite eruption (Navon, 1999; Gurney et al., 2010).

2. Vanished diamondiferous cratonic root beneath the Southern Superior province: Evidence from diamond inclusions in the Wawa metaconglomerate

2.1 Summary

We studied diamonds from a 2.697-2.700 Ga Wawa metaconglomerate (Southern Superior craton) and identified mineral inclusions of high-Cr, low-Ca pyrope garnet, low-Ti Mg-chromite, olivine (Fo_{93}), and orthopyroxene (En_{94}). The diamonds have $\delta^{13}C$ of -2.5 to -4.0 ‰ and derive from the spinel-garnet and garnet facia of harzburgite. Geothermobarometry on non-touching, coexisting garnet-olivine and garnet-orthopyroxene pairs constrains the maximum geothermal gradient of 41 mW/m^2 for the Neoarchean and a minimum lithosphere thickness of 190 km. The depleted harzburgitic paragenesis equilibrated at a relatively cold geotherm suggests the presence of a pre-2.7 Ga diamondiferous cratonic root beneath the northern Wawa terrane or the Opatica terrane of the Southern Superior craton, i.e., beneath terranes identified as sources for the metaconglomerate diamonds. Geophysical surveys, geothermal data and petrology of mantle xenoliths emplaced in the Proterozoic-Mezozoic trace evolution of the mantle thermal regime and composition from the Archean to present. The root was thinned down to 150 km by the Jurassic, when the geotherm increased slightly to 41-42 mW/m^2. The diamondiferous root destruction was accompanied by more significant heating and was complete by 1.1 Ga in areas adjacent to the Midcontinent Rift. The geometry of the current high-velocity root and spatial correlations with boundaries of crustal terranes that docked to the nuclei of the Superior protocraton in the Neoarchean suggest that the root destruction in the Southern Superior may have been associated with tectonic erosion, craton amalgamation, and ensuing ingress of asthenospheric fluids.

2.2 Introduction

Archean cratons have particularly thick, cold, depleted roots protruding into the diamond stability field of the mantle and providing ideal conditions for formation and storage of diamonds until their eventual emplacement into the crust. Archean cratonic roots are generally considered to be long-lived, stable structures, surviving for billions of years in the hot surrounding mantle with little to no modification or activity. Despite cratons' reputation as stable, almost

indestructible terranes, there are a few cases where the cratonic roots are lost and the Archean crust is deceptively present above the mantle, which is no thicker or more depleted than the younger continental mantle. This root destruction was recorded for the North China (Liu et al., 2011; Zhang, 2012) and Dharwar (Griffin et al., 2009) cratons. In many other occurrences, root-destructive processes heated, thinned and modified the cratonic lithosphere, but stopped short of destroying it completely, like in the Kaapvaal (Griffin et al., 2003b) and other African cratons (Begg et al., 2009). This study shows that the diamondiferous root below the Southern Superior craton has also vanished. In contrast to the mantle in the northern part of the craton, the Southern Superior craton does not show high seismic velocities indicative of lithosphere thicker than 150 km (Faure et al., 2011). The thicker keel extending to the diamond stability field existed beneath this area prior to 2.7 Ga, as has been inferred from studies of diamonds in Neoarchean lamprophyres and related volcaniclastic breccias (Stachel et al., 2006; De Stefano et al., 2006) located 20 km north of the town of Wawa, within the Michipicoten Greenstone Belt (MGB). Here we present a detailed account on the composition and thermal state of the Archean mantle root below the Southern Superior.

Our study characterizes mineral inclusions in diamonds from another diamond occurrence within the MGB, separate from the lamprophyric dykes and breccias. Diamonds were extracted from a metaconglomerate unit 12 km northeast of the town of Wawa, in the Wawa-Abitibi terrane of the Superior craton (Figure 2.1). This terrane, which is partly juvenile and partly built on the continental crust (Ketchum et al., 2008), docked against the growing Superior craton from the south at ~2.695 Ga (Percival et al., 2006). The Wawa-Abitibi terrane is a collage of greenstone belts separated by late granitoids. The MGB contains mostly supracrustal volcanics; conglomerates and other sedimentary rocks that formed in a successor basin, which unconformably overlies the ~2.7 Ga bimodal mafic-felsic volcanics. All rocks were metamorphosed into the greenschist facies in the 2.68 Ga orogeny (Williams et al., 1991). The 2697–2701 Ma metaconglomerate preserved detrital heavy minerals and diamonds that were sourced from the northern Wawa terrane or the Opatica terrane of the Superior craton (Kopylova et al., 2011; Figure 2.1). These pre-2.7 Ga Superior protocratons developed diamondiferous roots that were sampled by kimberlites, which have now been completely eroded away (Kopylova et al., 2011).

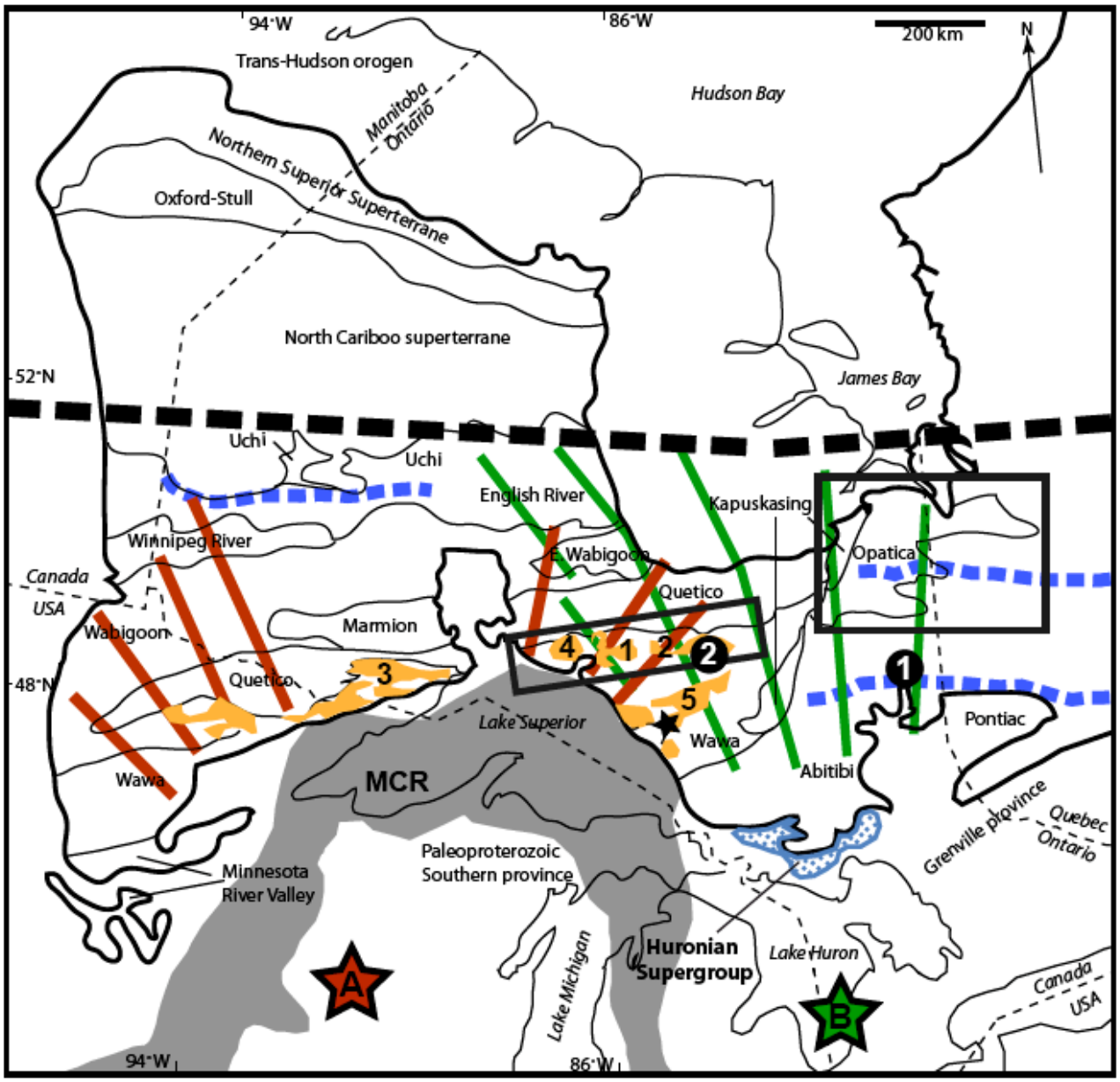

Figure 2.1. Regional map of tectonic terranes in the Superior craton after Williams et al. (1991) and Percival et al. (2006). *Dark outline* corresponds to the Superior craton boundary, whereas *thin lines* represent geographical boundaries between tectonic domains. *Shaded regions* correspond to greenstone belts in the Wawa terrane: 1- Shreibert-Hemlo; 2 - Manitouwadge-Hornepayne; 3- Shebandowan; 4- Winston Lake; 5- Michipicoten. The Wawa metaconglomerate host (*black star*) to the diamonds studied lies within the Michipicoten greenstone belt. *MCR* = Midcontinent Rift. *Rectangles* delineate areas identified as possible sources for the metaconglomerate detritus by Kopylova et al. (2011). *Thick dashed line* shows the southern border of the high-velocity cratonic root in the diamond stability field (Faure et al., 2011). *Solid dots* are locations of post-Archean kimberlites in the vicinity of Wawa: 1) Kirkland Lake (Heaman and Kjarsgaard, 2000; Heaman et al., 2004), 2) Wawa kimberlite (Kaminsky et al., 2002). *Star A* represents plume head location for the Marathon and Fort Frances plume and associated dyke swarm (Ernst and Bleeker, 2010). *Star B* indicates plume head location for the Matachewan plume and associated dykes (Ernst and Bleeker, 2010). *Dashed horizontal lines* indicate locations of subduction scars (Faure et al., 2011). Huronian Supergroup sediments (*spotted pattern*) may be remnants of the larger Proterozoic rift basin in this area (Young et al., 2001).

What are geologic processes that could remove or thin cratonic roots? Since the early review of "root-unfriendly events" (Helmstaedt and Gurney, 1995), multiple studies of individual cratons have presented us with various answers to this question. The mechanisms include delamination due to collision and lithospheric folding (Zhang, 2012), continental rifting and plume arrival (Helmstaedt and Gurney, 1995; Griffin et al., 2009), and metasomatism and fertilization by asthenospheric melts (Griffin et al., 2003a; Begg et al., 2009, Faure et al., 2011). Our study attempts to constrain the scenario of the root destruction below the Southern Superior province by identifying physicochemical changes that accompany various geological mechanisms listed above, and comparing these changes to petrological parameters recorded in the Southern Superior mantle samples of different ages. Evolution of the thermal state and the lithospheric lithologies sampled by post-Archean kimberlites in the vicinity of Wawa and the geometry of the current Superior root imply that the diamondiferous root was most likely destroyed by tectonic erosion and ensuing ingress of asthenospheric fluids.

2.3 Samples and analytical methods

We studied 65 inclusion-bearing diamonds selected from 83 carats extracted from Wawa metaconglomerate (Ryder et al., 2008; Kopylova et al., 2011) in Ontario. Macro-diamonds (>0.5 mm) were separated from approximately 300 tons of metaconglomerate by commercial dense media separation plants. Observations employing a binocular microscope documented diamond's morphology, resorption, weight, color, and surface features and the size, color, and orientation of each inclusion in the diamond (Appendix A). Note was made of any cracks in the diamonds and the inclusions' proximity to these cracks.

Diamonds were polished with a regular diamond-impregnated steel wheel to expose mineral inclusions and then mounted in an acrylic disc using a small amount of carbon putty and aluminum foil. Sample discs were carbon coated and inclusions identified using a Philips XL30 SEM with a Bruker Quantax 200 microanalysis system and light element XFLASH 2010 detector at the University of British Columbia, Department of Earth, Ocean, and Atmospheric Sciences.

Quantitative chemical analysis was done using a CAMECA SX-50 electron microprobe (UBC, Dept. of Earth, Ocean, and Atmospheric Sciences; Appendix B). Analysis of all elements,

except Zn in chromite, was done with a beam current of 20 nA, acceleration voltage of 15kV, peak count time of 20 s, and two 10 s backgrounds. One to five points of data were collected from each inclusion, depending on size, to test for heterogeneities within the inclusion. Detection limits for most oxides were below 0.06 wt%, most of them closer to 0.02 wt%, with the exception of Ni (0.07 wt%). Calculations for Fe^{3+} content were done using the program *Formula*, assuming perfect stoichiometry. For Zn analysis, a beam current of 100 nA, acceleration voltage of 20 kV, and count time of 100 s for both peak and background lowered the detection limit to approximately 100 ppm, similar to methods used by Lavrent'ev et al. (2005). Lavrent'ev et al. (2005) showed that reliable Zn concentrations with a precision level of ±30 ppm can be measured on an electron microprobe for Zn thermometry. Two to five analysis points were chosen for each grain dependent on grain size. Precision for Zn analyses was ±0.004 wt% (±40 ppm).

Measurements of the carbon isotope composition were performed using the Finnigan MAT Delta instrument in a dual inlet mode (Sobolev Institute of Geology and Mineralogy, Siberian Branch of RAS). A sample of 0.5-1 mg in weight, packed into platinum foil was placed into a reactor tube made of a fused quartz together with a purified copper oxide. The reactor was pumped down to the pressure of 10^{-4} Pa and then heated up to 950°C for 20 minutes to complete the combustion of the sample. Resulting carbon dioxide was purified and transferred to a detachable glass vial (Reutskii et al., 1999). The reproducibility of the carbon isotope composition measurements, including the sample preparation procedure, is better than or equal to 0.1‰. The USGS-24 standard (graphite with $\delta^{13}C$=-15.9‰ PDB) was used to control the isotope analysis procedure. All the $\delta^{13}C$ values are given in relation to the PDB standard.

2.4 Physical characteristics

Diamond samples, as reported in Appendix A, consist of both whole diamonds (71%) and fragments (29%). Whole crystals exhibit a dominantly octahedral morphology (52%), followed by dodecahedroids (24%), macle (9%), polycrystalline aggregates (9%), and cubo-octahedrons (6%) in order of decreasing abundance. More than half of the fragments (68%) can be identified as fragments of octahedral diamonds.

The subset of metaconglomerate diamonds chosen for this study is a good representative sample of the Wawa metaconglomerate diamond population, as sampled by the initial due diligence study (734 diamonds recovered through caustic fusion). The latter population is dominated by diamonds of octahedral morphology, with another 25% exhibiting cubic habits (Verley et al., 2007). The colors of these diamonds are white (63%), yellow (16%), amber (10%), gray (5.6%), black (4.1%), green (<1%), and pink (<1%) (Verley et al., 2007). Among diamonds with inclusions analyzed in this study, color ranges from colorless/white (60%), yellow (8%), and pink (8%) to brown (12%) and gray (12%). Sample weight ranges from 2.0 to 24.5 mg. Diamonds have different degrees of resorption, which varies between completely resorbed dodecahedroids to unresorbed octahedrons and fragments. Diamonds contain between one and twenty-one inclusions (averaging five inclusions per diamond), ranging from <100-500 μm in size in their longest dimension. Inclusions display purple, pink, dark brown, and dark red colors as well as colorless, with syngenetic cubo-octahedral morphology.

Fourteen samples from this study were analyzed for carbon isotope ratios. These samples yielded $\delta^{13}C$ values from -4.0 to -2.5‰ (Appendix C; Figure 2.2) falling within the typical range of mantle carbon (-8.0 to -2.0‰) along with >70% of the world's diamonds (Cartigny, 2005).

The metaconglomerate diamonds were previously characterized with respect to cathodoluminescence and nitrogen content. The crystals exhibit unusual cathodoluminescence colors of green and red, most likely a result of crustal storage followed by metamorphic annealing (Bruce et al., 2011). Diamonds contain <820 ppm N with 5-64% total aggregation (Bruce et al., 2011). Aggregation states for diamonds are dominated by Type IaA and IaAB (Bruce et al., 2011; Kopylova et al., 2011), corresponding to temperatures of 1000-1225°C for the mantle residence time of ~300 Ma.

2.5 Inclusion chemistry

Analysis of 173 mineral inclusions in 46 diamonds from the metaconglomerate has yielded four main mineral phases: pyrope garnet, Mg-chromite, olivine (Fo_{93}), and orthopyroxene (En_{93-95}). Mineral inclusion distribution within these 46 samples can be found in Table 2.1. The majority of the 46 selected diamonds (67%) only contain a single mineral phase, with chromite being the most abundant inclusion type in the suite. The coexisting phases chromite+olivine are the next

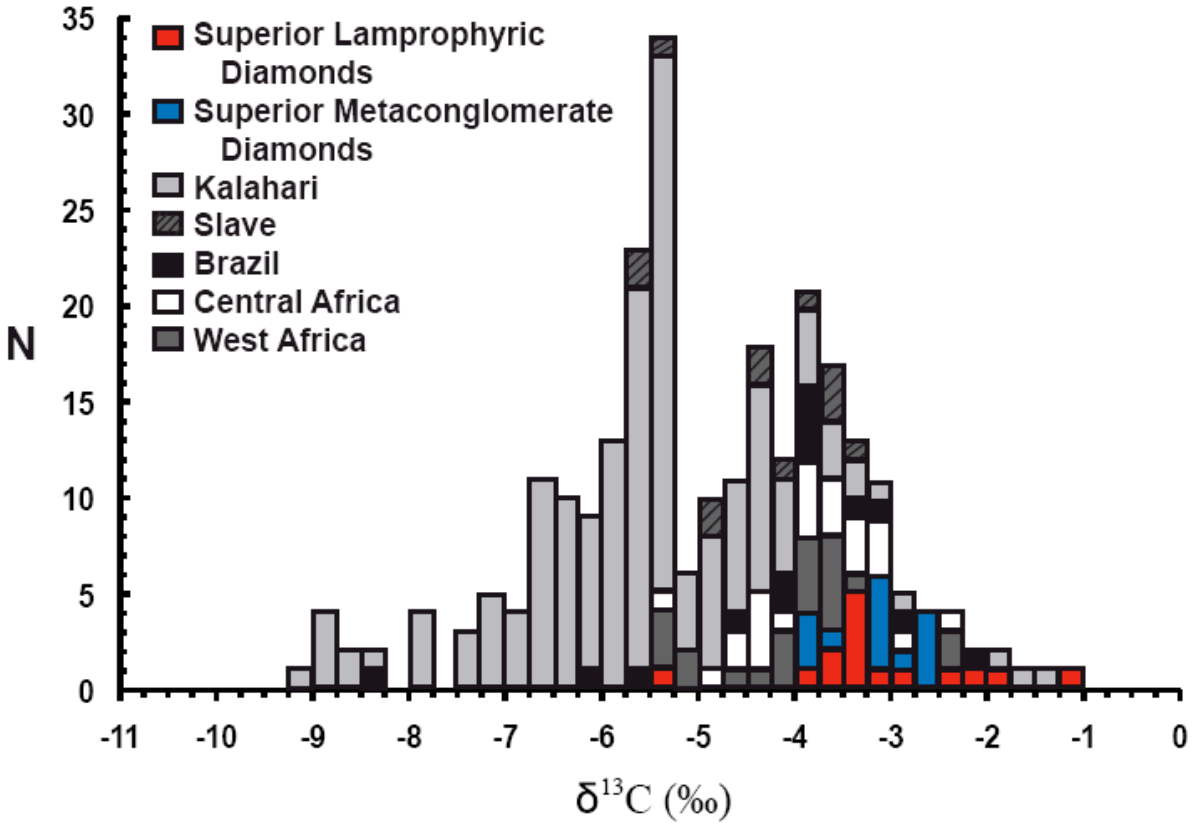

Figure 2.2. Carbon isotopic range for 14 metaconglomerate diamonds and octahedral harzburgitic diamonds from the Southern Superior lamprophyric volcanics (Stachel et al., 2006) plotted against worldwide harzburgitic diamond values by craton (Stachel et al., 2009).

Table 2.1. Identified inclusions from Wawa conglomerate diamonds

Inclusion species	No. of diamonds	No. of inclusions
Chromite	16	71
Olivine	12	27
Garnet	2	7
Orthopyroxene	1	7
Chromite, orthopyroxene	1	8, 2
Chromite, olivine	7	26, 13
Garnet, olivine	3	11, 7
Orthopyroxene, olivine	1	1, 5
Chromite, orthopyroxene, olivine	2	21, 4, 5
Garnet, orthopyroxene, olivine[a]	1	4, 1, 2

[a]garnet-olivine contact

most common assemblage, and only three samples contain three coexisting phases, with the assemblages chromite+olivine+orthopyroxene and garnet+olivine+orthopyroxene. Of all of the samples, only one has touching inclusions of two different mineral phases, garnet and olivine (Wsc13). Of the observed inclusions, 94 chromite inclusions, 50 olivine, 19 garnet, and 10 orthopyroxene have been analyzed on the electron microprobe. A representative sample of averaged chemical analyses is presented in Table 2.2, with the full version of this table included in Appendix B and raw data in Appendix D.

2.5.1 Chromite

Chromite is by far the most abundant inclusion in the metaconglomerate diamonds with 94 inclusions analyzed from 24 diamonds, exhibiting dark brown to deep red coloring depending on the size and thickness of the inclusion. Chromite contains between 60.4 and 69.0 wt% Cr_2O_3 and medium to high MgO (12.8-15.3 wt%), placing it within the diamond inclusion field of Gurney and Zweistra (1995; Figure 2.3a). The average Cr# (100*molar Cr/(Cr+Al)) for these samples is 87.2, with a range from 82.8-92.9, making it possible for the chromite to be stable within the diamond stability field (Girnis and Brey, 1999; Klemme and O'Neill, 2000; Klemme, 2004). The high FeO content of the chromite (10.3-13.5 wt%) is characteristic of chromite equilibrated with garnet (Boyd et al., 1997). With the exception of sample Wsc40, TiO_2 is less than 0.6 wt% (0.24 wt% TiO_2 average) corresponding to the general diamond inclusion (DI) constraint (Gurney and Zweistra, 1995; Sobolev et al., 2004; Figure 2.3b). The four chromite grains from sample Wsc40 with high TiO_2 are most likely a result of secondary alteration.

Chromite grains demonstrate the most significant compositional heterogeneity in Cr_2O_3, both within single grains and between multiple grains from a single diamond. Chromium oxide varies by more than 0.7 wt% Cr_2O_3 up to 2.0 wt% Cr_2O_3 in a few grains. Chromium oxide content also indicates zoning within some grains, with higher Cr_2O_3 content in the rims and lower Cr_2O_3 content in the core. A few examples of the reverse were also found, but higher Cr_2O_3 in the rims is more common. Iron oxide FeO also shows variations in excess of 0.7 wt% between grains. Assuming perfect stoichiometry and four oxygens per formula unit, Fe_2O_3 was calculated for chromite with a range of 0.9-4.7 wt% and average of 2.5 wt%. Concentrations of Zn yield a range of values between 250 and 600 ppm and an average of 365 ppm (Appendix E). Variations in Zn concentration within a single inclusion are <150 ppm, which could possibly be a result of

Table 2.2. Select mineral inclusion compositions and thermobarometry results

Sample	**Wsc01**					**Wsc13** (touching)			(touching)		**Wsc14**					
Mineral Phase[a]	chr	chr	chr	opx	opx	ol	opx	grt	grt	grt	chr	chr	chr	ol	ol	opx
# Analyses Avged	4	2	2	3	4	5	3	4	10	3	2	2	7	3	8	5
# of Grains	1	1	1	1	1	1	1	1	2	1	1	1	2	1	3	2
SiO_2	0.23	0.28	0.33	57.78	57.21	40.66	58.64	40.82	40.74	40.83	0.33	0.33	0.31	41.36	41.23	58.16
TiO_2	0.45	0.44	0.44	0.05							0.40	0.44	0.45			
Al_2O_3	6.41	6.03	6.16	0.58	0.56	0.05	0.49	16.42	16.21	16.31	7.87	7.26	7.34			0.75
Cr_2O_3	64.78	64.00	65.26	0.57	0.55	0.08	0.40	10.22	9.97	9.71	61.41	62.44	63.31	0.10	0.08	0.60
FeO	12.95	13.17	13.02	3.57	4.10	7.74	4.55	6.68	6.82	6.45	15.27	14.99	14.17	7.11	6.98	4.16
MnO				0.10	0.11	0.12	0.14	0.30	0.31	0.28				0.12	0.11	0.10
MgO	14.90	14.61	14.75	36.78	36.17	50.77	35.37	20.78	20.30	20.64	13.87	14.16	14.35	51.50	51.05	36.25
CaO				0.43	0.43	0.06	0.62	4.51	4.45	4.39				0.04	0.04	0.31
Na_2O				0.07			0.06	0.07	0.07							
NiO	0.14	0.13		0.13	0.09	0.34	0.10				0.12	0.13	0.15	0.34	0.34	0.09
Total	99.86	98.64	99.95	100.05	99.20	99.81	100.38	99.79	98.86	98.62	99.26	99.74	100.08	100.57	99.82	100.41
Mg/(Mg+Fe)	0.68	0.67	0.67	0.95	0.94	0.92	0.93	0.85	0.84	0.85	0.62	0.63	0.65	0.93	0.93	0.94
Cr/(Cr+Al)	0.87	0.88	0.88	0.40	0.40	0.72	0.35	0.29	0.29	0.29	0.84	0.85	0.85	0.77	0.75	0.35
TOW79[b]								1128	1069	1143						
PG06[c]								45	44	44						

Table 2.2. Select mineral inclusion compositions and thermobarometry results (Cont.)

Sample	Wsc18		Wsc21		Wsc25			Wsc36				Wsc51		Wsc54		Wsc62
Mineral Phase[a]	ol	opx	ol	grt	ol	grt	grt	chr	chr	ol	opx	ol	grt	grt	grt	grt
# Analyses Avged	8	5	4	6	9	12	6	11	2	3	2	3	3	11	1	3
# of Grains	3	1	2	2	3	4	2	4	1	1	1	1	1	3	1	1
SiO_2	41.18	57.30	41.24	41.01	41.33	41.14	41.02	0.27	0.35	41.48	58.01	41.31	42.61	41.80	41.35	41.48
TiO_2								0.08	0.06							
Al_2O_3	0.03	0.62	0.06	16.34	0.05	17.83	17.73	6.12	5.77		0.61		17.35	19.16	18.80	18.78
Cr_2O_3	0.09	0.51	0.06	9.89	0.07	8.25	8.32	65.21	62.79	0.04	0.53		6.12	6.83	6.75	7.38
FeO	6.59	3.90	6.90	6.18	7.14	5.91	5.82	13.52	16.82	5.95	3.66	7.90	7.47	5.82	5.68	6.37
MnO	0.10	0.09	0.11	0.28	0.10	0.27	0.24			0.10	0.08	0.11	0.33	0.25	0.24	0.24
MgO	51.66	36.66	51.18	21.92	50.84	21.68	21.99	14.38	13.23	52.35	37.25	50.61	22.16	22.68	21.94	22.45
CaO		0.18		2.82	0.05	3.51	3.46				0.12	0.06	3.38	2.71	2.77	2.69
Na_2O				0.06		0.05								0.06		0.10
NiO	0.35	0.09	0.33		0.37			0.12	0.15	0.36	0.10	0.34				
Total	100.00	99.35	99.88	98.49	99.94	98.63	98.56	99.68	99.16	100.29	100.34	100.33	99.41	99.31	97.53	99.50
Mg/(Mg+Fe)	0.93	0.94	0.93	0.86	0.93	0.87	0.87	0.66	0.59	0.94	0.95	0.92	0.84	0.87	0.87	0.86
Cr/(Cr+Al)	0.70	0.35	0.66	0.29	0.48	0.24	0.24	0.88	0.88	0.69	0.37	0.45	0.19	0.19	0.19	0.21
TOW79[b]				1076		1185	1232						1055			
PG06[c]				49		42	42						35	39	39	41

Blank entries below detection limit; TOW79= O'Neill and Wood (1979); PG06= Grutter et al. (2006)

[a]Mineral abbreviations: chr=chromite, ol=olivine, opx=orthopyroxene, grt=garnet

[b]T in Celcius @ 50 kbar

[c]P in kbar calculated for 41 mW/m^2 geotherm

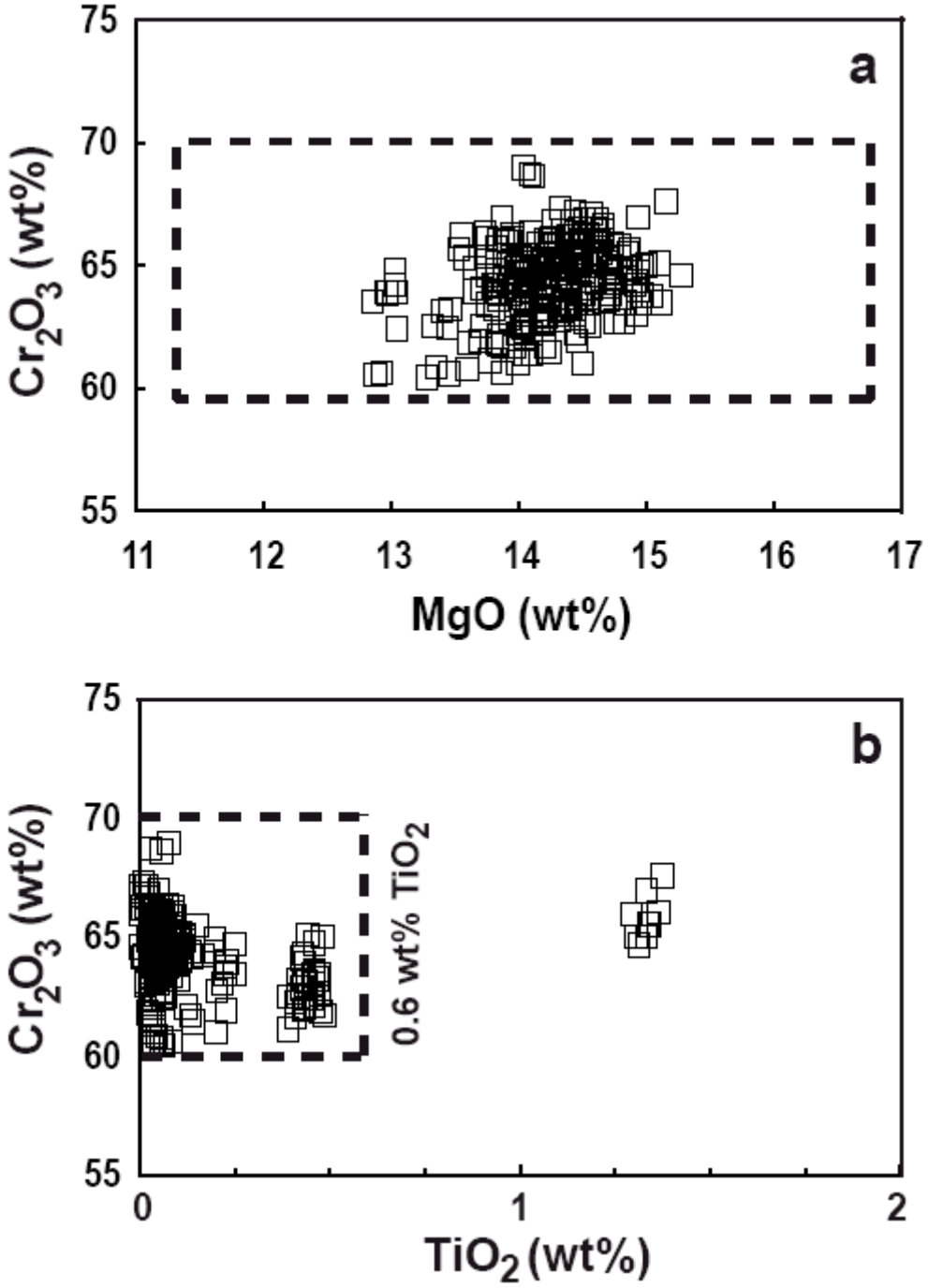

Figure 2.3. Composition of the DI chromite in the studied metaconglomerate diamonds on a Cr_2O_3 - MgO plot (a) and Cr_2O_3 - TiO_2 plot (b). The dashed line shows the diamond inclusion field for chromite (Gurney and Zweistra, 1995).

zoning within the grains. A slight trend of increasing Zn toward the edges of grains is observed in some samples, although the majority of the chromite grains analyzed do not appear to show significant zoning between cores and rims.

2.5.2 Olivine

Olivine inclusions are all colorless, with 50 inclusions analyzed from 24 diamonds. Average Mg# (100*molar Mg/(Mg+Fe)) for olivine is 92.8, with a minimum of 91.6 and maximum of 94.3 (Figure 2.4) classifying it as forsterite. The CaO content of olivine averages 0.04 wt% for the entire suite, with a maximum of 0.23 wt%. Similarly, Cr_2O_3 averages 0.06 wt% with a range of 0.04-0.30 wt%, and NiO averages 0.34 wt% with a range from 0.24-0.48 wt%. Heterogeneity within and between olivine grains in a single diamond reaches 0.6 wt% FeO, however, these variations do not appear to indicate zoning within mineral grains. Heterogeneity between olivine grains from different samples is more pronounced.

2.5.3 Garnet

Nineteen garnet inclusions were analyzed from six separate diamonds. Garnet is found as individual grains as well as coexisting with olivine and olivine+orthopyroxene. Garnets contain 2.5-4.5 wt% CaO and 6.1-10.3 wt% Cr_2O_3, and are classified as harzburgitic pyropes (Gurney and Zweistra, 1995; Figure 2.5) with average Mg# of 85.8 and a range of 71.8 -87.7. Iron content ranges from 4.5 to 7.0 wt% FeO, average Na_2O is <0.1 wt%, and TiO_2 is below detection limit. Compositions within individual garnet grains are relatively homogeneous, with internal variations for major element oxides falling below 0.5 wt%, and in some cases <0.2 wt% (Al_2O_3). No zoning within grains is evident. Diamonds containing multiple garnet inclusions exhibit the most significant heterogeneities in the Al_2O_3 and MgO content between inclusions, with variations exceeding 0.5 wt% in some instances.

2.5.4 Orthopyroxene

Orthopyroxene is the least abundant mineral phase found in the metaconglomerate diamonds. Ten colorless inclusions have been found and analyzed from six separate diamonds. Orthopyroxene Mg# ranges from 93.2-95.1 with an average of 94.2 (Figure 2.4) classifying

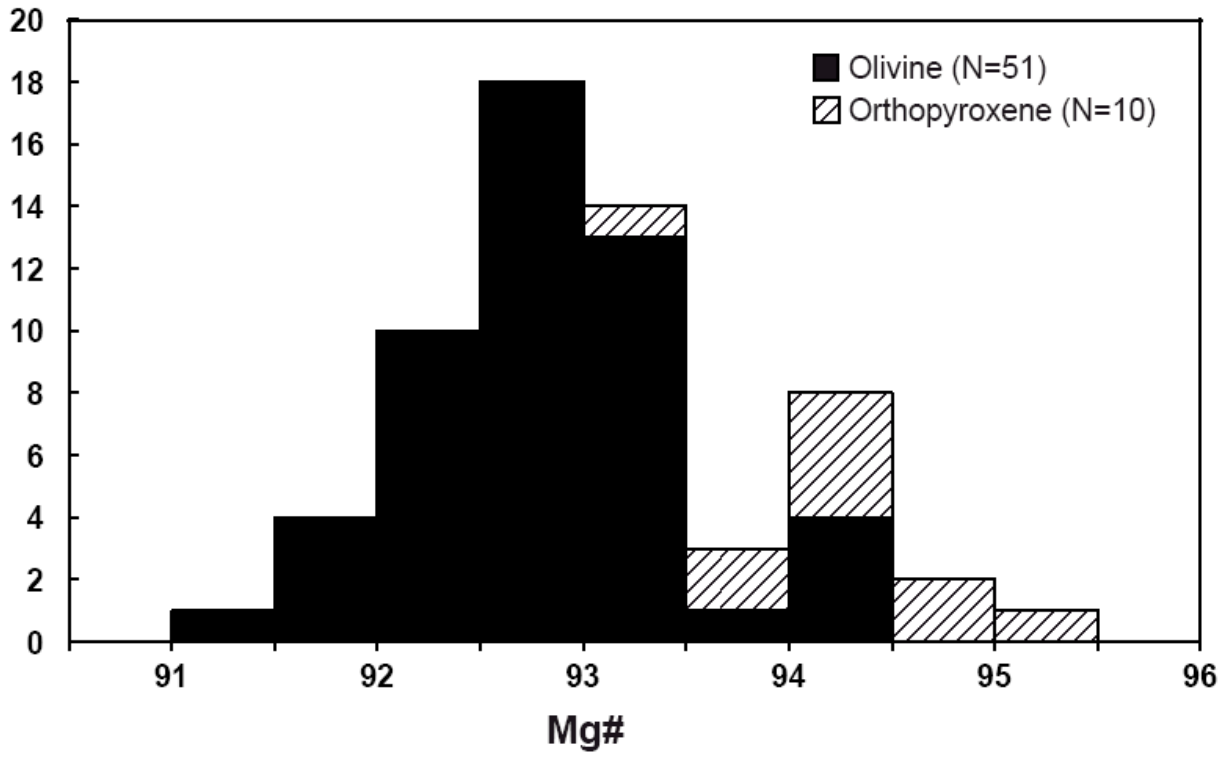

Figure 2.4. Histogram demonstrating the range of Mg# for olivine (*black*) and orthopyroxene (*striped*) in the metaconglomerate DI.

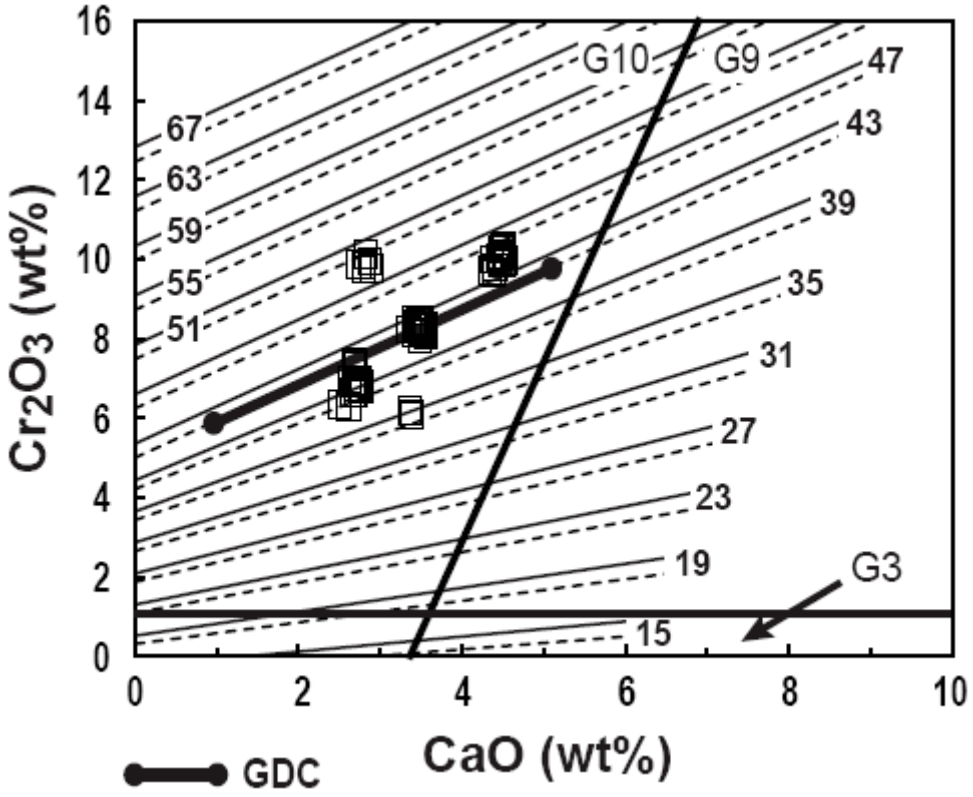

Figure 2.5. Garnet inclusion analyses from the Wawa metaconglomerate plotted on a CaO vs. Cr_2O_3 graph with G9/G10 divide and eclogitic field (<1.0 wt % Cr_2O_3) modeled after Gurney and Zweistra (1995). The labeled (in kbar) isobars of Grutter et al. (2006) are shown with *dashed lines* for a 38 mW/m^2 geotherm and with *solid lines* for a 41 mW/m^2 geotherm. The *thick line* shows the Graphite - Diamond Constraint (GDC) of Grutter et al. (2006).

orthopyroxene as enstatite. The higher Mg# of the orthopyroxene than in the DI olivine suggests their equilibration (e.g., Brey and Kohler, 1990) despite the lack of contact. The CaO content is low, averaging 0.35 wt%, while Al_2O_3 content averages 0.65 wt%. The low content of Al_2O_3 (0.4-1.5 wt%) is typical of orthopyroxene that has equilibrated with garnet (Boyd et al., 1997). Average TiO_2 and Na_2O content are also low, at 0.05 and 0.06 wt%, respectively. Variation in composition is most significant in FeO content, with little heterogeneity within grains and no zoning, but differences >0.6 wt% between grains in the same diamond.

2.6 Geothermobarometry

Diamond inclusion minerals are well equilibrated as a paragenesis, even though the majority of analyzed grains are not in contact with each other. This is evidenced by: 1) the higher Mg# of orthopyroxene than that of olivine typical of peridotite minerals in equilibrium (Brey and Kohler, 1990); 2) low Al content of orthopyroxene typical of garnet peridotite (Boyd et al., 1997); and 3) high Fe content of chromite characteristic of this phase in garnet peridotite (Boyd et al., 1997). These observations suggest that all minerals found as metaconglomerate DIs originated in the garnet-bearing facies of harzburgite, i.e., in spinel-garnet and garnet-only peridotite.

Ideally, data from inclusions of two different mineral phases that are touching within the diamond would be used for calculations to be analogous to thermobarometry results in polycrystalline rocks. Only one example of this occurs in sample Wsc13, in which a garnet and an olivine inclusion are in contact with one another. Because of the lack of such mineral pairs, temperature and pressure estimates are done with non-touching, but coexisting, sets of mineral inclusions within single diamonds. Thermobarometry results for non-touching DI pairs are typically higher, by ~100 °C on average, than temperature estimates for touching inclusions (Phillips et al., 2004). It is believed that non-touching inclusion pairs in diamonds represent conditions at the time of diamond formation, while touching inclusions may record temperatures and pressures of the cation exchange closure (Phillips et al., 2004). Therefore, temperatures of diamond formation calculated for the metaconglomerate diamonds may overestimate temperatures by ~100 °C with respect to more common xenolith geotherms.

Temperature calculations were done using two different thermometers for coexisting mineral pairs, i.e., Fe-Mg exchange between garnet and olivine (O'Neill and Wood, 1979; Table 2.2;

Figures 2.6-2.7) and Zn exchange between chromite and olivine (Zn-in-chromite thermometry of Ryan et al., 1996; Figure 2.6). Both of these thermometers are widely used for mantle xenolith-derived geotherms and thermobarometry for cratonic minerals. The olivine-garnet temperatures for studied diamonds range from 1055 to 1232°C at 50 kbar, with the single touching olivine-garnet pair from sample Wsc13 yielding a temperature of 1069°C. Figures 2.6 and 2.7 demonstrate univariant O'Neill and Wood (1979) P-T lines for all seven coexisting olivine-garnet pairs from four diamonds. The requirement that the olivine-garnet temperatures should fall within the diamond stability field for the studied samples constrain the highest possible heat flow at 41 mW/m^2 (Figures 2.6-2.7). Pressures and temperatures for equilibration of DI garnet and olivine were calculated as intersections between univariant olivine-garnet lines and the model 41 mW/m^2 geotherm, as well as the 39 mW/m^2 geotherm, the choice of which is discussed below.

The Zn-in-chromite temperature estimates (Ryan et al., 1996) should be comparable with the olivine-garnet temperatures, since all DIs are interpreted to be equilibrated with garnet. Contrary to this, the zinc temperatures are higher, ranging from 993 to 1558°C, with the mode of 1200-1300°C (Figure 2.6). The majority of the temperatures reported for the metaconglomerate diamonds are anomalously high for a variety of possible reasons: 1) known temperature overestimation of the thermometer that yields temperatures up to 1750°C in DIs (Cookenboo and Grutter, 2010); 2) incomplete Zn equilibration between non-touching chromite and olivine; 3) Zn zoning in the chromite that yields a temperature range as wide as 250°C within a single chromite grain (Appendix E); and 4) equilibration of chromite with olivine more enriched in Zn than assumed for the application of the thermometer.

Pressure estimates for the majority of chromite and garnet metaconglomerate DIs could be constrained based on the upper limit of the diamond stability field and on the chromite-garnet transition. One of the latter is the Grutter et al. (2006) barometer that estimates the metaconglomerate DI formation at P= 35-49 kbar (Figure 2.5). In this range, the pressures higher than 45 kbar match the diamond stability field of Figure 2.6 and therefore may have come from pyrope equilibrated with chromite. The lower pressures (35-43 kb), below the Graphite-Diamond Constraint of Figure 2.5, are assessed for the majority of garnets. These estimates provide only minimum pressure constraints due to lack of equilibration with chromite (Grutter et al., 2006).

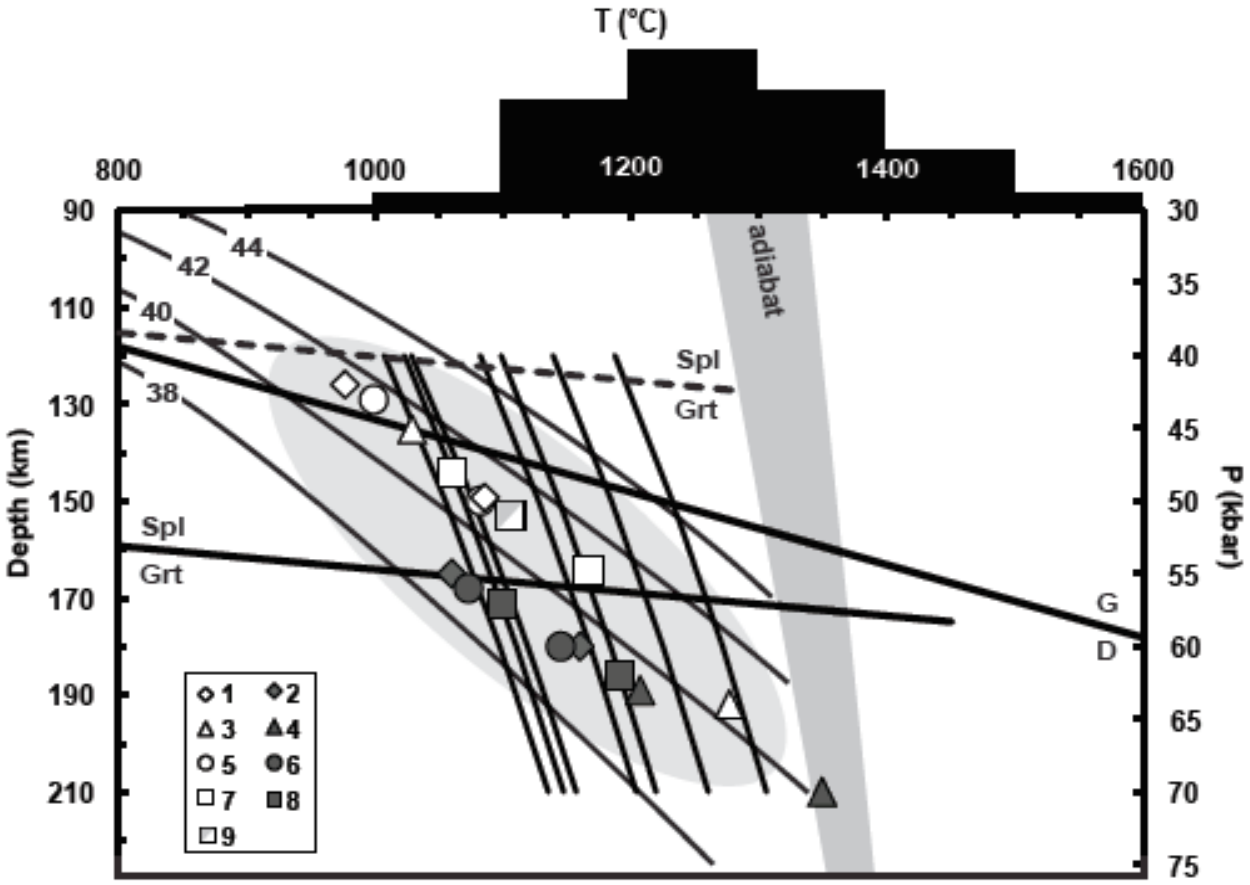

Figure 2.6. Pressure-temperature diagram illustrating thermobarometry calculations for metaconglomerate samples. Graphite-diamond transition is from Kennedy and Kennedy (1976); model geotherms are from Pollack and Chapman (1977). Range of the mantle adiabat from Rudnick et al. (1998). *Thick lines* represent univariant P-T lines for garnet-olivine pairs between 40 and 70 kbar for seven samples (O'Neill and Wood, 1979). The *solid spinel-garnet transition line* (Girnis and Brey, 1999) is based on average Cr# of metaconglomerate chromite and garnet and extrapolated to lower and higher temperature using the pressure-temperature gradient of O'Neill (1981). The *dashed spinel-garnet transition line* is calculated using the barometer of O'Neill (1981). Iterative solving of garnet-olivine and garnet-orthopyroxene thermometers with garnet-orthopyroxene barometers yielded a range of P-T points for a single diamond containing the inclusion assemblage garnet-olivine-orthopyroxene (Wsc13; *black and grey symbols*). *Grey oval field* represents PT range for peridotitic inclusions worldwide (Stachel and Harris 2008) using the garnet-orthopyroxene thermometer of Harley (1984) and garnet-orthopyroxene barometer of Brey and Kohler (1990). Thermometer and barometer pairs are as follows (abbreviations from Table 2.3): 1) $TBK90_{grt\text{-}opx}$/PBK90, 2) $TBK90_{grt\text{-}opx}$/PNG85, 3) TNG10/PBK90, 4) TNG10/PNG85, 5) THA84/ PBK90, 6) THA84/PNG85, 7) TOW79/ PBK90, 8) TOW79/PNG85, 9) $TBK90_{Ca\text{-}in\text{-}opx}$/PBK90. Zn-in-chromite temperatures (Ryan et al., 1996) are represented as a histogram.

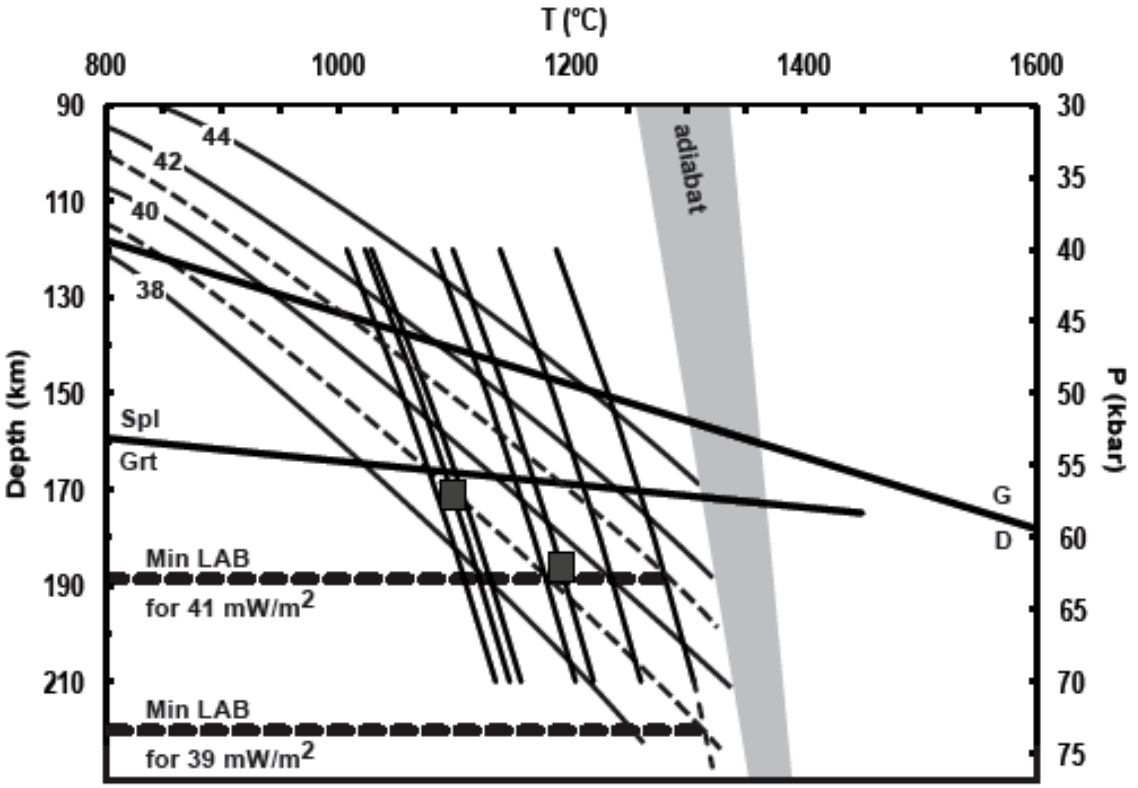

Figure 2.7. Pressure-temperature diagram showing preferred pressure-temperature estimates for the metaconglomerate diamonds. Graphite-diamond transition is from Kennedy and Kennedy (1976); model geotherms are from Pollack and Chapman (1977). *Thick lines* represent univariant P-T lines for garnet-olivine pairs between 40 and 70 kbar from seven samples (O'Neill and Wood, 1979). *Grey field* represents a range of mantle adiabats from Rudnick et al. (1998). The spinel-garnet transition line (Girnis and Brey, 1999) is calculated using average Cr# for chromite and garnet, extrapolated to lower and higher temperatures using the pressure-temperature gradient of O'Neill (1981). *Solid squares* are P-T estimates for sample Wsc13 using the O'Neill and Wood (1979) thermometer and Brey and Kohler Al-in-orthopyroxene barometer. *Thick dashed lines* of the minimal lithosphere thickness and lithosphere-asthenosphere boundary (LAB) represent the depth of the diamond sampling for the highest (41 mW/m^2) and lowest (39 mW/m^2) possible heat flow.

Another spinel-garnet barometer widely used for deep cratonic peridotites is the spinel-garnet barometer of O'Neill (1981). It yields the pressure of the chromite equilibration with garnet of ~40 kbar at 1000°C, i.e., in the graphite field (Figure 2.6) and thus underestimates pressure for our samples. The spinel-garnet barometer of Girnis and Brey (1999), which incorporates the Cr end-member of the garnet solid solution into the calibration, better satisfies petrologic constraints of the metaconglomerate DI suite. The average Cr/(Cr+Al) ratios of chromite and garnet in the metaconglomerate DIs yield pressures of 55-58 kbar at temperatures of 1000-1100°C (Figure 8 of Girnis and Brey, 1999; Figure 2.6). We conclude that all chromite-bearing and many garnet-bearing metaconglomerate diamonds must have come from P between 45 kb (the shallow limit of the diamond stability field) and 58 kb (the Girnis and Brey, 1999, spinel-garnet transition). Some garnet-bearing, chromite-free diamonds must have come from greater depths.

One sample, Wsc13, contains the three phase mineral assemblage garnet-olivine-orthopyroxene, which gives the unique opportunity to calculate both a pressure and temperature for the diamond. Several garnet-orthopyroxene thermometers (Harley, 1984; Brey and Kohler, 1990; Nimis and Grutter, 2010) were chosen along with the garnet-olivine thermometer of O'Neill and Wood (1979) to solve iteratively with Al-in-orthopyroxene barometers (Nickel and Green, 1985; Brey and Kohler, 1990) and yield a single P-T point. The recalibrated version of the Brey and Kohler (1990) barometer (Brey et al., 2008) was not chosen for calculations because it yielded unrealistically low pressures that fell outside of the diamond stability field. The results of the combined P-T calculations are presented in Table 2.3 and Figure 2.6. Two points exist for each thermometer-barometer pair because two separate and varied garnet compositions were used from Wsc13 for the calculations. Calculated P-T points show a range of temperatures and pressures (~1000-1350°C, 42-70 kbar) that fall between 39-41 mW/m^2 conductive geotherms (Pollack and Chapman, 1977) within the diamond stability field (except one point). All combined P-T points with pressures calculated using the orthopyroxene-garnet barometer of Brey and Kohler (1990) plot on the 41 mW/m^2 model geotherm, although they "slide" along this geotherm depending on the thermometer used (Figure 2.6). All combined P-T points with pressures calculated using the orthopyroxene-garnet barometer of Nickel and Green (1985) plot on the 39-40 mW/m^2 model geotherms and "shift" along the geotherms depending on the thermometer used (Figure 2.6). Together, the thermobarometric estimates dictate that the metaconglomerate DIs formed at the thermal regime consistent with 39-41 mW/m^2 heat flow.

Table 2.3. Iterative P-T point solving for sample Wsc13

Thermometer/Barometer	Garnet Grain #	T (°C)	P (kbar)
$TBK90_{grt\text{-}opx}$/PBK90	1	976	42
	2	1085	50
$TBK90_{grt\text{-}opx}$/PNG85	1	1060	55
	2	1160	60
TNG10/PBK90	1	1028	45
	2	1277	64
TNG10/PNG85	1	1207	63
	2	1349	70
THA84/PBK90	1	999	43
	2	1083	50
THA84/PNG85	1	1073	56
	2	1145	60
TOW79/PBK90	1	1059	48
	2	1166	55
TOW79/PNG85	1	1099	57
	2	1191	62
$TBK90_{Ca\text{-}in\text{-}opx}$/PBK90	1	1105	51
	2	1106	51

$TBK90_{grt\text{-}opx}$=Brey and Kohler (1990) garnet-orthopyroxene thermometer; PBK90=Brey and Kohler (1990) Al-in-orthopyroxene barometer; PNG85=Nickel and Green (1985) Al-in-orthopyroxene barometer; TNG10=Nimis and Grutter (2010) garnet-orthopyroxene thermometer; THA84= Harley (1984) garnet-orthopyroxene thermometer; TOW79= O'Neill and Wood (1979) garnet-olivine thermometer; $TBK90_{Ca\text{-}in\text{-}opx}$= Brey and Kohler (1990) Ca-in-orthopyroxene thermometer.

To simplify further discussion, we have chosen one combined P-T estimate among those discussed above. The chosen thermobarometric solution for sample Wsc13 (Figure 2.7) uses the O'Neill and Wood (1979) garnet-olivine thermometer and the Nickel and Green (1985) orthopyroxene-garnet barometer. Choosing the thermometer of O'Neill and Wood (1979) keeps the P-T points consistent with the other temperature calculations for the metaconglomerate diamonds. The barometer of Nickel and Green (1985) was chosen based on the recommendation of Wu and Zhao (2011). The latter authors checked how several barometers commonly used for deep peridotitic xenoliths reproduce known experimental pressures. Their results suggest that the Nickel and Green (1985) barometer is one of the two most reliable garnet-orthopyroxene barometers. This choice also correctly places sample Wsc13 within both the diamond and garnet stability fields. Figure 2.7 superimposes the best thermobarometric results from the metaconglomerate diamonds onto some pressure-temperature constraints, such as 39 and 41 mW/m^2 model geotherms, a range of mantle adiabats (Rudnick et al., 1998), and the diamond and garnet stability fields. Zn-in-chromite temperatures are not shown for being unrealistically high.

2.7 Discussion

2.7.1 Harzburgitic origin of metaconglomerate diamonds

With the presence of harzburgitic garnets, Mg-rich olivine and orthopyroxene, Mg-chromite, and a lack of clinopyroxene or high-Ca garnet, the chemistry of the metaconglomerate diamond inclusions strongly suggests a depleted harzburgitic parent rock for the diamonds. Carbon isotope data (-4.0 to -2.5‰) also supports this conclusion. Harzburgitic diamonds typically display a narrower range of $\delta^{13}C$ values (-9 to -1‰), while eclogitic diamonds have a wider range (Stachel et al., 2009) and more negative values (+3 to -41.0‰; De Stefano et al., 2009). Fewer eclogitic diamonds have $\delta^{13}C$ values heavier than the mantle value of -5.5‰ as compared to the harzburgitic diamond population (Stachel et al., 2009). The latter demonstrates a bimodal distribution related to distinct craton characteristics. The mode at -4.5 to -3‰ is observed for harzburgitic diamonds from the Slave, Brazil, West African and Congo cratons, whereas diamonds from the Kalahari cratons also show the second, prevalent mode at -5.5 to -6 ‰ (Stachel et al., 2009; Figure 2.2). The C isotope data for Wawa metaconglomerate diamonds, combined with analogous data previously reported for octahedral harzburgitic diamonds from the

Southern Superior (Stachel et al., 2006) now allow for comparison of the Superior craton with other cratons. The Superior harzburgitic diamonds have similar C isotopic sources to diamonds of the Slave, Brazil, West Africa and Congo cratons(Figure 2.2) and dissimilar to that of the Kalahari craton. This may be related to distinct tectonic histories of these cratons; i.e., different ages of craton stabilization superimposed on the subtle evolution of the C systematics of the mantle carbon, and a varying contribution of organic vs. carbonate crustal carbon. An alternative explanation for the distinct $\delta^{13}C$ signatures for various cratons is the different degree of isotopic fractionation. Diamonds with higher than -5 ‰ $\delta^{13}C$ were modeled to crystallize in a closed system from fractionating carbonatitic fluids (Stachel et al., 2009).

Metaconglomerate diamonds must be older than their ~2.7 Ga host rock, although the exact age of the diamond formation is unknown. Based on reported 3.5-3.2 Ga ages of all studied harzburgitic diamond suites on all cratons (Kaapvaal, Siberian, and Slave), the Wawa diamonds may have also formed then, in "a uniquely Archean process of formation for the harzburgitic host" (Helmstaedt et al., 2010). Eclogitic diamonds with ages predating 2.7 Ga are also known in some cratons. The onset of the eclogitic diamond formation coincides with the first episode of subduction and its timing is different under cratons with different tectonic histories (Helmstaedt et al., 2010). For example, the 2.9 Ga age of eclogitic diamonds below the Kaapvaal craton may be related to the 2.9 Ga tectonic amalgamation of the eastern and western Kaapvaal terranes as a result of subduction (Gurney et al., 2010). In the Southern Superior, Neoarchean subduction did not result in the presence of eclogitic diamonds in the metaconglomerate. Existence of several east-west trending zones with northerly directed subduction is inferred for Southern Superior at 2.75-2.68 Ga (Percival et al., 2006). Seismic data across the Opatica and Abitibi terranes reveals several north-dipping reflections, including a suture zone extending ~30 km into the mantle believed to be a remnant of the joining of these two provinces through ~2.69 Ga subduction (Calvert et al., 1995; Bellefleur et al., 1997; Calvert and Ludden, 1999). The main deformation event marking the tectonic accretion of the Wawa terrane, along with the adjacent Abitibi terrane, to the larger Superior superterrane occurred at ~2.68 Ga, during the Shebandowanian phase of the Kenoran Orogeny (Thurston, 1991; Percival et al., 2006). The absence of eclogitic diamonds in the metaconglomerate, despite the presence of subduction, may relate to a necessary maturation time required to metamorphose slab crustal rocks and form diamonds. An essentially coeval eruption of kimberlites on a Southern Superior protocraton with an episode of active subduction on the southern margin of this protocraton may not have given the slab rocks enough

time to recrystallize into eclogites. Alternatively, the subduction may have postdated the diamond emplacement in the terrane sampled by the Southern Superior kimberlites. The latter is reflected in the metamorphism of the metaconglomerate diamonds (Bruce et al., 2011).

2.7.2 Lithosphere and thermal regime of the Southern Superior in the Archean-Mesozoic

Thermobarometric calculations for the metaconglomerate diamond inclusions constrain the Archean thermal regime for this area as corresponding to a conductive geotherm range of 39-41 mW/m^2 (Table 2.4; Figure 2.6). The highest possible heat flow of 41 mW/m^2, constrained by the olivine-garnet univariant pressure-temperature lines, places the base of the lithosphere at a minimum depth of 190 km (Figure 2.7), but a cooler thermal regime with a thicker lithosphere is also possible. When considering the 39 mW/m^2 geotherm defined by the Wsc13 P-T points, temperature estimates place the lithosphere-asthenosphere boundary at 220 km depth. Thermal data match well with other estimates of the Archean-Proterozoic heat flow inferred from thermobarometry of peridotitic diamond inclusions around the world (Figure 2.6), i.e. ~37-42 mW/m^2 (Stachel and Harris, 2008). The cool thermal regime calculated for the metaconglomerate samples provides another data set strengthening the Archean paradox of cool lithosphere, with a heat flow similar to today's cratons, existing in a mantle of the much higher heat generation (Burke and Kidd, 1978; Lenardic, 2006).

Post-Archean kimberlites in the vicinity of Wawa are key in constraining the evolution of the root thickness and the thermal regime. We consider only kimberlites that occur adjacent to Southern Superior protocratons inferred as viable sources for Wawa metaconglomerate diamonds (Northern Wawa and Opatica terranes, Kopylova et al., 2011), i.e., Proterozoic Wawa kimberlite (Wawa terrane) and Mesozoic Kirkland Lake kimberlites of the Abitibi terrane (Figure 2.1). The kimberlites lack economic quantities of diamond. Kirkland Lake kimberlites have diamond grades ~ 100 times lower than those in minable kimberlites, 0.0199 ct/t in pipe C14 (Brummer, 1992), 0.0071 ct/t in pipe A4 and 0.0054 ct/t t in pipe B30 (Vicker, 1997). Mantle xenoliths in the kimberlites record temperatures and rock lithologies of the Southern Superior cratonic root for corresponding times. We assume that the maximal depth of the coarse peridotite occurrences reflect the minimal thickness of the lithosphere.

Table 2.4. Approximate P-T intersections of garnet-olivine temperature calculations with the minimum and maximum geothermal gradients for the Archean Southern Superior

Sample	P-T Intersect with 39 mW/m^2 geotherm (°C, kbar)	P-T Intersect with 41 mW/m^2 geotherm (°C, kbar)
Wsc13	1170, 63	1125, 53
	1080, 56	1050, 47
	1180, 64	1150, 55
Wsc21	1100, 57	1060, 49
Wsc25	1290, 67	1200, 58
	1300, 73	1250, 63
Wsc51	1060, 55	1040, 46

Wawa kimberlite dated at ~1.1 Ga contains dunite, harzburgite, wehrlite, and websterite xenoliths amenable to thermobarometry (Kaminsky et al., 2002). Kaminsky et al. (2002) used the Ca-in-orthopyroxene thermometer and Al-in-orthopyroxene barometer pair on three xenoliths containing orthopyroxene and garnet to calculate equilibration conditions. Two out of three computed pressures and temperatures fall on the 46 mW/m^2 conductive geotherm, whereas the third sample indicates an even higher thermal regime (Figure 2.8a). Using the same thermometer-barometer pair, we plotted thermobarometric results from this study for one diamond hosting orthopyroxene and garnet (Table 2.3; Figure 2.8a). A noticeable heating of the mantle can be seen by comparing the DI data with Proterozoic xenoliths. This heating may have resulted from coeval formation the Midcontinent Rift (MCR) immediately to the south from Wawa (Figure 2.1). The rift is an arcuate structure whose gravity and magnetic signatures can be traced for more than 2000 km. The rift system is related to the 1150-1085 Ma flood basalt province that produced at least 2 Mkm^3 of volcanic rocks and the Abitibi dyke swarm in three magmatic pulses (Ernst and Bleeker, 2010). The Archean Superior Province crust was extended to roughly one fourth of its original thickness before being thickened via intrusions and underplating (Clowes et al., 2010).

The minimal thickness of the cratonic root at 1.1 Ga could be inferred from the maximal depth of peridotitic garnet xenocryst's formation. We projected Ni-in-garnet temperature estimates for high-Cr, low-Ti garnet xenocrysts (Kaminsky et al., 2002) that were likely to have been equilibrated with olivine onto the model 46 mW/m^2 geotherm defined by the xenoliths. The resulting depths of garnet sampling are restricted to < 150 km, i.e., graphite-bearing peridotites (Figure 2.8a).

Jurassic (145.9-164.7 ±0.6-3.0 Ma, Heaman et al., 2004) Kirkland Lake kimberlites carry mantle xenoliths of coarse and deformed garnet peridotites (Meyer et al., 1994; Schulze, 1996; Vicker, 1997); eclogite xenoliths are found in only one pipe (A4; Vicker, 1997). To compare the xenolith-derived Jurassic geotherm (Meyer et al., 1994; Vicker, 1997) with the Archean thermobarometry data, we plotted Al-in-orthopyroxene pressures of Brey and Kohler (1990) and garnet-olivine temperatures of O'Neill and Wood (1979). Temperature-pressure estimates for the metaconglomerate sample Wsc13 demonstrate a slightly cooler thermal state when contrasted with Jurassic xenoliths falling onto the 41-42 mW/m^2 geotherm (Figure 2.8b). Coarse peridotites from the Jurassic mantle occur at depths 60-150 km, i.e., predominantly in the graphite stability

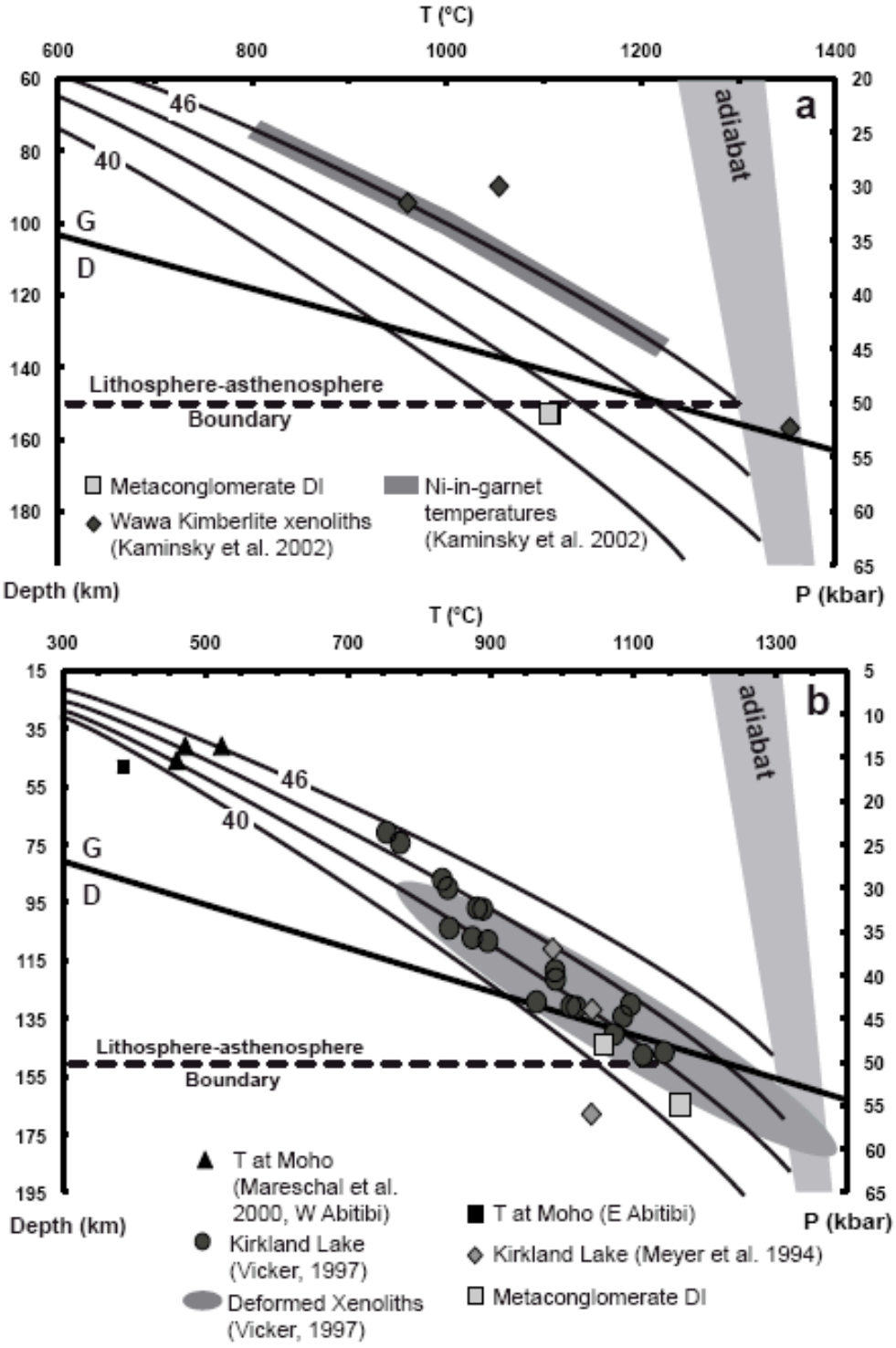

Figure 2.8. Pressure-temperature diagram comparing thermobarometry estimates for Archean DIs and post-Archean kimberlites. (a) Wawa kimberlites (Kaminsky et al., 2002). Samples are plotted using the Ca-in-orthopyroxene thermometer and Al-in-orthopyroxene barometer of Brey and Kohler (1990). *Grey field* represents Ni-in-garnet xenocryst temperature estimates from Kaminsky et al. (2002) falling along a 46 mW/m^2 geotherm. (b) Kirkland Lake kimberlites (Schulze 1996; Vicker 1997). DI sample and coarse xenoliths are plotted using the garnet-olivine thermometer of O'Neill and Wood (1979) and Al-in-orthopyroxene barometer of Brey and Kohler (1990). *Shaded field* corresponds to deformed xenolith PT data (Vicker, 1997). Graphite-diamond transition is from Kennedy and Kennedy (1976); model geotherms are from Pollack and Chapman (1977); adiabat range is from Rudnick et al. (1998).

field (Figure 2.8b), constraining the minimal thickness of the cratonic root at 156 Ma at 150 km. Another dataset indicative of the thermal regime of the Jurassic Southern Superior mantle is based on single clinopyroxene thermobarometry data for the Kirkland Lake xenoliths (Grutter, 2009). They plot within the graphite stability field and at a higher geothermal gradient than that of a typical cratonic locale (North and Central Slave craton), supporting the above findings that the Jurassic aged kimberlites did not encounter a cool lithospheric root in the diamond stability field. Yet another, complementary dataset on the composition of the mantle below Kirkland Lake refers to geochemistry of garnet macrocrysts (Griffin et al., 2004). The Jurassic upper mantle above 135 km has a high proportion of depleted garnets typical of the Archean mantle sections. Below ~ 140 km, the mantle demonstrates a sharp change, and the lower part of the section has higher proportions of depleted/metasomatised and fertile lherzolites, indicative of strongly modified Proterozoic sections (Griffin et al., 2004).

2.7.3 Present lithosphere and thermal regime of the Southern Superior

Current heat flow models in the Superior province, acquired through drill holes and conductivity measurements of different rock types, indicate an average 42 mW/m^2 geothermal gradient for the Superior Province (Drury and Taylor, 1987, and references therein), just slightly above the 41 mW/m^2 worldwide average for Archean crust (Chapman and Furlong, 1977; Nyblade and Pollack, 1993). Heat flow measurements at various sites throughout the Superior demonstrate significant variability. The closest site to the Kirkland Lake kimberlite in the Abitibi terrane shows the heat flow values of 37-42 mW/m^2 (Mareschal et al., 2000), whereas values for the Opatica terrane range from 29-33 mW/m^2, the site near the Wawa kimberlite in the Wawa terrane yields 41-42 mW/m^2 (Drury and Taylor ,1987), and the sites on the western Abitibi terrane, which could be the source for detrital grains in the metaconglomerate (Kopylova et al., 2011), yield an elevated heat flow of 48 mW/m^2 (Mareschal et al., 2000). These surface heat flows, however, are controlled mainly by heat generation in the upper crust and the abundance of granitic rocks (Mareschal et al., 2000). Surface heat flow values correlate with the ratio of granitic lithologies / metamorphic rocks of medium grades / greenstones and are independent of the age or the crust thickness (Mareschal et al., 2000). To estimate the mantle heat flow, one has to subtract the contribution of the variable upper crust heat flow (Russell and Kopylova, 1999). Such modeling of the Superior surface heat flow was done based on contributions from 3 crustal and mantle layers (Table 4 of Mareschal et al., 2000), constraining temperatures at the Moho.

They vary from 385 to 523°C at 41-46 km, and lie on or slightly lower than the Jurassic xenolith geotherms extrapolated to lower pressures (Figure 2.8b). There is no evidence for heating of the Southern Superior between the Jurassic and present times. The mantle remained in the steady state cold thermal regime in the last ~160 Ma, whereas some current high surface heat flow values relate to abundant lower crustal TTG intrusions (Mareschal et al., 2000).

Complementary to the modern heat flow data, seismic surveys also provide information regarding the thermal and compositional structure of the mantle. High compressional (Vp) and shear (Vs) velocities beneath northern and central parts of North America are indicative of relatively low temperatures and depleted mantle compositions (van der Lee, 2001) typical of the cratonic mantle. Large-scale, low-resolution seismic tomography of North America has established the maximal thicknesses (250 km) of the Superior root in the northern part of the craton (Grand, 1994). Many other continental-scale tomographic models for North America were published since then (Faure et al., 2011, and references therein). Relatively high-resolution data sets on Western Superior map a sharp interface between the North Caribou superterrane and terranes to the south based on broadband teleseismic and magnetotelluric data. The North Caribou superterrane is characterized by relatively high velocity and modest seismic and electrical anisotropy, whereas in the south, the lithosphere velocity declines as both electrical and seismic east-west anisotropy increase (Percival et al., 2006, and references therein). The boundary is marked by steeply dipping electrical and seismic anomalies consistent with slab-like features attributed to formation of the Superior craton through subduction–accretion processes (Craven et al., 2001; Kendall et al., 2002). The most recent high lateral resolution Rayleigh wave phase velocity survey maps of the Superior mantle significantly improved spatial resolution of seismic mapping and enabled conclusions on the depth and 3D structural patterns of the lithosphere (Faure et al., 2011). The survey found that the Northern Superior craton has the deepest mantle roots of North America (225-240 km) which are ~8 % faster than the Vs of Preliminary Reference Earth Model (PREM) corresponding to 170°C lower temperatures and 4 wt% depletion in Fe as compared to the model average (Godey et al., 2004). In the Southern Superior, by contrast, the velocities are <5 % higher than the PREM's. The sharp boundary between the higher and lower Vs domains corresponds to the boundary between Mesoarchean and Neoarchean crustal terranes of the Superior craton (Figure 2.1). Faure et al. (2011) propose that the mantle domain with velocities 6% above PREM outlines the highly depleted cold Archean mantle at depths below 145 km, and topography of the 6% surface maps the lithosphere

keel exactly as inferred from xenolith and macrocryst studies. If this is true, then the position of the Southern Superior outside of the 6% shell in Vs anomaly at depths of 100 km (Figure 5 of Faure et al., 2011) means the absence of the diamondiferous cratonic root.

2.7.4 Destruction of the diamondiferous cratonic root in the Archean-Proterozoic

The data discussed above trace the evolution of the mantle thermal regime from the Archean to present in the Southern Superior mantle. We see a slight increase in the geothermal gradient from 39-41 mW/m^2 in the Archean to 41-42 mW/m^2 in the Jurassic-Cenozoic on the northern Abitibi adjacent with the Opatica terrane. The contrasting evolution is observed for the Northern Wawa terrane where a more significant heating to the 46 mW/m^2 geotherm in the Proterozoic relaxes to 41-42 mW/m^2 of the modern heat flow. The 1.1 Ga temporal heating of the northern Wawa terrane may have resulted from development of the MCR and the Keweenawan flood basalts immediately to the south (Figure 2.1). Alternatively, an elevated Proterozoic geotherm could be just an artifact of highly serpentinized and altered xenoliths in the Wawa kimberlite (Kaminsky et al., 2002) not amenable to accurate thermobarometry.

One could also trace how the thickness of the Southern Superior cratonic root has changed with time. The root was at least 190 km thick in the Archean, but then it thinned due to destruction of its deepest, diamondiferous part. The pre-2.7 Ga cratonic root sampled by the metaconglomerate had already been removed below the Wawa terrane by ~1.1 Ga, i.e., by the time of the emplacement of barren Wawa kimberlites (Figure 2.8a). Thermobarometry of the Jurassic mantle xenoliths also demonstrates the absence of the diamondiferous lithosphere. In the Jurassic, potentially diamondiferous horizons of the mantle below 150 km were occupied by sheared peridotites whose texture and mineral composition testify to metasomatism by asthenospheric melts (Smith and Boyd, 1987; Griffin et al., 1989; Smith et al., 1991; Griffin and Ryan, 1995; Moore and Lock, 2001). These high-T peridotites never contain diamonds (Griffin and Ryan, 1995; Gurney and Zweistra, 1995). The higher proportions of metasomatised and fertile peridotites below ~140 km were also inferred from Jurassic garnet compositions (Griffin et al., 2004). The same depth intervals of 150-190 km in the Archean contained depleted coarse harzburgites with diamonds.

We therefore propose that after the Neoarchean, the Southern Superior diamondiferous root was modified due to interaction with asthenospheric melts, fertilized and recrystallized. This process was already accomplished by 1.1 Ga beneath the Northern Wawa terrane, assisted by the MCR and mantle heating. Beneath the Opatica terrane, an exact timing of the thinning of the diamondiferous lithosphere is more loosely constrained between 2.7 Ga and ~160 Ma, and involved only minor heating.

2.7.5 Mechanisms of root destruction

Cratonic roots can be destroyed by different kinds of geologic events. The root of the Dharwar craton was destroyed ~ 140 Ma by the plume that caused the breakup of Gondwana (Griffin et al., 2009). Continent-continent collision was proposed as the cause for removal of the root below the eastern North China Craton (e.g. Liu et al., 2011; Zhang, 2012). This best documented example of the root destruction enables constraints on the process derived from many parallel lines of evidence: compositional and thermobarometric (Zheng et al., 2006), geochronological and isotopic (Liu et al., 2011; Chu et al., 2009) and geodynamic (Zhang, 2012). All authors agree that the combined dataset is best explained by density foundering (delamination) of the old lithosphere and its replacement by upwelling asthenospheric mantle. It is recorded in the drastic heating of the mantle, from 40 mW/m^2 in the Early Paleozoic to 80 mW/m^2 in the Cenozoic (Zheng et al., 2006), the thinning of the lithosphere from 200 km to 60-120 km (Chu et al., 2009 and references therein), and the complete disappearance of Archean peridotites and their replacement by Phanerozoic-Proterozoic peridotites (Liu et al., 2011).

The cratonic root could also be significantly modified, but not completely destroyed, as has been recorded in the Kaapvaal craton between 110 and 95 Ma. During this time, the geotherm rose from 35 to 38 mW/m^2, which was accompanied by refertilization of the depleted mantle. This is seen as the increase in the degree of melt-related metasomatism in the lower part of the mantle section and thinning of the depleted layer from 200 to 170 km (Griffin et al., 2003b). The process was ascribed to the root-unfriendly influence of formation of an early Group 2 kimberlite province (Gurney et al., 2010) or to the plume-type activity responsible for the widespread Group I kimberlite magmatism (Griffin et al., 2003b). These low-degree asthenospheric melts are channeled along steep compositional boundaries that mark edges of tectonic blocks; the

passage of the fluids may be the major cause to a gradual and irreversible increase in fertility of the cratonic lithosphere that destroys it (Begg et al., 2009).

Tectonic erosion was theoretically predicted as one of possible mechanisms of root destruction (Helmstaedt et al., 2010). The process is envisioned as mechanical replacement of the subcontinental lithospheric mantle by the subducted oceanic lithospheric slab and also known as thermo-mechanical erosion or thermo-tectonic destruction (Chu et al., 2009, and references therein). The presence of the relic buried lithospheric slabs in the upper mantle is well documented with seismic reflection images as summarized in Clowes et al. (2010). Under many continental terranes, dipping anisotropic mantle anomalies and discontinuities align directly with the location of inferred subduction zones (White et al. 2003; Clowes et al., 2010 and references therein). An example of such a relic lithospheric slab in the Superior that has a potential to tectonically erode the earlier root is a shallow slab of subducted Neoarchean oceanic lithosphere underplated from the south beneath the 3.2 Ga Winnipeg River terrane (White et al., 2003). The same is true of other northern-trending relict subduction episodes in the Superior, marked on Figure 2.1. It was proposed that post-Archean mantle rarely survives the collision and/or accretion process (Begg et al., 2009).

We can theoretically predict testable consequences of tectonic erosion. Firstly, it should lead to higher proportion of eclogites in the mantle. These should be mappable by Vp and Vs surveys. In eclogite, seismic velocities increase more rapidly with depth than in peridotite as follows from contrasting first-order pressure derivatives of bulk isotropic moduli for eclogite and peridotite, and from the lower compressibility of eclogite at high pressures. Contrasting depth derivatives for eclogites and peridotites forecast that eclogites should have slightly lower Vp below 100 km (below 130 km for Vs), but higher velocities at greater depths (Kopylova et al., 2004) when compared to peridotites. Correlation of lower compressional velocities with the presence of eclogitic diamonds in the Kaapvaal craton (Shirey et al., 2002) suggest that this correlation is mainly influenced by the shallow tomographic signal. Secondly, slab underplating should increase fine-scale anisotropic mantle layering (Mercier et al., 2008). Thirdly, tectonic erosion should not lead to major heating of the mantle, as the slab is colder than the ambient cratonic mantle (Stern, 2002).

2.7.6 How was the Southern Superior diamondiferous root destroyed?

A comparison of the observed evolution of mantle parameters in the Southern Superior craton with those recorded for various root destruction scenarios focuses on the most viable model. The Southern Superior root may not have been delaminated as this process is accompanied by the pronounced jump in the heat flow, almost doubling it. A major constraint on the mechanism of the root destruction is the localization of the current high-velocity cratonic root and spatial correlations with crustal terranes. The abrupt cut-off of the root along the east-west line parallel to boundaries of crustal terranes that docked to the nuclei of the Superior protocraton in the Neoarchean strongly suggests that the modification of the Southern Superior was related to the tectonic amalgamation of the craton and already started in the Neoarchean. As stated by Faure et al. (2011), "the formation of greenstone belts in the Neoarchean produced a permanent scar that was subsequently re-used during younger tectonothermal events to produce the current seismic response."

In our opinion, multiple post-Archean magmatic events could not have caused the disappearance of the Southern Superior cratonic root. The Cretaceous Meteor Hotspot commonly quoted as the reason for the low-velocity zone in the Southern Superior (Faure et al., 2011, and references therein), cannot explain the absence of the root in the Jurassic. The most significant modification of the Southern Superior lithosphere was associated with a large 1.1 Ga Midcontinent Rift (Figure 2.1), but even this event of extensive mantle melting is not recorded in the architecture of the current high-velocity root, which is totally independent of the rift outline. Other various Proterozoic events in the Southern Superior may have played only a minor role in the thinning and heating of the lithosphere since they do not show up in the current sheared wave velocity structure (Figure 5 of Faure et al., 2011). These include large igneous province (LIP) events (Ernst and Bleeker, 2010) and continental rifting along the southern border of the Abitibi (Young et al., 2001; Long, 2004). The Matachewan LIP event produced 2490-2445 Ma dykes, and at 2125-2070 Ma, the Marathon and Fort Frances dyke swarms formed from the plume localized to the south from Wawa (Ernst and Bleeker, 2010 and references therein; Figure 2.1). LIP events generated dyke swarms rather than voluminous volcanics of MCR attesting to the less intense mantle melting. Continental rifting to the south of Abitibi produced extensional strike-slip basin (the Huronian ocean) at 2.4 Ga (Long, 2004), which accumulated bimodal rift-related Thessalon volcanics and 12 km of the Huronian Supergroup sediments (Figure 2.1). The upper Huronian

units with ages >2.2 Ga indicate the switch to a southward facing passive margin before closure of the ocean at ~ 1,87 Ga (Young et al., 2001; Long, 2004).

We postulate that the root destruction in the Southern Superior may be an example of mantle changes associated with tectonic erosion and craton amalgamation. Steep discontinuity in resistivity, anisotropy and seismic velocity of the mantle at the edge of the present day lithosphere at the southern margin of the North Caribou terrane was ascribed to relic slabs arrested during subduction–accretion processes (Craven et al., 2001; Kendall et al., 2002). They were active at this margin for 300 Ma and stopped at <2.646 Ga (Percival et al., 2006). The northerly subduction beneath the southern margin of the Wawa-Abitibi terrane was active from 2.75 to 2.68 Ga, ~100 Ma longer than subduction on its northern margin, and ended only with a complete disappearance of the ocean floor that initially separated the Minnesota River Valley terrane from the Wawa-Abitibi terrane on the north (Percival et al., 2006). The roots may have been thinned by subduction episodes at 2.69 Ga when the Abitibi terrane docked the Opatica terrane from the south (Calvert et al., 1995; Bellefleur et al., 1997; Calvert and Ludden, 1999).

The observed seismic and thermal characteristics of the post-Archean Southern Superior mantle do not contradict the conclusion on tectonic erosion. The Northern Wawa and Opatica terranes demonstrate Vs' 5% above PREM. A decrease in Vs of only 1% (0.05 km/s below the common mantle Vs of 4.8 km/s) would be sufficient to remove the mantle from the outlined high velocity 6% perturbation shell. This would be possible if eclogites are added to the mantle at depths above 130 km. Only a small addition of eclogite (4.5 km/s at 100-120 km) is required to lower the shear wave velocities for the 4.8 km/s peridotitic mantle (Figure 3 of Kopylova et al., 2004). Eclogite xenoliths indeed were found in the A4 Kirkland Lake kimberlite (Vicker, 1997).

Subduction and tectonic erosion are always accompanied by magmatism. Orogenic processes, which start with physical changes in the lithosphere, always continue with compositional changes of the mantle and involve ascent of asthenospheric melts, the shallow mantle and crustal melting and granite-generation. This orogenic magmatism played a role in the lithosphere thinning. It is observed as the gentle heating (from 39 to 42 mW/m^2) and replacement of the diamondiferous lithosphere with sheared fertile peridotites impregnated by asthenospheric melts. The parameters of this process fit well the characteristics associated with the Cretaceous lithosphere thinning of the Kaapvaal (Griffin et al., 2003b). Seismically, progressive

metasomatism that fertilizes low-temperature lithospheric peridotite and transforms it to high-temperature peridotite leads to a mantle 0.03 km/s slower in Vs (Kopylova et al., 2004). This seismic response is mainly governed by 100°C heating (Figure 2.8b), as mineralogical changes associated with the metasomatic thinning are small (Table 3 of Kopylova et al., 2004).

2.8 Concluding remarks

We show that at ~2.7 Ga the Southern Superior protocraton had the >190 km-thick diamondiferous harzburgitic root with the thermal state corresponding to a cold, 39-41 mW/m^2 geotherm. This root was thinned down to 150 km by the Jurassic, when the mantle was heated to 41-42 mW/m^2. The root destruction was accompanied by more significant, ~150°C heating and was complete by 1.1 Ga in areas adjacent to the Midcontinent Rift. We propose that the root destruction in the Southern Superior may be associated with tectonic erosion, craton amalgamation and ensuing orogenic magmatism and ingress of asthenospheric fluids.

The same process of orogeny and stacking of subducted slabs is commonly quoted as a mechanism for craton root formation (Helmstaedt and Schulze, 1989; Pearson and Wittig, 2008), rather than destruction. If orogeny could either build or erode cratonic roots, the age of the overriding plate and the timing of the orogeny seem to exert the major control. If the cratonic plates are older than 3 Ga and the collision occurred at 2.9-2.8 Ga, the original roots of the amalgamated terranes survive and merge, as we see for the 2.9 Ga amalgamation of the Kaapvaal craton (Helmstaedt et al., 2010). In the Superior, only northern terranes still possess the high-velocity deep root today, but younger Neoarchean southern terranes that docked to the craton later could not keep the diamondiferous roots intact. The critical timing when the root-building is reversed may be the Neoarchean for Africa, as the post-Archean juvenile lithosphere is likely to be recycled rather than to survive the accretion (Begg et al., 2009). For other continents, the analogous critical time when cratonic roots cannot grow any more may be different, as it depends on the density contrast between juvenile and Archean lithosphere (Griffin et al., 2003b), which, in turn, is controlled by melting parameters and metasomatism specific to the craton.

3. Fibrous diamond formation by "cold" metasomatism: new constraints on the timing and conditions involved in fibrous diamond growth

3.1 Summary

Comparison of mineral inclusion compositions in non-fibrous and fibrous diamonds from one location highlights metasomatic processes that formed fibrous diamonds. We analyzed mineral microinclusions in fibrous diamonds from the Wawa metaconglomerate (Superior craton) and Diavik mine (Slave craton) and compared them with published compositions of large mineral inclusions in non-fibrous diamonds from these localities. The comparison, together with similar datasets available for Ekati and Koffiefontein kimberlites, suggest two systematic trends in mineral chemistry that accompany fibrous diamond formation. The first involves Ca and Fe enrichment of peridotitic garnet and pyroxenes and Fe enrichment of olivine. Although this increase in mafic magmaphile elements is common to cratonic metasomatism, trace element characteristics and thermobarometry indicate that fibrous diamonds formed in a distinct, rare metasomatic event. The second trend controls a shift to more magnesian olivine and eclogitic clinopyroxene. Forsterite 95-98 may have crystallized in fibrous diamonds due to oxidizing conditions or carbonatitic nature of the fluid. Thermometry suggests that fibrous diamonds formed at low (<1050 °C) temperatures, in the subsolidus of alkali-bearing peridotite saturated with CO_2. An influx of K-rich, hydrous carbonatitic fluid was able to generate the diamonds only at ambient low temperatures of the cratonic geotherm below the mantle solidus, as the absence of melt enhances kinetics of diamond crystallization. "Cold" temperatures of the fibrous diamond formation could account for the dominance of type IaA aggregation in fibrous diamond worldwide, and a critical mass of new observations on diamond geochemistry and kimberlite geology deem the genetic and temporal link between kimberlites and fibrous diamonds unnecessary.

3.2 Introduction

Two types of diamond, octahedrally-grown and fibrous, offer a direct source of information about the mantle. Both of these diamond varieties contain mineral inclusions that could be used as "snapshots" of mineral chemistry and processes at the time of the respective diamond

formation. Fibrous diamond formed by rapid, dendritic growth (Boyd et al., 1994) in the presence of hydrous silicic-saline-carbonatitic fluid (Schrauder and Navon, 1994; Izraeli et al., 2001; Klein-Ben David et al., 2009), in a separate growth event postdating crystallization of octahedrally-grown, non-fibrous, diamonds **(**Boyd et al., 1987; 1994). Comparison of contrasting mineral inclusion compositions in fibrous and non-fibrous diamonds from one kimberlite (Panda kimberlite in Ekati mine) shows metasomatic interaction of the primary mantle minerals, like those trapped in non-fibrous diamonds, with the fluid (Tomlinson et al., 2006). The metasomatism decreased Mg# values (molar Mg/(Mg+Fe)×100) and increased CaO content of the minerals captured in fibrous diamonds, suggesting fertilization by Fe- and Ca-rich carbonatitic fluid found in their fluid inclusions. The metasomatism and growth of fibrous diamonds occurred not as a result of a thermal event but due to an arrival of externally-derived metasomatic fluid (Tomlinson et al., 2006).

Our work tests these conclusions on the chemistry and thermal regime of the metasomatism on a larger dataset of fibrous and non-fibrous diamonds. For this, we studied mineral inclusions from diamonds recovered from kimberlites mined at Diavik (Slave craton) and a metaconglomerate of the Wawa subprovince (Superior craton). Fibrous diamonds from Diavik include diamond-forming fluids that span the entire range of known fluid compositions from saline to carbonatitic, to hydrous silica-rich end-members (Klein-Ben David et al., 2006). The range of fluids is expanded to silicic as compared to previously studied mineral inclusions in fibrous diamonds, which only reflected metasomatism associated with saline-carbonatitic fluids (Tomlinson et al., 2006). We show that despite drastically different fluid compositions, the metasomatism commonly causes similar evolution in mineral composition—the influx in Ca and Fe to garnet, olivine and pyroxenes.

The thermal regime of fibrous diamond precipitation is constrained based on thermobarometry of coexisting minerals in Wawa diamonds. Our calculations confirm that fibrous diamonds crystallize at the ambient cratonic thermal regime in the absence of melt. Moreover, low-temperature flooding of the mantle by hydrous alkaline carbonatitic fluids seems to be the only way to quickly precipitate diamond.

We also compare diamond-producing metasomatism to other, more common types of mantle metasomatism recorded in cratonic rocks, such as high-temperature asthenospheric melt

metasomatism (O'Reilly and Griffin 2010, and references therein), low-temperature metasomatism, and the secular, irreversible fertilization of the mantle (Griffin et al., 1998). A relatively "cold" thermal regime during fibrous diamond growth and constant Zr/Y ratios observed in non-fibrous and fibrous diamonds rule out common types of mantle metasomatism as a trigger for fibrous diamond formation. We conclude that fibrous diamonds have formed in a distinct, relatively rare metasomatic event that is not necessarily related to kimberlite formation.

3.3 Samples and methods

3.3.1 Samples

Mineral inclusions analyzed in this study are hosted in fibrous diamonds from two different locations, Wawa (10 diamonds, ~1 mm in size) and Diavik (5 diamonds, 1.5 to 3 mm in size). The Wawa diamond suite is from a 2.701-2.697 Ga metaconglomerate located in the Michipicoten greenstone belt of the Wawa terrane (Kopylova et al., 2011). The primary source for the metaconglomerate diamonds is interpreted to be a kimberlite, now completely eroded away, that was originally emplaced in either the northern Wawa or the Opatica terranes of the Southern Superior craton (Kopylova et al., 2011). Fibrous diamonds from this location contain 230-330 ppm N in cuboids and 1000-2000 ppm N in fibrous coats, all aggregated as type IaA with no B-center aggregation. Fluid inclusions in these diamonds trap a saline diamond-forming fluid with an unradiogenic Sr-isotope signature (Smith et al., in press). The other fibrous diamond samples are from the Diavik mine in the Lac de Gras kimberlite field of the central Slave craton. The mine consists of four separate pipes, which have been dated at 55-56 Ma (Graham et al., 1999). Fibrous diamonds from this location exhibit IaA type N aggregation, and trap fluid microinclusions with compositions that span the range within both saline—high-Mg carbonatitic and silicic—low-Mg carbonatitic trends (Klein-Ben David et al., 2004; 2006). Fibrous diamonds are dominated by a cuboid habit, typical of fibrous samples, and display a grey to black, turbid appearance.

Analyzed mineral compositions of microinclusions in the fibrous diamonds are compared to larger inclusions in non-fibrous diamonds from the same locations. The notable differences in diamond morphology, appearance, inclusion frequency, and inclusion size between the fibrous samples and the non-fibrous samples are displayed in Figure 3.1. Non-fibrous diamond

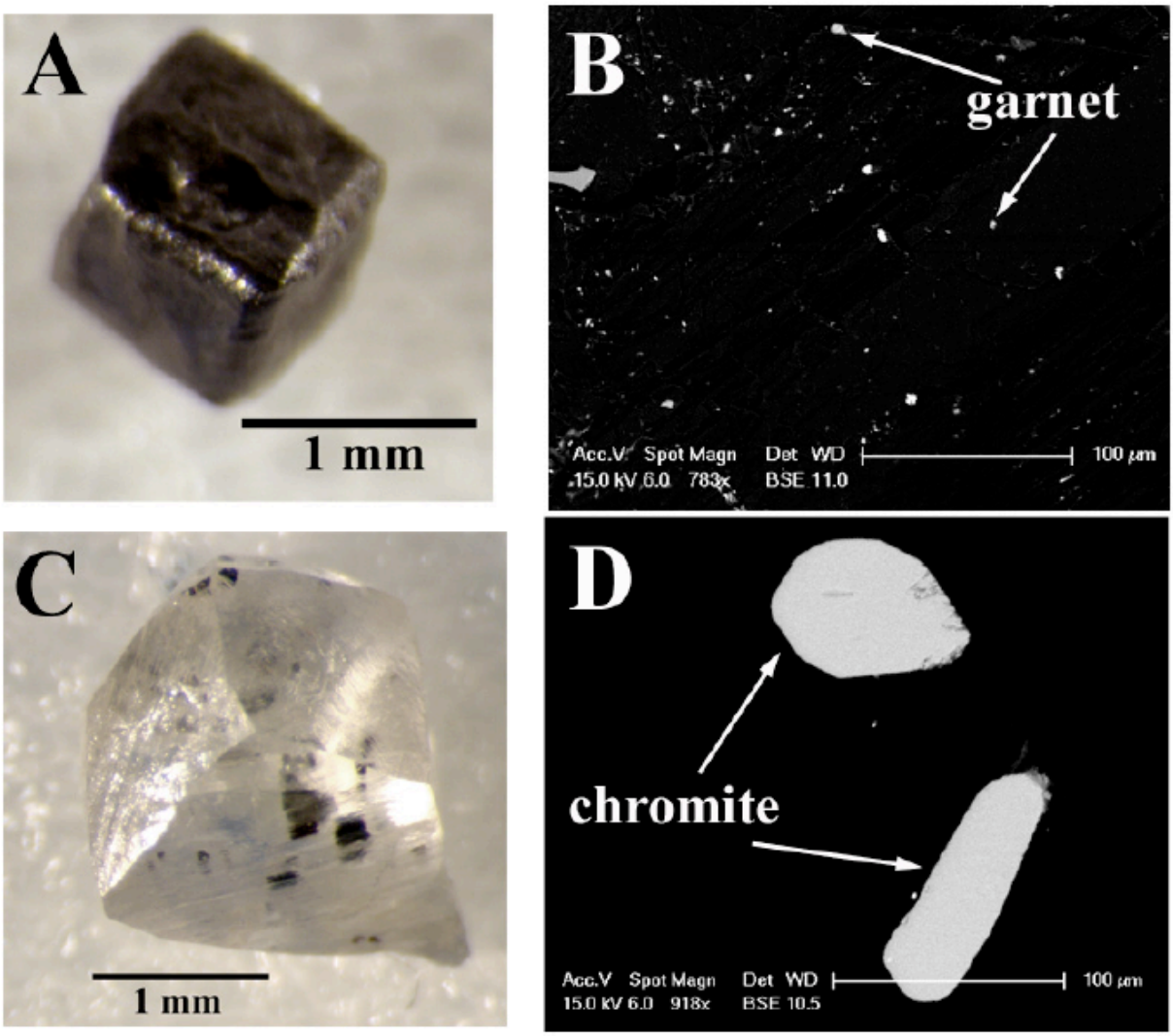

Figure 3.1. Comparison of fibrous and non-fibrous diamond samples and their mineral inclusions. (A) Wawa fibrous cube (W53) containing garnet microinclusions (B). Unlabelled bright spots in (B) consist of carbonate and fluid inclusions. (C) Wawa non-fibrous resorbed diamond (Wsc41) containing large chromite inclusions (D) analyzed in Miller et al. (2012; Chapter 2).

inclusions (DI) from the Wawa metaconglomerate indicate a harzburgitic paragenesis formed in a cool cratonic root (Miller et al., 2012; Chapter 2). These diamonds are dominantly colorless octahedra, with <270 to 800 ppm N displaying 5-64% B aggregated N, and an unusual luminescence due to metamorphism (Bruce et al., 2010). Inclusions in non-fibrous diamonds from the Diavik mine (A154 South pipe) largely belong to a harzburgitic paragenesis, similar to other locations of the central Slave (Donnelly et al., 2007; Van Rythoven and Schulze, 2009).

3.3.2 Analysis

The majority of fibrous diamond samples from both the Wawa metaconglomerate and Diavik mine were cleaved for EMP analysis, only one polished diamond was used. Cleaving was chosen over polishing for several reasons: 1) due to abundant cavities in fibrous diamonds, iron from the polishing scaife builds up, contaminating the sample and requiring an intensive cleaning process; 2) inclusions in polished fibrous samples would be subsurface during analysis, lowering totals on the microprobe, whereas with cleaved samples inclusions are exposed at surface for more direct analysis and higher microprobe totals; and 3) cleaving allows for more time-efficient data collection than repeated polishing.

After cleaving, samples were mounted in acrylic discs using a small amount of carbon putty and aluminum foil in order to do both scanning electron microscope and electron microprobe analyses. After mounting, discs were ultrasonically cleaned in distilled water and allowed to air-dry, then cleaned with ethanol before carbon coating. Inclusions were identified on a Philips XL30 SEM with a Bruker Quantax 200 microanalysis system and light element XFLASH 2010 detector at the University of British Columbia, Department of Earth, Ocean and Atmospheric Sciences. Quantitative chemical analysis was done using a CAMECA SX-50 electron microprobe with four wavelength-dispersive spectrometers (WDS; EOAS UBC). All microprobe analyses were done at a beam current of 20 nA, accelerating voltage of 15 kV, and 40° takeoff angle.

A total of 112 analyses from both diamond suites were collected for microinclusions 1 to 10 μm in size. The 90 inclusions analyzed from 10 Wawa diamonds consisted of 41 inclusions analyzed as garnets and 49 inclusions analyzed as olivines. Four of the ten diamonds contained both garnet and olivine, while the other six contained only one phase. All 22 inclusions analyzed from 5

Diavik diamonds were analyzed as olivines. No garnet was found in the Diavik samples. Despite a common presence of fluid trapped along with mineral microinclusions (Israeli et al., 2004; Kopylova et al., 2010), its amount was minimal for the best mineral analyses in this study. It is evidenced by the lack of Cl peaks on SEM-EDS spectra collected prior to microprobe analysis, whilst fluid in Wawa fibrous diamonds is ~40 ml% Cl on a carbonate and water free basis (Smith et al., in press). Minor presence of fluid was detected by high Ca concentrations (0.2- 5 wt% CaO) in almost pure olivine, but such analyses were discarded.

Due to their small size, microprobe analysis totals were not the desired 100%, but instead ranged from 1.37 to 93.87 wt%, with an average of 41.96 wt%. Data below the microprobe detection limits were removed and analyses were renormalized to 100%. Stoichiometry was calculated based on 4 oxygens for olivine and 12 oxygens for garnet (Table 3.1).

3.3.3 Quantitative analysis of microinclusions: methodology and accuracy

Microprobe analysis of microinclusions has been accomplished successfully before. Izraeli et al. (2004) and Weiss et al. (2008) ran analyses on submicron- and <5 micron sized inclusions, obtaining microprobe totals from 1.2-57.7 wt% (average 7 wt%) and 1.5-43 wt%, respectively. When compared to compositions of large inclusions, microinclusion analyses have accuracy within 15% for major elements for both studies (Figure 3.2). The size of the inclusions and the fact that they were subsurface explain the low totals for analyses. Our inclusions differ in that they are slightly larger, and exposed at surface, resulting in higher average totals on the microprobe.

In addition to inclusion size and exposure, the unpolished surface for the majority of studied samples may also affect the accuracy of analyses. It is possible that the irregular fractured surfaces of the diamonds and inclusions have influenced the scattering of the x-rays detected by the microprobe. The four WDS detectors are set at a takeoff angle of 40° from the sample plane, given a horizontal, polished surface. Extreme topography on the inclusion or a tilt in the inclusion surface could distort the take-off angle and the travel distance for x-rays within the sample, resulting in increased or decreased absorption of x-rays before emergence, interfering with the intensity recorded (Wiens et al., 1994; Reed, 1996). It is possible that the effect has different magnitude for various elements, as lighter elements have less energetic X-rays, more

Table 3.1. Electron microprobe analyses for fibrous diamond inclusions from Wawa and Diavik.

Sample	**W6**											**W13**			**W15**	
Avg. of	5				2		4	2					2	2	4[a]	4[b]
Mineral Phase	ol	ol*	ol	ol	ol	ol	grt	grt*	grt	grt	grt	ol*	grt*	grt	ol	ol
SiO_2	40.86	41.16	40.97	41.03	39.95	42.60	40.78	41.73	42.38	41.61	43.57	41.90	38.48	40.14	37.91	42.23
Al_2O_3	0.08		0.09	0.10	0.09		18.32	17.78	18.40	19.78	16.88	1.00	12.05	9.88	0.27	
Cr_2O_3		0.09					7.61	7.86	7.06	5.94	4.60	0.10	15.30	17.48	0.69	
FeO	7.25	6.68	6.57	7.61	6.98	5.94	7.27	5.97	7.44	6.60	8.38	6.48	8.17	8.76	11.05	3.25
MnO	0.16		0.11		0.15	0.12	0.48	0.33	0.45	0.35	0.77	0.16	0.49	0.58	0.12	0.16
MgO	51.64	51.71	51.84	50.82	52.45	51.06	19.04	18.65	17.94	20.04	18.39	49.91	16.07	11.96	49.62	54.14
CaO	0.28			0.07	0.14		6.49	7.46	6.35	5.58	7.25	0.13	9.29	10.96	0.06	
Na_2O								0.45		0.11	0.17		0.30	0.47		
NiO	0.35	0.35	0.42	0.37	0.36	0.28						0.30			0.34	0.22
Total	100.00	100.00	100.00	100.00	100.00	100.00	100.00	100.00	100.00	100.00	100.00	100.00	100.00	100.00	100.00	100.00
Initial Total		34.70	71.82	50.91		53.54			47.91	59.25	46.78	66.50				
Si	0.990	0.996	0.991	0.996	0.971	1.023	2.969	3.026	3.067	2.990	3.160	1.009	2.928	3.085	0.943	1.003
Al	0.002		0.002	0.003	0.002		1.572	1.519	1.570	1.675	1.443	0.029	1.080	0.894	0.008	
Cr		0.002					0.439	0.451	0.404	0.337	0.264	0.002	0.920	1.064	0.014	
Fe	0.147	0.135	0.133	0.154	0.142	0.119	0.443	0.362	0.450	0.397	0.508	0.131	0.520	0.564	0.231	0.065
Mn	0.002		0.002		0.003	0.002	0.029	0.021	0.027	0.021	0.047	0.003	0.031	0.038	0.003	0.003
Mg	1.867	1.864	1.870	1.840	1.901	1.828	2.067	2.015	1.936	2.146	1.989	1.792	1.823	1.368	1.841	1.921
Ca	0.007			0.002	0.004		0.507	0.580	0.492	0.430	0.563	0.003	0.758	0.904	0.002	
Na								0.063		0.015	0.024		0.044	0.072		
Ni	0.007	0.007	0.008	0.007	0.007	0.005						0.006			0.007	0.004
Total	3.009	3.004	3.007	3.002	3.028	2.977	8.026	8.005	7.946	8.011	7.998	2.975	8.083	7.953	3.046	2.997
Mg#	92.70	93.24	93.36	92.25	93.05	93.88	82.35	84.77	81.13	84.40	79.65	93.21	77.81	70.80	88.84	96.72
Mg+Fe	2.014	1.999	2.003	1.994	2.043	1.947						1.923			2.071	1.986
Mg+Fe+Ca							3.017	2.957	2.878	2.973	3.061		3.101	2.836		
O'Neill and Wood (1979) @ 50 kbar		1030°C										750°C				

Table 3.1. Electron microprobe analyses for fibrous diamond inclusions from Wawa and Diavik. (cont)

Sample	W16						W17				W40		W41	W52	
Avg. of				2	4		2						2	2	4[c]
Mineral Phase	ol	ol*	grt	grt	grt*	grt	ol	ol	ol	ol	ol	ol	grt	ol	ol
SiO_2	39.28	40.59	38.73	38.90	40.69	41.77	42.51	41.17	42.39	44.68	43.06	42.66	39.95	41.52	42.36
Al_2O_3	0.38	0.10	15.70	16.54	16.07	16.91	0.13	0.08	0.08				22.27		0.08
Cr_2O_3	0.10		11.41	11.72	10.25	9.79	0.15								0.06
FeO	6.65	5.42	9.03	7.08	6.97	7.46	6.72	5.08	3.36	2.27	6.24	5.07	16.16	5.26	6.10
MnO			0.48	0.35	0.37	0.37	0.19	0.15	0.21			0.16	0.41	0.16	0.14
MgO	53.36	53.32	17.03	19.92	18.83	18.29	49.83	53.20	53.67	52.91	50.18	51.71	11.54	52.70	50.91
CaO		0.13	7.63	5.50	6.65	5.41	0.20	0.06			0.18		9.39	0.09	0.06
Na_2O					0.36								0.55		
NiO	0.23	0.43					0.44	0.26	0.28	0.14	0.34	0.40		0.32	0.35
Total	100.00	100.00	100.00	100.00	100.00	100.00	100.00	100.00	100.00	100.00	100.00	100.00	100.00	100.00	100.00
Initial Total	37.81	42.28	52.16			41.10		62.03	53.37	55.94	26.07	49.81			
Si	0.954	0.979	2.900	2.868	2.987	3.044	1.025	0.989	1.008	1.050	1.034	1.021	2.984	0.998	1.018
Al	0.011	0.003	1.385	1.437	1.390	1.453	0.004	0.002	0.002				1.960		0.002
Cr	0.002		0.676	0.683	0.595	0.564	0.003								0.001
Fe	0.135	0.109	0.565	0.436	0.428	0.454	0.136	0.102	0.067	0.045	0.125	0.102	1.009	0.106	0.123
Mn			0.030	0.022	0.023	0.023	0.004	0.003	0.004			0.003	0.026	0.003	0.003
Mg	1.933	1.917	1.901	2.189	2.061	1.987	1.791	1.906	1.903	1.853	1.796	1.845	1.285	1.888	1.826
Ca		0.003	0.612	0.434	0.523	0.422	0.005	0.001			0.005		0.751	0.002	0.001
Na					0.051								0.079		
Ni	0.005	0.008					0.009	0.005	0.005	0.003	0.006	0.008		0.006	0.007
Total	3.039	3.020	8.069	8.071	8.040	7.948	2.972	3.009	2.990	2.950	2.966	2.979	8.056	3.002	2.980
Mg#	93.47	94.60	77.08	83.38	82.81	81.39	92.96	94.92	96.61	97.65	93.48	94.78	56.01	94.69	93.68
Mg+Fe	2.068	2.026					1.927	2.008	1.970	1.898	1.921	1.947		1.994	1.949
Mg+Fe+Ca			3.078	3.060	3.012	2.864							3.046		
O'Neill and Wood (1979) @ 50 kbar		740°C													

Table 3.1. Electron microprobe analyses for fibrous diamond inclusions from Wawa and Diavik. (cont)

Sample	**W53**		**Dvk1**	**Dvk9**					**Dvk14**		**Dvk15**	**Dvk23**		
Avg. of				2										
Mineral Phase	ol*	grt*	ol	ol	ol	ol	ol	ol	ol	ol	ol	ol	ol	ol
SiO_2	43.79	38.66	41.94	41.17	41.23	39.40	38.43	40.95	40.65	40.11	38.71	39.65	41.31	39.28
Al_2O_3		17.99	1.52				0.10	0.17			1.52	0.15	0.37	0.07
Cr_2O_3		9.07					0.06			0.08			0.18	
FeO	4.21	8.02	3.11	5.92	7.02	7.79	8.23	6.96	6.70	7.96	9.95	11.15	6.49	8.73
MnO		0.32				0.13	0.12				0.16	0.23		
MgO	51.60	19.57	53.43	52.43	51.28	52.33	52.68	51.49	52.30	51.58	49.44	48.35	50.98	51.47
CaO		6.21		0.61	0.14			0.06	0.07		0.23	0.18	0.40	
Na_2O		0.15												
NiO	0.41			0.37	0.33	0.34	0.38	0.36	0.28	0.28		0.29	0.27	0.46
Total	100.00	100.00	100.00	100.00	100.00	100.00	100.00	100.00	100.00	100.00	100.00	100.00	100.00	100.00
Initial Total	42.31	93.73	21.63		50.03	46.27	68.57	51.18	62.93	50.65	81.22	46.27	25.16	41.69
Si	1.040	2.849	0.994	0.992	0.998	0.963	0.943	0.992	0.984	0.978	0.953	0.982	0.998	0.963
Al		1.563	0.042				0.003	0.005			0.044	0.004	0.011	0.002
Cr		0.528					0.001			0.001			0.003	
Fe	0.084	0.494	0.062	0.119	0.142	0.159	0.169	0.141	0.136	0.162	0.205	0.231	0.131	0.179
Mn		0.020				0.003	0.002				0.003	0.005		
Mg	1.828	2.150	1.887	1.885	1.851	1.906	1.928	1.859	1.888	1.875	1.814	1.784	1.836	1.882
Ca		0.491		0.016	0.004			0.002	0.002		0.006	0.005	0.010	
Na		0.021												
Ni	0.008			0.007	0.006	0.007	0.007	0.007	0.005	0.005		0.006	0.005	0.009
Total	2.960	8.116	2.985	3.008	3.002	3.037	3.055	3.006	3.016	3.022	3.025	3.016	2.995	3.036
Mg#	95.63	81.31	96.84	94.04	92.87	92.29	91.94	92.95	93.30	92.03	89.86	88.55	93.34	91.31
Mg+Fe	1.911		1.949	2.004	1.993	2.065	2.097	2.000	2.024	2.037	2.019	2.015	1.967	2.061
Mg+Fe+Ca		3.135												
O'Neill and Wood (1979) @ 50 kbar	580°C													

Blank cells below detection limit; Na2O not analyzed for olivine; NiO not analyzed for garnet; Mg#=Mg/(Mg+Fe)*100; grt=garnet; ol=olivine

[a]Average of 4 replicate analyses with Mg# range of 84.30-91.78; [b]Average of 4 replicate analyses with Mg# range of 96.25-97.16; [c]Average of 4 replicate analyses with Mg# range of 92.42-94.80

*Used in thermometry calculations

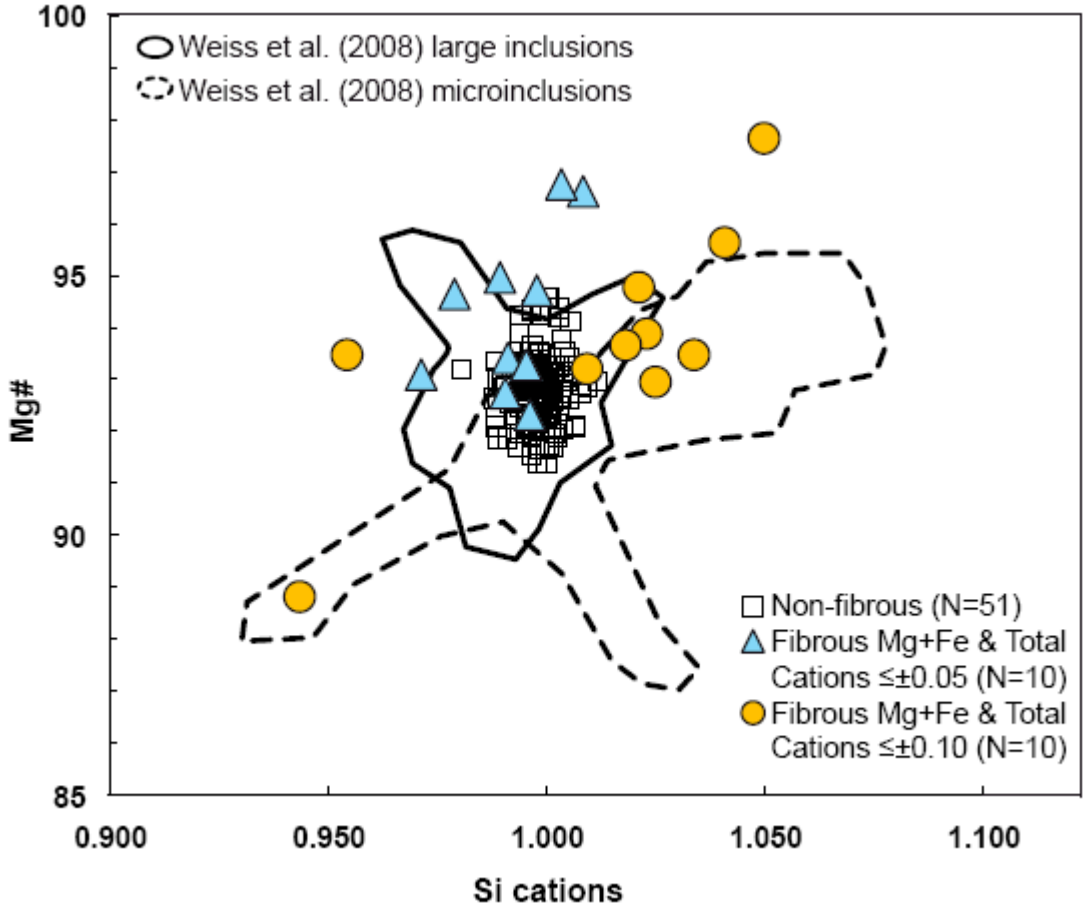

Figure 3.2. Plot of Si cations versus Mg# for Wawa olivine in fibrous and non-fibrous diamonds. Fibrous olivine data from this study represent analyses deemed acceptable based on criteria described in section 3.3.3, after averaging. Samples marked with *triangles and circles* have both total cations and Mg+Fe within ±0.05 and ±0.10 of their ideal values, respectively. Open squares mark olivine compositions in Wawa non-fibrous diamonds (Miller et al., 2012; Chapter 2). *Fields* outline compositions of olivine inclusions in non-fibrous diamonds and microinclusions in fibrous diamonds worldwide (Weiss et al. 2008).

susceptible to attenuation. Also, measurements of different elements are assigned across 4 detectors spaced regularly every 90° about the sample plane, giving 4 different takeoff angle distortions.

To compensate for the effect of local tilt in a sample for EMP energy-dispersive spectroscopy, Wiens et al. (1994) designed a special procedure. It could be applied to samples with a tilt <20°, i.e., to all studied samples. A cleaved diamond surface is almost flat, and the irregular topography is not severely pronounced due to extremely small sizes of microinclusions. Wiens et al. (1994) found that a reasonable analysis can be obtained through averaging two replicate analyses gathered at two sample positions, rotated 180° after the first analysis. This principle was applied to the data collection and reduction in this work. Several analyses of olivine microinclusions were carried out at four different orientations with respect to the detectors, each 90° apart in rotation from the previous analysis, to account for all four WDS detectors on the microprobe. This replicate analysis was done on the largest olivine inclusions from the Wawa fibrous diamonds because larger inclusions (7-10 μm) would be more likely to have significant surface topography to produce variations in x-ray detection. The replicate analysis of rotated olivine microinclusions resulted in the scatter of Mg-numbers of 95.2-97.1 (W15B), 92.4-94.8 (W52) and 84.3-91.8 (W15A), i.e. ΔMg# of 1-2 in two samples, and an extreme ΔMg# of 8 in one sample (Table 3.1; Appendix F). The latter microinclusion has the highest Fe content and the most variance of Fe between replicate analyses, implying that the sample orientation has the strongest effect on high-Fe grains. The observed effect of orientation of unpolished samples on the analysis was the maximum expected for the studied samples, which contain smaller and less ferrous inclusions.

The screening of the analyses was done using the following procedure and criteria (Appendix G). For olivine inclusions, total cations and Mg+Fe cations were used as constraining variables. Acceptable inclusion analyses fall within two categories: 1) Both total cations and Mg+Fe fall within ±0.05 of their ideal values (3.000 cations and 2.000 cations, respectively), 2) Both total cations and Mg+Fe fall within ±0.10 of their ideal values. For Wawa olivines, 22 analyses were rejected using these criteria, and 27 analyses were deemed acceptable. Nine Diavik olivine analyses were rejected and 13 accepted. Garnet inclusions were constrained using Si cation totals, overall cation totals, and Mg+Fe+Ca cations as variables. Constraining limits for garnet were set broader due to the unknown Fe^{2+}/Fe^{3+} ratios. Three categories exist for garnet analyses:

1) All three variables fall within ±0.05 of their ideal values (3.000 Si cations, 8.000 total cations, and 3.000 Mg+Fe+Ca), 2) All three variables fall within ±0.10 of their ideal values, 3) All three variables fall within ±0.20 of their ideal values. Of the 41 inclusions analyzed as garnet, 17 were rejected on these grounds and 24 were deemed acceptable (Table 3.1). The acceptable analyses that showed good stoichiometry were deemed to represent inclusions with a flat horizontal surface. These analyses were reported without averaging. The rest of the analyses were averaged where possible (i.e. if the analyses were acquired from a single grain or from different grains in a close proximity, within 200 μm of each other). The lack of any correlation between composition of the inclusion and the category it falls in with respect to the quality of the analysis (Figures 3-5) attests to the overall data quality and justifies the use of all analyses for interpretation.

3.4 Results

3.4.1 Mineral chemistry

The 27 accepted olivine inclusions from Wawa have varied compositions spanning $Fo_{88.7-97.6}$ (avg. $Fo_{93.6}$). Mg# shows a wide spread of values, with a group of four olivines exhibiting unusually high Mg# (95.6-97.6; Figure 3.3). Weight percent CaO ranges from 0.06 to 0.3 wt% and NiO ranges from 0.14 to 0.5 wt%. Diavik fibrous olivine composition for the 13 accepted analyses spans $Fo_{88.5-96.8}$ (avg. $Fo_{92.5}$; Figure 3.4), with CaO from 0.06 to 0.4 wt% and NiO from 0.3 to 0.5 wt%. Al_2O_3, Cr_2O_3, and MnO were commonly below detection limits for olivine grains from both locations.

The 24 accepted garnet inclusions from Wawa fibrous diamonds display a wide variation in chemistry, with 23 peridotitic Cr-pyropes and 1 eclogitic garnet (Figure 3.5). The latter has Cr_2O_3 contents <1.2 wt%. Total FeO content of the garnets ranges from 5.5 to 16.6 wt%; Cr_2O_3 (4.6 to19.3 wt%) and CaO (5.4 to 11.6 wt%) values also cover a wide range, falling within the harzburgitic, lherzolitic, and wehrlitic fields (Grutter et al. 2004) on the CaO-Cr_2O_3 plot (Figure 3.5).

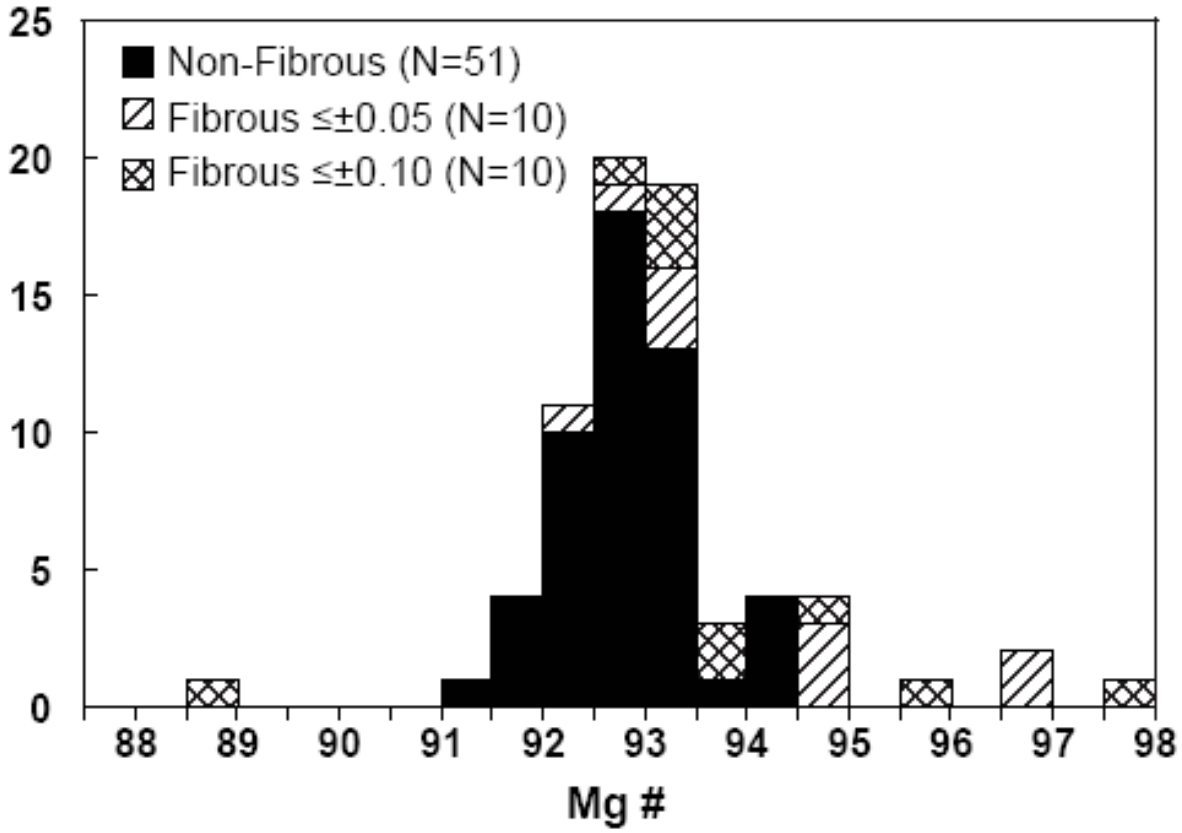

Figure 3.3. Histogram of Mg# for olivine inclusions in Wawa fibrous and non-fibrous diamonds. Non-fibrous DI data are from Miller et al. (2012; Chapter 2). Compositions of olivine microinclusions in fibrous diamonds are divided into two categories according to the quality of the analysis, as described in section 3.3.3.

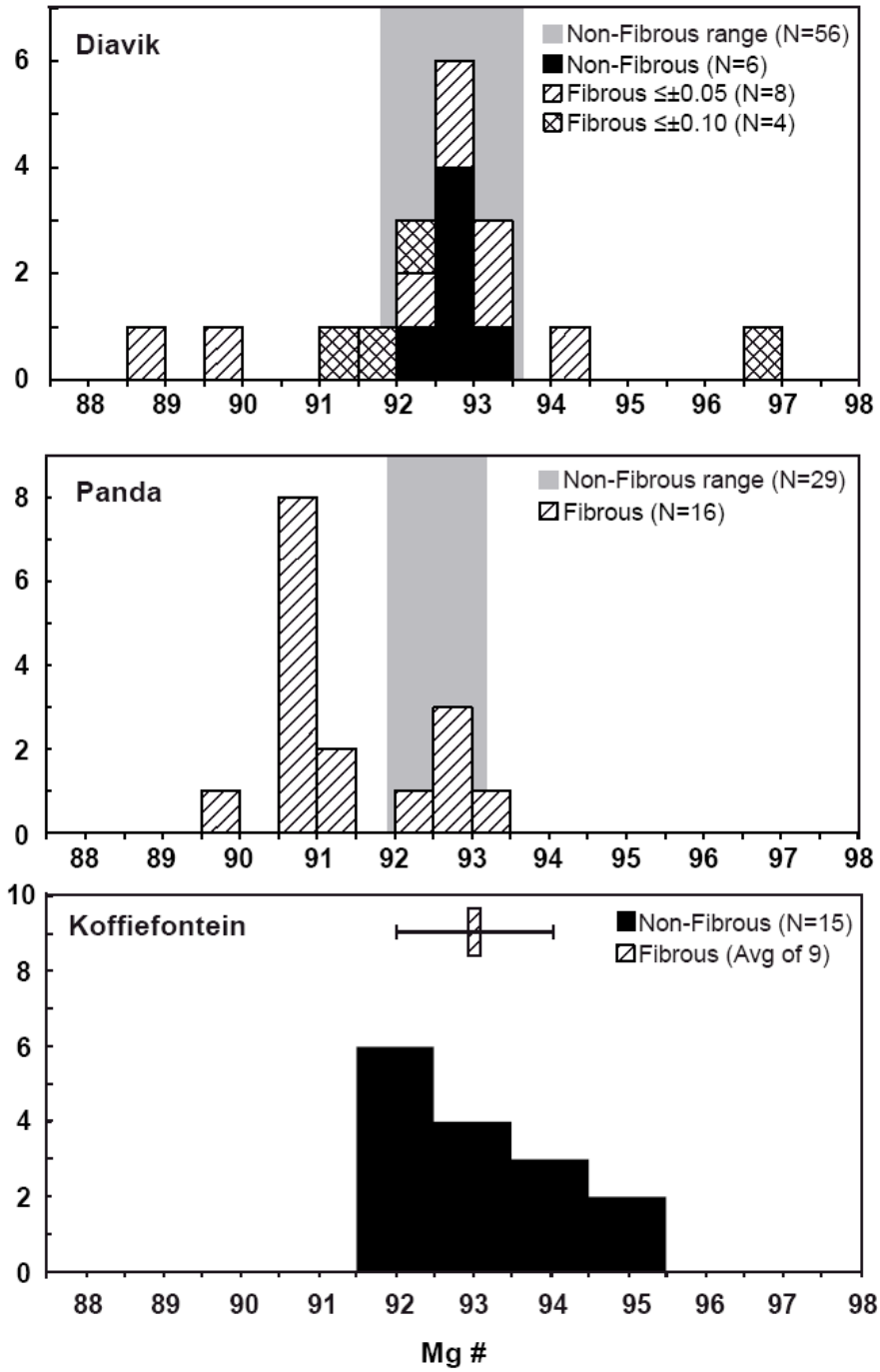

Figure 3.4. Histograms of Mg# for olivine inclusions in fibrous and non-fibrous diamonds for Diavik, Panda and Koffiefontein kimberlites. Ranges of values represented by fields where more detailed published data was not available. Compositions of olivine in non-fibrous diamonds for Diavik are from Donnelly et al. (2007) and Rythoven and Schulze (2009); analogous data for fibrous diamonds are reported in this study and are divided into two categories according to the quality of the analysis, as described in section 3.3.3. Compositions of olivine inclusions in fibrous and non-fibrous diamonds for Panda are from Tomlinson et al. (2006) and Tappert et al. (2005), respectively. Compositions of olivine inclusions in fibrous and non-fibrous diamonds for Koffiefontein are from Izraeli et al. (2004) (representing an average of nine olivine inclusions with the range of error) and Rickard et al. (1989), respectively. Note that at Koffiefontein areas of fibrous growth occur in various parts of octahedrally-grown crystals, cores, mantles around the core or external diamond faces (Izraeli et al., 2001).

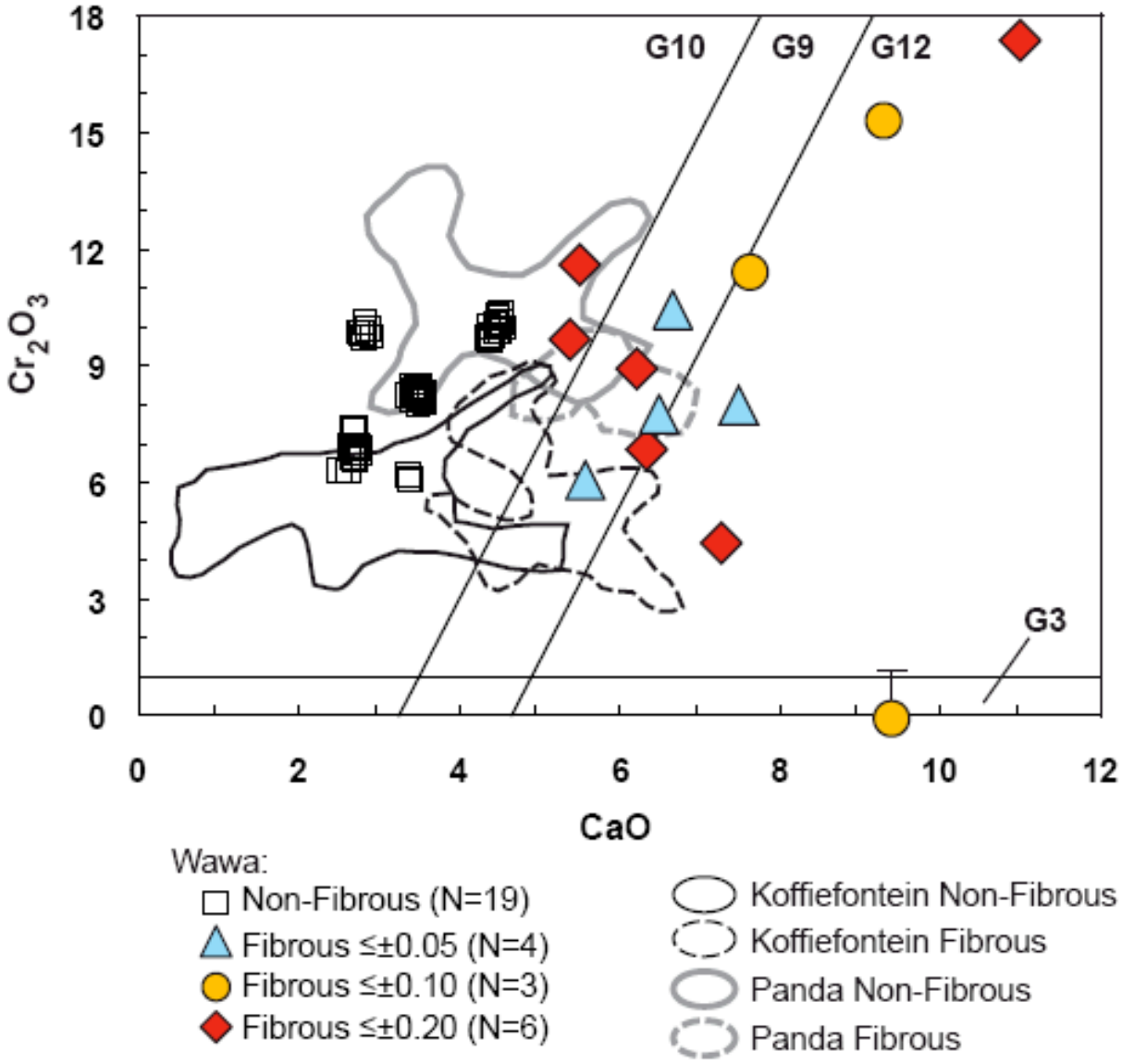

Figure 3.5. Compositions of garnet in Wawa fibrous and non-fibrous diamonds on the CaO-Cr_2O_3 graph of Grutter et al. 2004. Graph divisions are G10- harzburgitic, G9-lherzolitic, G12-wehrlitic, G3-eclogitic. *Open squares* denote compositions of garnet from non-fibrous Wawa diamonds (Miller et al. 2012; Chapter 2). Compositions of olivine microinclusions in Wawa fibrous diamonds are divided into three categories (labeled with *triangles, circles and diamonds*) according to the quality of the analysis, as described in section 3.3.3. *Fields* outline garnet compositions from Koffiefontein non-fibrous diamonds (Rickard et al. 1989), Koffiefontein fibrous diamonds (Izraeli et al. 2004), Panda non-fibrous diamonds (Tappert et al. 2005), and Panda fibrous diamonds (Tomlinson et al. 2006).

3.4.2 Thermometry

Four of the ten Wawa fibrous diamonds contained at least one inclusion each of garnet and olivine, making the samples amenable to the garnet-olivine thermometry (O'Neill and Wood, 1979). For samples containing more than one inclusion of either phase, the most accurate garnet and olivine analyses for each sample were chosen for calculations based on stoichiometry (Table 3.1). Temperatures for the fibrous samples exhibit a wide range from 580-1030 °C at 50 kbar, with an average of 780 °C (Table 3.1, Figure 3.6A). Temperature of 1030 °C is deemed most accurate as it is calculated for grains showing the least deviation from the ideal stoichiometry (sample W6). The lowest temperature of 580 °C is unreasonable, and likely a result of imperfect stoichiometry for inclusion analyses in that sample.

3.5 Discussion

3.5.1 Evolution of mineral compositions during formation of fibrous diamonds

To reveal changes in mineral chemistry that accompany formation of fibrous diamonds, we compared compositions of microinclusions with those of large DI in octahedrally-grown diamonds from the same location. In addition to Wawa and Diavik, we summarized previously published analogous data from the Panda (Ekati mine, Slave craton) (Tomlinson et al., 2006) and Koffiefontein (RSA, Kaapvaal craton) kimberlites (Izraeli et al., 2004).

Magnesium numbers of olivine microinclusions in fibrous diamonds from Wawa are higher than that of large, non-fibrous inclusions, with a group of four olivine inclusions exhibiting unusually high Mg# >95 (Figure 3.3). Mg#'s of olivine from the Diavik mine microinclusions generally have the same value, or lower than those for non-fibrous olivines (Figure 3.4). Studies on Diavik non-fibrous diamond inclusions (Donnelly et al., 2007; Van Rythoven and Schulze, 2009) report olivine Mg# between 91.8 and 93.6 for a total of 56 inclusions analyzed. Of the 12 fibrous Diavik olivine analyses from this study, 10 fall below a Mg# of 93.6. Olivine microinclusions from Panda (Tomlinson et al., 2006) and Koffiefontein (Israeli et al., 2004) also exhibit similar Fe-enrichment, with lower Mg#'s recorded for microinclusions than for large, non-fibrous inclusions (Figure 3.4).

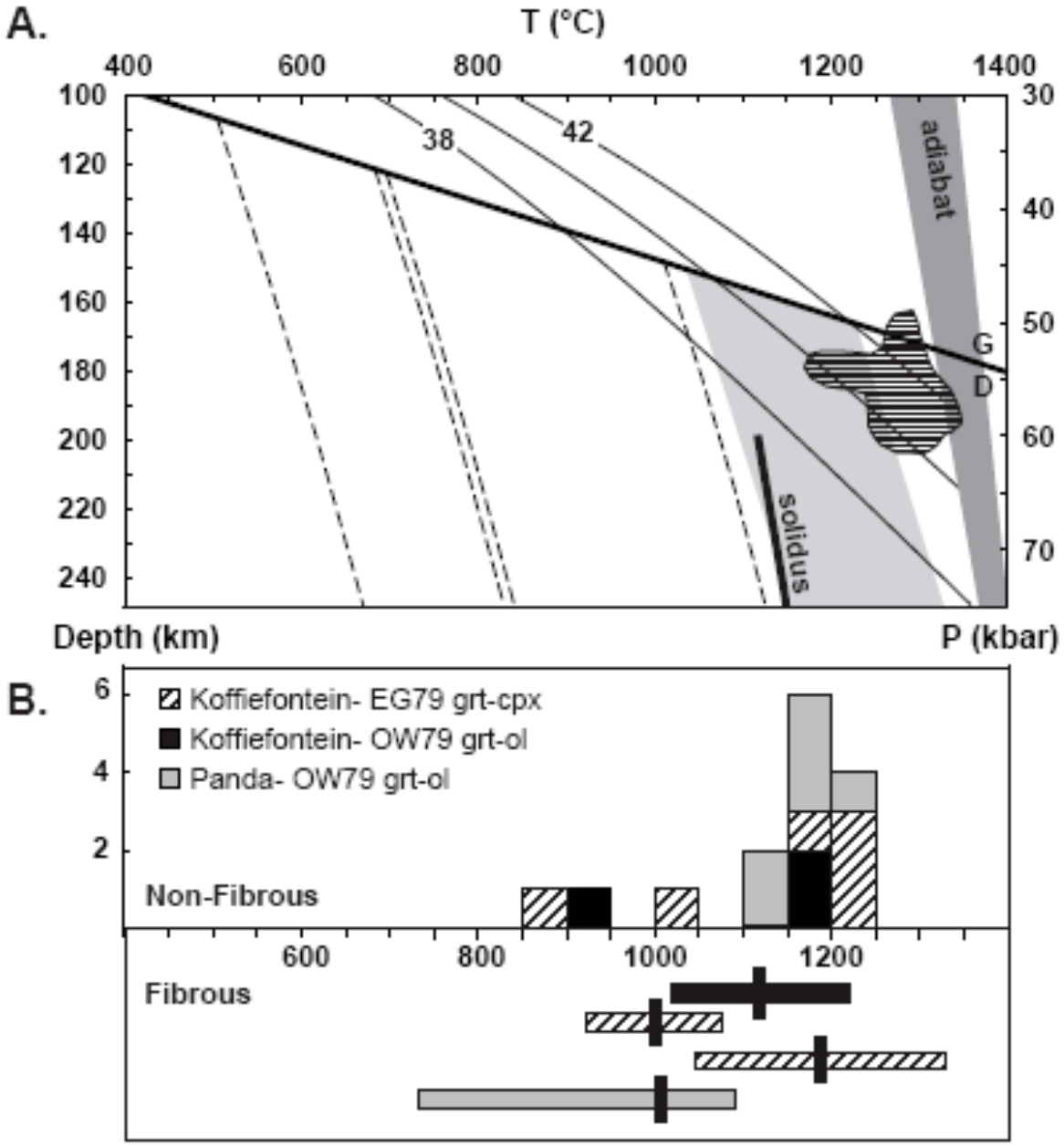

Figure 3.6. (A) Pressure-temperature diagram of equilibrium conditions for Wawa diamonds. Dashed lines are garnet-olivine temperatures (O'Neill and Wood, 1979) for Wawa fibrous diamonds; *grey field* shows a range of analogous temperatures for Wawa non-fibrous diamonds (Miller et al., 2012; Chapter 2). P-T conditions of the modal high-T metasomatism (*horizontal striped field*) are represented by Brey and Kohler (1990) pressures and temperatures for Jericho high-T sheared peridotites (Kopylova et al., 1999). The solidus of alkali-bearing peridotite saturated with CO_2 is from Brey et al., 2010. Graphite-diamond constraint from Kennedy and Kennedy (1976); geothermal gradients from Pollack and Chapman (1977); adiabat range from Rudnick et al. (1998). (B) A comparison between equilibrium temperatures of 50 kbar for inclusions in non-fibrous (*histogram*) and fibrous (*bars*) temperatures for Koffiefontein and Panda kimberlites. Garnet-clinopyroxene temperatures (Ellis and Green, 1979) for Koffiefontein DIs (Rickard et al., 1989; Izraeli et al., 2004) are marked with a *striped pattern*. Garnet-olivine temperatures (O'Neill and Wood, 1979) for Koffiefontein DIs (Rickard et al., 1989; Izraeli et al., 2004) are shown in *black*. Garnet-olivine temperatures (O'Neill and Wood, 1979) for Panda DIs Tappert et al., 2005; Tomlinson et al., 2006) are *grey*. For the latter, average fibrous temperature for Panda sample PAN8 is paired with a bar representing the range of temperatures calculated due to compositional variations (Tomlinson et al., 2006).

Garnet microinclusions from Wawa fibrous diamond are shifted towards the lherzolitic and wehrlitic fields of the CaO-Cr_2O_3 graph compared to garnets within the non-fibrous diamonds (Figure 3.5). Many of the garnets retain their high-Cr_2O_3 content despite this CaO increase, implying that they are a result of secondary alteration, not the growth of new crystals (Tomlinson et al., 2006). The same increase in CaO is observed at Panda (Tomlinson et al., 2006) and Koffiefontein (Israeli et al., 2004). Peridotitic garnet inclusions in fibrous diamonds from all three locations also show an overall increase in total Fe content when compared with garnets from the non-fibrous samples (Figures 3.7, 3.8). The enrichment of the mantle with Ca, Fe and other mafic magmaphile elements is analogous to evolution of garnet compositions traced by diamond inclusions and xenoliths or xenocrysts from the same kimberlite (i.e. Kopylova et al., 1997; Creighton et al., 2008).

Our datasets from Wawa and Diavik do not contain pyroxenes, but these could be compared with data from Panda and Koffiefontein. Orthopyroxene microinclusions from Panda show a trend toward higher Fe content, whereas peridotitic clinopyroxenes from both Panda and Koffiefontein fibrous samples show mild increases in CaO (Figure 3.7). Fibrous diamond inclusion composition trends also generally move towards the composition of the fluid trapped within these diamonds (Figure 3.7), linking inclusions in non-fibrous and fibrous diamonds and the fluid. The exception to this pattern is the evolution of eclogitic clinopyroxenes at Koffiefontein where grains become more magnesian and calcic (Figure 3.7).

The observed changes in the compositions of inclusions reveal two consistent trends of metasomatic alteration during formation of fibrous diamond. One of them is a common trend of an increase in mafic magmaphile element concentrations, in our examples represented by Ca and Fe. The second, rarer trend evolves towards magnesian compositions of olivine (Wawa) and eclogitic clinopyroxene (Koffiefontein). A process, which may have contributed to crystallization of high-Mg olivines (Fo_{94-98}), is recrystallization in oxidizing conditions. Such recrystallization accompanied by increase of Mg# from regular values of 74.9-94.4 to exotically high values of 97.2-99.8 has been observed in the thin, upper basaltic flows of the Big Pine volcanic field, California (Blondes et al., 2012). A similar redox process may also be responsible for genesis of more Fe-rich garnet (Figure 3.8) coexisting with olivine according to a reaction involving diamond growth from carbonate:

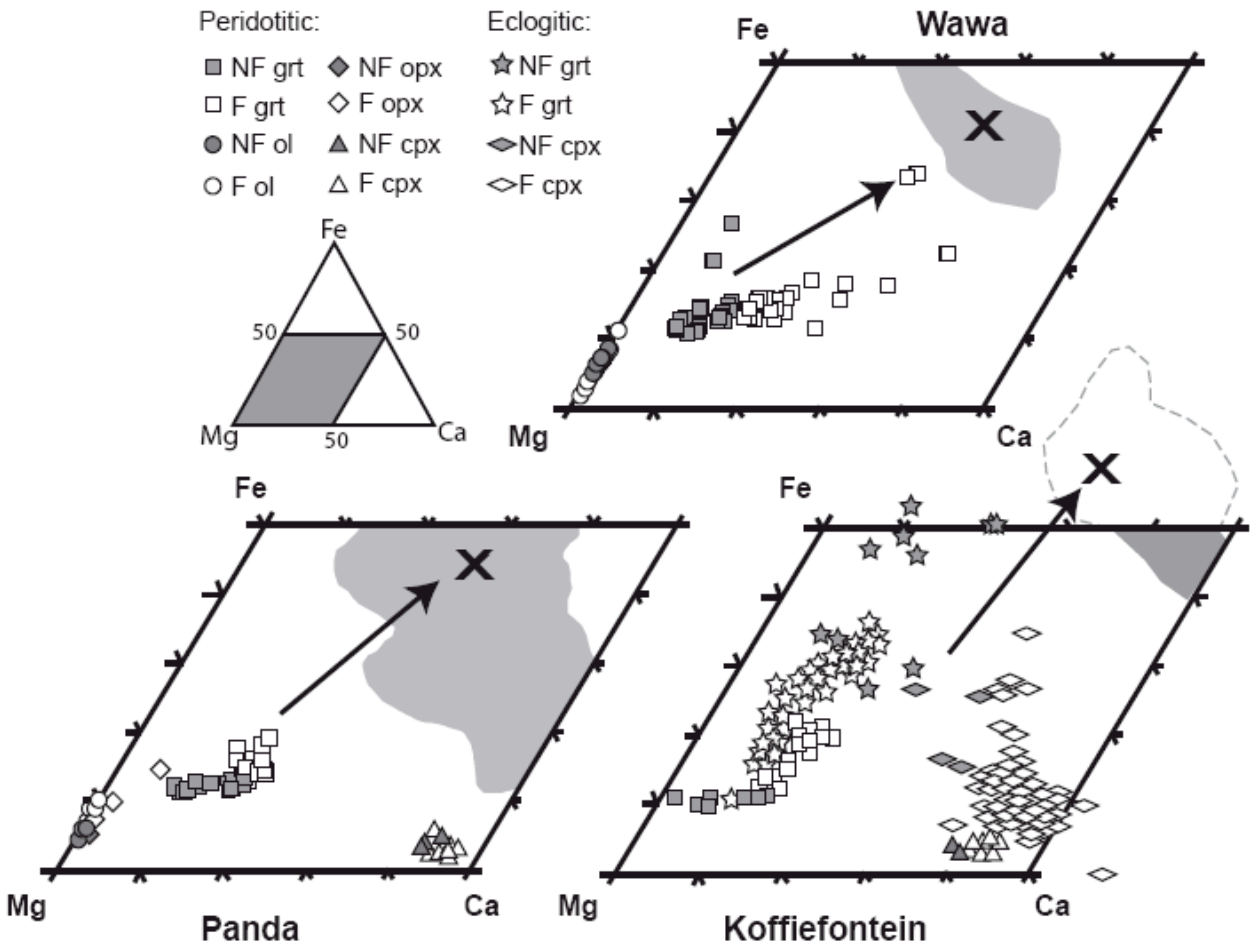

Figure 3.7. Ternary plots (in molar amounts of Mg, Ca and Fe) of mineral inclusion compositions from fibrous (F) and non-fibrous (NF) diamonds from Wawa, Panda, and Koffiefontein. Data from Wawa are from Miller et al. (2012; Chapter 2) and this study. Data from Panda are from Tomlinson et al. (2006). Data from Koffiefontein are from Izraeli et al. (2004). *Grey fields* represent fluid composition at each location with the average composition (*marked X*) as analyzed in fluid inclusions in fibrous diamonds (Izraeli et al., 2001; Tomlinson et al., 2006; Smith et al., in press). Arrows indicate trends toward fluid compositions.

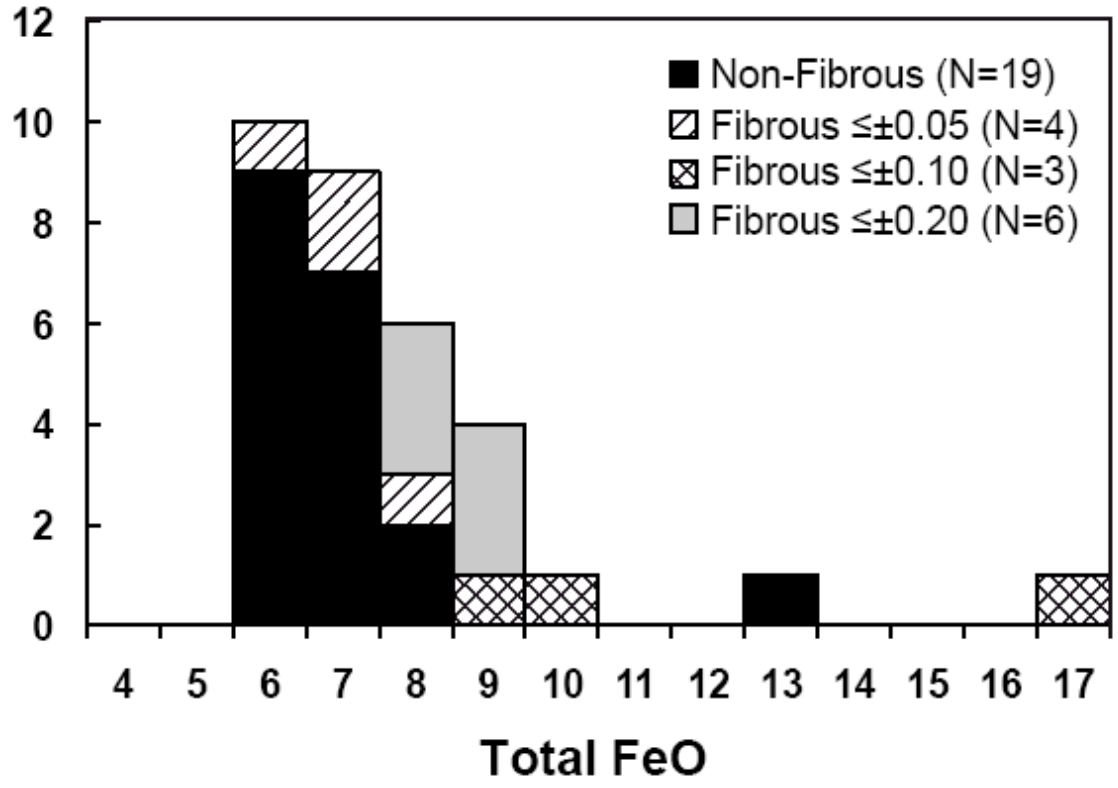

Figure 3.8. Histogram of total FeO content for garnet inclusions in Wawa fibrous and non-fibrous diamonds. Non-fibrous DI data are from Miller et al. (2012; Chapter 2). Compositions of garnet microinclusions in fibrous diamonds are divided into three categories according to the quality of the analysis, as described in section 3.3.3.

$$MgCO_3 + 3Fe_2SiO_4 + 3FeSiO_3 \Leftrightarrow Fe_5^{2+}MgFe_4^{3+}Si_6O_{24} + C$$
carbonate olivine orthopyroxene garnet diamond

The Mg increase in eclogitic clinopyroxene matches the most common trend of its mineral chemistry evolution reported in many kimberlite-derived eclogite xenoliths globally and attributed to partial melting of grain rims and metasomatism (e.g., De Stefano et al., 2009, and references therein).

3.5.2 Evolution of the thermal regime accompanying formation of fibrous diamonds

The most accurate garnet-olivine temperature for Wawa fibrous diamonds (1030 °C at 50 kbar; O'Neill and Wood, 1979) is slightly lower than those calculated for non-fibrous diamonds. Garnet-olivine temperatures for non-fibrous inclusions at Wawa (1050-1230 °C at 50 kbar; Figure 3.6A) paired with garnet-orthopyroxene thermobarometry indicate a cool, cratonic geotherm at 39-41 mW/m^2 (Miller et al., 2012; Chapter 2). A similar absence of heating and thermal disturbance is observed through comparison of garnet-olivine and garnet-clinopyroxene thermometry for fibrous and non-fibrous diamonds from both Koffiefontein and Panda (Figure 3.6B).

Both peridotitic and eclogitic minerals pairs from non-fibrous Koffiefontein diamonds indicate diamond formation on a cratonic geotherm around 40 mW/m^2 (Rickard et al., 1989). Garnet-olivine temperatures (O'Neill and Wood, 1979) for harzburgitic non-fibrous diamonds are 950-1200 °C at 50 kbar, within the range of garnet-clinopyroxene (Ellis and Green, 1979) temperatures for eclogitic diamonds (900-1250 °C at 50 kbar; Figure 3.6B). When the same thermometers are applied to mineral pairs in Koffiefontein fibrous diamonds, temperatures again fall within this range (1000-1200 °C, Figure 3.6B), showing the lack of heating during fibrous diamond growth (Izraeli et al., 2004).

A similar conclusion was also reached by Tomlinson et al. (2006) for Panda diamonds. At 50 kbar, garnet-olivine temperatures for these non-fibrous diamonds fall between 1060-1075 °C for touching inclusions and 1100-1230 °C for non-touching inclusions, i.e. on a geothermal gradient around 38 mW/m^2 (Tappert et al., 2005). Thermometry for mineral pairs in fibrous diamonds suggests slightly lower temperatures of 930-1010 °C, with the single garnet-olivine pair yielding a temperature of 1000 °C at 50 kbar (Figure 3.6B; Tomlinson et al., 2006). The geothermal

gradient approximated for fibrous diamonds is also similar to that represented by the garnet-orthopyroxene pairs in non-fibrous diamonds (Tappert et al., 2005; Tomlinson et al., 2006).

For all above examples it was assumed that new local bulk chemical compositions of the mantle created by the metasomatic flux did not affect the accuracy of thermobarometry, and elemental equilibrium between phases reflected mainly temperatures rather than the new distribution coefficients in the presence of fluid. The assumption is justified by the uniform trend in temperatures evident in all 4 locations independent on whether they are calculated for Mg-poor or Mg-rich olivines. The latter may be controlled by distinct distribution coefficients for carbonatitic melts, as shown below.

The thermobarometry suggests that fibrous diamond formation was triggered by "cold" fluids thermally equilibrated with the ambient mantle. In contrast, the growth of octahedral, non-fibrous diamond is accompanied by a pulse of transient heating by about 100-150 °C, as evidenced by non-touching and touching mineral pairs as thermometers of growth and mantle storage, respectively (Stachel and Harris, 2008). The low temperatures of fibrous diamond growth would be subsolidus for alkali-bearing peridotite saturated with CO_2 (Figure 3.6A) and supersolidus in the presence of water. An absence or low degree of partial melting of the mantle during fibrous diamond formation match low Si contents of the trapped fluid (Israeli et al., 2001; Tomlinson et al., 2004; Smith et al., in press).

3.5.3 Metasomatism accompanying fibrous diamond growth

We can now compare characteristics of the metasomatism that creates fibrous diamonds with common types of cratonic mantle metasomatism. It always replenishes the mantle with incompatible and mafic magmaphile elements, such as Ca and Fe, but other traits of the metasomatism allow for further distinction of types.

The first and most conspicuous of these is modal metasomatism with melt-related asthenospheric fluids resulting in formation of high-T peridotites (Griffin and Ryan, 1995; O'Reilly and Griffin, 2010 and references therein). The fluids, loaded with incompatible elements, metasomatised depleted lithospheric peridotites (Griffin et al., 1999; O'Reilly and Griffin, 2010), oxidized and resorbed their diamonds (Gurney and Zweistra, 1995), and recrystallized the peridotitic mantle

immediately before kimberlite generation (Goetze, 1975). All this happened in a temporary thermal disturbance manifested by a shift from a steady-state geotherm in the deepest parts of the lithosphere and the asthenosphere to a range of high temperatures at the same pressure (Boyd and Gurney, 1986; Harte and Hawkesworth, 1989). Since megacrysts relate by composition and P-T parameters to high-T peridotites (Harte and Hawkesworth, 1989) and to kimberlitic fluids (Kopylova et al., 2009 and references therein), this thermal perturbation accompanies generation of the entire series of rocks, leading from coarse peridotites to kimberlites.
Formation of fibrous diamonds cannot be related to this high-T metasomatism shortly predating kimberlites (by thousands of years, Smith and Boyd, 1992) because it is associated with significant heating (Figure 3.6A). The high-T metasomatism also occurs later than formation of fibrous diamonds, as more time is required to aggregate nitrogen atoms in the diamond crystal lattice (Ma scales; Boyd et al., 1994).

Other types of cratonic metasomatism are cryptic and do not involve recrystallization and formation of new phases. One type of this metasomatism is irreversible fertilization of the mantle lithosphere over time, revealed by study of peridotites and Cr-pyrope grains (Griffin et al. 1998). This change makes garnet more calcic and less chromian, increases Y and lowers Zr/Y from the Archean to the Phanerozoic.

Another cryptic process of Ca addition introduces Zr independent of Y, along with Ti. It is recorded on the scale of a single zoned garnet grain (Griffin et al., 1999) and is accompanied by an increase in relative oxygen fugacity of approximately two log-bar units (McCammon et al., 2001). This metasomatism is associated with negligible heating of 30-50 °C (Table 3 of McCammon et al., 2001) at relatively low temperatures (900-1100 °C; Griffin et al. 1998). Griffin et al. (1998) speculated that this metasomatism particularly affected Archean mantle lithosphere due to its low abundances of clinopyroxene and garnet, which would normally act in a buffering capacity.

The temporal irreversible fertilization of the mantle and the low temperature metasomatism could be distinguished by contrasting trace element signatures. The former results in the decreasing Zr/Y ratios, whereas the latter increases Zr/Y ratios in garnet (Figure 13 of Griffin et al. 1998). Since the composition of garnet is directly controlled by the bulk composition of the mantle (Griffin et al., 1998), Zr/Y ratios of mantle segments affected by the metasomatism

should also be different. We assume that non-fibrous diamonds reflect the composition and Zr/Y ratio of the ambient mantle, and fibrous diamonds mirror the composition and Zr/Y ratio of the metasomatised mantle. Then the characteristics of the metasomatism can be investigated through comparison of Zr/Y ratios of non-fibrous and fibrous diamonds. For this comparison (Figure 3.9), we used trace element data for non-fibrous diamonds from several worldwide locations and a variety of parageneses (Araujo et al., 2009; McNeill et al., 2009; Rege et al., 2010). Fibrous diamond trace element data were collected for both fibrous cubic stones as well as fibrous coats on monocrystalline cores (Araujo et al., 2009; Tomlinson et al., 2009; Klein-Ben David et al., 2010; Rege et al., 2010; Zedgenizov et al., 2011). The Zr/Y ratios demonstrated no change (Figure 3.9) indicating that neither low-temperature metasomatism, nor temporal fertilization is a major contributor to fibrous diamond formation.

Fibrous diamonds therefore seem to have formed in a distinct metasomatic event that has no parallels among common types of cratonic metasomatism. This matches the relative scarcity of fibrous diamonds, in contrast to common presence of metasomatised rocks in the mantle.

The agent of this metasomatism was K-rich hydrous carbonatitic fluid, trapped in fluid inclusions in many fibrous diamonds. Potassium at P>60 GPa could only be introduced to the mantle with fluid, as K does not have a host mantle mineral it can reside in (Brey et al., 2010). The fluid influx generated diamonds only where and when it occurred at ambient low temperatures of the cratonic geotherm, below the solidus of the alkali-bearing peridotite saturated with CO_2 (Brey et al., 2010). Experiments on diamond synthesis have demonstrated a crucial role of water and alkalis in promoting diamond crystallization by reducing the induction period preceding diamond nucleation and increasing the solubility of carbon and the rate of carbon mass transfer. The lowest P-T conditions of cratonic diamond nucleation are characteristic of the alkaline-carbonate-H_2O-CO_2-C system (Sokol and Pal'yanov, 2008, and references therein) in comparison to silicate-bearing and alkali-free systems. Fibrous diamond growth is likely to occur by the reduction of carbonate from infiltrating fluids (Tomlinson et al., 2006). Recrystallization of pre-existing metastable graphite may also account for fibrous diamond growth, triggered by the arrival of the fluid rich in H_2O and K that alters kinetics of diamond crystallization (Sokol and Pal'yanov, 2008 and references therein). If the host already contains carbonate in equibilibrium with the metastable graphite, this scenario does not require a change in the redox state or any redox reactions to produce fibrous diamonds with carbonatitic fluid inclusions. High

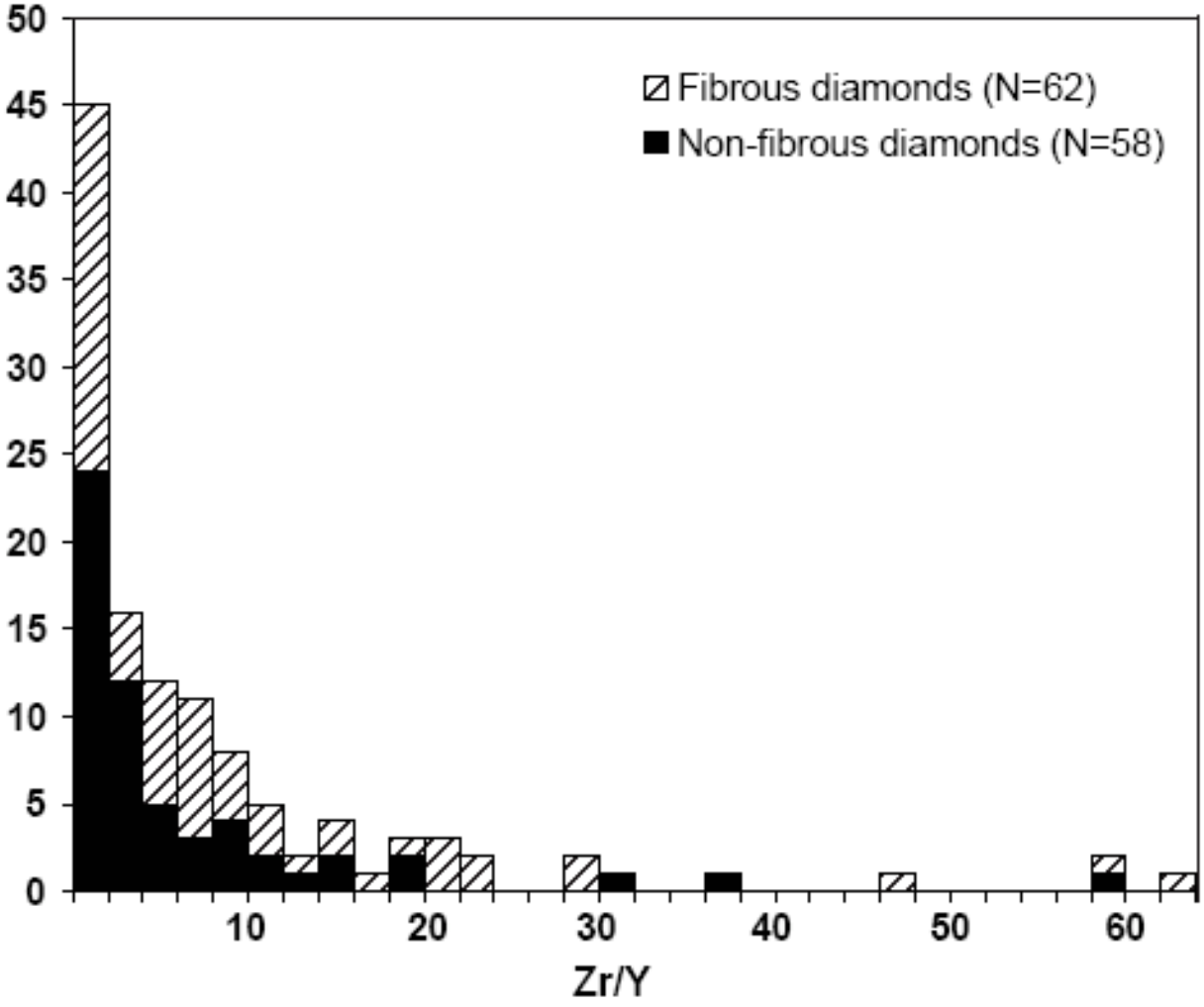

Figure 3.9. Plot of Zr/Y ratios in non-fibrous and fibrous diamonds from locations worldwide reported in McNeill et al., 2009; Araujo et al., 2009; Tomlinson et al., 2009; Klein-Ben David et al., 2010; Rege et al., 2010; and Zedgenizov et al., 2011.

temperatures significantly inhibit diamond growth as melting results in a decrease of H_2O concentration, from ~80% (at 5-6 GPa) in the fluid phase to 30% in the water-saturated melt (Stalder et al., 2001). Disappearance of a fluid phase upon melting of mantle rocks and the generation of water-bearing silicate melt can cause a sharp decrease in the diamond formation rate (Sokol and Pal'yanov, 2008). It is therefore not coincidental that observed temperatures of the fibrous diamond formation (1030 °C at 50 kb in Wawa) are below the solidus of alkali-bearing peridotite saturated with CO_2 (Brey et al., 2010; Figure 3.6A).

The K-rich hydrous carbonatitic fluid may be compositionally very diverse, especially its carbonatitic end-member, which could show the predominance of Ca (most commonly), Fe (Klein-Ben David, 2009; Zedgenizov et al. 2009, Kopylova et al., 2010) or Mg (Klein-Ben David, 2009). Interaction with these fluids shifts composition of mantle minerals towards respective fluids (Figure 3.7). Another effect of the fluid influx is a change in elemental distribution coefficients. This is evident, for example, for Wawa microinclusions. Fluids in Wawa are equilibrated with more Fe-rich garnet (Figure 3.8) and more Mg-rich olivine (Figure 3.3); this indicates changes in the Mg and Fe olivine-garnet distribution coefficients in the new fluid-rich environment. Experiments demonstrated that the partition coefficient of Ca between garnet and K-rich carbonate-silicate melt is higher than in K-poor system implying that Ca activity in melt increases with the addition of K (Brey et al., 2010). This pattern explains consistent evolution of garnet towards Ca-rich compositions (Figure 3.5) even when it interacts with saline fluids. Changes in ratios of CO^{3-} and Si activities in the fluid also significantly alter the chemistry of minerals. Carbonatites and carbonatite-related rocks (phoscorites) crystallize more forsteritic olivine than olivines of silicate rocks from the same complex (Gaspar et al., 1998). Carbonatite olivine (e.g. Fo_{94-98} in the Jacupiranga; Gaspar, 1998; Fo_{98} in Kerimasi; Guzmics et al., 2011) is similar in composition to Mg-rich olivine in fibrous Wawa diamonds (Figure 3.3) implying its equilibration with a fluid with high CO^{3-}/Si.

3.5.4 Are fibrous diamonds older and not grown from proto-kimberlitic fluids?

The current view on the origin of fibrous diamonds emphasizes their low Type IaA nitrogen aggregation state (Boyd et al., 1987; 1994) as an indication of a relatively short time period between growth of the fibrous diamond coats and kimberlite eruption (5-7 Ma; Navon, 1999). Moreover, this temporal relationship and the uniformity of fibrous diamonds with respect to their

N aggregation has been used as evidence for a genetic relationship between kimberlite magmatism and fibrous diamond growth (Boyd et al., 1994). The relationship has been strengthened by Sr isotope (Akagi and Masuda, 1988), trace element evidence (Tomlinson et al., 2005; 2009; Zedgenizov et al., 2007) and alkaline- and chloride-rich compositions of reconstructed primary kimberlites similar to those of fluid inclusions in fibrous diamonds (Kamenetsky et al., 2004). Below we show that new data on low temperatures of the fibrous diamond formation and a critical mass of new observations on diamond geochemistry and kimberlite geology deem the link between kimberlites and fibrous diamonds unnecessary.

Relatively low (<1030 °C) ambient temperatures of fibrous diamond formation and lack of diamonds displaying type Ib aggregation found in this study render impossible constraints on the diamond's residence time. It is known experimentally that at T<1050 °C nitrogen aggregation from A to B-centers does not occur (Taylor et al., 1990; 1996), which would explain and maintain the dominance of type IaA aggregation in fibrous diamonds worldwide, despite possible extended residence times. If one assumes slightly higher temperatures of fibrous diamond formation (1100 °C) at which the A to B aggregation could take place, and pairs this with the worldwide nitrogen content mode for fibrous diamonds of 1000 ppm (Cartigny, 2005), the calculations would yield residence times upwards of 28 Ma, much longer than the previously assumed 7 Ma. This estimate would apply for the vastly prevailing majority of fibrous diamonds and disregard only very rare Type IaAB fibrous diamonds (e.g., Zedgenizov et al., 2006; 2011) and one occurrence of yellow Type Ib diamonds (Taylor et al., 1996). For the latter, the shortest residence time of several million years is estimated, as type Ib diamonds quickly aggregate their C-centers to A-centers (<7 Ma at T>950 °C, Taylor et al., 1996). However, fibrous diamonds could incorporate nitrogen directly as A-centers during growth (Boyd et al., 1994), making an intermediate step of C- to A-center aggregation unnecessary.

There has been only one estimate of the absolute age for fibrous diamonds (Burgess et al., 2002). The Ar-Ar dating of fibrous coats on Aikhal kimberlite yielded apparent ages 3-4 Ga, 1.44 Ga and 131 Ma. The age of the host kimberlite is unknown, but assumed to be within the range for other kimberlites of the host Alekit field (350–380 Ma).

Fluids deposited fibrous diamonds do not resemble kimberlites compositionally. The fluids have varied major element chemistry, significantly different (especially in higher K and volatile

contents) from kimberlites (Klein-Ben David et al., 2010). The claim that alkali and halogen enrichment of fluid inclusions in fibrous diamonds is similar to that in the so-called "exceptionally fresh" kimberlite melt of the Udachnaya-East pipe (Kamenetsky et al. 2004; Pal'yanov et al., 2007; Zedgenizov et al., 2009, 2011) is misleading and results from inappropriate compositional space chosen for representation of the compositional data (Figure 3 of Kamenetsky et al., 2004). The conventional (K+Na)-Ca-Si plot groups all alkalis together and masks significant differences between Na and Ca-rich Udachnaya compositions (Kopylova et al., submitted; Kostrovitsky et al., submitted) and more K-rich diamond inclusions (Israeli et al., 2004; Klein Ben-David et al, 2009; Zedgenizov et al., 2009, 2011; Kopylova et al., 2010). When a different triangular diagram, Na-K-Ca (Figure 3.10) is used for the comparison, chemical differences between the Udachnaya East kimberlite and fluids in diamonds are well resolved and significant. Udachnaya East kimberlite plots mostly around the Ca apex, with few analyses trending towards the Na corner. Fluid inclusions in diamonds range in composition from Ca- to K-rich and show no overlap (except for 1 specimen) with Udachnaya East kimberlite. The reason for the contrast in the geochemistry stems from a crustal origin of Na, K and Cl minerals in the Udachnaya East kimberlite, which have been introduced through assimilation of evaporate xenoliths and interaction with buried brines (Kopylova et al., submitted; Kostrovitsky et al., submitted).

Trace element evidence for the origin of fibrous diamond fluid is more controversial. The few trace elements that can be analyzed by EPMA directly in inclusions are drastically different from kimberlite abundances. Chlorine and Ba enrichment in diamond fluids (up to 16 wt% BaO, Klein-Ben David et al., 2009; Kopylova et al. 2010; Smith et al., in press) is never matched by kimberlite melts. Formation of Cl-rich kimberlite magma from chloride–carbonate bearing peridotites is unlikely as it requires unrealistically high temperatures and degrees of melting (Litasov and Ohtani, 2009). Evaporite-contaminated Udachnaya kimberlite is S- and B-rich (Kopylova et al., submitted; Kostrovitsky et al., submitted). When trace elements are measured by mass-spectrometry or ICP-MS in bulk diamond, the resulting trace element signatures are conservative, decoupled from major element composition (Klein-Ben David et al., 2010) and resemble kimberlites and carbonatites. This inspired models with a direct genetic link between fibrous diamond fluids and kimberlites (e.g., Tomlinson et al., 2005, 2009; Zedgenizov et al., 2007). Since publication of these models, however, we have learned more about the parent fluid of non-fibrous diamonds. These diamonds that resided billions of years in the mantle and

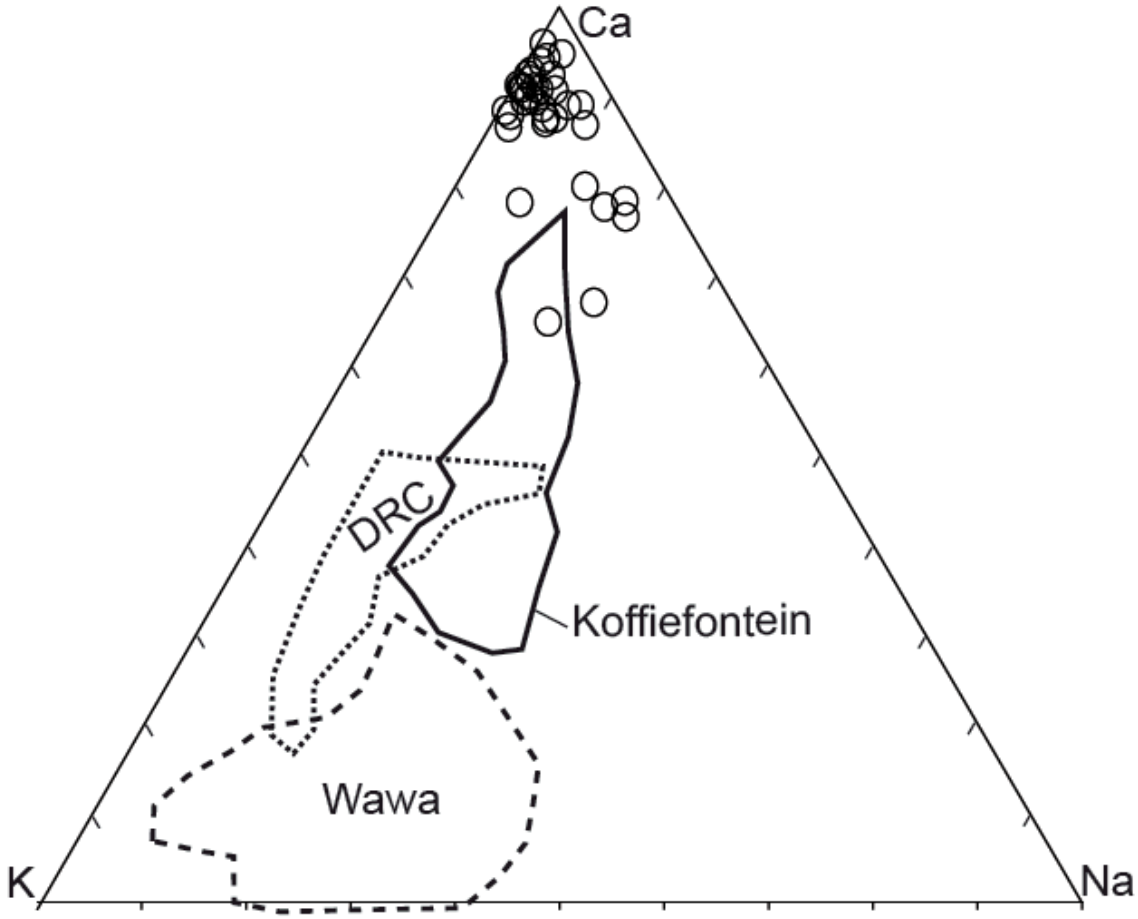

Figure 3.10. A Ca-Na-K (wt%) ternary diagram of compositions of fluid inclusions in diamonds and the Udachnaya East serpentine-free kimberlite. The latter is labeled by *open circles* and are taken from Kopylova et al., (submitted). Fluid inclusion compositions are represented by for saline-carbonatitic fibrous diamonds in Koffiefontein (Izraeli et al., 2004), silicic-carbonatitic diamonds from DRC (Kopylova et al., 2010), and saline diamonds from Wawa metaconglomerate (Smith et al., in press).

indisputably unrelated to kimberlites share many similarities with fibrous diamonds with respect to trace elements ratios (Araujo et al., 2009; McNeill et al., 2009; Klein-Ben David, 2010), including Zr/Y, as demonstrated in this study. Trace element signatures of silicate inclusions trapped within fibrous and non-fibrous diamonds are very similar and may be imposed by the same fluid composition (Tomlinson et al., 2009).

We would therefore argue that formation of fibrous diamonds is not necessarily related to kimberlites. Fibrous diamonds are not found exclusively in kimberlites, but also occur in mantle xenoliths (Anand et al., 2004; Zedgenizov and Ragozin, 2007; Liu et al., 2009). In rare cases, fibrous diamond growth is overgrown by octahedral diamond with marked N aggregation, indicating a clear temporal separation between fibrous diamond growth and kimberlite eruption (Zedgenizov et al., 2006; Rondeau et al., 2007). The global uniformity of Type IaA aggregation in fibrous diamond as the proof for a causal relationship to kimberlite could instead be explained by the relict, "frozen" character of N below the temperatures of A to B aggregation. Moreover, the scarcity of older fibrous diamond with higher N aggregation than Type IaA may result from their preferential dissolution compared to octahedral diamond, due to the imperfect crystal structure and high impurity content (Klein-Ben David et al., 2007). However, the sharp, unresorbed octahedral cores typical of fibrous-coated diamonds suggest that such packages have eluded significant dissolution/resorption. All these data, together with a lack of absolute ages of fibrous diamonds, allow for an alternative explanation of their formation. Fibrous diamonds no longer should be tied temporally and genetically to kimberlites, although one of metasomatic agents of the fibrous diamond formation is asthenospheric (Klein-Ben David et al., 2010, and references therein), like kimberlite and many other magmas.

4. Conclusions

Silicate mineral inclusions in diamonds from a metaconglomerate in the Wawa subprovince of the Superior craton and from the Diavik mine were studied to infer the thermal state and lithology of the diamondiferous mantle. Inclusions from non-fibrous and fibrous diamonds were analyzed on the electron microprobe to determine mineral chemistry and calculate equilibrium pressures and temperatures. These data were analyzed along with published data from Wawa, Kirkland Lake, Panda and Koffiefontein kimberlites to infer evolution of the thermal regime of the mantle and temporal processes that affected the lithosphere. The implications of this study help to clarify cratonic root stability and the connection between kimberlites and fibrous diamond growth. The following conclusions can be drawn:

1. Non-fibrous diamonds from the Wawa metaconglomerate contain inclusions of Cr-pyrope, Mg-chromite, olivine (Fo_{93}), and orthopyroxene (En_{94}) typical of a peridotitic paragenesis. Garnet chemistry narrows the mantle host rock more specifically to harzburgite. This paragenesis is typical for diamonds formed in cratonic roots, indicating the presence of a cratonic root beneath the Southern Superior prior to 2.7 Ga.

2. Fibrous diamonds from Wawa contain mineral inclusions of garnet and olivine (Fo_{94}). Garnet chemistry also suggests a dominantly peridotitic paragenesis, but is more varied than non-fibrous diamonds, corresponding to harzburgitic, lherzolitic, wehrlitic and eclogitic compositions. Olivine inclusions display unusually high Mg content, with a group of four inclusions displaying Mg# >95 (95.6-97.6). Diavik fibrous inclusions consist only of olivines (Fo_{93}).

3. Comparison of mineral inclusion chemistry between non-fibrous diamonds and fibrous diamonds from four locations (Wawa metaconglomerate, Diavik mine, Koffiefontein kimberlite, Panda kimberlite) reveal trends of changing mantle compositions due to metasomatism associated with fibrous diamond growth. Two major trends are seen among the data sets: 1) an increase in incompatible elements (i.e., Ca and Fe) seen in fibrous diamond garnet, olivine, and pyroxene microinclusions; 2) evolution toward more magnesian compositions in Wawa fibrous diamond olivine microinclusions and eclogitic

pyroxenes from Koffiefontein. These changes resulted from interaction with K-rich hydrous carbonatitic fluid, which may be associated with more oxidizing conditions.

4. Coexisting garnet and olivine inclusions in Wawa diamonds constrain equilibration temperatures of 1050-1250 °C in non-fibrous crystals and 580-1030 °C for fibrous crystals at 50 kb.

5. The thermal evolution of the lithospheric mantle beneath the Southern Superior craton was traced from the Archean to present day using mineral inclusions in non-fibrous Archean diamonds, and xenolith data from younger kimberlites, representing the Proterozoic and Phanerozoic. Thermobarometry calculations for these different datasets reveal an increase in the heat flow over time from a cool, cratonic geotherm in the Archean (39-41 mW/m^2) to a hotter geotherm (46 mW/m^2) as early as 1.1 Ga beneath the Wawa subprovince. This increased thermal regime is matched with a decrease in reconstructed lithospheric mantle thickness, indicating that the diamondiferous portion of the Southern Superior cratonic root was destroyed in some areas by 1.1 Ga. In other areas, as evidenced by the Kirkland Lake kimberlites, only minor heating was involved, but xenoliths still record a thinning of the lithosphere from 190 km to ~150 km, removing it from the diamond stability field.

6. High-lateral resolution seismic surveys indicate the absence of the diamondiferous root in the Southern Superior, where it was present at 2.7 Ga. Cold, high-velocity lithospheric mantle still exists beneath the northern Superior craton, with the southern boundary corresponding to terrane boundaries. This abrupt cutoff of the root parallel to terrane boundaries strongly suggests that the tectonic amalgamation of the younger, Neoarchean terranes to the Superior protocraton played a major role in modification of the lithospheric mantle. Tectonic erosion by subducting slabs during craton amalgamation is the favored model for the destruction of the diamondiferous portion of the lithospheric mantle root.

7. Fibrous diamonds from Wawa, as well as from Panda and Koffiefontein, record cool temperatures of formation (generally <1050°C), which are less than or equal to temperatures recorded for non-fibrous diamonds at these three locations. This implies

growth of fibrous diamonds from short-lived, externally derived, "cold" metasomatic fluids that maintain ambient mantle temperatures, and do not require melting of the mantle. This contrasts with non-fibrous diamond growth, which is associated with transient heating of the mantle by about 100-150°C (Stachel and Harris, 2008). Low calculated temperatures for fibrous diamond growth below the solidus of alkali-bearing peridotite saturated with CO_2 may be a critical factor allowing diamond precipitation, according to experiments on diamond synthesis (Sokol and Pal'yanov, 2008).

8. Fibrous diamond growth may not be as closely connected to kimberlite generation and associated fluids as previously believed. Low temperatures of fibrous diamond formation make determination of residence time based on nitrogen aggregation state impossible; therefore dominance of type IaA aggregation in fibrous diamond cannot be immediately connected to short mantle residence times. Furthermore, major element chemistry varies significantly between kimberlite and fluid inclusions in diamonds. Therefore, it is plausible that fibrous diamonds formed in an event unrelated to kimberlite generation, and a temporal and genetic connection to kimberlite emplacement is unnecessary.

9. The disconnect between fibrous diamond growth and kimberlite generation separates fibrous diamond growth from the thermal disturbance associated with the "root-unfriendly" process of kimberlite propagation and suggests that fibrous diamond precipitates as a separate and distinct event. This makes possible the addition of fibrous diamond growth to the list of "root-friendly" processes, occurring at ambient mantle temperatures, and playing no role in lithospheric root destruction.

References

Akagi, T and Masuda, A (1988) Isotopic and elemental evidence for a relationship between kimberlite and Zaire cubic diamonds. *Nature* 336, 665-667.

Anand, M, Taylor, LA, Misra, KC, Carlson, WD, Sobolev, NV (2004) Nature of diamonds in Yakutian eclogites: views from eclogite tomography and mineral inclusions in diamonds. *Lithos* 77(1-4), 333-348.

Araujo, DP, Griffin, WL, O'Reilly, SY, Grant, KJ, Ireland, T, Holden, P, van Achterbergh, E (2009) Microinclusions in monocrystalline octahedral diamonds and coated diamonds from Diavik, Slave Craton: clues to diamond genesis. *Lithos* 112S, 724-735.

Arima, M, Kozai, Y, Akaishi, M (2002) Diamond nucleation and growth by reduction of carbonate melts under high-pressure and high-temperature conditions. *Geology* 30 (8), 691-694.

Begg, GC, Griffin, WL, Natapov, LM, O'Reilly, SY, Grand, SP, O'Neill, CJ, Hronsky, JMA, Djomani, YP, Swain, CJ, Deen, T, Bowden, P (2009) The lithospheric architecture of Africa: seismic tomography, mantle petrology, and tectonic evolution. *Geosphere* 5, 23-50.

Bellefleur, G, Calvert, AJ, Chouteau, MC (1997) A link between deformation history and the orientation of reflective structures in the 2.68-2.83 Ga Opatica belt of the Canadian Superior Province. *Journal of Geophysical Research* 102, 15,243-15,257.

Blondes, MS, Brandon, MT, Reiners, PW, Page, FZ, Kita, NT (2012) Generation of forsteritic olivine ($Fo_{99.8}$) by subsolidus oxidation in basaltic flows. *Journal of Petrology* 53, 971-984.

Boyd, FR and Gurney, JJ (1986) Diamonds and the African lithosphere. *Science* 232 (4749), 472-477.

Boyd, SR, Mattey, DP, Pillinger, CT, Milledge, HJ, Mendelssohn, M, Seal, M (1987) Multiple growth events during diamond genesis: an integrated study of carbon and nitrogen isotopes and nitrogen aggregation state in coated stones. *Earth and Planetary Science Letters* 86, 341-353.

Boyd, SR, Pineau, F, Javoy, M (1994) Modelling the growth of natural diamonds. *Chemical Geology* 116, 29-42.

Boyd, FR, Pokhilenko, NP, Pearson, DG, Mertzman, SA, Sobolev, NV, Finger, LW (1997) Composition of the Siberian cratonic mantle: evidence from Udachnaya peridotite xenoliths. *Contributions to Mineralogy and Petrology* 128, 228-246.

Brey, GP and Kohler, T (1990) Geothermobarometry in four-phase lherzolites II. New thermobarometers, and practical assessment of existing thermobarometers. *Journal of Petrology* 31, 1353-1378.

Brey, GP, Bulatov, VK, Girnis, AV (2008) Geobarometry for peridotites: experiments in simple and natural systems from 6 to 10 GPa. *Journal of Petrology* 49, 3-24.

Brey, GP, Bulatov, VK, Girnis, AV (2010) Melting of K-rich carbonated peridotite at 6-10 GPa and the stability of K-phases in the upper mantle. *Chemical Geology* 281(3-4), 333-342.

Bruce, LF, Kopylova, MG, Longo, M, Ryder, J, Dobrzhinetskaya, LF (2011) Luminescence of diamonds from metamorphic rocks. *American Mineralogist* 96, 14-22.

Brummer, JJ, MacFayden, DA, Pegg, CC (1992) Discovery of kimberlites in the Kirkland Lake area northern Ontario, Canada. PART II: kimberlite discoveries, sampling, diamond content, ages and emplacement. *Exploration Mining and Geology* 1, 351-370.

Bulanova, GP (1995) The formation of diamond: *Journal of Geochemical Exploration*, v. 53, p. 1-23.

Bureau, H, Langenhorst, F, Auzende, A-L, Frost, DJ, Esteve, I, Siebert, J (2012) The growth of fibrous, cloudy and polycrystalline diamonds. *Geochimica et Cosmochimica Acta* 77, 202-214.

Burgess, R, Layzelle, E, Turner, G, Harris, JW (2002) Constraints on the age and halogen composition of mantle fluids in Siberian coated diamonds. *Earth and Planetary Science Letters* 197, 193-203.

Burke, K and Kidd, WSF (1978) Were Archean continental geothermal gradients much steeper than those of today? *Nature* 272, 240-241.

Calvert, AJ, Sawyer, EW, Davis, WJ, Ludden, JN (1995) Archean subduction inferred from seismic images of a mantle suture in the Superior Province. *Nature* 375, 670-674.

Calvert, AP and Ludden, JN (1999) Archean continental assembly in the southeastern Superior Province of Canada. *Tectonophysics* 18, 412-429.

Cartigny, P (2005) Stable isotopes and the origin of diamond. *Elements* 1, 79-84.

Chapman, DS and Furlong, KP (1977) Continental heat flow-age relationships. EOS Trans AGU (abstract) 58, 1240.

Chu, ZY, Wu, FY, Walker, RJ, Rudnick, RL, Pitcher, L, Puchtel, IS, Yang, YH, Wilde, SA (2009) Temporal evolution of the lithospheric mantle beneath the Eastern North China Craton. *Journal of Petrology* 50(10), 1857-1898.

Clowes, RM, White, DJ, Hajnal, Z, (2010) Mantle heterogeneities and their significance: results from Lithoprobe seismic reflection and refraction - wide-angle reflection studies. *Canadian Journal of Earth Sciences* 47(4), 409-443.

Cookenboo, HO and Grutter, HS (2010) Mantle-derived indicator mineral compositions as applied to diamond exploration. *Geochemistry: Exploration, Environment Analysis* 10, 81-95.

Craven, JA, Kurtz, RD, Boerner, DE, Skulski, T, Spratt, J, Ferguson, IJ, Wu, X, Bailey, RC (2001) Conductivity of western Superior province upper mantle in northwestern Ontario. Geological Survey of Canada, Current Research 2001-E6.

Creighton, S, Stachel, T, McLean, H, Muehlenbachs, K, Simonetti, A, Eichenberg, D, Luth, R (2008) Diamondiferous peridotitic microxenoliths from the Diavik diamond mine, NT. *Contributions to Mineralaogy and Petrology* 155, 541-554.

De Stefano, A, Lefebvre, N, Kopylova, M (2006) Enigmatic diamonds in Archean calc-alkaline lamprophyres of Wawa, southern Ontario, Canada. *Contributions to Mineralogy and Petrology* 151, 158-173.

De Stefano, A, Kopylova, MG, Cartigny, P, Afanasiev, V (2009) Diamonds and eclogites of the Jericho kimberlite (Northern Canada). *Contributions to Mineralogy and Petrology* 158, 295-315.

Donnelly, CL, Stachel, T, Creighton, S, Muehlenbachs, K, Whiteford, S 920070 Diamonds and their mineral inclusions from the A154 South pipe, Diavik diamond mine, Northwest Territories, Canada. *Lithos* 98, 160–176.

Drury, M and Taylor, A (1987) Some new measurements of heat flow in the Superior Province of the Canadian Shield. *Canadian Journal of Earth Sciences* 24, 1486-1489.

Ellis, DJ and Green, DH (1979) An experimental study of the effect of Ca upon garnet-clinopyroxene Fe-Mg exchange equilibria. *Contributions to Mineralogy and Petrology* 71, 13-22.

Ernst, R and Bleeker, W (2010) Large igneous provinces (LIPs), giant dyke swarms, and mantle plumes: significance for breakup events within Canada and adjacent regions from 2.5 Ga to the present. *Canadian Journal of Earth Sciences* 47, 695-739.

Faure, S, Godey, S, Fallara, F, Trepanier, S (2011) Seismic architecture of the Archean North American mantle and its relationship to diamondiferous kimberlite fields. *Economic Geology* 106, 223-240.

Frost, DJ and McCammon, CA (2008) The redox state of Earth's mantle. *Annual Review of Earth and Planetary Sciences* 36, 389-420.

Gaspar, JC, Araújo, DP, Melo, MVLC (1998) Olivine in carbonatitic and silicate rocks in carbonatite complexes. Extended Abstract, 7th International Kimberlite Conference, 239-241.

Girnis, AV and Brey, GP (1999) Garnet-spinel-olivine-orthopyroxene equilibria in the FeO-MgO-Al_2O_3-SiO_2-Cr_2O_3 system: II. Thermodynamic analysis. *European Journal of Mineralogy* 11, 619-636.

Godey, S, Deschamps, F, Tramper, J (2004) Thermal and compositional anomalies beneath the North American continent. *Journal of Geophysical Research*, doi: 10.1029/2002JB002263.

Grand, SP (1994) Mantle shear structure beneath the Americas and surrounding oceans. *Journal of Geophysical Research* 99, 11591-11621.

Goetze, C (1975) Sheared lherzolites: from the point of view of rock mechanics. *Geology* 3(4), 172-173.

Graham, I, Burgess, JL, Bryan, D, Ravenscroft, PJ, Thomas, E, Doyle, BJ, Hopkins, R, Armstrong, KA (1999) Exploration history and geology of the Diavik Kimberlites, Lac de Gras, Northwest Territories, Canada. In: Gurney, JJ, Gurney, JL, Pascoe, MD, Richardson, SH (Eds.), Proceedings of the VIIth International Kimberlite Conference, The J.B. Dawson Volume. Red Roof Design, Cape Town, 262–279.

Griffin, WL and Ryan, CG (1995) Trace elements in indicator minerals: area selection and target evaluation in diamond exploration. *Journal of Geochemical Exploration* 53, 311-337.

Griffin, WL, Smith, D, Boyd, FR, Cousens, DR, Ryan, CG, Sie, SH, Suter, GF (1989) Trace element zoning in garnets from sheared mantle xenoliths. *Geochimica et Cosmochimica Acta* 53, 561-567.

Griffin, WL, O'Reilly, SY, Ryan, CG, Gaul, O, Ionov, DA (1998) Secular variation in the composition of subcontinental lithospheric mantle: geophysical and geodynamic implications. *Geodynamics Series* 26, 1-26.

Griffin, WL, Shee, SR, Ryan, CG, Win, TT, Wyatt, BA (1999) Harzburgite to lherzolite and back again: metasomatic processes in ultramafic xenoliths from the Wesselton kimberlite, Kimberley, South Africa. *Contributions to Mineralogy and Petrology* 134(2-3), 232-250.

Griffin, WL, O'Reilly, SY, Natapov, LM, Ryan, CG (2003a) The evolution of lithospheric mantle beneath the Kalahari Craton and its margins. *Lithos* 71, 215-242.

Griffin,WL, O'Reilly, SY, Abe, N, Aulbach, S, Davies, RM, Pearson, NJ, Doyle, BJ, Kivi, K (2003b) The origin and evolution of the Archean lithospheric mantle. *Precambrian Research* 127, 19-41.

Griffin, WL, O'Reilly, SY, Doyle, BJ, Pearson, NJ, Coopersmith, H, Kivi, K, Malkovets, V, Pokhilenko, N (2004) Lithospheric mapping beneath the North American plate. *Lithos* 77, 873-922.

Griffin, WL, Kobussen, AF, Babu, EVSSK, O'Reilly, SY, Norris, R, Sengupta, P (2009) A translithospheric suture in the vanished 1-Ga lithospheric root of South India: evidence from contrasting lithosphere sections in the Dharwar craton. *Lithos* 112S, 1109-1119.

Grutter, H, Gurney, JJ, Menzies, AH, Winter, F (2004) An updated classification scheme for mantle-derived garnet, for use by diamond explorers. *Lithos* 77, 841-857.

Grutter, H, Latti, D, Menzies, A (2006) Cr-Saturation arrays in concentrate garnet compositions from kimberlite and their use in mantle barometry. *Journal of Petrology* 47, 801-820.

Grutter, H (2009) Pyroxene xenocrysts geotherms: techniques and application. *Lithos* 112S, 1167-1178.

Gurney, JJ and Zweistra, P (1995) The interpretation of the major element compositions of mantle minerals in diamond exploration. *Journal of Geochemical Exploration* 53, 293-309.

Gurney, JJ, Helmstaedt, HH, Richardson, SH, Shirey, SB (2010) Diamonds through time. *Economic Geology* 105, 689-712.

Guzmics, T, Mitchell, RH, Szabo, C, Berkesi, M, Milke, R, Abart, R (2011) Carbonatite melt inclusions in coexisting magnetite, apatite and monticellite in Kerimasi calciocarbonatite, Tanzania: melt evolution and petrogenesis. *Contributions to Mineralogy and Petrology* 161(2), 177-196.

Harley, SL (1984) An experimental study of the partitioning of Fe and Mg between garnet and orthopyroxene. *Contributions to Mineralogy and Petrology* 86, 359-373.

Harte, B and Hawkesworth, CJ (1989) Mantle domains and mantle xenoliths. Special Publication-Geological Society of Australia 14(2), 649-686.

Heaman, LM and Kjarsgaard, BA (2000) Timing of eastern North American kimberlite magmatism: continental extension of the Great Meteor hotspot track? *Earth and Planetary Science Letters* 178, 253-268.

Heaman, LM, Kjarsgaard, BA, Creaser, RA (2004) The temporal evolution of North American kimberlites. *Lithos* 76, 377-397.

Helmstaedt, HH and Schulze, DJ (1989) Southern African kimberlites and their mantle sample: implications for Archean tectonics and lithosphere evolution. In: Ross, J et al. (ed) Kimberlites and Related Rocks, Proc. IV Kimberlite Conf (Perth 1986), Geological Society of Australia, Special Publication, 14: 358-368.

Helmstaedt, HH and Gurney, JJ (1994) Geotectonic controls on the formation of diamonds and their kimberlitic and lamproitic host rocks: Applications to diamond exploration. *In:* H.O.A. Meyer and O.H. Leonardos (Eds.), Diamonds: Characterization, Genesis and Exploration. CPRM Special Publication 1/B, 236-250.

Helmstaedt, HH and Gurney, JJ (1995) Geotectonic controls of primary diamond deposits: implications for area selection. *Journal of Geochemical Exploration* 53, 125-144.

Helmstaedt, HH, Gurney, JJ, Richardson, SH (2010) Ages of cratonic diamond and lithosphere evolution: constraints on Precambrian tectonics and diamond exploration. *Canadian Mineralogist* 48, 1385-1408.

Izraeli, ES, Harris, JW, Navon, O (2001) Brine inclusions in diamonds: a new upper mantle fluid. *Earth and Planetary Science Letters* 187 (3–4), 323–332.

Izraeli, ES, Harris, JW, Navon, O (2004) Fluid and mineral inclusions in cloudy diamonds from Koffiefontein, South Africa. *Geochimica et Cosmochimica Acta* 68, 2561-2575.

James, DE, Boyd, FR, Schutt, D, Bell, DR, Carlson, RW (2004) Xenolith constraints on seismic velocities in the upper mantle beneath southern Africa: *Geochemistry Geophysics Geosystems* 5, doi: 10.1029/2003GC000551.

Kamenetsky, MB, Sobolev, AV, Kamenetsky, VS, Maas, R, Danyushevsky, LV, Thomas, R, Pokhilenko, NP, Sobolev, NV (20040 Kimberlite melts rich in alkali chlorides and carbonates: A potent metasomatic agent in the mantle. *Geology* 32 (10), 845-848.

Kaminsky, FV, Sablukov, SM, Sablukova, LI, Shchukin, VS, Canil, D (2002) Kimberlites from the Wawa area, Ontario. *Canadian Journal of Earth Sciences* 39, 1819-1838.

Kendall, JM, Sol, S, Thomson, CJ, White, DJ, Asudeh, I, Snell, CS, Sutherland, FH (2002) Seismic heterogeneity and anisotropy in the Western Superior Province, Canada: insights into the evolution of an Archean craton. In: Fowler, CMR, Ebinger, CJ, Hawkesworth, CJ (eds) The Early Earth: Physical, Chemical, and Biological Development. Geological Society of London, Special Publications 199, 27-44.

Kennedy, CS and Kennedy, GC (1976) The equilibrium boundary between graphite and diamond. *Journal of Geophysical Research* 81, 2467-2470.

Ketchum, JWF, Ayer, JA, van Breemen, O, Pearson, NJ, Becker, JK (2008) Pericontinental crustal growth of the southwestern Abitibi subprovince, Canada- U-Pb, Hf, and Nd isotope evidence. *Economic Geology* 103, 1151-1184.

King, SD (2005) Archean cratons and mantle dynamics: *Earth and Planetary Science Letters* 234, 1-14.

Klein-Ben David, O, Izraeli, ES, Hauri, E, Navon, O (2004) Mantle fluid evolution- a tale of one diamond. *Lithos* 77, 243-253.

Klein-Ben David, O, Wirth, R, Navon, O (2006) TEM imaging and analysis of microinclusions in diamonds: A close look at diamond-growing fluids. *American Mineralogist* 91, 353-365.

Klein-Ben David, O, Wirth, R and Navon, O (2007) Micrometer-scale cavities in fibrous and cloudy diamonds - a glance into diamond dissolution events. *Earth and Planetary Science Letters* 264, 89-103.

Klein-Ben David, O, Logvinova, AM, Schrauder, M, Spetius, ZV, Weiss, Y, Hauri, EH, Kaminsky, FV, Sobolev, NV, Navon, O (2009) High-Mg carbonatitic microinclusions in some Yakutian diamonds-a new type of diamond-forming fluid. *Lithos* 112(S2), 648-659.

Klein-Ben David, O, Pearson, DG, Nowell, GM, Ottley, C, McNeill, JCR, Cartigny, P (2010) Mixed fluid sources involved in diamond growth constrained by Sr-Nd-Pb-C-N isotopes and trace elements. *Earth and Planetary Science Letters* 289, 123-133.

Klemme, S (2004) The influence of Cr on the garnet-spinel transition in the Earth's mantle: experiments in the system MgO-Cr_2O_3-SiO_2 and thermodynamic modeling. *Lithos* 77, 639-646.

Klemme, S and O'Neill, H StC (2000) The near-solidus transition from garnet lherzolite to spinel lherzolite. *Contributions to Mineralogy and Petrology* 138, 237-248.

Kopylova, MG, Gurney, JJ, Daniels, LRM (1997) Mineral inclusions in diamonds from the River Ranch kimberlite, Zimbabwe. *Contributions to Mineralogy and Petrology* 129, 366-384.

Kopylova, MG, Russell, JK, Cookenboo, H (1999) Petrology of peridotite and pyroxenites xenoliths form the Jericho Kimberlite: implications for the thermal state of the mantle beneath the Slave craton, Northern Canada. *Journal of Petrology* 40, 79-104.

Kopylova, MG, Lo, J, Christensen, NI (2004) Petrological constraints on seismic properties of the Slave upper mantle (Northern Canada). *Lithos* 77, 493-510.

Kopylova, MG, Nowell, GM, Pearson, DG, Markovic, G (2009) Crystallization of megacrysts from protokimberlitic fluids: Geochemical evidence from high-Cr megacrysts in the Jericho kimberlite. *Lithos* 112, 284-295.

Kopylova, M, Navon, O, Dubrovinsky, L, Khachatryan, G (2010) Carbonatitic mineralogy of natural diamond-forming fluids. *Earth and Planetary Science Letters* 291(1-4), 126-137.

Kopylova, MG, Afanasiev, VP, Bruce, LF, Thurston, P, Ryder, J (2011) Metaconglomerate preserves evidence for kimberlite, diamondiferous root and medium grade terrane of a pre-2.7 Ga Southern Superior protocraton. *Earth and Planetary Science Letters* 312, 213-225.

Kopylova, MG, Kostrovitsky, SI, Egorov, KN. Salts in southern Yakutian kimberlites and the problem of primary alkali kimberlite melts, Submitted to Earth Science Reviews, June 2012.

Kostrovitsky, SI, Kopylova, MG, Egorov, KN, Yakovlev, DA, Sandimirova, GP. The "exceptionally fresh" Udachnaya-east kimberlite: evidence for brine and evaporate contamination. Submitted to 10th IKC Proceedings Volume, February 2012.

Lavrent'ev, YG, Usova, LV, Korolyuk, VN, Logvinova, AM (2005) Electron probe microanalysis of Cr-spinel for zinc and nickel traces as applied to study of the geothermometry of peridotites. *Russian Geology and Geophysics* 46, 741-745.

Lenardic, A (2006) Continental growth and the Archean paradox. In: Benn, K, Mareschal, JC, Condie, KC (ed) Archean Geodynamics and Environments, American Geophysical Union, Washington, DC pp. 33-45.

Litasov, KD, Ohtani, E (2009) Phase relations in the peridotite-carbonate-chloride system at 7.0-16.5 GPa and the role of chlorides in the origin of kimberlite and diamond. *Chemical Geology* 262(1-2), 29-41.

Liu, Y, Taylor, LA, Sarbadhikari, AB, Valley, JW, Ushikubo, T, Spicuzza, MJ, Kita, N, Ketcham, RA, Carlson, W, Shatsky, V, Sobolev, NV (2009) Metasomatic origin of diamonds in the world's largest diamondiferous eclogite. *Lithos* 112, 1014-1024.

Long, DGF (2004) The tectonostratigraphic evolution of the Huronian basement and the subsequent basin fill: geological constraints on impact models of the Sudbury event. *Precambrian Research* 129, 203-223.

Liu, JG, Rudnick, RL, Walker, RJ, Gao, S, Wu, FY, Piccoli, PM, Yuan, HL, Xu, WL, Xu, YG (2011) Mapping lithospheric boundaries using Os isotopes of mantle xenoliths: An example from the North China Craton. *Geochimica et Cosmochimica Acta* 75(13), 3881-3902.

Mareschal, JC, Jaupart, C, Gariepy, C, Cheng, LZ, Guillou-Frottier, L, Bienfait, G, Lapointe, R (2000) Heat flow and deep thermal structure near the southeastern edge of the Canadian Shield. *Canadian Journal of Earth Sciences* 37, 399-414.

McCammon, CA, Griffin, WL, Shee, SR, O'Neill, HSC (2001) Oxidation during metasomatism in ultramafic xenoliths from the Wesselton kimberlite, South Africa: implications for the survival of diamond. *Contributions to Mineralogy and Petrology* 141, 287-296.

McNeill, J, Pearson, DG, Klein-Ben David, O, Nowell, GM, Ottley, CJ, Chinn, I (2009) Quantitative analysis of trace element concentrations in some gem-quality diamonds. *Journal of Physics: Condensed Matter* 21, doi: 10.1088/0953-8984/21/36/364207.

Mercier, J-P, Bostock, MG, Audet, P, Gaherty, JB, Garnero, EJ, Revenaugh, J (2008) The teleseismic signature of fossil subduction: Northwestern Canada. *Journal of Geophysical Research* 113, (B04308).

Meyer, HOA, Waldman, MA, Garwood, BL (1994) Mantle xenoliths from kimberlite near Kirkland Lake, Ontario. *Canadian Mineralogist* 32, 295-306.

Miller, CM, Kopylova, MG, Ryder, J (2012) Vanished diamondiferous cratonic root beneath the Southern Superior province: evidence from diamond inclusions in the Wawa metaconglomerate. *Contributions to Mineralogy and Petrology*. doi: 10.1007/s00410-012-0773-1.

Moore, AE and Lock, NP (2001) The origin of mantle-derived megacrysts and sheared peridotites-evidence from kimberlites in the northern Lesotho- Orange Free State (South Africa) and Botswana pipe clusters. *South African Journal of Geology* 104, 23-38.

Navon, O, Hutcheon, ID, Rossman, GR, Wasserburg, GJ (1988) Mantle-derived fluids in diamond micro-inclusions. *Nature* 335, 784-789.

Navon, O (1999) Diamond formation in the Earth's mantle, in Gurney, J.J., et al. (eds.), Proceedings of the 7th International Kimberlite Conference: Cape Town, South Africa, Red Roof Design, 584–604.

Nickel, KG and Green, DH (1985) Empirical geothermobarometry for garnet peridotites and implications for the nature of the lithosphere, kimberlites and diamonds. *Earth and Planetary Science Letters* 73, 158-170.

Nimis, P and Grutter, H (2010) Internally consistent geothermometers for garnet peridotites and pyroxenites. *Contributions to Mineralogy and Petrology* 159, 411-427.

Nyblade, AA and Pollack, HN (1993) A global analysis of heat flow from Precambrian terrains: implications for the thermal structure of Archean and Proterozoic lithosphere. *Journal of Geophysical Research* 98, 12,207-12,218.

O'Neill, CJ (1981) The transition between spinel lherzolite and garnet lherzolite, and its use as a geobarometer. *Contributions to Mineralogy and Petrology* 77, 185-194.

O'Neill, CJ and Wood, BJ (1979) An experimental study of Fe-Mg partitioning between garnet and olivine and its calibration as a geothermometer *Contributions to Mineralogy and Petrology* 70, 59-70.

O'Reilly, SY and Griffin, WL (20100 The continental lithosphere–asthenosphere boundary: Can we sample it? *Lithos* 120 (1-2), 1-13.

Pal'yanov, YN and Sokol, AG (2009) The effect of composition of mantle fluids/melts on diamond formation processes. *Lithos* 112S, 690-700.

Pal'yanov, YN, Sokol, AG, Sobolev, NV (2005) Experimental modeling of mantle diamond-forming processes. *Russian Geology and Geophysics*. 46, 1271-1284.

Pal'yanov, YN, Sokol, AG, Borzdov, YM, Khokhryakov, AF, Sobolev, NV (1999) Diamond formation from mantle carbonate fluids. *Nature* 400, 417-418.

Pal'yanov, YN, Sokol, AG, Borzdov, YM, Khokhryakov, AF, Sobolev, NV (2002) Diamond formation through carbonate-silicate interaction. *American Mineralogist* 87, 1009-1013.

Pal'yanov, YN, Shatsky, VS, Sobolev, NV, Sokol, AG (2007) The role of mantle ultrapotassic fluids in diamond formation. Proceedings of the National Academy of Sciences of the United States of America 104(22), 9122-9127.

Pearson, DG and Wittig, N (2008) Formation of Archean continental lithosphere and its diamonds: the root of the problem. *Journal of the Geological Society of London* 165, 895-914.

Percival, JA, Sanborn-Barrie, M, Skulski, T, Stott, GM, Helmstaedt, H, White, DJ (2006) Tectonic evolution of the western Superior Province from NATMAP and Lithoprobe studies. *Canadian Journal of Earth Sciences* 43, 1085-1117.

Phillips, D, Harris, JW, Viljoen, KS (2004) Mineral chemistry and thermobarometry of inclusions from De Beers Pool diamonds, Kimberley, South Africa. *Lithos* 77, 155-179.

Pollack, HN and Chapman, DS (1977) On the regional variation of heat flow, geotherms, and lithospheric thickness. *Tectonophys*ics 38, 279-296.

Pollack, HN, Hurter, SJ, Johnston, JR (1993) Heat flow from the Earth's interior: analysis of the global data set. *Reviews of Geophysics* 31(3), 267–280.

Reed, SJB (1996) Electron microprobe analysis and scanning electron microscopy in geology. Cambridge University Press, Great Britain.

Rege, S, Griffin, WL, Pearson, NJ, Araujo, D, Zedgenizov, D, O'Reilly, SY (2010) Trace-element patterns of fibrous and monocrystalline diamonds: insights into mantle fluids. *Lithos* 118, 313-337.

Reutskii, VN, Logvinova, AM, Sobolev, NV (1999) Carbon isotopic composition of polycrystalline diamond aggregates with chromite inclusions from the Mir kimberlite pipe, Yakutia. *Geochemistry International* 37, 1073.

Rickard, RS, Harris, JW, Gurney, JJ, Cardoso, P (1989) Mineral inclusions in diamonds from Koffiefontein Mine. in: Ross, J, Jaques, AL, Ferguson, J, Green, DH, O'Reilly, SY, Danchin, RV, Janse, AJA (eds.) Kimberlites and Related Rocks Volume 2. Proceedings of the 4th International Kimberlite Conference. Perth, Blackwell Scientific Publications, 1054-1062.

Rudnick, RL, McDonough, WF, O'Connell, RJ (1998) Thermal structure, thickness and composition of continental lithosphere. *Chemical Geology* 145, 395-411.

Russell, JK and Kopylova, MG (1999) A steady state conductive geotherm for the north central Slave, Canada: inversion of petrological data from the Jericho kimberlite pipe. *Journal of Geophysical Research* 104, 7089-7101.

Ryan, CG, Griffin, WL, Pearson, NJ (1996) Garnet geotherms: pressure-temperature data from Cr-pyrope garnet xenocrysts in volcanic rocks. *Journal of Geophysical Research* 101, 5611-5625.

Ryder, J, Verley, CG, Miller, A, Martel, B, Khoun, R (2008) The diamondiferous conglomerates of the Leadbetter Project. 9th International Kimberlite Conference, Extended Abstract no. 9IKC-A-00110.

Schrauder, M and Navon, O (1994) Hydrous and carbonatitic mantle fluids in fibrous diamonds from Jwaneng, Botswana. *Geochimica et Cosmochimica Acta* 58 (2), 761–771.

Schulze, DJ (1996) Kimberlites in the vicinity of Kirkland Lake and Lake Timiskaming, Ontario and Quebec. In: AN LeCheminant, DG Richardson, RNW DiLabio, and KA Richardson (eds). Searching for Diamonds in Canada, Geological Survey of Canada, Open File 3228, 73-78.

Shirey, SB, Harris, JW, Richardson, SH, Fouch, MJ, James, DE, Cartigny, P, Deines, P, Viljoen, F (2002) Diamond genesis, seismic structure, and evolution of the Kaapvaal-Zimbabwe craton. *Science* 297, 1683-1686.

Sleep, NH (2003) Survival of Archean cratonal lithosphere: *Journal of Geophysical Research* 108, No. B6, 2302, doi:10.1029/2001JB000169.

Smith, D and Boyd, FR (1987) Compositional heterogeneities in a high-temperature lherzolite nodule and implications for mantle processes. In: PH Nixon (ed) Mantle Xenoliths, Wiley, New York, pp. 551-561.

Smith, D and Boyd, FR (1992) Compositional zonation in garnets in peridotite xenoliths. *Contributions to Mineralogy and Petrology* 112(1), 134-147.

Smith, D, Griffin, WL, Ryan, CG, Sie, SH (1991) Trace-element zonation in garnets from The Thumb: heating and melt infiltration below the Colorado Plateau. *Contributions to Mineralogy and Petrology* 107, 60-79.

Smith, EM, Kopylova, MG, Nowell, GM, Pearson, DG, Ryder, J (2012) Archean mantle fluids preserved in fibrous diamonds from Wawa, Superior craton. Geology, accepted pending revisions

Sobolev, NV, Logvinova, AM, Zedgenizov, DA, Seryotkin, YV, Yefimova, ES, Floss, C, Taylor, LA (2004) Mineral inclusions in microdiamonds and macrodiamonds from kimberlites of Yakutia: a comparative study. *Lithos* 77, 225-242.

Sokol, AG and Pal'yanov, YN (2008) Diamond formation in the system MgO-SiO_2-H_2O-C at 7.5 GPa and 1,600 degrees C. *Contributions to Mineralogy and Petrology* 155(1), 33-43.

Stachel T, Banas A, Muehlenbachs K, Kurszlaukis S, Walker EC (2006) Archean diamonds from Wawa (Canada): samples from deep cratonic roots predating cratonization of the Superior Province. *Contributions to Mineralogy and Petrology* 151(6), 737-750.

Stachel, T and Harris, JW (2008) The origin of cratonic diamonds- constraints from mineral inclusions. *Ore Geology Review* 34, 5-32.

Stachel, T, Harris, JW, Muehlenbachs, K (2009) Sources of carbon in inclusion bearing diamonds. *Lithos* 112, 625-637.

Stalder, R, Ulmer, P, Thompson, AB, Gunther, D (2001) High pressure fluids in the system MgO-SiO_2-H_2O under upper mantle conditions. *Contributions to Mineralogy and Petrology* 140, 607-618.

Stern, RJ (2002) Subduction zones. *Review of Geophysics* 40(4), 3-38.

Stern, RA and Bleeker, W (1998) Age of the world's oldest rocks refined using Canada's SHRIMP: the Acasta Gneiss complex, Northwest Territories, Canada. *Geoscience Canada* 25, 27-31.

Tappert, R, Stachel, T, Harris, JW, Shimizu, N, Brey, GP (2005) Mineral inclusions in diamonds from the Panda kimberlite, Slave Province, Canada. *European Journal of Mineralogy* 17, 423-440.

Taylor, WR, Jaques, AL, Ridd, M (1990) Nitrogen-defect aggregation characteristics of some Australian diamonds: time-temperature constraints on the source regions of pipe and alluvial diamonds. *American Mineraogist* 75, 1290-1310.

Taylor, WR, Canil, D, Milledge, HJ (1996) Kinetics of Ib to IaA nitrogen aggregation in diamond. *Geochimica et Cosmochimica Acta* 60, 4725-4733.

Thurston, PC (1991) Geology of Ontario: introduction. In: Thurston, PC, Williams, HR, Sutcliffe, RH, Stott, GM (ed) Geology of Ontario, OGS, Special Vol 4, pp. 3-25.

Tomlinson, EL, Jones, AP, Harris, JW (20060 Co-existing fluid and silicate inclusions in mantle diamond. *Earth and Planetary Science Letters* 250, 581-595.

Tomlinson, EL, Muller, W, EIMF (2009) A snapshot of mantle metasomatism: trace element analysis of coexisting fluid (LA-ICP-MS) and silicate (SIMS) inclusions in fibrous diamonds. *Earth and Planetary Science Letters* 279, 362-372.

Van der Lee, S (2001) Deep below North America. *Science* 294, 1297-1298.

Van Rythoven, AD and Schulze, DJ (2009) In-situ analysis of diamonds and their inclusions from the Diavik mine, Northwest Territories, Canada: mapping diamond growth. *Lithos* 112, 870-879.
Verley, CG, D'Amours, C, Martel, BO (2007) Preliminary tonnage estimate for the diamondiferous conglomerates of the Leadbetter Diamond Project. Dianor Resources Inc.

Vicker, PH (1997) Garnet peridotite xenoliths from kimberlite near Kirkland Lake, Canada. MSc Thesis, University of Toronto, 128 p. https://tspace.library.utoronto.ca/handle/ 1807/11731.

Weiss, Y, Griffin, WL, Elhlou, S, Navon, O (2008) Comparison between LA-ICP-MS and EPMA analysis of trace elements in diamonds. *Chemical Geology* 252, 158-168.

White DJ, Musacchio G, Helmstaedt HH, Harrap RM, Thurston PC, van der Velden A, Hall K (2003) Images of a lower-crustal oceanic slab: Direct evidence for tectonic accretion in the Archean western Superior province. *Geology* 31(11), 997-1000.

Wiens, RC, Burnnett, DS, Armstrong, JT, Johnson, ML (1994) A simple method to recognize and correct for surface roughness in scanning electron microscope energy-dispersive spectroscopy. *Microbean Analysis* 3, 117-124.

Wilde, SA, Valley, JW, Peck, WH, Graham, CM (2001) Evidence from detrital zircons for the existence of continental crust and oceans on the Earth 4.4 Gyr ago. *Nature* 409, 175-178.

Williams HR, Stott GM, Heather KB, Muir TL, Sage RP (1991) Wawa subprovince. In: Thurston PC, Williams HR, Sutcliffe RH, Stott GM (eds) Geology of Ontario, Part 1. Ministry of Northern Development and Mines, 485- 539.

Windley, BF (1998) Tectonic models for the geological evolution of crust, cratons, and continents in the Archean. *Revista Brasileira de Geociencias* 28, 183-188.

Wu, CM and Zhao, G (2011) The applicability of garnet-orthopyroxene geobarometry in mantle xenoliths. *Lithos* 125, 1-9.

Young, GM, Long, DGF, Fedo, CM, Nesbitt, HW (2001) Paleoproterozoic Huronian basin: product of a Wilson cycle punctuated by glaciations and a meteorite impact. *Sedimentary Geology* 141-142, 233-254.

Zedgenizov, DA and Ragozin, AL (2007) Chloride-carbonate fluid in diamonds from the eclogite xenolith. *Doklady Earth Sciences* 415(6), 961-964.

Zedgenizov, DA, Ragozin, AL, Shatsky, VS, Araujo, D, Griffin, WL, Kagi, H (2009) Mg and Fe-rich carbonate-silicate high-density fluids in cuboid diamonds from the Internationalnaya kimberlite pipe (Yakutia). *Lithos* 112(S2), 638-647.

Zedgenizov, DA, Ragozin, AL, Shatsky, VS, Araujo, D, Griffin, WL (2011) Fibrous diamonds from the placers of the northeastern Siberian Platform: carbonate and silicate crystallization media. *Russian Geology and Geophysics* 52, 1298-1309.

Zhang, K-J (2012) Destruction of the North China craton: lithosphere folding-induced removal of lithospheric mantle? *Journal of Geodynamics* 53, 8-17.

Zheng J, Griffin WL, O'Reilly SY, Yang J, Li T, Zhang M, Zhang RY, Liou JG (2006) Mineral chemistry of peridotites from Paleozoic, Mesozoic and Cenozoic lithosphere: constraints on mantle evolution beneath Eastern China. *Journal of Petrology* 47(11), 2233-2256.

Appendix A: Wawa non-fibrous diamond characteristics

Diamonds:							Inclusions:				
Lot #/ sieve size	sample #	Morphology	Resorption Class	Weight (mg)	Color	Surface Features/Other	Inclusion designation	Color	Longest Dimension (µm)	Location in Diamond	Comments
136/ +5	Wsc01	octahedron	4	12.5	colorless	hexagonal pit	Wsc01-A	dark brown	300-500	rim	
							Wsc01-B	dark brown	<100	rim	
							Wsc01-C	dark brown	<100	core	
							Wsc01-D	dark brown	100-300	core	
							Wsc01-E	dark brown	100-300	core	
							Wsc01-F	dark brown	100-300	core	
							Wsc01-G	colorless	<100	core	
							Wsc01-H	dark brown	<100	rim	
							Wsc01-I	colorless	<100	rim	
							Wsc01-J	dark brown	<100	rim	
136/ +5	Wsc02	octahedron (fragment)	unresorbed	11.4	colorless	polycentric faces					internal fractures filled with dark material, but no mineral inclusions
136/ +5	Wsc03	octahedron (fragment)	1	12.2	colorless	square stepped pit	Wsc03-A	dark brown	300-500	rim	
							Wsc03-C	colorless	100-300	rim	
							Wsc03-D	dark brown	100-300	rim	
							Wsc03-E	dark brown	100-300	core	
							Wsc03-F	colorless	100-300	core	
136/ +5	Wsc04	octahedron	2	22.9	colorless		Wsc04-A	colorless	100-300	core	crack through whole sample, no inclusions touching it
							Wsc04-B	colorless	300-500	core	
							Wsc04-C	colorless	100-300	core	
							Wsc04-D	colorless	100-300	core	
							Wsc04-E	colorless	100-300	core	
136/ +5	Wsc05	octahedron (fragment)	2	12.2	colorless	hexagonal pits stepped sides	Wsc05-A	dark brown	300-500	rim	
							Wsc05-B	dark brown	100-300	rim	
							Wsc05-C	dark brown	<100	rim	
							Wsc05-D	dark brown	100-300	rim	
							Wsc05-E	dark brown	100-300	rim	
							Wsc05-F	dark brown	<100	core	
							Wsc05-G	dark brown	<100	rim	
							Wsc05-H	dark brown	100-300	rim	
							Wsc05-I	dark brown	<100	rim	
136/ +5	Wsc06	octahedron	2	15.9	colorless		Wsc06-A	dark brown	<100	rim	
							Wsc06-B	dark brown	<100	rim	
							Wsc06-D	dark brown	<100	rim	
136/ +3	Wsc07	fragment	partially resorbed	4.8	grey		Wsc07-A	colorless	100-300	rim	
							Wsc07-B	colorless	<100	rim	
							Wsc07-C	dark red	<100	core	
136/ +3	Wsc08	macle (fragment)	partially resorbed	5.1	pale pink	twinning line on sides	Wsc08-A	colorless	<100	core	

Diamonds:							Inclusions:				
Lot #/ sieve size	sample #	Morphology	Resorption Class	Weight (mg)	Color	Surface Features/Other	Inclusion designation	Color	Longest Dimension (µm)	Location in Diamond	Comments
136/ +3	Wsc09	octahedron (fragment)	unresorbed	4.8	pale yellow		Wsc09-A	dark brown	100-300	core	
							Wsc09-B	colorless	<100	core	
							Wsc09-D	dark brown	100-300	core	
							Wsc09-E	dark brown	<100	core	
							Wsc09-F	dark brown	<100	core	
							Wsc09-G	dark brown	<100	core	
							Wsc09-H	dark brown	<100	core	
							Wsc09-I	dark brown	100-300	rim	
136/ +3	Wsc10	octahedron	5	5.6	colorless						
136/ +1	Wsc11	macle (fragment)	unresorbed	2.4	pale pink						
136/ +1	Wsc12	flat dodecahedroid	1	4.6	colorless		Wsc12-A	dark brown	100-300	rim	
							Wsc12-B	dark brown	<100	rim	
136/ +1	Wsc13	cubo-octahedron	6	3.5	colorless	oval shaped irregular pit	Wsc13-B	purple	100-300	rim	
							Wsc13-C	purple	100-300	core	
							Wsc13-D	purple	300-500	core	
							Wsc13-E	colorless	300-500	core	
							Wsc13-F	colorless	<100	core	
							Wsc13-G	colorless	<100	core	
							Wsc13-H	colorless	<100	core	
							Wsc13-I	purple	<100	rim	
136/ +1	Wsc14	octahedron	2	4.4	colorless		Wsc14-A	colorless	100-300	core	
							Wsc14-B	colorless	<100	rim	
							Wsc14-C	colorless	300-500	rim	
							Wsc14-D	colorless	<100	rim	
							Wsc14-F	dark brown	100-300	core	
							Wsc14-G	dark brown	<100	core	
							Wsc14-H	dark brown	<100	core	
							Wsc14-I	dark brown	100-300	core	
							Wsc14-J	dark brown	<100	rim	
							Wsc14-K	dark brown	<100	core	
							Wsc14-L	dark brown	100-300	core	
							Wsc14-M	dark brown	100-300	core	
							Wsc14-N	dark brown	100-300	core	
							Wsc14-O	dark brown	<100	core	
							Wsc14-P	dark brown	<100	core	
							Wsc14-Q	dark brown	100-300	rim	
							Wsc14-R	dark brown	100-300	rim	
							Wsc14-S	dark brown	<100	core	
							Wsc14-T	colorless	<100	core	
							Wsc14-U	colorless	<100	core	
							Wsc14-V	colorless	<100	rim	

Diamonds:							Inclusions:				
Lot #/ sieve size	sample #	Morphology	Resorption Class	Weight (mg)	Color	Surface Features/Other	Inclusion designation	Color	Longest Dimension (μm)	Location in Diamond	Comments
136/ +1	Wsc15	octahedron	2	4.9	pale yellow	trigons	Wsc15-A	colorless	<100	core	
						triangular pits	Wsc15-B	colorless	<100	rim	
							Wsc15-E	colorless	<100	rim	
136/ +7	Wsc16	elongated octahedron (partially fragmented)	6	24.5	pale pink	hexagonal pits	Wsc16-A	colorless	300-500	rim	
						overlapping trigons	Wsc16-B	colorless	<100	rim	
							Wsc16-C	colorless	<100	rim	
184/ +5	Wsc17	octahedron (fragment)	unresorbed	14.2	brown		Wsc17-A	dark brown	100-300	core	
							Wsc17-B	dark brown	<100	core	
184/ +5	Wsc18	dodecahedroid	1	9.0	colorless		Wsc18-A	colorless	100-300	core	
							Wsc18-B	colorless	100-300	core	
							Wsc18-C	colorless	<100	rim	
							Wsc18-D	colorless	<100	rim	
							Wsc18-F	colorless	<100	core	
							Wsc18-G	colorless	<100	core	
184/ +5	Wsc19	dodecahedroid	1	12.3	colorless		Wsc19-A	colorless	<100	core	
184/ +3	Wsc20	octahedron (fragment)	5	3.8	colorless		Wsc20-A	colorless	100-300	rim	
							Wsc20-B	colorless	100-300	core	
							Wsc20-C	colorless	100-300	core	
184/ +3	Wsc21	elongated octahedron (fragment)	unresorbed	4.1	colorless	triangular pits	Wsc21-A	purple	100-300	rim	
							Wsc21-B	colorless	100-300	core	
							Wsc21-C	purple	<100	rim	
							Wsc21-D	colorless	<100	rim	
184/ +3	Wsc22	octahedron (fragment)	unresorbed	5.9	colorless	stepped growth pattern	Wsc22-A	dark brown	100-300	rim	
							Wsc22-C	dark brown	100-300	core	
							Wsc22-D	dark brown	<100	core	
184/ +3	Wsc23	dodecahedroid	1	3.4	colorless		Wsc23-A	dark brown	<100	core	
184/ +1	Wsc24	octahedron	4	3.3	light brown	inverted trigons					small internal fractures, but no visible mineral inclusions
184/ +1	Wsc25	elongated octahedron	5	3.7	colorless	inverted trigons	Wsc25-A	pink	100-300	rim	
							Wsc25-C	colorless	<100	rim	
							Wsc25-D	colorless	100-300	rim	
							Wsc25-E	pink	100-300	core	
							Wsc25-F	pink	<100	core	
							Wsc25-G	pink	<100	core	
							Wsc25-H	pink	<100	core	
							Wsc25-I	pink	<100	core	
							Wsc25-J	pink	<100	core	
							Wsc25-K	colorless	<100	core	
							Wsc25-L	pink	100-300	rim	
							Wsc25-M	colorless	100-300	rim	

Diamonds:							Inclusions:				
Lot #/ sieve size	sample #	Morphology	Resorption Class	Weight (mg)	Color	Surface Features/Other	Inclusion designation	Color	Longest Dimension (µm)	Location in Diamond	Comments
184/ +1	Wsc26	flat dodecahedroid	1	2.0	colorless						internal fractures filled with dark material, but no visible mineral crystals
184/ +1	Wsc27	dodecahedroid (fragment)	1	3.4	colorless		Wsc27-A	colorless	100-300	core	
							Wsc27-B	colorless	<100	core	
							Wsc27-C	colorless	<100	core	
							Wsc27-D	colorless	<100	core	
184/ +1	Wsc28	octahedron	6	2.4	grey	intergrowth of smaller octahedron on larger					small internal fractures, but no visible mineral inclusions
184/ +1	Wsc29	octahedron (fragment)	2	2.6	colorless		Wsc29-A	dark brown	100-300	rim	
							Wsc29-B	dark red	100-300	rim	
							Wsc29-C	dark red	<100	core	
							Wsc29-D	dark red	<100	core	
							Wsc29-E	dark red	<100	core	
							Wsc29-F	dark brown	<100	core	
							Wsc29-G	dark brown	100-300	core	
184/ +1	Wsc30	octahedron	4	4.6	colorless						small internal fractures, but no visible mineral inclusions
184/ +1	Wsc31	cleaved fragment	unresorbed	3.0	light brown		Wsc31-A	dark brown	<100	rim	
							Wsc31-B	dark brown	100-300	rim	
184/ +1	Wsc32	aggregate octahedrons	5	3.3	colorless	inverted trigons polycentric faces	Wsc32-A	dark red	<100	core	
							Wsc32-B	dark red	<100	rim	
							Wsc32-C	colorless	<100	core	
							Wsc32-D	colorless	<100	core	
184/ +1	Wsc33	flat dodecahedroid	1	3.0	colorless		Wsc33-A	dark red	<100	core	
							Wsc33-B	colorless	<100	core	
401/ +5	Wsc34	broken octahedron	unresorbed	12.8	light grey	polycentric faces	Wsc34-A	colorless	100-300	core	sample lost during polishing before any analyses could be done
						II striations on edges	Wsc34-B	colorless	<100	core	
							Wsc34-C	colorless	<100	core	
							Wsc34-D	colorless	<100	core	
							Wsc34-E	colorless	<100	rim	
							Wsc34-F	colorless	<100	rim	
							Wsc34-G	colorless	<100	core	
							Wsc34-H	colorless	<100	core	
							Wsc34-I	dark brown	<100	core	
401/ +5	Wsc35	polycrystalline aggregate	unresorbed	10.6	dark grey	inverted trigons					aggregate, too dark and cloudy to see inside
401/ +5	Wsc36	octahedron	4	10.9	colorless	inverted trigons	Wsc36-A	colorless	<100	rim	
							Wsc36-B	dark red	<100	rim	
							Wsc36-C	colorless	<100	rim	
							Wsc36-D	dark brown	<100	core	
							Wsc36-E	dark brown	300-500	core	
							Wsc36-F	dark brown	<100	core	
							Wsc36-G	dark brown	100-300	rim	
							Wsc36-H	dark brown		rim	
							Wsc36-I	colorless	<100	core	
							Wsc36-K	dark brown	<100	core	

Diamonds:							Inclusions:				
Lot #/ sieve size	sample #	Morphology	Resorption Class	Weight (mg)	Color	Surface Features/Other	Inclusion designation	Color	Longest Dimension (µm)	Location in Diamond	Comments
401/ +5	Wsc37	dodecahedroid	1	16.0	pale pink	hexagonal pit	Wsc37-A	dark brown	100-300	core	
							Wsc37-B	dark brown	<100	core	
							Wsc37-C	dark brown	<100	core	
							Wsc37-D	dark brown	<100	core	
							Wsc37-E	dark brown	<100	core	
401/ +5	Wsc38	dodecahedroid	1	14.1	pale yellow	deep square pit	Wsc38-A	dark brown	<100	rim	
							Wsc38-B	dark brown	300-500	rim	
							Wsc38-C	dark brown	<100	rim	
							Wsc38-D	dark brown	100-300	core	
							Wsc38-E	dark brown	<100	core	
							Wsc38-F	dark brown	<100	core	
							Wsc38-G	dark brown		rim	
401/ +5	Wsc39	broken octahedron	2	16.6	colorless	inverted trigons	Wsc39-A	dark brown	100-300	rim	
							Wsc39-B	dark brown	<100	core	
							Wsc39-C	dark brown	100-300	rim	
							Wsc39-D	dark brown	100-300	rim	
							Wsc39-E	dark brown	<100	rim	
401/ +5	Wsc40	irregular dodecahedroid	1	18.8	brown	polycentric faces	Wsc40-A	dark brown	100-300	core	
						trigons	Wsc40-B	dark brown	100-300	core	
						hexagonal pits	Wsc40-C	dark brown	100-300	core	
							Wsc40-D	dark brown	100-300	rim	
401/ +5	Wsc41	dodecahedroid	1	13.2	colorless	hexagonal pits	Wsc41-A	dark brown	100-300	rim	
							Wsc41-B	dark brown	<100	rim	
							Wsc41-C	dark brown	300-500	rim	
							Wsc41-D	dark brown	<100	rim	
							Wsc41-E	dark brown	<100	rim	
							Wsc41-F	dark brown	<100	rim	
							Wsc41-G	dark brown	<100	rim	
							Wsc41-H	dark brown	100-300	core	
							Wsc41-I	dark brown	100-300	core	
							Wsc41-J	colorless	<100	rim	
							Wsc41-K	colorless	<100	core	
							Wsc41-L	colorless	<100	core	
							Wsc41-M	dark brown	<100	rim	
401/ +5	Wsc42	octahedron (fragment)	unresorbed	11.5	dark grey	stepped growth					
401/ +3	Wsc43	octahedron	2	5.0	colorless		Wsc43-B	dark brown	100-300	rim	
							Wsc43-C	dark brown	<100	rim	

Diamonds:							Inclusions:				
Lot #/ sieve size	sample #	Morphology	Resorption Class	Weight (mg)	Color	Surface Features/Other	Inclusion designation	Color	Longest Dimension (µm)	Location in Diamond	Comments
401/ +3	Wsc44	macle	partially resorbed	4.8	colorless		Wsc44-A	gold/brown		core	sample lost during polishing before any analyses could be done
							Wsc44-B	dark brown		core	
							Wsc44-C	dark brown		core	
							Wsc44-D	dark brown		core	
							Wsc44-E	dark brown		core	
							Wsc44-F	dark brown		core	
							Wsc44-G	purple		core	
							Wsc44-H	dark brown		core	
							Wsc44-I	colorless		core	
							Wsc44-J	colorless		core	
							Wsc44-K	dark brown		rim	
							Wsc44-L	dark brown		rim	
							Wsc44-M	dark brown		core	
401/ +3	Wsc45	cubo-octahedron	2	5.8	colorless	square pits on cubic face					
401/ +3	Wsc46	polycrystalline aggregate	unresorbed	6.0	dark grey/brown						aggregate, too dark and cloudy to see inside
401/ +3	Wsc47	octahedron	6	5.7	colorless	polycentric faces trigons					small internal fractures, but no visible mineral inclusions
401/ +3	Wsc48	macle (fragment)		4.9	pale yellow	hexagonal pits triangular pits polycentric faces	Wsc48-A	dark brown	100-300	rim	
							Wsc48-B	dark brown	<100	rim	
							Wsc48-C	dark brown	<100	rim	
							Wsc48-D	dark brown	<100	rim	
							Wsc48-E	dark brown	<100	rim	
							Wsc48-F	dark brown	<100	rim	
							Wsc48-G	dark brown	100-300	rim	
							Wsc48-I	dark brown	<100	rim	
401/ +3	Wsc49	octahedron	6	4.7	colorless	overlapping trigons hexagonal pits triangular pits	Wsc49-A	colorless	<100	core	
401/ +3	Wsc50	macle	partially resorbed	3.8	light brown		Wsc50-A	dark brown	100-300	core	
							Wsc50-B	dark brown	<100	core	
							Wsc50-C	dark brown	<100	core	
401/ +3	Wsc51	macle	partially resorbed	6.1	colorless	trigons in parallel rows polycentric faces	Wsc51-A	pink	100-300	core	
							Wsc51-B	colorless	100-300	core	
401/ -3+1	Wsc52	octahedron (fragment)	partially resorbed	4.3	pale pink		Wsc52-B	dark brown	<100	core	
							Wsc52-C	dark brown	100-300	core	
							Wsc52-D	dark brown	<100	core	
							Wsc52-E	dark brown	<100	rim	

Diamonds:							Inclusions:				
Lot #/ sieve size	sample #	Morphology	Resorption Class	Weight (mg)	Color	Surface Features/Other	Inclusion designation	Color	Longest Dimension (µm)	Location in Diamond	Comments
401/ -3+1	Wsc53	elongated octahedron	4	4.8	colorless	inverted trigons	Wsc53-A	colorless	100-300	core	
							Wsc53-B	colorless	100-300	core	
							Wsc53-C	colorless	100-300	core	
401/ -3+1	Wsc54	octahedron	6	2.9	colorless	minor polycentric faces	Wsc54-A	purple	300-500	rim	
							Wsc54-B	colorless	<100	rim	
							Wsc54-C	purple	<100	core	
							Wsc54-D	purple	<100	core	
							Wsc54-E	colorless	<100	core	
							Wsc54-F	colorless	<100	core	
401/ -3+1	Wsc55	cubo-octahedron	6	4.0	colorless		Wsc55-A	purple	300-500	core	
							Wsc55-B	purple	300-500	core	
							Wsc55-C	purple	<100	core	
							Wsc55-D	purple	300-500	core	
							Wsc55-E	colorless	100-300	rim	
							Wsc55-F	colorless	<100	core	
							Wsc55-G	colorless	<100	core	
401/ -3+1	Wsc56	flat dodecahedroid	1	4.2	colorless		Wsc56-A	dark brown	100-300	rim	
							Wsc56-C	dark brown	100-300	rim	
							Wsc56-D	dark brown	<100	rim	
							Wsc56-E	dark brown	<100	rim	
							Wsc56-F	dark brown	100-300	rim	
401/ -3+1	Wsc57	broken macle	unresorbed	3.2	colorless		Wsc57-A	colorless	<100	core	
401/ -3+1	Wsc58	octahedron (fragment)	unresorbed	2.7	brown	polycentric faces	Wsc58-A	colorless	<100	core	
							Wsc58-C	colorless	100-300	core	
							Wsc58-D	colorless	100-300	rim	
401/ -3+1	Wsc59	octahedron	4	3.7	colorless		Wsc59-A	colorless	<100	core	
401/ -3+1	Wsc60	octahedron	4	4.9	pale yellow	trigons	Wsc60-A	colorless	100-300	core	
401/ -3+1	Wsc61	polycrystalline aggregate	unresorbed	6.6	dark grey	polycentric faces					aggregate, too dark and cloudy to see inside
401/ -3+1	Wsc62	octahedron	3	3.2	colorless		Wsc62-A	purple	300-500	core	
401/ -3+1	Wsc63	octahedron	6	3.1	light brown	polycentric faces	Wsc63-A	dark brown	<100	core	
							Wsc63-B	colorless	<100	core	
							Wsc63-D	colorless	<100	core	
							Wsc63-F	dark red	<100	core	
401/ -3+1	Wsc64	polycrystalline aggregate	unresorbed	4.0	dark grey	stepped areas					aggregate, too dark and cloudy to see inside
401/ -3+1	Wsc65	elongated octahedron	6	4.1	light brown		Wsc65-A	colorless	100-300	core	
							Wsc65-B	colorless	<100	core	
							Wsc65-C	colorless	<100	core	

Blank spaces indicate no mineral inclusions visible or found

Appendix B: Wawa non-fibrous diamond inclusion electron microprobe analyses

Sample	Wsc01							Wsc03		
				Pt 1 Gr 1	Pt 2 Gr 1					
Mineral Phase[a]	chr	chr	chr	chr	chr	opx	opx	chr	chr	chr
# Analyses Averaged	4	2	2			3	4	3	2	2
# of Grains	1	1	1			1	1	1	1	1
SiO_2	0.23	0.28	0.33	0.26	0.25	57.78	57.21	0.42	0.32	0.26
TiO_2	0.45	0.44	0.44	0.43	0.46	0.05		0.06		0.06
Al_2O_3	6.41	6.03	6.16	5.85	6.09	0.58	0.56	6.21	7.37	7.98
Cr_2O_3	64.78	64.00	65.26	62.04	63.57	0.57	0.55	64.16	63.20	62.66
FeO_{Total}	12.95	13.17	13.02	16.37	14.10	3.57	4.10	14.54	13.84	15.05
MnO						0.10	0.11			
MgO	14.90	14.61	14.75	14.05	14.71	36.78	36.17	13.88	14.36	14.06
CaO						0.43	0.43			
Na_2O						0.07				
NiO	0.14	0.13			0.18	0.13	0.09			0.12
Total	99.86	98.64	99.95	99.00	99.36	100.05	99.20	99.28	99.07	100.18
Fe^{3+} calc[d]	2.17	2.35	1.81	4.61	3.27	1.03		2.47	2.49	2.96
Fe^{2+} calc[d]	10.78	10.82	11.21	11.76	10.83	2.54	4.10	12.07	11.35	12.09
Mg/(Mg+Fe)	0.68	0.67	0.67	0.61	0.66	0.95	0.94	0.63	0.65	0.63
Cr/(Cr+Al)	0.87	0.88	0.88	0.88	0.88	0.40	0.40	0.87	0.85	0.84
TOW79[b]										
PG06[c]										

Blank entries below detection limit; TOW79= O'Neill and Wood (1979); PG06= Grutter et al. (2006); *Used in thermobarometry

[a]Mineral abbreviations: chr=chromite, ol=olivine, opx=orthopyroxene, grt=garnet

[b]T in Celcius @ 50 kbar

[c]P in kbar calculated for 41 mW/m^2 geotherm

[d]Fe^{3+} calculated assuming perfect stoichiometry, based on 12 oxygens for grt and 4 oxygens for chr

Sample	Wsc03				Wsc04			Wsc05		
	Pt 1 Gr 1	Pt 2 Gr 1								
Mineral Phase[a]	chr	chr	ol	ol	ol	ol	ol	chr	chr	chr
# Analyses Averaged			3	2				6	6	6
# of Grains			1	1				2	2	3
SiO_2	0.26	0.28	41.02	40.79	41.10	41.00	40.99	0.33	0.28	0.26
TiO_2	0.06				0.00			0.07	0.06	0.06
Al_2O_3	7.78	7.90				0.06		6.34	6.40	6.33
Cr_2O_3	60.58	61.37	0.07	0.08	0.04			64.12	64.71	65.47
FeO_{Total}	17.00	15.57	6.78	6.88	7.79	7.59	7.94	14.38	13.39	12.81
MnO			0.10	0.08	0.11	0.10	0.11			0.17
MgO	13.46	14.06	51.89	51.18	50.72	49.93	50.93	14.01	14.31	14.61
CaO					0.04	0.07	0.03			
Na_2O					0.00					
NiO	0.11	0.15	0.34	0.34	0.36	0.38	0.36	0.14	0.14	0.14
Total	99.25	99.33	100.21	99.34	100.15	99.13	100.35	99.38	99.29	99.85
Fe^{3+} calc[d]	4.37	3.83			0.04		0.80	2.68	2.22	1.97
Fe^{2+} calc[d]	12.63	11.74	6.78	6.88	7.75	7.59	7.13	11.71	11.17	10.84
Mg/(Mg+Fe)	0.59	0.62	0.93	0.93	0.92	0.92	0.92	0.64	0.66	0.67
Cr/(Cr+Al)	0.84	0.84	0.54	0.67	0.60	0.07	0.33	0.87	0.87	0.87
TOW79[b]										
PG06[c]										

Blank entries below detection limit; TOW79= O'Neill and Wood (1979); PG06= Grutter et al. (2006); *Used in thermobarometry

[a]Mineral abbreviations: chr=chromite, ol=olivine, opx=orthopyroxene, grt=garnet

[b]T in Celcius @ 50 kbar

[c]P in kbar calculated for 41 mW/m^2 geotherm

[d]Fe^{3+} calculated assuming perfect stoichiometry, based on 12 oxygens for grt and 4 oxygens for chr

Sample	Wsc06		Wsc07	Wsc08	Wsc09			Wsc12		
						Pt 1 Gr 1	Pt 2 Gr 1	Pt 1 Gr 1	Pt 2 Gr 1	Pt 1 Gr 2
Mineral Phase[a]	chr	chr	ol	ol	chr	ol	ol	chr	chr	chr
# Analyses Averaged	2	1	4	3	3					
# of Grains	1	1	1	1	2					
SiO_2	0.26	0.35	40.93	41.54	0.47	41.06	40.54	0.32	0.33	0.28
TiO_2	0.08	0.06			0.33			0.07	0.10	
Al_2O_3	7.33	7.27	0.04		5.75			6.79	6.84	7.03
Cr_2O_3	64.17	62.77	0.08	0.10	65.00	0.24	0.30	63.75	64.68	65.88
FeO_{Total}	13.24	13.55	6.96	6.23	13.15	7.01	7.73	13.51	13.39	12.84
MnO	0.13		0.10	0.11		0.16	0.08			
MgO	14.59	14.32	51.55	52.21	14.82	51.14	50.03	14.19	14.21	14.73
CaO			0.05		0.06		0.06			
Na_2O										
NiO	0.12		0.36	0.32	0.16	0.31	0.32	0.15	0.15	0.10
Total	99.90	98.32	100.06	100.50	99.72	99.92	99.06	98.78	99.70	100.86
Fe^{3+} calc[d]	2.22	2.40			2.25	0.23	0.18	2.23	1.75	1.68
Fe^{2+} calc[d]	11.02	11.15	6.96	6.23	10.90	6.78	7.55	11.28	11.64	11.16
Mg/(Mg+Fe)	0.67	0.66	0.93	0.94	0.67	0.93	0.92	0.66	0.66	0.67
Cr/(Cr+Al)	0.85	0.85	0.76	0.73	0.88	1.00	1.00	0.86	0.86	0.86
TOW79[b]										
PG06[c]										

Blank entries below detection limit; TOW79= O'Neill and Wood (1979); PG06= Grutter et al. (2006); *Used in thermobarometry

[a]Mineral abbreviations: chr=chromite, ol=olivine, opx=orthopyroxene, grt=garnet

[b]T in Celcius @ 50 kbar

[c]P in kbar calculated for 41 mW/m^2 geotherm

[d]Fe^{3+} calculated assuming perfect stoichiometry, based on 12 oxygens for grt and 4 oxygens for chr

Sample	Wcs12	Wsc13							Wsc14	
	Pt 2 Gr 2	(touching)	Avg 1 Gr 1	Avg 2 Gr 2			(touching)			
Mineral Phase[a]	chr	ol*	ol	ol	opx	grt*	grt*	grt*	chr	chr
# Analyses Averaged		5			3	4	10	3	2	2
# of Grains		1			1	1	2	1	1	1
SiO_2	0.28	40.66	41.10	40.29	58.64	40.82	40.74	40.83	0.33	0.33
TiO_2									0.40	0.44
Al_2O_3	7.06	0.05		0.11	0.49	16.42	16.21	16.31	7.87	7.26
Cr_2O_3	64.85	0.08	0.06	0.04	0.40	10.22	9.97	9.71	61.41	62.44
FeO_{Total}	12.99	7.74	7.62	8.09	4.55	6.68	6.82	6.45	15.27	14.99
MnO		0.12	0.12	0.11	0.14	0.30	0.31	0.28		
MgO	14.89	50.77	50.64	49.11	35.37	20.78	20.30	20.64	13.87	14.16
CaO		0.06	0.05	0.13	0.62	4.51	4.45	4.39		
Na_2O					0.06	0.07	0.07			
NiO	0.14	0.34	0.34	0.30	0.10				0.12	0.13
Total	100.21	99.81	99.92	98.18	100.38	99.79	98.86	98.62	99.26	99.74
Fe^{3+} calc[d]	2.31					1.16	0.61	0.35	2.79	2.88
Fe^{2+} calc[d]	10.68	7.74	7.62	8.09	4.55	5.52	6.21	6.10	12.48	12.11
Mg/(Mg+Fe)	0.68	0.92	0.92	0.92	0.93	0.85	0.84	0.85	0.62	0.63
Cr/(Cr+Al)	0.86	0.72	0.69	0.21	0.35	0.29	0.29	0.29	0.84	0.85
TOW79[b]						1364	1167	1208		
PG06[c]						45	44	44		

Blank entries below detection limit; TOW79= O'Neill and Wood (1979); PG06= Grutter et al. (2006); *Used in thermobarometry

[a]Mineral abbreviations: chr=chromite, ol=olivine, opx=orthopyroxene, grt=garnet

[b]T in Celcius @ 50 kbar

[c]P in kbar calculated for 41 mW/m^2 geotherm

[d]Fe^{3+} calculated assuming perfect stoichiometry, based on 12 oxygens for grt and 4 oxygens for chr

Sample	Wsc14									
		Pt 1 Gr 1	Pt 2 Gr 1	Avg 1 Gr 2	Avg 2 Gr 2	Pt 1 Gr 3	Pt 2 Gr 3			
Mineral Phase[a]	chr	chr	chr	chr	chr	chr	chr	ol	ol	opx
# Analyses Averaged	7							3	8	5
# of Grains	2							1	3	2
SiO_2	0.31	0.35	0.37	0.34	0.33	0.28	0.31	41.36	41.23	58.16
TiO_2	0.45	0.43	0.46	0.48	0.44	0.48	0.39			
Al_2O_3	7.34	7.23	7.25	7.18	7.23	7.09	7.14			0.75
Cr_2O_3	63.31	61.94	63.01	61.92	62.66	61.87	62.52	0.10	0.08	0.60
FeO_{Total}	14.17	15.32	14.71	15.29	14.69	15.51	15.14	7.11	6.98	4.16
MnO								0.12	0.11	0.10
MgO	14.35	13.70	14.19	13.86	13.98	13.61	13.71	51.50	51.05	36.25
CaO								0.04	0.04	0.31
Na_2O										
NiO	0.15	0.11	0.11	0.16	0.14	0.13	0.15	0.34	0.34	0.09
Total	100.08	99.08	100.10	99.22	99.46	98.97	99.36	100.57	99.82	100.41
Fe^{3+} calc[d]	2.25	2.76	2.45	2.89	2.42	2.86	2.55			0.17
Fe^{2+} calc[d]	11.92	12.56	12.26	12.40	12.28	12.65	12.59	7.11	6.98	3.99
Mg/(Mg+Fe)	0.65	0.62	0.64	0.62	0.63	0.61	0.62	0.93	0.93	0.94
Cr/(Cr+Al)	0.85	0.85	0.85	0.85	0.85	0.85	0.85	0.77	0.75	0.35
TOW79[b]										
PG06[c]										

Blank entries below detection limit; TOW79= O'Neill and Wood (1979); PG06= Grutter et al. (2006); *Used in thermobarometry

[a]Mineral abbreviations: chr=chromite, ol=olivine, opx=orthopyroxene, grt=garnet

[b]T in Celcius @ 50 kbar

[c]P in kbar calculated for 41 mW/m^2 geotherm

[d]Fe^{3+} calculated assuming perfect stoichiometry, based on 12 oxygens for grt and 4 oxygens for chr

Sample	Wsc16	Wsc17			Wsc18		Wsc19	Wsc20		Wsc21
			Pt 1 Gr 1	Pt 2 Gr 1						
Mineral Phase[a]	ol	chr	chr	chr	ol	opx	ol	ol	ol	ol*
# Analyses Averaged	9	3			8	5	3	6	3	4
# of Grains	3	1			3	1	1	2	1	2
SiO_2	40.83	0.40	0.19	0.26	41.18	57.30	41.44	41.58	41.01	41.24
TiO_2		0.10	0.06	0.09						
Al_2O_3		6.66	6.13	6.22	0.03	0.62		0.04	0.03	0.06
Cr_2O_3	0.06	64.08	65.95	65.12	0.09	0.51	0.05	0.08	0.06	0.06
FeO_{Total}	7.69	14.02	13.03	12.97	6.59	3.90	7.26	7.12	7.07	6.90
MnO	0.11				0.10	0.09	0.09	0.09	0.11	0.11
MgO	50.52	14.43	14.63	14.58	51.66	36.66	51.18	50.91	51.47	51.18
CaO	0.04					0.18	0.04	0.05	0.04	
Na_2O										
NiO	0.35	0.15	0.16	0.16	0.35	0.09	0.34	0.32	0.34	0.33
Total	99.61	99.84	100.15	99.40	100.00	99.35	100.41	100.19	100.14	99.88
Fe^{3+} calc[d]		2.63	2.25	2.20						
Fe^{2+} calc[d]	7.69	11.39	10.78	10.77	6.59	3.90	7.26	7.12	7.07	6.90
Mg/(Mg+Fe)	0.92	0.65	0.67	0.67	0.93	0.94	0.93	0.93	0.93	0.93
Cr/(Cr+Al)	0.79	0.87	0.88	0.88	0.70	0.35	0.67	0.60	0.70	0.66
TOW79[b]										
PG06[c]										

Blank entries below detection limit; TOW79= O'Neill and Wood (1979); PG06= Grutter et al. (2006); *Used in thermobarometry

[a]Mineral abbreviations: chr=chromite, ol=olivine, opx=orthopyroxene, grt=garnet

[b]T in Celcius @ 50 kbar

[c]P in kbar calculated for 41 mW/m^2 geotherm

[d]Fe^{3+} calculated assuming perfect stoichiometry, based on 12 oxygens for grt and 4 oxygens for chr

Sample	Wsc21	Wsc22					Wsc25			
			Pt 1 Gr 1	Pt 2 Gr 1	Pt 1 Gr 2	Pt 2 Gr 2				
Mineral Phase[a]	grt*	chr	chr	chr	chr	chr	ol	ol*	grt*	grt*
# Analyses Averaged	6	3					2	9	12	6
# of Grains	2	1					1	3	4	2
SiO_2	41.01	0.24	0.66	0.56	0.29	0.31	40.06	41.33	41.14	41.02
TiO_2		0.07	0.06	0.05	0.07	0.09				
Al_2O_3	16.34	4.03	3.79	3.82	3.82	3.67		0.05	17.83	17.73
Cr_2O_3	9.89	68.77	66.11	66.94	66.35	66.24	0.05	0.07	8.25	8.32
FeO_{Total}	6.18	13.13	14.32	13.96	13.84	14.08	8.13	7.14	5.91	5.82
MnO	0.28						0.07	0.10	0.27	0.24
MgO	21.92	14.08	13.75	13.87	14.10	13.55	48.91	50.84	21.68	21.99
CaO	2.82		0.06	0.05		0.05	0.11	0.05	3.51	3.46
Na_2O	0.06								0.05	
NiO		0.13			0.12		0.37	0.37		
Total	98.49	100.44	98.75	99.25	98.59	97.99	97.71	99.94	98.63	98.56
Fe^{3+} calc[d]	0.27	1.64	2.34	2.15	2.95	2.46			0.25	0.67
Fe^{2+} calc[d]	5.91	11.49	11.98	11.81	10.89	11.62	8.13	7.14	5.66	5.15
Mg/(Mg+Fe)	0.86	0.66	0.64	0.64	0.65	0.64	0.91	0.93	0.87	0.87
Cr/(Cr+Al)	0.29	0.92	0.92	0.92	0.92	0.92	0.33	0.48	0.24	0.24
TOW79[b]	1124								1237	1401
PG06[c]	49								42	42

Blank entries below detection limit; TOW79= O'Neill and Wood (1979); PG06= Grutter et al. (2006); *Used in thermobarometry

[a]Mineral abbreviations: chr=chromite, ol=olivine, opx=orthopyroxene, grt=garnet

[b]T in Celcius @ 50 kbar

[c]P in kbar calculated for 41 mW/m^2 geotherm

[d]Fe^{3+} calculated assuming perfect stoichiometry, based on 12 oxygens for grt and 4 oxygens for chr

Sample	Wsc25		Wsc27		Wsc29					
	Pt 1 Gr 1	Pt 2 Gr 1						Pt 1 Gr 1	P 2 Gr 1	Pt 1 Gr 2
Mineral Phase[a]	grt	grt	ol	ol	chr	chr	chr	chr	chr	chr
# Analyses Averaged			9	3	3	5	1			
# of Grains			3	1	1	2	1			
SiO_2	41.27	40.51	41.33	40.86	0.33	0.38	0.46	0.31	0.23	0.34
TiO_2					0.13	0.11	0.10	0.09	0.09	0.08
Al_2O_3	17.81	17.80	0.06	0.04	6.05	6.14	5.82	5.87	6.04	6.10
Cr_2O_3	8.28	8.47	0.06	0.07	64.48	65.13	63.21	64.08	65.39	64.73
FeO_{Total}	5.80	6.03	6.76	6.72	14.25	13.65	15.52	15.21	14.22	14.23
MnO	0.34	0.23	0.10	0.10						
MgO	21.87	21.87	51.61	52.01	13.93	14.20	13.47	13.71	13.92	14.05
CaO	3.41	3.50	0.06	0.05		0.04	0.08			
Na_2O										
NiO			0.34	0.28	0.16	0.12	0.13	0.10		0.15
Total	98.78	98.41	100.33	100.12	99.34	99.77	98.79	99.37	99.89	99.68
Fe^{3+} calc[d]	0.15	1.34			2.42	1.99	3.16	3.05	2.28	2.48
Fe^{2+} calc[d]	5.65	4.69	6.76	6.72	11.83	11.66	12.36	12.16	11.94	11.75
Mg/(Mg+Fe)	0.87	0.87	0.93	0.93	0.64	0.65	0.61	0.62	0.64	0.64
Cr/(Cr+Al)	0.24	0.24	0.64	0.66	0.88	0.88	0.88	0.88	0.88	0.88
TOW79[b]										
PG06[c]										

Blank entries below detection limit; TOW79= O'Neill and Wood (1979); PG06= Grutter et al. (2006); *Used in thermobarometry

[a]Mineral abbreviations: chr=chromite, ol=olivine, opx=orthopyroxene, grt=garnet

[b]T in Celcius @ 50 kbar

[c]P in kbar calculated for 41 mW/m^2 geotherm

[d]Fe^{3+} calculated assuming perfect stoichiometry, based on 12 oxygens for grt and 4 oxygens for chr

Sample	Wsc29			Wsc31	Wsc32	Wsc33	Wsc36			
	Pt 2 Gr 2	Pt 1 Gr 3	Pt 2 Gr 3							
Mineral Phase[a]	chr	chr	chr	chr	ol	chr	chr	chr	ol	opx
# Analyses Averaged				2	3	3	11	2	3	2
# of Grains				1	1	1	4	1	1	1
SiO_2	0.40	0.30	0.28	0.30	41.45	0.33	0.27	0.35	41.48	58.01
TiO_2	0.09	0.09	0.12	0.05		0.13	0.08	0.06		
Al_2O_3	5.97	6.14	6.07	6.62		8.23	6.12	5.77		0.61
Cr_2O_3	63.95	65.87	65.08	64.48	0.08	61.74	65.21	62.79	0.04	0.53
FeO_{Total}	15.14	13.89	14.08	13.77	6.68	14.37	13.52	16.82	5.95	3.66
MnO					0.09				0.10	0.08
MgO	13.65	14.15	14.07	14.10	51.50	14.12	14.38	13.23	52.35	37.25
CaO			0.04							0.12
Na_2O										
NiO	0.18		0.14	0.13	0.33	0.13	0.12	0.15	0.36	0.10
Total	99.38	100.44	99.88	99.45	100.13	99.06	99.68	99.16	100.29	100.34
Fe^{3+} calc[d]	2.86	2.01	2.39	2.14		2.55	2.37	4.10		1.05
Fe^{2+} calc[d]	12.28	11.88	11.69	11.63	6.68	11.82	11.15	12.73	5.95	2.61
Mg/(Mg+Fe)	0.62	0.65	0.64	0.65	0.93	0.64	0.66	0.59	0.94	0.95
Cr/(Cr+Al)	0.88	0.88	0.88	0.87	0.82	0.83	0.88	0.88	0.69	0.37
TOW79[b]										
PG06[c]										

Blank entries below detection limit; TOW79= O'Neill and Wood (1979); PG06= Grutter et al. (2006); *Used in thermobarometry

[a]Mineral abbreviations: chr=chromite, ol=olivine, opx=orthopyroxene, grt=garnet

[b]T in Celcius @ 50 kbar

[c]P in kbar calculated for 41 mW/m^2 geotherm

[d]Fe^{3+} calculated assuming perfect stoichiometry, based on 12 oxygens for grt and 4 oxygens for chr

Sample	Wsc37								Wsc38	
			Pt 1 Gr 1	Pt 2 Gr 1	Pt 1 Gr 2	Pt 2 Gr 2	Pt 1 Gr 3	Pt 2 Gr 3		
Mineral Phase[a]	chr	chr	chr	chr	chr	chr	chr	chr	chr	chr
# Analyses Averaged	2	1							3	3
# of Grains	1	1							1	1
SiO_2	0.46	0.28	0.29	0.32	0.51	0.47	0.43	0.41	0.29	0.28
TiO_2	0.07	0.07				0.06			0.07	0.08
Al_2O_3	8.40	8.31	8.43	8.40	7.46	7.60	7.59	7.65	6.27	6.52
Cr_2O_3	62.41	62.73	61.49	60.63	61.82	60.76	61.75	63.21	64.92	63.44
FeO_{Total}	13.30	12.52	13.94	14.58	15.58	15.64	14.57	14.14	13.80	15.33
MnO										
MgO	14.50	14.82	14.24	13.87	13.83	13.60	13.84	14.02	14.32	13.80
CaO										
Na_2O										
NiO	0.13		0.13			0.13		0.12	0.15	0.15
Total	99.26	98.73	98.52	97.80	99.20	98.26	98.18	99.55	99.81	99.60
Fe^{3+} calc[d]	1.85	1.90	2.58	2.77	3.21	3.28	2.57	2.05	2.47	3.27
Fe^{2+} calc[d]	11.45	10.62	11.36	11.81	12.37	12.36	12.00	12.09	11.33	12.06
Mg/(Mg+Fe)	0.66	0.68	0.65	0.63	0.62	0.61	0.63	0.64	0.65	0.62
Cr/(Cr+Al)	0.83	0.83	0.83	0.83	0.85	0.84	0.85	0.85	0.87	0.87
TOW79[b]										
PG06[c]										

Blank entries below detection limit; TOW79= O'Neill and Wood (1979); PG06= Grutter et al. (2006); *Used in thermobarometry

[a]Mineral abbreviations: chr=chromite, ol=olivine, opx=orthopyroxene, grt=garnet

[b]T in Celcius @ 50 kbar

[c]P in kbar calculated for 41 mW/m^2 geotherm

[d]Fe^{3+} calculated assuming perfect stoichiometry, based on 12 oxygens for grt and 4 oxygens for chr

Sample	Wsc38				Wsc39					
			Pt 1 Gr 1	Pt 2 Gr 1			Pt 1 Gr 1	Pt 2 Gr 1	Pt 3 Gr 1	Pt 4 Gr 1
Mineral Phase[a]	chr	chr	chr	chr	chr	chr	chr	chr	chr	chr
# Analyses Averaged	2	7			3	4				
# of Grains	1	2			1	2				
SiO_2	0.21	0.24	0.24	0.26	0.29	0.24	0.41	0.51	0.34	0.37
TiO_2	0.09	0.08	0.06	0.07		0.06	0.07	0.06	0.07	0.05
Al_2O_3	6.20	6.54	6.55	6.54	7.02	6.97	6.50	6.37	6.58	6.69
Cr_2O_3	64.91	64.38	65.81	64.88	64.55	63.38	62.55	60.44	64.30	64.98
FeO_{Total}	13.88	14.24	13.63	13.98	14.56	13.78	16.53	17.32	14.02	13.59
MnO	0.12			0.12						
MgO	13.99	14.15	14.29	14.38	13.97	14.22	13.32	13.28	14.10	14.32
CaO										
Na_2O										
NiO	0.14	0.13		0.12	0.15		0.12	0.18	0.11	0.14
Total	99.53	99.76	100.58	100.35	100.54	98.64	99.50	98.16	99.52	100.14
Fe^{3+} calc[d]	2.30	2.66	1.95	2.64	2.36	2.58	3.59	4.73	2.30	1.98
Fe^{2+} calc[d]	11.58	11.58	11.68	11.34	12.20	11.20	12.94	12.59	11.72	11.61
Mg/(Mg+Fe)	0.65	0.64	0.65	0.65	0.63	0.65	0.60	0.58	0.65	0.66
Cr/(Cr+Al)	0.88	0.87	0.87	0.87	0.86	0.86	0.87	0.86	0.87	0.87
TOW79[b]										
PG06[c]										

Blank entries below detection limit; TOW79= O'Neill and Wood (1979); PG06= Grutter et al. (2006); *Used in thermobarometry

[a]Mineral abbreviations: chr=chromite, ol=olivine, opx=orthopyroxene, grt=garnet

[b]T in Celcius @ 50 kbar

[c]P in kbar calculated for 41 mW/m^2 geotherm

[d]Fe^{3+} calculated assuming perfect stoichiometry, based on 12 oxygens for grt and 4 oxygens for chr

Sample	Wsc39		Wsc40					Wsc41		
	Pt 1 Gr 2	Pt 2 Gr 2				Pt 1 Gr 1	Pt 2 Gr 1			Pt 1 Gr 1
Mineral Phase[a]	chr	chr	chr	chr	chr	chr	chr	chr	chr	chr
# Analyses Averaged			3	2	2			7	3	
# of Grains			1	1	1			3	2	
SiO_2	0.32	0.38	0.33	0.34	0.35	0.33	0.25	0.29	0.22	0.24
TiO_2			1.32	1.35	1.34	1.31	1.36	0.06		
Al_2O_3	6.81	6.73	3.47	3.62	3.46	3.36	3.36	5.41	5.43	5.50
Cr_2O_3	64.05	63.94	65.19	67.27	66.85	64.67	66.05	66.29	66.89	67.15
FeO_{Total}	14.60	15.57	14.47	12.13	12.77	14.90	14.83	13.03	13.05	13.12
MnO										
MgO	14.17	13.81	14.50	15.05	14.57	14.06	14.20	14.49	14.42	14.45
CaO										
Na_2O										
NiO	0.14		0.19	0.15	0.13	0.11		0.11	0.11	0.11
Total	100.09	100.43	99.48	99.90	99.46	98.74	100.05	99.68	100.12	100.57
Fe^{3+} calc[d]	2.87	2.98	2.80	1.07	1.15	2.75	2.54	2.13	1.99	1.92
Fe^{2+} calc[d]	11.73	12.59	11.67	11.07	11.62	12.15	12.29	10.90	11.06	11.20
Mg/(Mg+Fe)	0.64	0.62	0.65	0.69	0.67	0.63	0.63	0.67	0.67	0.67
Cr/(Cr+Al)	0.86	0.86	0.93	0.93	0.93	0.93	0.93	0.89	0.89	0.89
TOW79[b]										
PG06[c]										

Blank entries below detection limit; TOW79= O'Neill and Wood (1979); PG06= Grutter et al. (2006); *Used in thermobarometry

[a]Mineral abbreviations: chr=chromite, ol=olivine, opx=orthopyroxene, grt=garnet

[b]T in Celcius @ 50 kbar

[c]P in kbar calculated for 41 mW/m^2 geotherm

[d]Fe^{3+} calculated assuming perfect stoichiometry, based on 12 oxygens for grt and 4 oxygens for chr

Sample	Wsc41									
	Pt 2 Gr 1	Pt 1 Gr 2	Pt 2 Gr 2	Pt 1 Gr 3	Pt 2 Gr 3	Pt 1 Gr 4	Pt 2 Gr 4		Pt 1 Gr 1	Pt 2 Gr 1
Mineral Phase[a]	chr	chr	chr	chr	chr	chr	chr	ol	ol	ol
# Analyses Averaged								3		
# of Grains								1		
SiO_2	0.21	0.20	0.22	0.23	0.24	0.26	0.27	41.67	41.73	41.60
TiO_2						0.05	0.06			
Al_2O_3	5.47	5.44	5.52	5.33	5.19	5.48	5.50			
Cr_2O_3	66.28	66.44	65.77	67.32	66.11	66.04	65.25	0.06		
FeO_{Total}	13.18	12.53	12.68	13.43	13.51	12.89	13.37	5.55	5.79	5.62
MnO	0.16						0.16	0.11		0.08
MgO	14.51	14.66	14.44	14.32	14.26	14.66	14.43	52.24	51.87	52.73
CaO										
Na_2O										
NiO	0.14		0.11		0.11			0.35	0.35	0.37
Total	99.95	99.27	98.74	100.63	99.42	99.38	99.04	99.98	99.73	100.41
Fe^{3+} calc[d]	2.51	2.06	2.09	2.03	2.43	2.26	2.66			
Fe^{2+} calc[d]	10.67	10.47	10.59	11.40	11.08	10.63	10.71	5.55	5.79	5.62
Mg/(Mg+Fe)	0.67	0.68	0.68	0.66	0.66	0.67	0.66	0.94	0.94	0.94
Cr/(Cr+Al)	0.89	0.89	0.89	0.89	0.90	0.89	0.89	0.62	1.00	0.40
TOW79[b]										
PG06[c]										

Blank entries below detection limit; TOW79= O'Neill and Wood (1979); PG06= Grutter et al. (2006); *Used in thermobarometry

[a]Mineral abbreviations: chr=chromite, ol=olivine, opx=orthopyroxene, grt=garnet

[b]T in Celcius @ 50 kbar

[c]P in kbar calculated for 41 mW/m^2 geotherm

[d]Fe^{3+} calculated assuming perfect stoichiometry, based on 12 oxygens for grt and 4 oxygens for chr

Sample	Wsc43		Wsc48							Wsc49
						Pt 1 Gr 1	Pt 2 Gr 1	Pt 1 Gr 2	Pt 2 Gr 2	Pt 1 Gr 1
Mineral Phase[a]	chr	chr	chr	chr	chr	chr	chr	chr	chr	ol
# Analyses Averaged	2	1	5	3	3					
# of Grains	1	1	3	1	1					
SiO_2	0.41	0.51	0.31	0.50	0.31	0.38	0.40	0.24	0.26	41.17
TiO_2	0.06		0.22	0.22	0.21	0.24	0.24	0.23	0.20	
Al_2O_3	5.24	4.95	7.60	7.17	7.43	7.34	7.27	7.97	8.04	
Cr_2O_3	65.50	63.52	63.23	64.65	63.99	63.74	64.58	61.90	61.02	
FeO_{Total}	15.15	16.24	12.95	12.23	12.74	12.27	12.07	14.15	13.78	7.41
MnO		0.13								0.12
MgO	13.55	12.85	14.92	14.91	14.94	15.04	15.28	14.46	14.51	51.72
CaO			0.04	0.06						
Na_2O										
NiO	0.11	0.13	0.14		0.11		0.12	0.20		0.35
Total	100.02	98.33	99.40	99.74	99.73	99.01	99.96	99.15	97.81	100.78
Fe^{3+} calc[d]	2.59	3.19	2.30	1.19	2.02	1.78	1.72	2.95	2.93	
Fe^{2+} calc[d]	12.56	13.05	10.65	11.04	10.72	10.49	10.35	11.20	10.85	7.41
Mg/(Mg+Fe)	0.62	0.59	0.68	0.69	0.68	0.69	0.70	0.65	0.66	0.93
Cr/(Cr+Al)	0.89	0.90	0.85	0.86	0.85	0.85	0.85	0.84	0.84	0.96
TOW79[b]										
PG06[c]										

Blank entries below detection limit; TOW79= O'Neill and Wood (1979); PG06= Grutter et al. (2006); *Used in thermobarometry

[a]Mineral abbreviations: chr=chromite, ol=olivine, opx=orthopyroxene, grt=garnet

[b]T in Celcius @ 50 kbar

[c]P in kbar calculated for 41 mW/m^2 geotherm

[d]Fe^{3+} calculated assuming perfect stoichiometry, based on 12 oxygens for grt and 4 oxygens for chr

Sample	Wsc49	Wsc50			Wsc51		Wsc52			
	Pt 2 Gr 1		Pt 1 Gr 1	Pt 2 Gr 1					Pt 1 Gr 1	Pt 1 Gr 2
Mineral Phase[a]		chr	chr	chr	ol*	grt*	chr	chr	chr	chr
# Analyses Averaged		2			3	3	3	3		
# of Grains		1			1	1	1	1		
SiO_2	40.91	0.38	0.44	0.42	41.31	42.61	0.39	0.25	0.20	0.22
TiO_2		0.12	0.12	0.11			0.06	0.06	0.09	
Al_2O_3		5.64	5.61	5.46		17.35	5.17	5.12	5.25	5.21
Cr_2O_3		66.26	65.00	63.98		6.12	65.81	66.02	66.03	64.91
FeO_{Total}	7.13	13.42	14.72	15.39	7.90	7.47	14.36	14.06	14.72	14.96
MnO					0.11	0.33				
MgO	50.67	14.56	14.30	14.05	50.61	22.16	13.96	13.80	13.88	13.65
CaO		0.05			0.06	3.38				
Na_2O										
NiO	0.32	0.16	0.17	0.12	0.34		0.11	0.11		0.14
Total	99.03	100.58	100.36	99.53	100.33	99.41	99.86	99.43	100.17	99.09
Fe^{3+} calc[d]		2.17	3.10	3.67		0.81	2.50	2.26	2.75	3.11
Fe^{2+} calc[d]	7.13	11.26	11.62	11.72	7.90	6.66	11.86	11.80	11.97	11.85
Mg/(Mg+Fe)	0.93	0.66	0.64	0.63	0.92	0.84	0.64	0.64	0.63	0.62
Cr/(Cr+Al)	0.48	0.89	0.89	0.89	0.45	0.19	0.90	0.90	0.89	0.89
TOW79[b]						1177				
PG06[c]						35				

Blank entries below detection limit; TOW79= O'Neill and Wood (1979); PG06= Grutter et al. (2006); *Used in thermobarometry

[a]Mineral abbreviations: chr=chromite, ol=olivine, opx=orthopyroxene, grt=garnet

[b]T in Celcius @ 50 kbar

[c]P in kbar calculated for 41 mW/m^2 geotherm

[d]Fe^{3+} calculated assuming perfect stoichiometry, based on 12 oxygens for grt and 4 oxygens for chr

Sample	Wsc53				Wsc54		Wsc56			
			Pt 1 Gr 1	Pt 2 Gr 1					Pt 1 Gr 1	Pt 2 Gr 1
Mineral Phase[a]	ol	ol	ol	ol	grt*	grt*	chr	chr	chr	chr
# Analyses Averaged	4	2			11	1	4	2		
# of Grains	1	1			3	1	2	1		
SiO_2	40.89	40.79	40.89	40.63	41.80	41.35	0.37	0.42	0.30	0.31
TiO_2								0.05		
Al_2O_3		0.04	0.15	0.17	19.16	18.80	7.72	7.71	7.49	7.42
Cr_2O_3	0.10	0.07	0.08	0.10	6.83	6.75	63.79	63.07	63.83	63.00
FeO_{Total}	6.84	5.57	6.64	6.67	5.82	5.68	13.32	13.37	14.16	14.36
MnO	0.10	0.09	0.11	0.11	0.25	0.24				
MgO	51.03	51.53	50.35	49.54	22.68	21.94	14.66	14.53	14.51	14.45
CaO	0.04	0.05	0.18	0.23	2.71	2.77	0.06	0.07		
Na_2O					0.06					
NiO	0.31	0.28	0.31	0.39			0.11	0.11	0.11	0.14
Total	99.32	98.42	98.71	97.82	99.31	97.53	100.02	99.33	100.40	99.68
Fe^{3+} calc[d]					0.20	0.00	2.13	2.17	2.73	3.11
Fe^{2+} calc[d]	6.84	5.57	6.64	6.67	5.62	5.68	11.19	11.20	11.43	11.25
Mg/(Mg+Fe)	0.93	0.94	0.93	0.93	0.87	0.87	0.67	0.66	0.65	0.65
Cr/(Cr+Al)	0.74	0.55	0.26	0.28	0.19	0.19	0.85	0.85	0.85	0.85
TOW79[b]										
PG06[c]					39	39				

Blank entries below detection limit; TOW79= O'Neill and Wood (1979); PG06= Grutter et al. (2006); *Used in thermobarometry

[a]Mineral abbreviations: chr=chromite, ol=olivine, opx=orthopyroxene, grt=garnet

[b]T in Celcius @ 50 kbar

[c]P in kbar calculated for 41 mW/m^2 geotherm

[d]Fe^{3+} calculated assuming perfect stoichiometry, based on 12 oxygens for grt and 4 oxygens for chr

Sample	Wsc57	Wsc58			Wsc59	Wsc60	Wsc62	Wsc63			Wsc65
									Pt 1 Gr 1	Pt 2 Gr 1	
Mineral Phase[a]	ol	opx	opx	opx	ol	ol	grt*	chr	chr	chr	ol
# Analyses Averaged	3	3	4	3	1	2	3	2			6
# of Grains	1	1	1	1	1	1	1	2			2
SiO_2	41.66	57.84	58.12	57.19	41.47	40.89	41.48	0.29	0.25	0.22	41.18
TiO_2			0.05					0.09			
Al_2O_3	0.06	0.73	0.72	0.71		0.08	18.78	6.11	5.65	5.56	
Cr_2O_3	0.09	0.48	0.50	0.55	0.06		7.38	64.05	63.90	64.81	0.06
FeO_{Total}	6.41	3.98	3.71	4.14	6.86	7.77	6.37	15.72	15.69	15.96	6.93
MnO	0.09	0.11	0.12	0.09	0.09	0.09	0.24				0.10
MgO	51.59	36.23	36.93	36.49	50.93	49.90	22.45	13.00	13.05	13.03	51.41
CaO	0.07	0.35	0.32	0.30		0.09	2.69				0.03
Na_2O		0.07	0.04				0.10				
NiO	0.35	0.10	0.05	0.10	0.33	0.34		0.15	0.11	0.17	0.34
Total	100.31	99.88	100.57	99.57	99.74	99.14	99.50	99.39	98.65	99.75	100.05
Fe^{3+} calc[d]		0.28		1.50			0.63	2.52	2.95	2.92	
Fe^{2+} calc[d]	6.41	3.71	3.71	2.64	6.86	7.77	5.73	13.21	12.74	13.04	6.93
Mg/(Mg+Fe)	0.93	0.94	0.95	0.94	0.93	0.92	0.86	0.60	0.60	0.60	0.93
Cr/(Cr+Al)	0.50	0.31	0.32	0.34	0.56	0.00	0.21	0.88	0.88	0.89	0.78
TOW79[b]											
PG06[c]							41				

Blank entries below detection limit; TOW79= O'Neill and Wood (1979); PG06= Grutter et al. (2006); *Used in thermobarometry

[a]Mineral abbreviations: chr=chromite, ol=olivine, opx=orthopyroxene, grt=garnet

[b]T in Celcius @ 50 kbar

[c]P in kbar calculated for 41 mW/m^2 geotherm

[d]Fe^{3+} calculated assuming perfect stoichiometry, based on 12 oxygens for grt and 4 oxygens for chr

Appendix C: Wawa non-fibrous diamond carbon isotope analyses

Sample	$\delta^{13}C$ PDB[a] (‰)
Wsc10	-3.6
Wsc11	-3.2
Wsc15	-2.7
Wsc23	-3.2
Wsc24	-3.1
Wsc27	-2.8
Wsc30	-3.9
Wsc33	-3.1
Wsc35	-4.0
Wsc45	-2.7
Wsc50	-2.5
Wsc55	-2.6
Wsc61	-3.1
Wsc64	-3.8

Samples analyzed through combustion at the Sobolev Institute for Geology and Mineralogy

[a]PDB= Pee Dee Belemnite standard

Appendix D: Raw electron microprobe data for non-fibrous diamond mineral inclusions indicating screening process used for accuracy of analyses

Red text = rejected analysis based on oxide total
Cations calculated based on 12 oxygens for garnet, 4 oxygens for olivine and chromite, and 6 oxygens for orthopyroxene
Inclusion analyses grouped by mineral phase and sample number

Label	Min Phase	SiO_2	TiO_2	Al_2O_3	Cr_2O_3	FeO	MnO	MgO	CaO	Na_2O	NiO	Total	Si	Ti	Al	Cr	Fe	Mn	Mg	Ca	Ni	Total	Mg#
Wsc13B-1	grt	40.73		16.44	9.98	6.55	0.30	20.66	4.54	0.04		99.24	2.984		1.420	0.578	0.401	0.019	2.256	0.357	0.006	8.020	
Wsc13B-2	grt	40.86		16.41	10.26	6.61	0.27	20.69	4.48	0.02		99.59	2.984		1.413	0.593	0.404	0.016	2.253	0.350	0.002	8.015	
Wsc13B-3	grt	41.07		16.39	10.29	6.70	0.28	20.95	4.48	0.07		100.23	2.982		1.403	0.591	0.407	0.017	2.267	0.349	0.010	8.026	
Wsc13B-4	grt	40.63		16.44	10.34	6.38	0.33	20.82	4.52	0.03		99.49	2.971		1.417	0.598	0.390	0.020	2.269	0.354	0.004	8.023	
Wsc13C-1	grt	40.21		15.97	10.11	6.16	0.34	20.02	4.48	0.01		97.31	3.002		1.405	0.597	0.385	0.022	2.228	0.358	0.002	7.998	
Wsc13C-2	grt	40.01		15.86	9.80	6.42	0.33	20.11	4.57	0.05		97.15	2.996		1.399	0.580	0.402	0.021	2.245	0.367	0.007	8.017	
Wsc13C-3	grt	40.19		15.80	9.72	6.57	0.25	19.96	4.44	0.03		96.96	3.013		1.396	0.576	0.412	0.016	2.230	0.357	0.004	8.004	
Wsc13C-4	grt	39.84		15.80	9.41	6.40	0.34	19.75	4.46	0.00		96.00	3.014		1.409	0.562	0.405	0.022	2.228	0.361	0.000	8.001	
Wsc13C-1	grt	40.52		15.88	9.91	7.46	0.33	19.98	4.47	0.10		98.64	3.001		1.386	0.580	0.462	0.020	2.205	0.355	0.014	8.023	
Wsc13C-2	grt	40.54		15.99	10.12	7.30	0.28	19.98	4.48	0.08		98.77	2.996		1.393	0.591	0.451	0.017	2.202	0.355	0.011	8.017	
Wsc13C-3	grt	40.63		16.09	9.69	7.35	0.28	20.37	4.40	0.06		98.87	2.996		1.399	0.565	0.454	0.017	2.239	0.347	0.009	8.026	
Wsc13C-4	grt	40.74		16.09	9.92	7.13	0.29	20.27	4.51	0.04		98.98	3.000		1.396	0.578	0.439	0.018	2.225	0.356	0.006	8.017	
Wsc13D-1	grt	40.30		16.12	9.56	6.78	0.29	19.94	4.39	0.09		97.46	3.006		1.417	0.564	0.423	0.018	2.218	0.351	0.013	8.010	
Wsc13D-2	grt	38.64		15.45	9.57	9.07	0.25	19.27	4.24	0.12		96.61	2.951		1.391	0.578	0.579	0.016	2.195	0.347	0.018	8.074	
Wsc13D-3	grt	40.46		16.08	10.06	6.85	0.27	20.00	4.45	0.12		98.30	2.998		1.405	0.589	0.425	0.017	2.210	0.353	0.018	8.014	
Wsc13D-4	grt	39.59		15.66	9.32	7.10	0.27	19.75	4.32	0.19		96.21	3.000		1.399	0.558	0.450	0.017	2.231	0.351	0.028	8.035	
Wsc13D-5	grt	40.65		16.33	10.10	6.42	0.30	20.32	4.47	0.05		98.63	2.995		1.418	0.588	0.395	0.019	2.231	0.353	0.007	8.006	
Wsc13D-1	grt	40.93		16.53	9.99	6.20	0.35	20.51	4.47	0.04		99.02	2.999		1.427	0.579	0.380	0.022	2.240	0.351	0.005	8.001	
Wsc13D-2	grt	41.01		16.28	10.01	6.28	0.30	20.55	4.37	0.06		98.85	3.009		1.407	0.581	0.385	0.018	2.248	0.343	0.009	8.001	
Wsc13D-3	grt	41.03		16.41	9.73	6.34	0.27	20.46	4.35	0.07		98.66	3.014		1.420	0.565	0.389	0.017	2.241	0.342	0.010	7.998	
Wsc13D-4	grt	40.91		16.41	10.12	6.23	0.38	20.56	4.51	0.05		99.16	2.996		1.416	0.586	0.381	0.023	2.244	0.354	0.007	8.007	
Wsc13I-1	grt	40.88		16.44	9.64	6.14	0.23	20.77	4.39	0.01		98.51	3.005		1.424	0.560	0.377	0.015	2.276	0.346	0.001	8.004	
Wsc13I-2	grt	40.80		16.01	9.69	6.79	0.29	20.43	4.39	0.00		98.40	3.013		1.394	0.566	0.420	0.018	2.250	0.347	0.001	8.007	
Wsc13I-3	grt	40.82		16.47	9.81	6.31	0.33	20.73	4.40	0.00		98.87	2.995		1.424	0.569	0.387	0.020	2.267	0.346	0.000	8.009	
Wsc21A-1	grt	40.88		16.16	10.12	6.01	0.26	21.92	2.82	0.00		98.18	3.004		1.400	0.588	0.369	0.016	2.402	0.222	0.000	8.002	
Wsc21A-2	grt	40.72		16.22	9.77	6.16	0.26	21.83	2.90	0.02		97.89	3.002		1.409	0.570	0.380	0.016	2.399	0.229	0.003	8.009	
Wsc21A-3	grt	40.90		16.29	9.89	6.01	0.27	21.85	2.74	0.00		97.95	3.010		1.412	0.575	0.370	0.017	2.397	0.216	0.000	7.997	
Wsc21A-4	grt	40.88		16.17	9.95	6.10	0.27	21.74	2.87	0.03		98.01	3.010		1.403	0.579	0.376	0.017	2.387	0.226	0.005	8.002	
Wsc21C-1	grt	41.20		16.55	9.74	6.46	0.30	22.05	2.80	0.05		99.15	3.000		1.420	0.561	0.393	0.018	2.394	0.219	0.007	8.012	
Wsc21C-2	grt	41.45		16.67	9.85	6.19	0.29	22.15	2.79	0.06		99.44	3.005		1.424	0.565	0.375	0.018	2.393	0.217	0.008	8.005	
Wsc25A-1	grt	41.02		17.89	8.33	6.03	0.25	21.64	3.56	0.00		98.72	2.986		1.534	0.480	0.367	0.016	2.348	0.278	0.000	8.008	
Wsc25A-2	grt	41.11		17.98	8.19	5.98	0.35	21.67	3.55	0.00		98.83	2.988		1.540	0.471	0.363	0.021	2.348	0.277	0.000	8.007	
Wsc25A-3	grt	41.04		17.93	8.25	5.99	0.28	21.52	3.53	0.01		98.53	2.991		1.540	0.475	0.365	0.017	2.338	0.276	0.001	8.002	
Wsc25A-4	grt	41.34		17.94	8.26	6.04	0.26	21.52	3.55	0.01		98.93	3.000		1.534	0.474	0.367	0.016	2.328	0.276	0.002	7.997	
Wsc25A-5	grt	40.98		17.99	8.13	6.07	0.27	21.77	3.56	0.01		98.78	2.981		1.542	0.467	0.369	0.017	2.361	0.277	0.001	8.015	
Wsc25E-1	grt	41.17		17.51	8.44	5.96	0.26	21.76	3.46	0.05		98.60	3.000		1.503	0.486	0.363	0.016	2.364	0.270	0.008	8.009	
Wsc25E-2	grt	41.19		17.41	8.31	6.04	0.27	21.52	3.49	0.04		98.27	3.011		1.500	0.480	0.369	0.017	2.345	0.274	0.006	8.001	
Wsc25E-3	grt	40.47		17.23	7.98	6.11	0.24	21.18	3.33	0.04		96.57										0.000	

Label	Min Phase	SiO_2	TiO_2	Al_2O_3	Cr_2O_3	FeO	MnO	MgO	CaO	Na_2O	NiO	Total	Si	Ti	Al	Cr	Fe	Mn	Mg	Ca		Ni	Total	Mg#
Wsc25F-1	grt	41.27		17.81	8.28	5.79	0.34	21.87	3.41	0.00		98.77	2.997		1.524	0.475	0.351	0.021	2.368	0.265	0.000		8.003	
Wsc25F-2	grt	40.51		17.80	8.47	5.90	0.23	21.87	3.50	0.01		98.29	2.964		1.535	0.490	0.361	0.014	2.385	0.274	0.001		8.024	
Wsc25F-3	grt	40.97		17.68	8.14	5.62	0.20	21.88	3.42	0.02		97.93	2.997		1.524	0.471	0.344	0.013	2.387	0.268	0.003		8.007	
Wsc25G-1	grt	41.07		17.78	8.01	5.68	0.24	22.07	3.48	0.00		98.33	2.993		1.527	0.461	0.346	0.015	2.398	0.272	0.000		8.013	
Wsc25G-2	grt	41.15		17.75	8.29	5.86	0.27	21.92	3.42	0.00		98.67	2.993		1.521	0.477	0.357	0.017	2.377	0.267	0.000		8.008	
Wsc25H-1	grt	41.14		17.61	8.24	5.53	0.25	21.94	3.35	0.03		98.10	3.004		1.515	0.476	0.338	0.015	2.389	0.262	0.004		8.003	
Wsc25H-2	grt	40.58		17.82	8.32	5.84	0.19	22.04	3.44	0.02		98.25	2.967		1.536	0.481	0.357	0.012	2.402	0.270	0.002		8.026	
Wsc25H-3	grt	41.37		17.73	8.38	5.70	0.26	21.91	3.41	0.00		98.76	3.003		1.517	0.481	0.346	0.016	2.371	0.265	0.001		7.999	
Wsc25J-1	grt	40.99		17.63	8.30	5.66	0.25	22.02	3.47	0.02		98.32	2.990		1.516	0.479	0.345	0.015	2.395	0.271	0.002		8.014	
Wsc25J-2	grt	40.89		17.81	8.41	5.56	0.22	22.06	3.48	0.01		98.44	2.979		1.529	0.484	0.339	0.014	2.397	0.272	0.001		8.015	
Wsc25J-3	grt	41.09		17.76	8.46	5.80	0.22	21.94	3.41	0.00		98.68	2.988		1.522	0.487	0.352	0.014	2.379	0.266	0.000		8.008	
Wsc25J-4	grt	40.93		17.64	8.44	5.92	0.21	21.92	3.49	0.02		98.57	2.984		1.515	0.486	0.361	0.013	2.383	0.273	0.003		8.017	
Wsc25L-1	grt	41.18		17.95	8.10	5.73	0.29	21.50	3.56	0.00		98.32	3.002		1.542	0.467	0.349	0.018	2.337	0.278	0.000		7.993	
Wsc25L-2	grt	40.97		18.04	8.16	5.90	0.27	21.62	3.52	0.01		98.49	2.985		1.549	0.470	0.360	0.017	2.348	0.275	0.001		8.006	
Wsc25L-3	grt	41.11		17.96	8.19	5.64	0.28	21.77	3.52	0.02		98.47	2.992		1.541	0.471	0.343	0.017	2.362	0.274	0.002		8.003	
Wsc51A-1	grt	42.66		17.49	6.20	7.52	0.27	22.35	3.36	0.03		99.89	3.064		1.481	0.352	0.452	0.016	2.393	0.258	0.005		8.022	
Wsc51A-2	grt	42.63		17.22	6.07	7.24	0.34	21.94	3.38	0.03		98.85	3.089		1.471	0.348	0.439	0.021	2.370	0.262	0.005		8.004	
Wsc51A-3	grt	42.53		17.33	6.08	7.40	0.39	22.20	3.39	0.01		99.33	3.072		1.475	0.347	0.447	0.024	2.391	0.263	0.001		8.018	
Wsc54A-1	grt	39.57	0.00	17.97	6.29	10.89	0.20	20.92	2.61	0.09	0.02	98.57	2.936	0.000	1.571	0.369	0.676	0.013	2.313	0.208	0.013	0.001	8.100	
Wsc54A-2	grt	38.02	0.01	17.13	6.34	13.79	0.25	19.76	2.51	0.08	0.08	97.98	2.890	0.001	1.534	0.381	0.877	0.016	2.238	0.205	0.012	0.005	8.158	
Wsc54A-3	grt	38.30	0.00	17.30	6.40	12.21	0.27	19.95	2.63	0.06	0.05	97.17	2.911	0.000	1.550	0.385	0.776	0.017	2.260	0.215	0.009	0.003	8.126	
Wsc54A-1	grt	41.54		19.24	6.90	5.80	0.31	22.60	2.73	0.06		99.18	2.984		1.628	0.392	0.348	0.019	2.420	0.210	0.008		8.010	
Wsc54A-2	grt	41.93		19.07	6.94	5.84	0.26	22.51	2.74	0.05		99.35	3.005		1.610	0.393	0.350	0.016	2.405	0.211	0.007		7.997	
Wsc54A-3	grt	41.57		19.20	6.75	5.89	0.26	22.68	2.75	0.06		99.16	2.986		1.626	0.383	0.354	0.016	2.429	0.212	0.008		8.013	
Wsc54A-4	grt	42.03		19.13	6.93	5.89	0.27	22.72	2.71	0.03		99.72	3.001		1.610	0.391	0.352	0.016	2.419	0.208	0.004		8.001	
Wsc54B-1	grt	41.00		18.64	6.62	5.72	0.29	22.00	2.71	0.01		97.00	3.008		1.612	0.384	0.351	0.018	2.407	0.213	0.001		7.994	
Wsc54B-2	grt	40.91		18.78	6.65	5.87	0.31	21.92	2.81	0.02		97.28	2.997		1.621	0.385	0.360	0.019	2.394	0.221	0.003		8.001	
Wsc54B-3	grt	41.35		18.80	6.75	5.68	0.24	21.94	2.77	0.04		97.55	3.015		1.616	0.389	0.346	0.015	2.384	0.216	0.005		7.986	
Wsc54B-4	grt	37.95	0.02	17.09	5.94	11.76	0.23	19.99	2.55	0.11	0.03	95.67	2.921	0.001	1.551	0.362	0.757	0.015	2.294	0.210	0.017	0.002	8.130	
Wsc54B-5	grt	38.24	0.02	17.49	6.30	11.50	0.26	20.33	2.62	0.06	0.05	96.86	2.906	0.001	1.566	0.378	0.731	0.016	2.302	0.214	0.008	0.003	8.125	
Wsc54B-6	grt	39.97	0.00	17.94	6.72	8.57	0.23	21.01	2.63	0.15	0.04	97.25	2.974	0.000	1.573	0.395	0.533	0.014	2.330	0.209	0.022	0.002	8.054	
Wsc54C-1	grt	41.72		19.03	6.90	5.66	0.20	22.71	2.73	0.00		98.95	2.999		1.612	0.392	0.340	0.012	2.434	0.210	0.001		7.999	
Wsc54C-2	grt	41.97		19.22	6.79	5.67	0.24	22.71	2.71	0.01		99.32	3.003		1.621	0.384	0.339	0.015	2.423	0.208	0.001		7.995	
Wsc54C-3	grt	41.80		19.16	6.95	5.77	0.21	22.80	2.63	0.02		99.33	2.994		1.618	0.393	0.346	0.013	2.434	0.202	0.002		8.002	
Wsc54C-4	grt	41.53		19.06	6.65	5.67	0.21	22.50	2.66	0.02		98.32	3.002		1.624	0.380	0.343	0.013	2.425	0.206	0.003		7.997	
Wsc54D-1	grt	40.12		18.27	5.79	4.92	0.18	22.02	2.39	0.05		93.74	3.026		1.624	0.345	0.310	0.012	2.475	0.193	0.008		7.994	
Wsc54D-2	grt	40.26		18.05	5.58	4.56	0.19	21.88	2.41	0.00		92.92	3.054		1.613	0.335	0.289	0.012	2.474	0.196	0.000		7.972	
Wsc54D-3	grt	39.86		18.10	5.45	4.59	0.14	21.94	2.42	0.02		92.52	3.038		1.626	0.329	0.293	0.009	2.493	0.197	0.003		7.986	
Wsc54D-4	grt	41.77		19.15	6.62	5.81	0.23	22.67	2.70	0.05		99.00	3.001		1.621	0.376	0.349	0.014	2.428	0.208	0.006		8.004	
Wsc54D-5	grt	42.04		19.28	6.88	5.95	0.25	22.89	2.77	0.03		100.07	2.992		1.617	0.387	0.354	0.015	2.429	0.211	0.004		8.008	
Wsc54D-6	grt	41.92		19.18	6.87	5.86	0.27	22.72	2.68	0.02		99.52	2.998		1.617	0.389	0.351	0.016	2.423	0.205	0.003		8.001	
Wsc62A-1	grt	41.44	0.01	18.83	7.42	6.37	0.26	22.53	2.68	0.00	0.02	99.56	2.978	0.000	1.595	0.422	0.383	0.016	2.413	0.206	0.000	0.001	8.014	
Wsc62A-2	grt	41.66	0.05	18.79	7.39	6.15	0.25	22.44	2.71	0.00	0.00	99.43	2.992	0.002	1.590	0.420	0.369	0.015	2.403	0.208	0.000	0.000	8.000	
Wsc62A-3	grt	41.34	0.00	18.73	7.33	6.39	0.22	22.38	2.69	0.10	0.02	99.19	2.982	0.000	1.592	0.418	0.385	0.014	2.406	0.208	0.014	0.001	8.020	
Wsc03A-1	chr	0.43	0.06	6.13	63.89	14.49	0.00	13.82	0.01		0.10	98.92	0.014	0.001	0.240	1.679	0.403	0.000	0.685	0.000		0.003	3.025	
Wsc03A-2	chr	0.40	0.06	6.27	64.17	14.13	0.04	14.00	0.00		0.10	99.17	0.013	0.001	0.245	1.679	0.391	0.001	0.691	0.000		0.003	3.024	
Wsc03A-3	chr	0.44	0.07	6.22	64.43	14.28	0.04	13.83	0.00		0.09	99.39	0.014	0.002	0.242	1.683	0.395	0.001	0.681	0.000		0.002	3.021	
Wsc03D-1	chr	0.32	0.05	7.31	63.36	13.68	0.00	14.40	0.00		0.07	99.19	0.011	0.001	0.283	1.646	0.376	0.000	0.705	0.000		0.002	3.024	
Wsc03D-2	chr	0.31	0.05	7.42	63.03	13.51	0.01	14.31	0.00		0.10	98.73	0.010	0.001	0.288	1.644	0.373	0.000	0.704	0.000		0.003	3.023	
Wsc03E-1	chr	0.26	0.06	7.78	60.58	16.56	0.07	13.46	0.01		0.11	98.88	0.009	0.001	0.305	1.593	0.461	0.002	0.667	0.000		0.003	3.041	
Wsc03E-2	chr	0.28	0.04	7.90	61.37	15.18	0.07	14.06	0.02		0.15	99.06	0.009	0.001	0.307	1.601	0.419	0.002	0.692	0.001		0.004	3.036	
Wsc03E-3	chr	0.25	0.04	7.99	62.61	14.91	0.04	14.06	0.01		0.12	100.03	0.008	0.001	0.308	1.616	0.407	0.001	0.684	0.000		0.003	3.029	
Wsc03E-4	chr	0.27	0.06	7.97	62.70	14.59	0.00	14.05	0.00		0.11	99.75	0.009	0.001	0.307	1.621	0.399	0.000	0.685	0.000		0.003	3.026	

Label	Min Phase	SiO_2	TiO_2	Al_2O_3	Cr_2O_3	FeO	MnO	MgO	CaO	Na_2O	NiO	Total	Si	Ti	Al	Cr	Fe	Mn	Mg	Ca	Ni	Total	Mg#
Wsc05A-1	chr	0.34	0.07	6.33	63.95	14.23	0.05	14.10	0.00		0.13	99.17	0.011	0.002	0.247	1.673	0.394	0.001	0.696	0.000	0.003	3.027	
Wsc05A-2	chr	0.36	0.04	6.39	63.84	14.57	0.05	13.94	0.01		0.08	99.27	0.012	0.001	0.249	1.670	0.403	0.001	0.688	0.000	0.002	3.027	
Wsc05A-3	chr	0.40	0.03	6.28	64.14	14.39	0.01	13.92	0.01		0.16	99.33	0.013	0.001	0.245	1.677	0.398	0.000	0.686	0.000	0.004	3.025	
Wsc05D-1	chr	0.44	0.05	6.40	64.71	13.11	0.02	14.47	0.02		0.13	99.35	0.015	0.001	0.248	1.682	0.360	0.001	0.709	0.001	0.003	3.019	
Wsc05D-2	chr	0.33	0.04	6.42	64.90	12.66	0.05	14.28	0.00		0.19	98.86	0.011	0.001	0.250	1.695	0.350	0.001	0.703	0.000	0.005	3.016	
Wsc05D-3	chr	0.27	0.05	6.42	64.83	12.91	0.03	14.35	0.00		0.08	98.94	0.009	0.001	0.250	1.693	0.357	0.001	0.706	0.000	0.002	3.019	
Wsc05E-1	chr	0.25	0.06	6.61	65.15	12.70	0.05	14.60	0.00		0.07	99.50	0.008	0.001	0.255	1.688	0.348	0.001	0.714	0.000	0.002	3.018	
Wsc05E-2	chr	0.22	0.05	6.46	65.37	12.70	0.04	14.71	0.00		0.06	99.62	0.007	0.001	0.250	1.693	0.348	0.001	0.719	0.000	0.002	3.020	
Wsc05F-1	chr	0.20	0.07	6.43	64.67	13.57	0.03	14.22	0.00		0.15	99.35	0.007	0.002	0.250	1.686	0.374	0.001	0.699	0.000	0.004	3.023	
Wsc05F-2	chr	0.22	0.02	6.46	64.93	13.12	0.03	14.35	0.00		0.12	99.26	0.007	0.000	0.251	1.691	0.362	0.001	0.705	0.000	0.003	3.021	
Wsc05F-3	chr	0.21	0.06	6.26	64.19	13.66	0.01	14.21	0.00		0.12	98.71	0.007	0.002	0.245	1.686	0.379	0.000	0.704	0.000	0.003	3.026	
Wsc05G1-1	chr	0.29	0.05	6.15	65.78	12.22	0.00	14.79	0.00		0.15	99.42	0.009	0.001	0.238	1.706	0.335	0.000	0.723	0.000	0.004	3.017	
Wsc05G1-2	chr	0.25	0.06	6.26	65.30	12.44	0.17	14.69	0.00		0.02	99.19	0.008	0.001	0.243	1.699	0.342	0.005	0.721	0.000	0.001	3.020	
Wsc05G2-1	chr	0.27	0.08	6.25	65.86	12.91	0.00	14.42	0.00		0.09	99.89	0.009	0.002	0.241	1.704	0.353	0.000	0.704	0.000	0.002	3.016	
Wsc05G2-2	chr	0.28	0.05	6.22	65.38	12.67	0.00	14.47	0.00		0.13	99.19	0.009	0.001	0.241	1.703	0.349	0.000	0.711	0.000	0.003	3.018	
Wsc05H-1	chr	0.27	0.06	6.26	64.21	14.48	0.02	13.82	0.01		0.11	99.25	0.009	0.002	0.244	1.683	0.401	0.001	0.683	0.001	0.003	3.026	
Wsc05H-2	chr	0.29	0.01	6.45	64.25	13.87	0.00	14.10	0.02		0.08	99.06	0.010	0.000	0.251	1.681	0.384	0.000	0.696	0.001	0.002	3.024	
Wsc05H-3	chr	0.32	0.02	6.33	64.32	13.13	0.03	14.20	0.00		0.15	98.51	0.011	0.001	0.248	1.689	0.365	0.001	0.703	0.000	0.004	3.020	
Wsc06B-1	chr	0.35	0.06	7.27	62.77	13.31	0.03	14.32	0.04		0.07	98.21	0.011	0.002	0.284	1.645	0.369	0.001	0.708	0.001	0.002	3.023	
Wsc06A-1	chr	0.27	0.08	7.36	64.29	13.14	0.13	14.61	0.01		0.11	99.99	0.009	0.002	0.282	1.655	0.358	0.004	0.709	0.000	0.003	3.021	
Wsc06A-2	chr	0.24	0.07	7.29	64.04	12.90	0.06	14.57	0.00		0.12	99.29	0.008	0.002	0.282	1.659	0.353	0.002	0.712	0.000	0.003	3.020	
Wsc09D-1	chr	0.48	0.38	5.79	64.96	12.77	0.00	14.98	0.02		0.14	99.52	0.016	0.009	0.224	1.685	0.350	0.000	0.732	0.001	0.004	3.021	
Wsc09D-2	chr	0.48	0.30	5.72	65.47	13.18	0.00	14.85	0.03		0.07	100.10	0.016	0.007	0.220	1.691	0.360	0.000	0.723	0.001	0.002	3.021	
Wsc09F-1	chr	0.46	0.29	5.80	64.69	13.04	0.00	14.71	0.04		0.08	99.09	0.015	0.007	0.225	1.687	0.360	0.000	0.723	0.001	0.002	3.021	
Wsc09F-2	chr	0.45	0.33	5.68	64.88	12.70	0.07	14.73	0.06		0.17	99.07	0.015	0.008	0.221	1.693	0.351	0.002	0.725	0.002	0.005	3.020	
Wsc12A-1	chr	0.32	0.07	6.79	63.75	13.29	0.07	14.19	0.02		0.15	98.64	0.011	0.002	0.265	1.668	0.368	0.002	0.700	0.001	0.004	3.020	
Wsc12A-2	chr	0.33	0.10	6.84	64.68	13.21	0.00	14.21	0.03		0.15	99.54	0.011	0.003	0.264	1.677	0.362	0.000	0.694	0.001	0.004	3.015	
Wsc12B-1	chr	0.28	0.05	7.03	65.88	12.67	0.07	14.73	0.02		0.10	100.84	0.009	0.001	0.268	1.681	0.342	0.002	0.709	0.001	0.003	3.015	
Wsc12B-2	chr	0.26	0.06	7.10	65.66	12.72	0.03	14.87	0.01		0.12	100.84	0.008	0.002	0.270	1.675	0.343	0.001	0.715	0.000	0.003	3.018	
Wsc12B-3	chr	0.28	0.02	7.06	64.85	12.75	0.02	14.89	0.00		0.14	100.01	0.009	0.001	0.271	1.668	0.347	0.001	0.722	0.000	0.004	3.021	
Wsc12B-4	chr	0.26	0.06	6.98	65.10	12.81	0.06	14.57	0.00		0.08	99.92	0.009	0.001	0.268	1.678	0.349	0.002	0.708	0.000	0.002	3.017	
Wsc14-1	chr	0.34	0.41	7.81	61.69	14.90	0.00	13.97	0.01		0.06	99.18	0.011	0.010	0.303	1.604	0.410	0.000	0.685	0.000	0.001	3.025	
Wsc14-2	chr	0.31	0.39	7.93	61.12	15.08	0.05	13.77	0.00		0.12	98.78	0.010	0.010	0.309	1.597	0.417	0.001	0.679	0.000	0.003	3.027	
Wsc14L-1	chr	0.30	0.47	7.19	62.62	14.49	0.00	14.21	0.03		0.15	99.47	0.010	0.012	0.278	1.627	0.398	0.000	0.696	0.001	0.004	3.026	
Wsc14L-2	chr	0.36	0.41	7.32	62.25	14.90	0.02	14.11	0.00		0.11	99.48	0.012	0.010	0.284	1.618	0.410	0.001	0.691	0.000	0.003	3.028	
Wsc14M-1	chr	0.30	0.47	7.37	63.26	13.80	0.01	14.36	0.02		0.16	99.74	0.010	0.012	0.284	1.634	0.377	0.000	0.699	0.001	0.004	3.020	
Wsc14M-2	chr	0.31	0.46	7.29	63.43	14.20	0.00	14.55	0.01		0.14	100.38	0.010	0.011	0.279	1.630	0.386	0.000	0.705	0.000	0.004	3.025	
Wsc14M-3	chr	0.27	0.46	7.34	63.48	13.84	0.05	14.37	0.01		0.13	99.94	0.009	0.011	0.282	1.637	0.378	0.001	0.699	0.000	0.003	3.020	
Wsc14N-1	chr	0.32	0.43	7.36	63.21	13.67	0.01	14.31	0.01		0.06	99.39	0.011	0.011	0.284	1.637	0.374	0.000	0.699	0.000	0.002	3.018	
Wsc14N-2	chr	0.29	0.47	7.34	63.44	13.83	0.00	14.37	0.00		0.13	99.87	0.009	0.012	0.282	1.636	0.377	0.000	0.699	0.000	0.003	3.020	
Wsc14N-3	chr	0.36	0.42	7.31	63.20	14.37	0.05	14.16	0.02		0.12	100.02	0.012	0.010	0.281	1.631	0.392	0.001	0.689	0.001	0.003	3.022	
Wsc14N-4	chr	0.34	0.44	7.36	63.14	13.88	0.01	14.35	0.03		0.20	99.75	0.011	0.011	0.283	1.631	0.379	0.000	0.699	0.001	0.005	3.021	
Wsc14P-1	chr	0.35	0.43	7.23	61.94	15.04	0.10	13.70	0.03		0.11	98.92	0.012	0.011	0.282	1.622	0.417	0.003	0.677	0.001	0.003	3.026	
Wsc14P-2	chr	0.37	0.46	7.25	63.01	14.47	0.03	14.19	0.01		0.11	99.89	0.012	0.011	0.279	1.629	0.396	0.001	0.692	0.000	0.003	3.023	
Wsc14P-3	chr	0.35	0.42	7.27	62.55	14.53	0.07	14.02	0.01		0.10	99.32	0.011	0.010	0.282	1.627	0.400	0.002	0.688	0.000	0.003	3.024	
Wsc14Q-1	chr	0.34	0.49	7.23	61.72	14.98	0.06	13.88	0.02		0.05	98.76	0.011	0.012	0.282	1.617	0.415	0.002	0.686	0.001	0.001	3.027	
Wsc14Q-2	chr	0.35	0.45	7.29	62.44	14.33	0.02	14.03	0.03		0.14	99.08	0.011	0.011	0.283	1.627	0.395	0.001	0.689	0.001	0.004	3.022	
Wsc14Q-3	chr	0.33	0.46	7.13	62.11	15.02	0.06	13.84	0.01		0.16	99.11	0.011	0.011	0.278	1.624	0.415	0.002	0.682	0.000	0.004	3.027	
Wsc14Q-4	chr	0.31	0.43	7.16	62.87	14.56	0.06	13.93	0.02		0.08	99.42	0.010	0.011	0.277	1.635	0.401	0.002	0.683	0.001	0.002	3.023	
Wsc14Q-1	chr	0.41	0.47	7.32	59.43	13.58	0.04	13.74	0.02		0.10	95.11	0.014	0.012	0.295	1.608	0.389	0.001	0.701	0.001	0.003	3.023	
Wsc14Q-2	chr	0.40	0.48	7.13	59.57	14.22	0.08	13.79	0.05		0.08	95.80	0.014	0.012	0.287	1.605	0.405	0.002	0.700	0.002	0.002	3.029	
Wsc14Q-3	chr	0.66	0.43	7.13	58.81	14.86	0.03	13.55	0.07		0.06	95.59	0.023	0.011	0.287	1.589	0.425	0.001	0.690	0.003	0.002	3.029	
Wsc14Q-4	chr	0.43	0.45	7.21	59.42	14.36	0.07	13.69	0.05		0.04	95.73	0.015	0.011	0.290	1.602	0.410	0.002	0.696	0.002	0.001	3.028	
Wsc14R-1	chr	0.28	0.48	7.09	61.87	15.22	0.03	13.61	0.00		0.13	98.70	0.009	0.012	0.278	1.626	0.423	0.001	0.675	0.000	0.003	3.027	
Wsc14R-2	chr	0.26	0.44	7.11	62.47	15.32	0.05	13.44	0.01		0.13	99.23	0.008	0.011	0.277	1.635	0.424	0.001	0.663	0.001	0.004	3.025	
Wsc14R-3	chr	0.31	0.39	7.14	62.52	14.89	0.00	13.71	0.00		0.15	99.10	0.010	0.010	0.278	1.634	0.412	0.000	0.676	0.000	0.004	3.024	
Wsc17A-1	chr	0.19	0.06	6.13	65.95	12.80	0.05	14.63	0.00		0.16	99.96	0.006	0.002	0.236	1.707	0.350	0.001	0.714	0.000	0.004	3.021	
Wsc17A-2	chr	0.26	0.09	6.22	65.12	12.75	0.01	14.58	0.00		0.16	99.19	0.009	0.002	0.241	1.696	0.351	0.000	0.716	0.000	0.004	3.020	
Wsc17B-1	chr	0.40	0.11	6.63	64.17	13.54	0.06	14.30	0.00		0.15	99.35	0.013	0.003	0.257	1.669	0.372	0.002	0.701	0.000	0.004	3.021	
Wsc17B-2	chr	0.39	0.11	6.64	64.35	14.06	0.07	14.59	0.01		0.10	100.30	0.013	0.003	0.255	1.659	0.383	0.002	0.709	0.000	0.003	3.027	
Wsc17B-3	chr	0.40	0.09	6.72	63.71	13.66	0.07	14.41	0.01		0.08	99.14	0.013	0.002	0.261	1.660	0.376	0.002	0.708	0.000	0.002	3.024	

Label	Min Phase	SiO_2	TiO_2	Al_2O_3	Cr_2O_3	FeO	MnO	MgO	CaO	Na_2O	NiO	Total	Si	Ti	Al	Cr	Fe	Mn	Mg	Ca	Ni	Total	Mg#
Wsc22A-1	chr	0.66	0.06	3.79	66.11	14.08	0.01	13.75	0.06		0.09	98.61	0.022	0.002	0.150	1.758	0.396	0.000	0.689	0.002	0.003	3.022	
Wsc22A-2	chr	0.56	0.05	3.82	66.94	13.74	0.05	13.87	0.05		0.09	99.17	0.019	0.001	0.150	1.769	0.384	0.001	0.691	0.002	0.002	3.020	
Wsc22A-3	chr	0.51	0.03	3.84	66.26	13.52	0.07	13.95	0.03		0.15	98.37	0.017	0.001	0.152	1.764	0.381	0.002	0.701	0.001	0.004	3.024	
Wsc22C-1	chr	0.22	0.03	4.07	68.73	12.74	0.08	14.09	0.02		0.14	100.10	0.007	0.001	0.158	1.796	0.352	0.002	0.694	0.001	0.004	3.015	
Wsc22C-2	chr	0.24	0.06	4.00	68.61	13.18	0.05	14.12	0.01		0.04	100.31	0.008	0.001	0.156	1.791	0.364	0.001	0.695	0.000	0.001	3.018	
Wsc22C-3	chr	0.25	0.08	4.01	68.96	12.98	0.00	14.04	0.02		0.11	100.46	0.008	0.002	0.156	1.797	0.358	0.000	0.690	0.001	0.003	3.014	
Wsc22D-1	chr	0.29	0.07	3.82	66.35	13.54	0.04	14.10	0.02		0.12	98.36	0.010	0.002	0.152	1.769	0.382	0.001	0.709	0.001	0.003	3.028	
Wsc22D-2	chr	0.31	0.09	3.67	66.24	13.83	0.00	13.55	0.05		0.07	97.81	0.010	0.002	0.147	1.780	0.393	0.000	0.687	0.002	0.002	3.024	
Wsc29A-1	chr	0.31	0.09	5.87	64.08	14.90	0.01	13.71	0.00		0.10	99.08	0.010	0.002	0.230	1.687	0.415	0.000	0.681	0.000	0.003	3.029	
Wsc29A-2	chr	0.23	0.09	6.04	65.39	13.99	0.05	13.92	0.00		0.10	99.81	0.007	0.002	0.235	1.704	0.385	0.001	0.684	0.000	0.003	3.021	
Wsc29A-3	chr	0.27	0.12	6.05	64.60	14.31	0.05	13.76	0.00		0.13	99.29	0.009	0.003	0.236	1.693	0.397	0.001	0.680	0.000	0.004	3.023	
Wsc29B-1	chr	0.31	0.13	6.11	64.40	13.89	0.03	13.89	0.00		0.17	98.93	0.010	0.003	0.239	1.690	0.386	0.001	0.688	0.000	0.004	3.022	
Wsc29B-2	chr	0.34	0.14	6.04	64.19	14.18	0.00	13.85	0.03		0.15	98.92	0.011	0.003	0.237	1.687	0.394	0.000	0.686	0.001	0.004	3.023	
Wsc29B-3	chr	0.35	0.12	6.01	64.85	13.95	0.04	14.06	0.02		0.17	99.56	0.012	0.003	0.234	1.692	0.385	0.001	0.692	0.001	0.005	3.023	
Wsc29C-1	chr	0.38	0.09	6.14	65.23	13.73	0.00	14.03	0.01		0.10	99.71	0.013	0.002	0.238	1.696	0.378	0.000	0.688	0.000	0.003	3.018	
Wsc29C-2	chr	0.35	0.15	6.14	65.48	13.49	0.00	14.24	0.04		0.11	100.01	0.011	0.004	0.237	1.696	0.370	0.000	0.696	0.002	0.003	3.018	
Wsc29C-3	chr	0.32	0.09	6.16	64.91	13.72	0.00	14.17	0.01		0.01	99.40	0.011	0.002	0.239	1.693	0.378	0.000	0.697	0.000	0.000	3.021	
Wsc29D-1	chr	0.40	0.09	5.97	63.95	14.85	0.03	13.65	0.02		0.18	99.14	0.013	0.002	0.234	1.681	0.413	0.001	0.677	0.001	0.005	3.027	
Wsc29D-2	chr	0.34	0.08	6.10	64.73	13.98	0.00	14.05	0.02		0.15	99.44	0.011	0.002	0.237	1.690	0.386	0.000	0.692	0.001	0.004	3.023	
Wsc29E-1	chr	0.46	0.10	5.82	63.21	15.20	0.08	13.47	0.08		0.13	98.54	0.015	0.003	0.230	1.675	0.426	0.002	0.673	0.003	0.003	3.030	
Wsc29F-1	chr	0.30	0.09	6.14	65.87	13.69	0.04	14.15	0.01		0.09	100.38	0.010	0.002	0.237	1.702	0.374	0.001	0.690	0.000	0.002	3.018	
Wsc29F-2	chr	0.28	0.09	6.04	65.08	13.94	0.01	13.95	0.00		0.14	99.52	0.009	0.002	0.235	1.699	0.385	0.000	0.687	0.000	0.004	3.021	
Wsc29F-3	chr	0.28	0.12	6.07	65.08	13.84	0.05	14.07	0.04		0.14	99.69	0.009	0.003	0.236	1.696	0.382	0.001	0.691	0.001	0.004	3.022	
Wsc29G-1	chr	0.43	0.09	6.10	64.97	13.11	0.03	14.34	0.04		0.12	99.23	0.014	0.002	0.237	1.693	0.361	0.001	0.705	0.001	0.003	3.018	
Wsc29G-2	chr	0.43	0.10	6.14	65.08	13.20	0.04	14.24	0.05		0.09	99.37	0.014	0.002	0.238	1.694	0.363	0.001	0.699	0.002	0.003	3.017	
Wsc31B-1	chr	0.26	0.03	6.66	64.53	13.34	0.00	14.22	0.03		0.07	99.13	0.009	0.001	0.259	1.682	0.368	0.000	0.699	0.001	0.002	3.019	
Wsc31B-2	chr	0.27	0.04	6.81	62.78	13.17	0.15	14.20	0.01		0.09	97.51	0.009	0.001	0.269	1.661	0.369	0.004	0.708	0.000	0.002	3.024	
Wsc31B-3	chr	0.34	0.05	6.58	64.43	13.77	0.01	13.98	0.01		0.13	99.30	0.011	0.001	0.256	1.679	0.380	0.000	0.687	0.000	0.003	3.018	
Wsc33A-1	chr	0.34	0.13	8.29	61.72	13.99	0.02	14.21	0.00		0.04	98.74	0.011	0.003	0.321	1.604	0.385	0.000	0.696	0.000	0.001	3.023	
Wsc33A-2	chr	0.30	0.12	8.23	62.07	14.00	0.07	14.05	0.00		0.12	98.96	0.010	0.003	0.318	1.612	0.385	0.002	0.688	0.000	0.003	3.022	
Wsc33A-3	chr	0.34	0.14	8.18	61.44	14.36	0.09	14.11	0.00		0.14	98.79	0.011	0.003	0.317	1.600	0.396	0.002	0.693	0.000	0.004	3.027	
Wsc36A-1	chr	0.21	0.07	6.08	65.45	13.12	0.04	14.60	0.00		0.09	99.64	0.007	0.002	0.235	1.700	0.360	0.001	0.715	0.000	0.002	3.023	
Wsc36A-2	chr	0.24	0.04	6.00	65.45	13.65	0.11	14.23	0.02		0.13	99.86	0.008	0.001	0.233	1.702	0.375	0.003	0.698	0.001	0.003	3.024	
Wsc36A-3	chr	0.21	0.08	6.07	65.18	13.26	0.07	14.49	0.00		0.09	99.45	0.007	0.002	0.236	1.698	0.365	0.002	0.712	0.000	0.002	3.024	
Wsc36D-1	chr	0.17	0.03	6.36	65.17	12.85	0.10	14.44	0.02		0.09	99.21	0.005	0.001	0.247	1.698	0.354	0.003	0.710	0.001	0.002	3.021	
Wsc36D-2	chr	0.15	0.03	6.27	65.15	13.29	0.01	14.19	0.00		0.09	99.18	0.005	0.001	0.244	1.702	0.367	0.000	0.699	0.000	0.002	3.021	
Wsc36E-1	chr	0.34	0.09	5.87	65.19	13.66	0.10	14.20	0.00		0.10	99.54	0.011	0.002	0.228	1.700	0.377	0.003	0.698	0.000	0.003	3.022	
Wsc36E-2	chr	0.38	0.08	5.98	64.93	13.14	0.09	14.30	0.01		0.08	99.00	0.013	0.002	0.233	1.698	0.364	0.003	0.705	0.000	0.002	3.020	
Wsc36E-3	chr	0.39	0.07	6.03	65.20	13.38	0.03	14.62	0.00		0.12	99.84	0.013	0.002	0.233	1.690	0.367	0.001	0.715	0.000	0.003	3.024	
Wsc36E-4	chr	0.41	0.09	6.10	65.55	13.09	0.10	14.40	0.00		0.09	99.84	0.014	0.002	0.236	1.698	0.359	0.003	0.704	0.000	0.002	3.017	
Wsc36H-1	chr	0.33	0.06	5.72	62.41	16.50	0.06	13.05	0.03		0.08	98.23	0.011	0.002	0.228	1.669	0.467	0.002	0.658	0.001	0.002	3.039	
Wsc36H-2	chr	0.37	0.02	5.81	63.16	16.32	0.00	13.40	0.04		0.15	99.26	0.012	0.000	0.229	1.668	0.456	0.000	0.668	0.001	0.004	3.039	
Wsc36I-1	chr	0.22	0.01	6.25	65.18	13.44	0.02	14.35	0.00		0.09	99.55	0.007	0.000	0.242	1.696	0.370	0.001	0.704	0.000	0.002	3.023	
Wsc36I-2	chr	0.22	0.05	6.26	64.82	13.23	0.02	14.37	0.01		0.08	99.05	0.007	0.001	0.244	1.694	0.366	0.001	0.708	0.000	0.002	3.023	
Wsc37A-1	chr	0.29	0.03	8.43	61.49	13.68	0.03	14.24	0.01		0.13	98.33	0.010	0.001	0.328	1.604	0.377	0.001	0.701	0.000	0.004	3.024	
Wsc37A-2	chr	0.32	0.03	8.40	60.63	14.30	0.02	13.87	0.00		0.09	97.67	0.011	0.001	0.329	1.595	0.398	0.001	0.688	0.000	0.003	3.026	
Wsc37A-3	chr	0.31	0.04	8.41	61.05	13.82	0.08	14.00	0.03		0.11	97.84	0.010	0.001	0.329	1.602	0.383	0.002	0.692	0.001	0.003	3.023	
Wsc37B-1	chr	0.51	0.02	7.46	61.82	15.26	0.05	13.83	0.02		0.08	99.07	0.017	0.000	0.291	1.615	0.421	0.002	0.681	0.001	0.002	3.030	
Wsc37B-2	chr	0.52	0.04	7.41	60.85	16.36	0.00	13.36	0.01		0.10	98.65	0.017	0.001	0.291	1.603	0.456	0.000	0.663	0.000	0.003	3.035	
Wsc37B-3	chr	0.47	0.06	7.60	60.76	15.31	0.04	13.60	0.01		0.13	97.98	0.016	0.001	0.299	1.605	0.428	0.001	0.677	0.000	0.003	3.031	
Wsc37C-1	chr	0.40	0.03	6.10	52.43	22.94	0.00	12.27	0.05		0.06	94.28	0.015	0.001	0.258	1.489	0.689	0.000	0.657	0.002	0.002	3.111	
Wsc37C-2	chr	0.24	0.03	6.31	53.86	21.49	0.08	12.80	0.03		0.05	94.89	0.008	0.001	0.264	1.511	0.638	0.003	0.677	0.001	0.001	3.104	
Wsc37C-1	chr	0.38	0.04	7.48	62.21	14.26	0.04	13.99	0.00		0.18	98.58	0.012	0.001	0.292	1.629	0.395	0.001	0.691	0.000	0.005	3.026	
Wsc37C-2	chr	0.43	0.04	7.59	61.75	14.32	0.02	13.84	0.01		0.09	98.10	0.014	0.001	0.298	1.623	0.398	0.001	0.686	0.001	0.002	3.024	
Wsc37C-3	chr	0.41	0.04	7.65	63.21	13.93	0.05	14.02	0.00		0.12	99.42	0.013	0.001	0.295	1.638	0.382	0.001	0.685	0.000	0.003	3.019	
Wsc37D-1	chr	0.44	0.07	8.37	62.27	13.12	0.01	14.44	0.00		0.13	98.85	0.014	0.002	0.323	1.611	0.359	0.000	0.705	0.000	0.003	3.017	
Wsc37D-2	chr	0.48	0.03	8.43	62.54	13.11	0.00	14.56	0.02		0.12	99.30	0.016	0.001	0.324	1.610	0.357	0.000	0.707	0.001	0.003	3.017	
Wsc37E-1	chr	0.28	0.07	8.31	62.73	12.33	0.04	14.82	0.02		0.06	98.67	0.009	0.002	0.320	1.622	0.337	0.001	0.723	0.001	0.002	3.018	

Label	Min Phase	SiO_2	TiO_2	Al_2O_3	Cr_2O_3	FeO	MnO	MgO	CaO	Na_2O	NiO	Total	Si	Ti	Al	Cr	Fe	Mn	Mg	Ca	Ni	Total	Mg#
Wsc38A-1	chr	0.29	0.09	6.29	65.26	13.61	0.06	14.25	0.01		0.16	100.01	0.009	0.002	0.243	1.691	0.373	0.002	0.696	0.000	0.004	3.021	
Wsc38A-2	chr	0.30	0.07	6.22	64.54	13.52	0.03	14.29	0.01		0.13	99.11	0.010	0.002	0.242	1.687	0.374	0.001	0.704	0.000	0.004	3.024	
Wsc38A-3	chr	0.28	0.05	6.29	64.97	13.53	0.06	14.41	0.00		0.09	99.69	0.009	0.001	0.243	1.688	0.372	0.002	0.706	0.000	0.002	3.024	
Wsc38B-1	chr	0.20	0.07	6.69	64.11	13.82	0.00	13.99	0.00		0.08	98.96	0.006	0.002	0.261	1.678	0.382	0.000	0.691	0.000	0.002	3.022	
Wsc38B-2	chr	0.21	0.07	6.72	64.39	14.19	0.01	14.08	0.00		0.08	99.74	0.007	0.002	0.260	1.673	0.390	0.000	0.690	0.000	0.002	3.025	
Wsc38B-3	chr	0.17	0.10	6.67	64.54	13.93	0.06	14.18	0.00		0.11	99.77	0.006	0.002	0.258	1.676	0.383	0.002	0.695	0.000	0.003	3.025	
Wsc38B-4	chr	0.21	0.09	6.73	64.37	13.86	0.08	14.07	0.00		0.15	99.56	0.007	0.002	0.261	1.675	0.381	0.002	0.690	0.000	0.004	3.023	
Wsc38C-1	chr	0.29	0.08	6.55	63.41	14.82	0.09	13.76	0.03		0.08	99.11	0.010	0.002	0.256	1.664	0.411	0.002	0.681	0.001	0.002	3.029	
Wsc38C-2	chr	0.24	0.05	6.55	63.26	15.49	0.02	13.81	0.02		0.15	99.58	0.008	0.001	0.255	1.656	0.429	0.001	0.681	0.001	0.004	3.035	
Wsc38C-3	chr	0.30	0.04	6.47	63.64	14.71	0.00	13.84	0.01		0.04	99.05	0.010	0.001	0.253	1.669	0.408	0.000	0.685	0.000	0.001	3.028	
Wsc38D-1	chr	0.18	0.09	6.22	64.87	13.42	0.05	13.98	0.00		0.14	98.96	0.006	0.002	0.243	1.700	0.372	0.001	0.691	0.000	0.004	3.020	
Wsc38D-2	chr	0.23	0.09	6.18	64.95	13.86	0.12	14.00	0.00		0.14	99.56	0.007	0.002	0.240	1.695	0.383	0.003	0.689	0.000	0.004	3.023	
Wsc38E-1	chr	0.26	0.07	6.54	64.88	13.72	0.12	14.38	0.00		0.12	100.09	0.008	0.002	0.252	1.679	0.375	0.003	0.702	0.000	0.003	3.025	
Wsc38E-2	chr	0.26	0.11	6.52	65.13	13.80	0.04	14.33	0.00		0.09	100.29	0.008	0.003	0.251	1.682	0.377	0.001	0.698	0.000	0.002	3.023	
Wsc38E-3	chr	0.24	0.06	6.55	65.81	13.44	0.05	14.29	0.01		0.07	100.51	0.008	0.001	0.251	1.695	0.366	0.001	0.694	0.000	0.002	3.018	
Wsc38G-1	chr	0.33	0.07	6.37	64.44	13.95	0.00	14.11	0.00		0.12	99.41	0.011	0.002	0.248	1.681	0.385	0.000	0.694	0.000	0.003	3.023	
Wsc38G-2	chr	0.27	0.09	6.29	64.24	14.15	0.04	14.23	0.02		0.13	99.46	0.009	0.002	0.245	1.676	0.391	0.001	0.700	0.001	0.003	3.028	
Wsc38G-3	chr	0.26	0.09	6.34	64.54	13.94	0.02	14.38	0.00		0.15	99.72	0.009	0.002	0.246	1.678	0.383	0.001	0.705	0.000	0.004	3.028	
Wsc39A-1	chr	0.31	0.04	7.00	64.17	14.33	0.08	13.80	0.00		0.18	99.91	0.010	0.001	0.271	1.665	0.393	0.002	0.675	0.000	0.005	3.021	
Wsc39A-2	chr	0.25	0.04	7.02	64.70	14.54	0.00	14.01	0.02		0.12	100.71	0.008	0.001	0.270	1.665	0.396	0.000	0.680	0.001	0.003	3.023	
Wsc39A-3	chr	0.30	0.05	7.05	64.79	14.11	0.05	14.09	0.02		0.10	100.57	0.010	0.001	0.270	1.667	0.384	0.002	0.683	0.001	0.003	3.020	
Wsc39B-1	chr	0.34	0.00	6.68	64.59	13.33	0.06	14.16	0.00		0.12	99.28	0.011	0.000	0.259	1.681	0.367	0.002	0.695	0.000	0.003	3.018	
Wsc39B-2	chr	0.48	0.05	6.72	64.39	13.52	0.02	14.39	0.02		0.17	99.76	0.016	0.001	0.259	1.666	0.370	0.000	0.702	0.001	0.005	3.020	
Wsc39B-3	chr	0.34	0.07	6.58	64.30	13.79	0.05	14.10	0.00		0.11	99.35	0.011	0.002	0.256	1.676	0.380	0.001	0.693	0.000	0.003	3.022	
Wsc39B-4	chr	0.37	0.05	6.69	64.98	13.39	0.03	14.32	0.00		0.14	99.98	0.012	0.001	0.258	1.679	0.366	0.001	0.698	0.000	0.004	3.018	
Wsc39B-1	chr	0.41	0.07	6.50	62.55	16.17	0.05	13.32	0.01		0.12	99.20	0.014	0.002	0.255	1.647	0.450	0.001	0.661	0.000	0.003	3.034	
Wsc39B-2	chr	0.60	0.08	6.30	60.62	17.70	0.06	12.93	0.02		0.14	98.46	0.020	0.002	0.250	1.616	0.499	0.002	0.650	0.001	0.004	3.044	
Wsc39B-3	chr	0.51	0.06	6.37	60.44	16.85	0.05	13.28	0.02		0.18	97.78	0.017	0.002	0.254	1.617	0.477	0.002	0.670	0.001	0.005	3.045	
Wsc39B-4	chr	0.47	0.04	6.34	60.55	17.47	0.05	12.88	0.02		0.11	97.93	0.016	0.001	0.253	1.623	0.495	0.001	0.651	0.001	0.003	3.045	
Wsc39C-1	chr	0.32	0.05	6.96	63.69	14.25	0.03	14.03	0.00		0.18	99.50	0.010	0.001	0.270	1.657	0.392	0.001	0.689	0.000	0.005	3.025	
Wsc39C-2	chr	0.32	0.03	6.81	64.05	14.32	0.02	14.17	0.03		0.14	99.89	0.011	0.001	0.263	1.661	0.393	0.001	0.693	0.001	0.004	3.027	
Wsc39C-3	chr	0.38	0.03	6.73	63.94	15.27	0.03	13.81	0.00		0.03	100.22	0.013	0.001	0.260	1.658	0.419	0.001	0.676	0.000	0.001	3.028	
Wsc39C-4	chr	0.32	0.03	6.76	63.81	14.81	0.05	13.84	0.01		0.06	99.68	0.011	0.001	0.263	1.662	0.408	0.001	0.680	0.000	0.001	3.027	
Wsc39D-1	chr	0.27	0.03	7.01	63.29	13.44	0.06	14.41	0.01		0.09	98.61	0.009	0.001	0.274	1.656	0.372	0.002	0.711	0.000	0.002	3.026	
Wsc39D-2	chr	0.24	0.06	7.03	63.43	13.31	0.03	14.45	0.01		0.07	98.64	0.008	0.001	0.274	1.658	0.368	0.001	0.712	0.000	0.002	3.025	
Wsc39E-1	chr	0.23	0.05	6.84	63.37	13.52	0.07	13.97	0.00		0.09	98.13	0.008	0.001	0.268	1.669	0.377	0.002	0.694	0.000	0.002	3.022	
Wsc39E-2	chr	0.23	0.03	6.98	63.42	13.79	0.03	14.06	0.02		0.06	98.61	0.008	0.001	0.273	1.663	0.382	0.001	0.695	0.001	0.002	3.024	
Wsc40A-1	chr	0.26	1.34	3.34	65.52	13.96	0.03	14.45	0.00		0.12	99.02	0.009	0.034	0.132	1.734	0.391	0.001	0.721	0.000	0.003	3.025	
Wsc40A-2	chr	0.28	1.29	3.41	65.98	14.81	0.00	13.94	0.00		0.07	99.78	0.009	0.032	0.134	1.739	0.413	0.000	0.693	0.000	0.002	3.022	
Wsc40A-3	chr	0.33	1.31	3.36	64.67	14.62	0.00	14.06	0.00		0.11	98.48	0.011	0.033	0.134	1.725	0.413	0.000	0.707	0.000	0.003	3.026	
Wsc40A-4	chr	0.25	1.36	3.36	66.05	14.58	0.06	14.20	0.01		0.10	99.98	0.008	0.034	0.132	1.736	0.405	0.002	0.704	0.000	0.003	3.024	
Wsc40B-1	chr	0.25	1.34	3.51	65.53	14.00	0.04	14.65	0.00		0.22	99.54	0.008	0.033	0.138	1.724	0.390	0.001	0.727	0.000	0.006	3.027	
Wsc40B-2	chr	0.36	1.33	3.45	65.04	14.46	0.00	14.48	0.00		0.15	99.27	0.012	0.033	0.136	1.718	0.404	0.000	0.721	0.000	0.004	3.028	
Wsc40B-3	chr	0.37	1.30	3.46	65.01	14.12	0.00	14.37	0.02		0.07	98.72	0.012	0.033	0.137	1.724	0.396	0.000	0.719	0.001	0.002	3.024	
Wsc40C-1	chr	0.30	1.33	3.65	66.94	12.11	0.09	14.94	0.02		0.15	99.53	0.010	0.033	0.142	1.749	0.335	0.003	0.736	0.001	0.004	3.012	
Wsc40C-2	chr	0.37	1.37	3.59	67.59	11.94	0.00	15.16	0.01		0.07	100.11	0.012	0.034	0.139	1.752	0.327	0.000	0.741	0.000	0.002	3.008	
Wsc40D-1	chr	0.36	1.33	3.44	66.83	12.63	0.05	14.62	0.00		0.15	99.42	0.012	0.033	0.135	1.753	0.350	0.001	0.723	0.000	0.004	3.011	
Wsc40D-2	chr	0.33	1.35	3.47	66.86	12.68	0.06	14.52	0.02		0.11	99.41	0.011	0.034	0.136	1.754	0.352	0.002	0.718	0.001	0.003	3.010	
Wsc41A-1	chr	0.25	0.02	5.54	66.31	12.75	0.05	14.45	0.01		0.15	99.52	0.008	0.001	0.215	1.728	0.351	0.001	0.710	0.000	0.004	3.019	
Wsc41A-2	chr	0.24	0.02	5.50	67.15	12.93	0.00	14.45	0.02		0.11	100.42	0.008	0.000	0.212	1.736	0.354	0.000	0.704	0.001	0.003	3.018	
Wsc41A-3	chr	0.21	0.01	5.47	66.28	12.93	0.16	14.51	0.00		0.14	99.71	0.007	0.000	0.212	1.726	0.356	0.004	0.713	0.000	0.004	3.023	
Wsc41B-1	chr	0.20	0.01	5.44	66.44	12.33	0.04	14.66	0.00		0.02	99.14	0.007	0.000	0.212	1.736	0.341	0.001	0.722	0.000	0.001	3.019	
Wsc41B-2	chr	0.22	0.03	5.52	65.77	12.47	0.06	14.44	0.00		0.11	98.63	0.007	0.001	0.216	1.728	0.347	0.002	0.716	0.000	0.003	3.020	
Wsc41C-1	chr	0.23	0.01	5.33	67.32	13.22	0.06	14.32	0.02		0.05	100.56	0.008	0.000	0.205	1.741	0.362	0.002	0.699	0.001	0.001	3.019	
Wsc41C-2	chr	0.22	0.03	5.31	66.37	13.12	0.07	14.35	0.01		0.13	99.62	0.007	0.001	0.207	1.733	0.362	0.002	0.706	0.000	0.003	3.022	
Wsc41C-3	chr	0.24	0.04	5.19	66.11	13.26	0.03	14.26	0.01		0.11	99.24	0.008	0.001	0.203	1.734	0.368	0.001	0.705	0.000	0.003	3.023	
Wsc41D-1	chr	0.29	0.04	5.36	66.15	13.26	0.02	14.39	0.00		0.10	99.61	0.010	0.001	0.209	1.726	0.366	0.001	0.708	0.000	0.003	3.022	
Wsc41D-2	chr	0.20	0.01	5.49	66.24	13.02	0.04	14.54	0.00		0.10	99.64	0.007	0.000	0.213	1.726	0.359	0.001	0.715	0.000	0.003	3.024	
Wsc41D-3	chr	0.22	0.02	5.45	66.66	12.82	0.05	14.66	0.00		0.03	99.90	0.007	0.000	0.211	1.731	0.352	0.001	0.718	0.000	0.001	3.022	

Label	Min Phase	SiO_2	TiO_2	Al_2O_3	Cr_2O_3	FeO	MnO	MgO	CaO	Na_2O	NiO	Total	Si	Ti	Al	Cr	Fe	Mn	Mg	Ca	Ni	Total	Mg#
Wsc41E-1	chr	0.36	0.06	5.41	66.51	12.39	0.06	14.48	0.00		0.13	99.39	0.012	0.001	0.210	1.734	0.342	0.002	0.712	0.000	0.003	3.015	
Wsc41E-2	chr	0.35	0.02	5.61	66.47	12.22	0.05	14.60	0.00		0.09	99.42	0.012	0.001	0.217	1.729	0.336	0.001	0.716	0.000	0.002	3.015	
Wsc41G-1	chr	0.30	0.00	5.31	65.99	12.89	0.04	14.49	0.03		0.06	99.11	0.010	0.000	0.207	1.728	0.357	0.001	0.716	0.001	0.002	3.022	
Wsc41G-2	chr	0.32	0.03	5.28	65.99	13.10	0.00	14.24	0.02		0.11	99.09	0.011	0.001	0.207	1.731	0.363	0.000	0.704	0.001	0.003	3.020	
Wsc41H-1	chr	0.21	0.00	5.56	67.11	12.59	0.05	14.57	0.00		0.04	100.13	0.007	0.000	0.215	1.737	0.345	0.001	0.711	0.000	0.001	3.017	
Wsc41I-1	chr	0.25	0.00	5.35	66.78	13.04	0.04	14.41	0.00		0.10	99.98	0.008	0.000	0.207	1.736	0.358	0.001	0.706	0.000	0.003	3.020	
Wsc41I-2	chr	0.21	0.02	5.39	66.78	12.92	0.03	14.27	0.01		0.12	99.76	0.007	0.001	0.209	1.740	0.356	0.001	0.701	0.000	0.003	3.018	
Wsc41M-1	chr	0.26	0.05	5.48	66.04	12.66	0.00	14.66	0.00		0.05	99.21	0.009	0.001	0.213	1.725	0.350	0.000	0.722	0.000	0.001	3.021	
Wsc41M-2	chr	0.27	0.06	5.50	65.25	13.10	0.16	14.43	0.02		0.05	98.85	0.009	0.002	0.215	1.714	0.364	0.004	0.715	0.001	0.001	3.025	
Wsc43B-1	chr	0.51	0.03	4.95	63.52	15.92	0.13	12.85	0.01		0.13	98.06	0.017	0.001	0.198	1.704	0.452	0.004	0.650	0.000	0.004	3.031	
Wsc43B-2	chr	1.00	0.06	4.75	60.50	18.11	0.07	12.24	0.06		0.11	96.92	0.035	0.002	0.193	1.651	0.523	0.002	0.630	0.002	0.003	3.041	
Wsc43B-3	chr	2.60	0.02	5.28	49.13	25.22	0.02	9.79	0.27		0.18	92.50	0.095	0.000	0.228	1.426	0.774	0.001	0.536	0.011	0.005	3.077	
Wsc43B-1	chr	0.30	0.06	4.96	63.20	15.32	0.07	12.96	0.02		0.10	96.99	0.010	0.001	0.200	1.712	0.439	0.002	0.662	0.001	0.003	3.031	
Wsc43B-2	chr	0.28	0.05	5.06	62.74	15.04	0.09	13.07	0.00		0.07	96.41	0.010	0.001	0.205	1.707	0.433	0.003	0.671	0.000	0.002	3.032	
Wsc43C-1	chr	0.38	0.06	5.21	65.68	14.91	0.02	13.53	0.03		0.11	99.92	0.013	0.001	0.203	1.721	0.413	0.001	0.668	0.001	0.003	3.024	
Wsc43C-2	chr	0.44	0.04	5.27	65.32	14.86	0.05	13.57	0.02		0.11	99.67	0.015	0.001	0.206	1.714	0.412	0.001	0.671	0.001	0.003	3.024	
Wsc48A-1	chr	0.23	0.22	7.67	63.48	12.95	0.01	14.84	0.00		0.12	99.52	0.007	0.006	0.295	1.636	0.353	0.000	0.721	0.000	0.003	3.022	
Wsc48A-2	chr	0.24	0.22	7.68	63.03	12.80	0.00	14.93	0.01		0.13	99.03	0.008	0.005	0.296	1.631	0.350	0.000	0.729	0.000	0.003	3.023	
Wsc48B-1	chr	0.34	0.25	7.64	63.44	12.51	0.00	14.96	0.00		0.15	99.30	0.011	0.006	0.294	1.635	0.341	0.000	0.727	0.000	0.004	3.018	
Wsc48B-2	chr	0.35	0.20	7.61	62.73	12.99	0.00	14.76	0.02		0.16	98.82	0.012	0.005	0.294	1.628	0.357	0.000	0.722	0.001	0.004	3.022	
Wsc48C-1	chr	0.38	0.20	7.38	63.49	12.34	0.07	15.12	0.04		0.12	99.15	0.012	0.005	0.284	1.639	0.337	0.002	0.736	0.001	0.003	3.021	
Wsc48D-1	chr	0.54	0.20	7.07	64.37	12.14	0.00	14.93	0.07		0.05	99.36	0.018	0.005	0.272	1.659	0.331	0.000	0.725	0.002	0.001	3.012	
Wsc48D-2	chr	0.52	0.25	7.25	64.70	12.05	0.00	14.94	0.05		0.05	99.81	0.017	0.006	0.277	1.658	0.327	0.000	0.722	0.002	0.001	3.010	
Wsc48D-3	chr	0.44	0.20	7.19	64.89	12.15	0.03	14.85	0.02		0.06	99.83	0.014	0.005	0.275	1.665	0.330	0.001	0.719	0.001	0.002	3.011	
Wsc48E-1	chr	0.38	0.24	7.34	63.74	12.09	0.04	15.04	0.03		0.07	98.96	0.012	0.006	0.283	1.648	0.331	0.001	0.733	0.001	0.002	3.017	
Wsc48E-2	chr	0.40	0.24	7.27	64.58	11.90	0.07	15.28	0.03		0.12	99.88	0.013	0.006	0.278	1.654	0.322	0.002	0.738	0.001	0.003	3.016	
Wsc48F-1	chr	0.24	0.23	7.97	61.90	13.85	0.00	14.46	0.02		0.20	98.86	0.008	0.006	0.309	1.609	0.381	0.000	0.709	0.001	0.005	3.027	
Wsc48F-2	chr	0.26	0.20	8.04	61.02	13.48	0.00	14.51	0.00		0.10	97.61	0.009	0.005	0.315	1.603	0.375	0.000	0.719	0.000	0.003	3.027	
Wsc48G-1	chr	0.31	0.23	7.36	63.78	12.57	0.04	14.97	0.01		0.09	99.37	0.010	0.006	0.283	1.645	0.343	0.001	0.729	0.000	0.002	3.020	
Wsc48G-2	chr	0.29	0.23	7.47	63.96	12.49	0.07	14.94	0.01		0.11	99.57	0.009	0.006	0.287	1.646	0.340	0.002	0.725	0.000	0.003	3.018	
Wsc48G-3	chr	0.34	0.17	7.46	64.22	12.55	0.05	14.92	0.02		0.06	99.77	0.011	0.004	0.286	1.650	0.341	0.001	0.723	0.001	0.002	3.017	
Wsc50A-1	chr	0.44	0.12	5.61	65.00	14.41	0.06	14.30	0.00		0.17	100.10	0.015	0.003	0.217	1.690	0.396	0.002	0.701	0.000	0.004	3.029	
Wsc50A-2	chr	0.45	0.11	5.58	64.92	14.75	0.03	14.02	0.00		0.09	99.95	0.015	0.003	0.217	1.693	0.407	0.001	0.690	0.000	0.003	3.028	
Wsc50A-3	chr	0.42	0.11	5.46	63.98	15.02	0.04	14.05	0.02		0.12	99.21	0.014	0.003	0.214	1.684	0.418	0.001	0.697	0.001	0.003	3.034	
Wsc50B-1	chr	0.42	0.13	5.66	66.50	13.03	0.00	14.62	0.05		0.08	100.48	0.014	0.003	0.218	1.714	0.355	0.000	0.710	0.002	0.002	3.017	
Wsc50B-2	chr	0.33	0.11	5.62	66.01	13.38	0.00	14.50	0.04		0.16	100.15	0.011	0.003	0.217	1.711	0.367	0.000	0.709	0.001	0.004	3.022	
Wsc52B-1	chr	0.39	0.06	5.18	66.10	13.95	0.10	13.95	0.01		0.07	99.80	0.013	0.001	0.202	1.727	0.385	0.003	0.687	0.000	0.002	3.021	
Wsc52B-2	chr	0.39	0.04	5.18	65.95	14.25	0.00	13.91	0.00		0.11	99.82	0.013	0.001	0.202	1.725	0.394	0.000	0.686	0.000	0.003	3.023	
Wsc52B-3	chr	0.39	0.04	5.15	65.37	14.12	0.06	14.02	0.00		0.10	99.25	0.013	0.001	0.202	1.718	0.393	0.002	0.695	0.000	0.003	3.026	
Wsc52C-1	chr	0.21	0.06	5.13	66.31	13.77	0.07	13.74	0.01		0.11	99.41	0.007	0.002	0.201	1.742	0.382	0.002	0.681	0.000	0.003	3.020	
Wsc52C-2	chr	0.27	0.06	5.13	65.73	14.10	0.08	13.83	0.00		0.02	99.23	0.009	0.002	0.201	1.730	0.393	0.002	0.686	0.000	0.001	3.024	
Wsc52C-3	chr	0.26	0.07	5.10	66.02	13.64	0.06	13.84	0.00		0.04	99.03	0.009	0.002	0.200	1.739	0.380	0.002	0.687	0.000	0.001	3.020	
Wsc52E-1	chr	0.21	0.06	5.35	65.43	14.39	0.08	13.89	0.00		0.11	99.52	0.007	0.002	0.209	1.718	0.399	0.002	0.688	0.000	0.003	3.028	
Wsc52E-2	chr	0.18	0.05	5.38	65.36	14.89	0.03	13.75	0.00		0.07	99.71	0.006	0.001	0.210	1.715	0.413	0.001	0.681	0.000	0.002	3.030	
Wsc52E-3	chr	0.20	0.09	5.25	66.03	14.45	0.01	13.88	0.00		0.07	99.97	0.007	0.002	0.205	1.726	0.399	0.000	0.684	0.000	0.002	3.026	
Wsc52E-4	chr	0.22	0.04	5.21	64.91	14.65	0.02	13.65	0.01		0.14	98.85	0.007	0.001	0.206	1.719	0.410	0.000	0.682	0.000	0.004	3.030	
Wsc56A-1	chr	0.32	0.03	7.78	63.84	13.41	0.00	14.72	0.03		0.10	100.22	0.011	0.001	0.297	1.636	0.363	0.000	0.711	0.001	0.003	3.022	
Wsc56A-2	chr	0.31	0.00	7.83	64.14	13.16	0.04	14.68	0.02		0.10	100.28	0.010	0.000	0.299	1.642	0.356	0.001	0.709	0.001	0.003	3.020	
Wsc56C-1	chr	0.34	0.05	7.70	63.69	12.96	0.00	14.55	0.04		0.13	99.46	0.011	0.001	0.296	1.643	0.354	0.000	0.708	0.001	0.003	3.018	
Wsc56C-2	chr	0.50	0.02	7.57	63.50	12.90	0.04	14.67	0.08		0.07	99.35	0.016	0.001	0.291	1.639	0.352	0.001	0.714	0.003	0.002	3.018	
Wsc56D-1	chr	0.28	0.05	7.54	63.61	13.98	0.00	14.24	0.00		0.10	99.80	0.009	0.001	0.290	1.643	0.382	0.000	0.694	0.000	0.003	3.023	
Wsc56D-2	chr	0.30	0.04	7.49	63.83	13.89	0.03	14.51	0.03		0.11	100.23	0.010	0.001	0.287	1.641	0.378	0.001	0.703	0.001	0.003	3.025	
Wsc56D-3	chr	0.31	0.02	7.42	63.00	14.05	0.00	14.45	0.03		0.14	99.42	0.010	0.000	0.287	1.634	0.385	0.000	0.707	0.001	0.004	3.029	
Wsc56F-1	chr	0.42	0.04	7.73	62.70	13.11	0.05	14.51	0.03		0.11	98.70	0.014	0.001	0.299	1.630	0.360	0.001	0.711	0.001	0.003	3.021	
Wsc56F-2	chr	0.42	0.05	7.69	63.44	13.20	0.08	14.54	0.07		0.06	99.55	0.014	0.001	0.295	1.636	0.360	0.002	0.707	0.003	0.002	3.020	
Wsc63A-1	chr	0.25	0.07	5.91	64.22	15.43	0.00	13.03	0.02		0.12	99.05	0.008	0.002	0.233	1.697	0.431	0.000	0.649	0.001	0.003	3.025	
Wsc63B-1	chr	0.33	0.10	6.30	63.87	15.50	0.02	12.97	0.01		0.17	99.26	0.011	0.002	0.247	1.681	0.431	0.001	0.644	0.000	0.004	3.022	
Wsc63F-1	chr	0.25	0.04	5.65	63.90	15.39	0.06	13.05	0.01		0.11	98.43	0.008	0.001	0.224	1.701	0.433	0.002	0.655	0.000	0.003	3.028	
Wsc63F-2	chr	0.22	0.04	5.56	64.81	15.67	0.01	13.03	0.02		0.17	99.53	0.008	0.001	0.219	1.709	0.437	0.000	0.648	0.001	0.004	3.027	
Wsc63F-3	chr	0.32	0.05	5.54	63.90	15.66	0.07	12.96	0.04		0.11	98.65	0.011	0.001	0.220	1.700	0.441	0.002	0.650	0.001	0.003	3.028	

Label	Min Phase	SiO_2	TiO_2	Al_2O_3	Cr_2O_3	FeO	MnO	MgO	CaO	Na_2O	NiO	Total	Si	Ti	Al	Cr	Fe	Mn	Mg	Ca	Ni	Total	Mg#
Wsc03F-1	ol	40.81		0.02	0.08	6.94	0.08	51.20	0.02		0.33	99.48	0.994		0.000	0.002	0.141	0.002	1.859	0.001	0.006	3.005	92.94
Wsc03F-2	ol	40.77		0.02	0.04	6.82	0.08	51.16	0.03		0.34	99.26	0.995		0.001	0.001	0.139	0.002	1.861	0.001	0.007	3.005	93.04
Wsc03C-1	ol	41.31		0.02	0.01	6.66	0.09	52.15	0.01		0.34	100.59	0.993		0.001	0.000	0.134	0.002	1.870	0.000	0.007	3.006	93.32
Wsc03C-2	ol	41.01		0.01	0.01	7.10	0.12	51.62	0.01		0.31	100.20	0.992		0.000	0.000	0.144	0.002	1.862	0.000	0.006	3.007	92.84
Wsc03C-3	ol	40.74		0.02	0.07	6.59	0.10	51.91	0.00		0.37	99.81	0.988		0.001	0.001	0.134	0.002	1.878	0.000	0.007	3.011	93.35
Wsc04A-1	ol	41.16		0.00	0.01	7.83	0.12	50.33	0.03		0.36	99.84	1.002		0.000	0.000	0.159	0.002	1.826	0.001	0.007	2.998	91.97
Wsc04A-2	ol	41.06		0.01	0.04	7.80	0.10	50.82	0.02		0.33	100.18	0.996		0.000	0.001	0.158	0.002	1.838	0.001	0.007	3.003	92.07
Wsc04B-1	ol	41.73		0.01	0.02	7.72	0.11	50.61	0.02		0.42	100.63	1.007		0.000	0.000	0.156	0.002	1.820	0.001	0.008	2.993	92.12
Wsc04B-2	ol	41.10		0.02	0.04	7.48	0.11	50.74	0.05		0.38	99.92	0.999		0.001	0.001	0.152	0.002	1.838	0.001	0.007	3.001	92.36
Wsc04B-3	ol	41.66		0.00	0.01	7.84	0.12	50.77	0.02		0.37	100.79	1.004		0.000	0.000	0.158	0.002	1.824	0.000	0.007	2.996	92.03
Wsc04C-1	ol	39.36		0.01	0.02	6.69	0.10	48.72	0.02		0.27	95.19	1.001		0.000	0.000	0.142	0.002	1.847	0.001	0.006	2.999	92.85
Wsc04C-2	ol	39.13		0.00	0.01	6.59	0.08	48.33	0.03		0.28	94.45	1.002		0.000	0.000	0.141	0.002	1.846	0.001	0.006	2.998	92.90
Wsc04C-3	ol	38.86		0.02	0.01	6.70	0.08	48.47	0.03		0.35	94.53	0.996		0.001	0.000	0.144	0.002	1.852	0.001	0.007	3.003	92.81
Wsc04C-4	ol	39.55		0.01	0.01	6.71	0.13	48.49	0.03		0.32	95.24	1.005		0.000	0.000	0.143	0.003	1.837	0.001	0.006	2.995	92.80
Wsc04C-1	ol	40.76		0.00	0.01	7.89	0.12	50.61	0.04		0.37	99.80	0.994		0.000	0.000	0.161	0.003	1.840	0.001	0.007	3.006	91.95
Wsc04C-2	ol	40.69		0.01	0.01	7.89	0.08	50.69	0.03		0.31	99.70	0.993		0.000	0.000	0.161	0.002	1.844	0.001	0.006	3.007	91.97
Wsc04C-3	ol	40.61		0.01	0.04	7.66	0.11	51.19	0.01		0.31	99.94	0.988		0.000	0.001	0.156	0.002	1.857	0.000	0.006	3.011	92.26
Wsc04D-1	ol	40.96		0.06	0.00	7.54	0.11	50.19	0.07		0.40	99.34	1.001		0.002	0.000	0.154	0.002	1.829	0.002	0.008	2.998	92.23
Wsc04D-2	ol	41.04		0.06	0.01	7.63	0.10	49.67	0.07		0.36	98.93	1.007		0.002	0.000	0.157	0.002	1.816	0.002	0.007	2.992	92.06
Wsc04E-1	ol	41.07		0.02	0.04	7.69	0.12	51.22	0.01		0.36	100.52	0.993		0.001	0.001	0.155	0.002	1.847	0.000	0.007	3.006	92.24
Wsc04E-2	ol	41.05		0.00	0.02	7.71	0.11	50.97	0.04		0.36	100.26	0.995		0.000	0.000	0.156	0.002	1.842	0.001	0.007	3.005	92.18
Wsc04E-3	ol	40.84		0.03	0.01	8.17	0.11	50.59	0.02		0.36	100.13	0.994		0.001	0.000	0.166	0.002	1.835	0.001	0.007	3.006	91.69
Wsc07A-1	ol	40.86		0.02	0.08	7.03	0.12	51.55	0.03		0.36	100.04	0.991		0.001	0.002	0.142	0.002	1.863	0.001	0.007	3.008	92.90
Wsc07A-2	ol	40.98		0.00	0.08	6.88	0.07	51.52	0.05		0.41	99.98	0.993		0.000	0.002	0.139	0.002	1.861	0.001	0.008	3.006	93.04
Wsc07A-3	ol	40.94		0.04	0.06	6.91	0.10	51.34	0.05		0.33	99.77	0.994		0.001	0.001	0.140	0.002	1.858	0.001	0.006	3.005	92.98
Wsc07A-4	ol	40.96		0.01	0.08	7.01	0.11	51.80	0.04		0.35	100.35	0.990		0.000	0.002	0.142	0.002	1.866	0.001	0.007	3.009	92.95
Wsc08A-1	ol	41.83		0.03	0.09	6.15	0.09	51.97	0.02		0.25	100.42	1.003		0.001	0.002	0.123	0.002	1.859	0.001	0.005	2.995	93.77
Wsc08A-2	ol	41.53		0.03	0.09	6.46	0.11	52.37	0.01		0.39	100.98	0.994		0.001	0.002	0.129	0.002	1.869	0.000	0.007	3.005	93.53
Wsc08A-3	ol	41.27		0.01	0.11	6.08	0.12	52.30	0.00		0.31	100.20	0.994		0.000	0.002	0.122	0.002	1.878	0.000	0.006	3.005	93.88
Wsc09B-1	ol	41.06		0.01	0.24	6.99	0.16	51.14	0.01		0.31	99.92	0.996		0.000	0.005	0.142	0.003	1.849	0.000	0.006	3.002	92.88
Wsc09B-2	ol	40.54		0.01	0.30	7.71	0.08	50.03	0.06		0.32	99.04	0.996		0.000	0.006	0.158	0.002	1.832	0.001	0.006	3.001	92.04
Wsc13E-1	ol	40.52		0.02	0.07	8.00	0.17	50.70	0.05		0.33	99.87	0.989		0.001	0.001	0.163	0.004	1.845	0.001	0.006	3.010	91.87
Wsc13E-2	ol	40.57		0.01	0.07	7.80	0.08	50.94	0.07		0.37	99.93	0.989		0.000	0.001	0.159	0.002	1.850	0.002	0.007	3.011	92.09
Wsc13E-3	ol	40.60		0.02	0.08	8.00	0.05	50.63	0.04		0.33	99.75	0.991		0.001	0.002	0.163	0.001	1.843	0.001	0.007	3.008	91.86
Wsc13E-4	ol	40.76		0.05	0.08	7.37	0.14	50.75	0.08		0.37	99.58	0.994		0.001	0.001	0.150	0.003	1.845	0.002	0.007	3.005	92.46
Wsc13E-5	ol	40.85		0.00	0.08	7.52	0.08	50.81	0.03		0.33	99.69	0.995		0.000	0.002	0.153	0.002	1.845	0.001	0.006	3.004	92.33
Wsc13F-1	ol	39.52		0.17	0.08	8.68	0.12	47.23	0.25		0.35	96.41	1.002		0.005	0.002	0.184	0.003	1.785	0.007	0.007	2.995	90.66
Wsc13F-2	ol	40.19		0.12	0.05	8.24	0.11	48.99	0.14		0.34	98.18	0.998		0.004	0.001	0.171	0.002	1.814	0.004	0.007	3.000	91.38
Wsc13F-3	ol	40.39		0.10	0.04	7.93	0.11	49.23	0.12		0.26	98.19	1.001		0.003	0.001	0.164	0.002	1.818	0.003	0.005	2.997	91.71
Wsc13F-1	ol	41.07		0.03	0.07	7.83	0.09	50.87	0.04		0.34	100.34	0.995		0.001	0.001	0.159	0.002	1.838	0.001	0.007	3.004	92.06
Wsc13F-2	ol	40.91		0.01	0.05	7.43	0.12	50.25	0.07		0.37	99.22	1.001		0.000	0.001	0.152	0.002	1.833	0.002	0.007	2.999	92.34
Wsc13F-3	ol	41.31		0.02	0.06	7.59	0.15	50.79	0.04		0.31	100.26	1.000		0.000	0.001	0.154	0.003	1.833	0.001	0.006	2.999	92.27
Wsc14C-1	ol	41.49		0.01	0.07	7.16	0.11	51.38	0.03		0.35	100.59	0.999		0.000	0.001	0.144	0.002	1.845	0.001	0.007	3.000	92.75
Wsc14C-2	ol	41.34		0.03	0.10	7.15	0.13	51.47	0.04		0.33	100.60	0.996		0.001	0.002	0.144	0.003	1.849	0.001	0.006	3.002	92.78
Wsc14C-3	ol	41.25		0.02	0.13	7.03	0.14	51.64	0.01		0.33	100.55	0.994		0.000	0.002	0.142	0.003	1.856	0.000	0.006	3.004	92.90
Wsc14D-1	ol	41.14		0.02	0.08	6.94	0.10	51.13	0.02		0.39	99.82	0.998		0.001	0.001	0.141	0.002	1.850	0.001	0.008	3.001	92.93
Wsc14D-2	ol	41.16		0.02	0.09	7.18	0.11	51.01	0.03		0.31	99.90	0.999		0.001	0.002	0.146	0.002	1.845	0.001	0.006	3.000	92.68
Wsc14D-3	ol	40.98		0.01	0.09	7.10	0.16	50.82	0.01		0.35	99.52	0.998		0.000	0.002	0.145	0.003	1.845	0.000	0.007	3.001	92.73
Wsc14T-1	ol	41.43		0.02	0.10	6.83	0.06	51.23	0.04		0.33	100.05	1.001		0.001	0.002	0.138	0.001	1.846	0.001	0.006	2.997	93.04
Wsc14T-2	ol	41.49		0.03	0.04	6.78	0.09	51.04	0.02		0.35	99.84	1.005		0.001	0.001	0.137	0.002	1.842	0.000	0.007	2.995	93.06
Wsc14V-1	ol	41.27		0.00	0.06	6.97	0.08	51.16	0.03		0.27	99.85	1.000		0.000	0.001	0.141	0.002	1.848	0.001	0.005	2.999	92.90
Wsc14V-2	ol	41.10		0.00	0.03	6.99	0.09	50.93	0.03		0.38	99.55	1.000		0.000	0.001	0.142	0.002	1.847	0.001	0.007	3.000	92.86
Wsc14V-3	ol	41.26		0.01	0.10	7.06	0.13	51.11	0.03		0.31	100.00	0.999		0.000	0.002	0.143	0.003	1.846	0.001	0.006	2.999	92.81
Wsc16A-1	ol	40.67		0.01	0.06	7.58	0.11	50.47	0.05		0.33	99.29	0.996		0.000	0.001	0.155	0.002	1.842	0.001	0.007	3.004	92.23
Wsc16A-2	ol	40.69		0.02	0.05	7.89	0.11	50.19	0.04		0.34	99.33	0.997		0.001	0.001	0.162	0.002	1.833	0.001	0.007	3.003	91.89
Wsc16A-3	ol	40.78		0.01	0.09	7.71	0.06	50.57	0.02		0.36	99.59	0.995		0.000	0.002	0.157	0.001	1.840	0.000	0.007	3.004	92.12
Wsc16A-4	ol	40.93		0.00	0.06	7.47	0.12	50.59	0.04		0.35	99.55	0.998		0.000	0.001	0.152	0.003	1.839	0.001	0.007	3.001	92.35
Wsc16A-5	ol	40.70		0.02	0.06	7.55	0.10	50.83	0.04		0.30	99.60	0.993		0.000	0.001	0.154	0.002	1.849	0.001	0.006	3.006	92.31
Wsc16B-1	ol	40.87		0.01	0.06	7.60	0.07	50.71	0.03		0.38	99.72	0.996		0.000	0.001	0.155	0.001	1.842	0.001	0.008	3.003	92.25
Wsc16B-2	ol	40.75		0.00	0.02	8.11	0.10	49.99	0.05		0.34	99.36	0.998		0.000	0.000	0.166	0.002	1.826	0.001	0.007	3.001	91.66
Wsc16C-1	ol	41.08		0.00	0.07	7.62	0.13	50.78	0.03		0.42	100.13	0.997		0.000	0.001	0.155	0.003	1.838	0.001	0.008	3.002	92.24
Wsc16C-2	ol	41.01		0.02	0.07	7.68	0.09	50.59	0.07		0.33	99.85	0.998		0.001	0.001	0.156	0.002	1.835	0.002	0.006	3.001	92.15

Label	Min Phase	SiO_2	TiO_2	Al_2O_3	Cr_2O_3	FeO	MnO	MgO	CaO	Na_2O	NiO	Total	Si	Ti	Al	Cr	Fe	Mn	Mg	Ca	Ni	Total	Mg#
Wsc18B-1	ol	41.22		0.03	0.12	6.90	0.08	51.56	0.02		0.38	100.31	0.995		0.001	0.002	0.139	0.002	1.856	0.000	0.007	3.003	93.02
Wsc18B-2	ol	41.42		0.01	0.16	6.51	0.12	51.60	0.03		0.39	100.25	0.999		0.000	0.003	0.131	0.002	1.855	0.001	0.008	2.999	93.39
Wsc18B-3	ol	41.21		0.02	0.05	6.53	0.04	51.76	0.01		0.33	99.95	0.996		0.001	0.001	0.132	0.001	1.866	0.000	0.006	3.003	93.39
Wsc18B-4	ol	41.21		0.03	0.03	6.27	0.10	51.78	0.02		0.39	99.84	0.997		0.001	0.001	0.127	0.002	1.867	0.000	0.008	3.002	93.64
Wsc18C-1	ol	41.23		0.00	0.05	6.63	0.12	51.56	0.02		0.34	99.94	0.998		0.000	0.001	0.134	0.002	1.860	0.000	0.007	3.002	93.27
Wsc18C-2	ol	40.83		0.02	0.09	6.93	0.10	51.77	0.01		0.34	100.09	0.989		0.001	0.002	0.140	0.002	1.869	0.000	0.007	3.010	93.02
Wsc18D-1	ol	41.18		0.03	0.06	6.60	0.08	51.48	0.02		0.29	99.73	0.998		0.001	0.001	0.134	0.002	1.860	0.000	0.006	3.001	93.29
Wsc18D-2	ol	41.17		0.03	0.07	6.38	0.09	51.76	0.02		0.31	99.84	0.996		0.001	0.001	0.129	0.002	1.867	0.001	0.006	3.003	93.53
Wsc19A-1	ol	41.43		0.02	0.04	7.52	0.09	51.20	0.04		0.32	100.66	0.999		0.001	0.001	0.152	0.002	1.840	0.001	0.006	3.001	92.39
Wsc19A-2	ol	41.54		0.03	0.05	7.17	0.09	51.23	0.02		0.36	100.48	1.001		0.001	0.001	0.145	0.002	1.841	0.001	0.007	2.998	92.72
Wsc19A-3	ol	41.36		0.00	0.05	7.11	0.06	51.10	0.01		0.35	100.04	1.001		0.000	0.001	0.144	0.001	1.844	0.000	0.007	2.998	92.76
Wsc20A-1	ol	42.01		0.05	0.08	6.87	0.08	50.85	0.03		0.35	100.31	1.012		0.001	0.002	0.138	0.002	1.825	0.001	0.007	2.987	92.95
Wsc20A-2	ol	41.83		0.01	0.09	7.11	0.07	50.91	0.07		0.35	100.44	1.008		0.000	0.002	0.143	0.002	1.828	0.002	0.007	2.991	92.73
Wsc20A-3	ol	41.81		0.03	0.09	6.97	0.07	50.83	0.02		0.31	100.12	1.009		0.001	0.002	0.141	0.001	1.829	0.001	0.006	2.989	92.86
Wsc20B-1	ol	41.13		0.03	0.08	7.23	0.12	51.19	0.04		0.33	100.15	0.996		0.001	0.002	0.146	0.003	1.848	0.001	0.006	3.003	92.66
Wsc20B-2	ol	41.08		0.01	0.05	6.89	0.06	51.63	0.02		0.32	100.05	0.994		0.000	0.001	0.139	0.001	1.863	0.000	0.006	3.005	93.03
Wsc20B-3	ol	40.83		0.01	0.06	7.09	0.10	51.59	0.01		0.36	100.05	0.990		0.000	0.001	0.144	0.002	1.865	0.000	0.007	3.009	92.85
Wsc20C-1	ol	41.22		0.04	0.05	7.24	0.09	50.72	0.06		0.32	99.76	1.001		0.001	0.001	0.147	0.002	1.837	0.002	0.006	2.998	92.59
Wsc20C-2	ol	41.40		0.03	0.07	7.22	0.10	51.21	0.04		0.29	100.36	1.000		0.001	0.001	0.146	0.002	1.843	0.001	0.006	2.999	92.67
Wsc20C-3	ol	41.24		0.05	0.07	7.31	0.10	50.94	0.05		0.29	100.06	0.999		0.001	0.001	0.148	0.002	1.840	0.001	0.006	2.999	92.55
Wsc21B-1	ol	41.08		0.02	0.07	7.07	0.12	51.36	0.03		0.26	100.01	0.995		0.000	0.001	0.143	0.003	1.855	0.001	0.005	3.004	92.83
Wsc21B-2	ol	41.44		0.00	0.07	6.95	0.14	51.31	0.02		0.37	100.30	1.000		0.000	0.001	0.140	0.003	1.847	0.001	0.007	2.999	92.94
Wsc21B-3	ol	41.37		0.01	0.05	6.74	0.09	51.22	0.01		0.35	99.86	1.002		0.000	0.001	0.136	0.002	1.849	0.000	0.007	2.998	93.13
Wsc21D-1	ol	41.08		0.06	0.05	6.85	0.08	50.83	0.03		0.32	99.31	1.001		0.002	0.001	0.140	0.002	1.846	0.001	0.006	2.998	92.97
Wsc25C-1	ol	39.91		0.12	0.03	8.22	0.11	48.49	0.10		0.34	97.33	1.000		0.004	0.001	0.172	0.002	1.810	0.003	0.007	2.998	91.31
Wsc25C-2	ol	40.13		0.08	0.06	8.20	0.08	48.77	0.12		0.35	97.78	1.000		0.002	0.001	0.171	0.002	1.812	0.003	0.007	2.998	91.39
Wsc25C-3	ol	39.99		0.07	0.05	8.07	0.07	49.05	0.11		0.40	97.79	0.996		0.002	0.001	0.168	0.001	1.822	0.003	0.008	3.002	91.55
Wsc25D-1	ol	41.08		0.04	0.08	7.11	0.09	51.20	0.05		0.33	99.98	0.996		0.001	0.001	0.144	0.002	1.850	0.001	0.007	3.003	92.77
Wsc25D-2	ol	41.67		0.05	0.07	7.10	0.08	50.92	0.06		0.41	100.36	1.005		0.001	0.001	0.143	0.002	1.831	0.002	0.008	2.993	92.74
Wsc25D-3	ol	41.38		0.05	0.04	7.25	0.12	51.12	0.04		0.48	100.48	0.999		0.002	0.001	0.146	0.002	1.840	0.001	0.009	3.000	92.63
Wsc25D-4	ol	41.33		0.04	0.00	7.15	0.09	50.73	0.05		0.36	99.75	1.003		0.001	0.000	0.145	0.002	1.836	0.001	0.007	2.996	92.67
Wsc25I-1	ol	38.64		1.04	0.06	11.90	0.07	42.30	1.18		0.52	95.71	1.004		0.032	0.001	0.259	0.001	1.639	0.033	0.011	2.979	86.37
Wsc25I-2	ol	39.52		0.64	0.06	9.79	0.06	44.61	0.87		0.41	95.97	1.012		0.019	0.001	0.210	0.001	1.702	0.024	0.009	2.978	89.04
Wsc25K-1	ol	41.26		0.05	0.08	7.12	0.12	50.92	0.04		0.34	99.93	1.000		0.001	0.002	0.144	0.002	1.840	0.001	0.007	2.998	92.73
Wsc25K-2	ol	41.55		0.03	0.05	7.23	0.11	50.76	0.05		0.35	100.12	1.005		0.001	0.001	0.146	0.002	1.831	0.001	0.007	2.994	92.60
Wsc25K-3	ol	41.45		0.04	0.07	6.88	0.10	50.48	0.06		0.35	99.43	1.008		0.001	0.001	0.140	0.002	1.830	0.002	0.007	2.991	92.90
Wsc25M-1	ol	41.16		0.03	0.06	7.30	0.08	50.47	0.06		0.31	99.47	1.003		0.001	0.001	0.149	0.002	1.833	0.002	0.006	2.996	92.49
Wsc25M-2	ol	41.14		0.02	0.05	7.12	0.10	50.94	0.04		0.36	99.77	0.999		0.000	0.001	0.145	0.002	1.845	0.001	0.007	3.000	92.73
Wsc25N-1	ol	39.47		0.66	0.04	8.92	0.08	45.13	0.94		0.44	95.67	1.010		0.020	0.001	0.191	0.002	1.722	0.026	0.009	2.980	90.02
Wsc25N-2	ol	39.14		0.80	0.05	9.32	0.10	44.31	1.02		0.41	95.15	1.009		0.024	0.001	0.201	0.002	1.703	0.028	0.008	2.978	89.44
Wsc25N-3	ol	40.27		0.56	0.07	8.23	0.08	47.08	0.66		0.38	97.33	1.008		0.016	0.001	0.172	0.002	1.757	0.018	0.008	2.983	91.07
Wsc27A-1	ol	41.35		0.03	0.05	6.89	0.13	51.68	0.06		0.39	100.59	0.996		0.001	0.001	0.139	0.003	1.855	0.002	0.008	3.003	93.04
Wsc27A-2	ol	41.73		0.08	0.07	7.13	0.10	51.36	0.11		0.38	100.96	1.001		0.002	0.001	0.143	0.002	1.837	0.003	0.007	2.997	92.77
Wsc27A-3	ol	41.54		0.05	0.06	6.66	0.10	51.57	0.05		0.38	100.41	1.000		0.001	0.001	0.134	0.002	1.851	0.001	0.007	2.999	93.24
Wsc27B-1	ol	40.91		0.02	0.08	6.74	0.09	51.71	0.03		0.24	99.81	0.992		0.000	0.002	0.137	0.002	1.869	0.001	0.005	3.007	93.19
Wsc27B-2	ol	41.14		0.02	0.05	6.60	0.06	51.99	0.04		0.27	100.15	0.993		0.000	0.001	0.133	0.001	1.871	0.001	0.005	3.006	93.35
Wsc27B-3	ol	40.53		0.04	0.08	6.81	0.12	52.32	0.05		0.32	100.28	0.981		0.001	0.002	0.138	0.002	1.887	0.001	0.006	3.018	93.20
Wsc27C-1	ol	41.30		0.01	0.05	6.78	0.07	51.66	0.03		0.38	100.29	0.997		0.000	0.001	0.137	0.001	1.858	0.001	0.007	3.003	93.14
Wsc27C-2	ol	41.43		0.00	0.06	6.78	0.13	51.63	0.03		0.33	100.39	0.998		0.000	0.001	0.137	0.003	1.855	0.001	0.006	3.001	93.14
Wsc27C-3	ol	41.08		0.01	0.06	6.50	0.04	51.53	0.04		0.30	99.56	0.997		0.000	0.001	0.132	0.001	1.865	0.001	0.006	3.002	93.39
Wsc27D-1	ol	41.29		0.00	0.06	6.76	0.09	51.72	0.02		0.28	100.23	0.996		0.000	0.001	0.136	0.002	1.861	0.001	0.005	3.003	93.17
Wsc27D-2	ol	41.24		0.01	0.06	6.70	0.08	51.78	0.03		0.29	100.19	0.996		0.000	0.001	0.135	0.002	1.864	0.001	0.006	3.004	93.23
Wsc27D-3	ol	41.02		0.00	0.03	6.65	0.04	51.55	0.04		0.34	99.68	0.995		0.000	0.001	0.135	0.001	1.865	0.001	0.007	3.004	93.25
Wsc32C-1	ol	41.44		0.01	0.09	6.68	0.07	51.75	0.00		0.32	100.36	0.998		0.000	0.002	0.135	0.001	1.858	0.000	0.006	3.001	93.25
Wsc32C-2	ol	41.42		0.02	0.08	6.73	0.11	51.44	0.01		0.36	100.18	1.000		0.001	0.002	0.136	0.002	1.851	0.000	0.007	2.999	93.16
Wsc32C-3	ol	41.47		0.00	0.07	6.63	0.09	51.32	0.01		0.31	99.90	1.003		0.000	0.001	0.134	0.002	1.850	0.000	0.006	2.996	93.25
Wsc33B-1	ol	39.26		0.29	0.13	9.69	0.09	45.66	0.34		0.26	95.72	1.007		0.009	0.003	0.208	0.002	1.745	0.009	0.005	2.988	89.36
Wsc33B-2	ol	38.79		0.24	0.08	10.65	0.12	46.26	0.28		0.30	96.72	0.991		0.007	0.002	0.227	0.003	1.761	0.008	0.006	3.005	88.57
Wsc36A-1	ol	41.62		0.00	0.04	5.73	0.07	52.49	0.01		0.34	100.31	0.999		0.000	0.001	0.115	0.001	1.878	0.000	0.007	3.001	94.23
Wsc36A-2	ol	41.45		0.03	0.05	6.39	0.10	51.91	0.01		0.36	100.29	0.998		0.001	0.001	0.129	0.002	1.864	0.000	0.007	3.001	93.54
Wsc36A-3	ol	41.38		0.01	0.03	5.74	0.14	52.65	0.00		0.38	100.33	0.994		0.000	0.001	0.115	0.003	1.885	0.000	0.007	3.006	94.24

Label	Min Phase	SiO_2	TiO_2	Al_2O_3	Cr_2O_3	FeO	MnO	MgO	CaO	Na_2O	NiO	Total	Si	Ti	Al	Cr	Fe	Mn	Mg	Ca		Ni	Total	Mg#
Wsc41J-1	ol	41.73		0.00	0.02	5.79	0.06	51.87	0.02		0.35	99.84	1.005		0.000	0.000	0.117	0.001	1.863	0.001		0.007	2.994	94.11
Wsc41J-2	ol	41.63		0.01	0.03	5.38	0.09	52.49	0.00		0.33	99.97	1.001		0.000	0.001	0.108	0.002	1.881	0.000		0.006	2.999	94.57
Wsc41J-3	ol	41.60		0.02	0.02	5.62	0.08	52.73	0.03		0.37	100.48	0.997		0.001	0.000	0.113	0.002	1.883	0.001		0.007	3.003	94.36
Wsc41K-1	ol	41.71		0.02	0.06	5.56	0.10	52.20	0.00		0.33	99.98	1.003		0.001	0.001	0.112	0.002	1.871	0.000		0.006	2.996	94.37
Wsc41K-2	ol	41.46		0.03	0.06	5.35	0.14	52.27	0.00		0.32	99.62	1.000		0.001	0.001	0.108	0.003	1.880	0.000		0.006	2.999	94.57
Wsc41K-3	ol	41.84		0.03	0.05	5.76	0.09	52.25	0.01		0.41	100.42	1.003		0.001	0.001	0.115	0.002	1.867	0.000		0.008	2.996	94.18
Wsc49A-1	ol	41.17		0.00	0.03	7.41	0.12	51.72	0.02		0.35	100.83	0.992		0.000	0.001	0.149	0.002	1.857	0.001		0.007	3.008	92.56
Wsc49A-2	ol	40.91		0.02	0.03	7.13	0.07	50.67	0.02		0.32	99.18	0.999		0.001	0.001	0.146	0.001	1.845	0.001		0.006	3.000	92.69
Wsc49A-3	ol	41.22		0.01	0.03	7.23	0.08	51.46	0.02		0.37	100.43	0.995		0.000	0.001	0.146	0.002	1.852	0.001		0.007	3.004	92.69
Wsc51B-1	ol	41.29		0.02	0.03	8.11	0.13	50.36	0.06		0.29	100.29	1.002		0.001	0.001	0.165	0.003	1.821	0.002		0.006	2.998	91.71
Wsc51B-2	ol	41.27		0.03	0.03	8.18	0.09	50.50	0.01		0.36	100.47	1.000		0.001	0.001	0.166	0.002	1.824	0.000		0.007	3.000	91.67
Wsc51B-3	ol	41.36		0.02	0.03	7.42	0.11	50.97	0.02		0.36	100.28	1.000		0.001	0.001	0.150	0.002	1.838	0.001		0.007	2.999	92.45
Wsc53A-1	ol	40.64	0.00	0.02	0.07	7.29	0.11	51.33	0.04		0.31	99.82	0.989	0.000	0.001	0.001	0.148	0.002	1.861	0.001		0.006	3.010	92.62
Wsc53A-2	ol	41.06	0.01	0.02	0.13	6.53	0.08	50.79	0.03		0.38	99.04	1.002	0.000	0.001	0.003	0.133	0.002	1.847	0.001		0.007	2.996	93.27
Wsc53A-3	ol	40.76	0.01	0.02	0.13	6.90	0.09	50.81	0.01		0.27	99.00	0.997	0.000	0.001	0.003	0.141	0.002	1.852	0.000		0.005	3.001	92.92
Wsc53A-4	ol	41.10	0.01	0.03	0.07	6.65	0.12	51.21	0.03		0.29	99.51	0.999	0.000	0.001	0.001	0.135	0.002	1.855	0.001		0.006	3.000	93.21
Wsc53B-1	ol	39.53		0.05	0.11	5.69	0.07	50.76	0.04		0.28	96.53	0.988		0.002	0.002	0.119	0.002	1.891	0.001		0.006	3.010	94.09
Wsc53B-2	ol	40.89		0.04	0.08	5.60	0.08	51.53	0.03		0.26	98.52	0.999		0.001	0.002	0.114	0.002	1.876	0.001		0.005	3.000	94.25
Wsc53B-3	ol	39.41		0.07	0.08	5.31	0.05	49.61	0.07		0.29	94.90	0.999		0.002	0.002	0.113	0.001	1.875	0.002		0.006	2.999	94.33
Wsc53B-4	ol	40.69		0.04	0.05	5.54	0.11	51.52	0.05		0.30	98.30	0.997		0.001	0.001	0.114	0.002	1.881	0.001		0.006	3.003	94.31
Wsc53C-1	ol	40.88		0.11	0.08	6.57	0.11	50.20	0.16		0.34	98.46	1.004		0.003	0.002	0.135	0.002	1.837	0.004		0.007	2.994	93.15
Wsc53C-2	ol	40.89		0.15	0.08	6.64	0.11	50.35	0.18		0.31	98.71	1.002		0.004	0.002	0.136	0.002	1.839	0.005		0.006	2.995	93.11
Wsc53C-3	ol	41.02		0.12	0.08	6.46	0.08	50.18	0.18		0.34	98.46	1.006		0.004	0.002	0.133	0.002	1.835	0.005		0.007	2.991	93.26
Wsc53C-4	ol	40.63		0.17	0.10	6.67	0.11	49.54	0.23		0.39	97.82	1.005		0.005	0.002	0.138	0.002	1.826	0.006		0.008	2.992	92.98
Wsc55E-1	ol	34.31		0.05	0.03	4.05	0.03	44.20	0.04		0.15	82.86	0.993		0.002	0.001	0.098	0.001	1.907	0.001		0.004	3.006	95.11
Wsc55E-2	ol	34.44		0.05	0.04	4.23	0.02	44.97	0.02		0.17	83.95	0.986		0.002	0.001	0.101	0.001	1.918	0.001		0.004	3.013	94.98
Wsc55E-2	ol	35.08		0.09	0.04	3.84	0.04	45.31	0.02		0.18	84.60	0.993		0.003	0.001	0.091	0.001	1.912	0.001		0.004	3.005	95.46
Wsc57A-1	ol	41.76		0.06	0.04	6.45	0.09	51.46	0.07		0.31	100.24	1.005		0.002	0.001	0.130	0.002	1.847	0.002		0.006	2.994	93.43
Wsc57A-2	ol	41.74		0.07	0.09	6.36	0.09	51.52	0.06		0.39	100.32	1.004		0.002	0.002	0.128	0.002	1.848	0.002		0.007	2.994	93.52
Wsc57A-3	ol	41.48		0.05	0.08	6.43	0.09	51.78	0.08		0.34	100.33	0.999		0.001	0.002	0.129	0.002	1.858	0.002		0.007	3.000	93.49
Wsc58A-1	ol	41.47		0.03	0.06	6.86	0.09	50.93	0.03		0.33	99.80	1.005		0.001	0.001	0.139	0.002	1.840	0.001		0.006	2.994	92.98
Wsc60A-1	ol	40.68		0.08	0.01	7.66	0.08	49.74	0.10		0.36	98.71	1.001		0.002	0.000	0.158	0.002	1.825	0.003		0.007	2.998	92.05
Wsc60A-2	ol	41.10		0.07	0.03	7.87	0.09	50.05	0.07		0.32	99.61	1.003		0.002	0.000	0.161	0.002	1.820	0.002		0.006	2.996	91.89
Wsc63D-1	ol	39.92		0.81	0.07	9.92	0.08	42.87	0.99		0.32	94.97	1.031		0.024	0.002	0.214	0.002	1.650	0.027		0.007	2.956	88.51
Wsc63D-1repeat	ol	39.54		0.82	0.06	9.83	0.10	42.47	1.05		0.32	94.19	1.030		0.025	0.001	0.214	0.002	1.649	0.029		0.007	2.957	88.51
Wsc65A-1	ol	41.39		0.01	0.06	6.94	0.15	51.35	0.02		0.37	100.30	0.999		0.000	0.001	0.140	0.003	1.848	0.000		0.007	3.000	92.95
Wsc65A-2	ol	41.19		0.01	0.07	6.89	0.07	51.13	0.03		0.34	99.72	1.000		0.000	0.001	0.140	0.002	1.850	0.001		0.007	3.000	92.97
Wsc65A-3	ol	41.42		0.01	0.05	6.92	0.11	51.37	0.02		0.31	100.21	1.000		0.000	0.001	0.140	0.002	1.849	0.001		0.006	2.999	92.98
Wsc65B-1	ol	41.18	0.00	0.00	0.06	6.54	0.10	51.68	0.03		0.34	99.94	0.996	0.000	0.000	0.001	0.132	0.002	1.863	0.001		0.007	3.003	93.37
Wsc65B-2	ol	40.69	0.02	0.01	0.05	7.30	0.08	51.52	0.01		0.35	100.04	0.988	0.000	0.000	0.001	0.148	0.002	1.865	0.000		0.007	3.011	92.63
Wsc65B-3	ol	41.23	0.00	0.02	0.03	6.99	0.07	51.41	0.02		0.32	100.08	0.998	0.000	0.001	0.001	0.141	0.002	1.854	0.000		0.006	3.002	92.91
Wsc01G-1	opx	57.92	0.03	0.59	0.60	3.46	0.13	37.04	0.41	0.05	0.14	100.36	1.969	0.001	0.024	0.016	0.098	0.004	1.878	0.015	0.003	0.004	4.012	95.03
Wsc01G-2	opx	57.97	0.04	0.59	0.58	3.39	0.06	36.83	0.46	0.02	0.07	100.01	1.975	0.001	0.024	0.016	0.096	0.002	1.871	0.017	0.001	0.002	4.004	95.10
Wsc01G-3	opx	57.61	0.03	0.57	0.55	3.50	0.09	36.62	0.42	0.08	0.15	99.62	1.973	0.001	0.023	0.015	0.100	0.003	1.870	0.016	0.005	0.004	4.010	94.91
Wsc01I-1	opx	57.07	0.04	0.57	0.59	4.26	0.10	35.93	0.45	0.03	0.07	99.12	1.971	0.001	0.023	0.016	0.123	0.003	1.850	0.016	0.002	0.002	4.009	93.76
Wsc01I-2	opx	56.91	0.01	0.56	0.51	4.22	0.14	36.10	0.40	0.04	0.03	98.92	1.969	0.000	0.023	0.014	0.122	0.004	1.863	0.015	0.003	0.001	4.013	93.85
Wsc01I-3	opx	57.36	0.03	0.51	0.57	4.09	0.07	36.14	0.42	0.00	0.09	99.26	1.976	0.001	0.021	0.015	0.118	0.002	1.856	0.015	0.000	0.002	4.006	94.04
Wsc01I-4	opx	57.50	0.02	0.58	0.53	3.82	0.08	36.49	0.44	0.04	0.06	99.54	1.973	0.001	0.023	0.014	0.110	0.002	1.866	0.016	0.002	0.002	4.009	94.45
Wsc13G-1	opx	58.94	0.01	0.50	0.47	4.58	0.06	35.27	0.63	0.06	0.10	100.63	2.002	0.000	0.020	0.013	0.130	0.002	1.786	0.023	0.004	0.003	3.983	93.21
Wsc13G-2	opx	58.41	0.02	0.50	0.36	4.53	0.11	35.38	0.62	0.06	0.06	100.06	1.996	0.000	0.020	0.010	0.130	0.003	1.803	0.023	0.004	0.002	3.990	93.30
Wsc13G-3	opx	58.56	0.00	0.47	0.36	4.55	0.17	35.45	0.60	0.07	0.06	100.30	1.997	0.000	0.019	0.010	0.130	0.005	1.802	0.022	0.005	0.002	3.991	93.28
Wsc14A-1	opx	57.96	0.03	0.76	0.60	4.13	0.09	36.38	0.31	0.01	0.08	100.36	1.974	0.001	0.030	0.016	0.118	0.003	1.847	0.011	0.001	0.002	4.003	94.02
Wsc14A-2	opx	58.12	0.03	0.77	0.65	4.15	0.10	36.52	0.32	0.03	0.11	100.80	1.972	0.001	0.031	0.017	0.118	0.003	1.847	0.012	0.002	0.003	4.004	94.00
Wsc14A-3	opx	58.13	0.00	0.77	0.63	4.13	0.07	36.27	0.31	0.03	0.08	100.43	1.977	0.000	0.031	0.017	0.118	0.002	1.839	0.011	0.002	0.002	4.000	93.99
Wsc14A-4	opx	57.89	0.03	0.75	0.59	4.24	0.11	36.65	0.34	0.02	0.12	100.73	1.967	0.001	0.030	0.016	0.120	0.003	1.856	0.012	0.002	0.003	4.010	93.91
Wsc14U-1	opx	58.27	0.01	0.74	0.59	4.21	0.11	36.09	0.29	0.00	0.07	100.38	1.982	0.000	0.030	0.016	0.120	0.003	1.831	0.010	0.000	0.002	3.995	93.85
Wsc14U-2	opx	58.31	0.03	0.73	0.55	4.09	0.12	35.97	0.30	0.03	0.10	100.23	1.986	0.001	0.029	0.015	0.117	0.004	1.826	0.011	0.002	0.003	3.992	94.00
Wsc18A-1	opx	57.50	0.00	0.64	0.52	3.98	0.12	36.92	0.18	0.00	0.08	99.95	1.966	0.000	0.026	0.014	0.114	0.004	1.882	0.007	0.000	0.002	4.014	94.30
Wsc18A-2	opx	57.44	0.01	0.66	0.55	3.91	0.08	36.67	0.19	0.03	0.08	99.61	1.969	0.000	0.027	0.015	0.112	0.002	1.874	0.007	0.002	0.002	4.011	94.35
Wsc18A-3	opx	57.44	0.00	0.63	0.49	4.03	0.08	37.03	0.17	0.02	0.06	99.94	1.964	0.000	0.025	0.013	0.115	0.002	1.888	0.006	0.001	0.002	4.017	94.25
Wsc18A-4	opx	56.91	0.01	0.62	0.50	3.99	0.09	36.49	0.18	0.02	0.06	98.87	1.967	0.000	0.025	0.014	0.115	0.003	1.880	0.007	0.001	0.002	4.014	94.22
Wsc18A-5	opx	57.44	0.01	0.61	0.49	3.71	0.06	36.49	0.18	0.00	0.10	99.08	1.976	0.000	0.025	0.013	0.107	0.002	1.872	0.007	0.000	0.003	4.004	94.61
Wsc36F-1	opx	57.90	0.01	0.62	0.51	3.58	0.08	37.26	0.13	0.01	0.10	100.21	1.970	0.000	0.025	0.014	0.102	0.002	1.890	0.005	0.001	0.003	4.011	94.88
Wsc36F-2	opx	58.11	0.01	0.59	0.55	3.52	0.07	37.23	0.11	0.02	0.05	100.27	1.974	0.000	0.024	0.015	0.100	0.002	1.886	0.004	0.001	0.001	4.007	94.96
Wsc58A-1	opx	57.36	0.00	0.73	0.45	3.93	0.12	36.14	0.34	0.02	0.09	99.21	1.975	0.000	0.030	0.012	0.113	0.004	1.855	0.013	0.002	0.002	4.005	94.25
Wsc58A-2	opx	57.94	0.02	0.73	0.52	4.07	0.13	36.06	0.39	0.06	0.05	99.96	1.980	0.000	0.029	0.014	0.116	0.004	1.837	0.014	0.004	0.001	4.000	94.05
Wsc58A-3	opx	58.21	0.02	0.72	0.47	3.86	0.08	36.48	0.32	0.08	0.11	100.35	1.979	0.000	0.029	0.013	0.110	0.002	1.849	0.012	0.005	0.003	4.002	94.39
Wsc58C-1	opx	56.63	0.02	0.69	0.53	4.04	0.09	36.25	0.30	0.03	0.05	98.63	1.964	0.001	0.028	0.015	0.117	0.003	1.874	0.011	0.002	0.001	4.015	94.12
Wsc58C-2	opx	57.52	0.00	0.73	0.54	3.98	0.10	36.79	0.29	0.02	0.11	100.08	1.965	0.000	0.029	0.015	0.114	0.003	1.873	0.011	0.001	0.003	4.014	94.29
Wsc58C-3	opx	57.41	0.00	0.72	0.58	3.93	0.09	36.43	0.31	0.04	0.08	99.60	1.969	0.000	0.029	0.016	0.113	0.003	1.863	0.011	0.003	0.002	4.010	94.29
Wsc58D-1	opx	58.10	0.00	0.68	0.48	3.69	0.07	36.98	0.30	0.03	0.06	100.38	1.973	0.000	0.027	0.013	0.105	0.002	1.873	0.011	0.002	0.002	4.007	94.70
Wsc58D-2	opx	58.16	0.03	0.76	0.57	3.86	0.04	36.60	0.38	0.04	0.09	100.53	1.975	0.001	0.030	0.015	0.109	0.001	1.852	0.014	0.003	0.002	4.003	94.42
Wsc58D-3	opx	58.00	0.05	0.70	0.51	3.69	0.16	36.98	0.28	0.02	0.05	100.44	1.970	0.001	0.028	0.014	0.105	0.005	1.873	0.010	0.001	0.001	4.008	94.70
Wsc58D-4	opx	58.22	0.02	0.73	0.45	3.62	0.06	37.17	0.32	0.03	0.04	100.66	1.971	0.001	0.029	0.012	0.103	0.002	1.876	0.012	0.002	0.001	4.008	94.82

Appendix E: Wawa non-fibrous diamond inclusion Zn-in-chromite analyses

Sample-Point #	Zn content (ppm)	T (Celcius)
Wsc01F-1	552	1038
Wsc01F-2	431	1161
Wsc01F-3	431	1161
Wsc01F-4	460	1126
Wsc01F-5	498	1086
Wsc03D-1	314	1356
Wsc03D-2	338	1306
Wsc03D-3	374	1242
Wsc03D-4	406	1194
Wsc03E-1	407	1193
Wsc03E-2	363	1260
Wsc03E-3	427	1166
Wsc03E-4	456	1131
Wsc05H-1	398	1205
Wsc05H-2	461	1125
Wsc05H-3	461	1125
Wsc05H-4	334	1314
Wsc05A-1	298	1394
Wsc05A-2	284	1430
Wsc05A-3	378	1236
Wsc05A-4	390	1217
Wsc05D-1	293	1406
Wsc05D-2	367	1254
Wsc05D-3	352	1280
Wsc05E-1	346	1291
Wsc05E-2	370	1249
Wsc06A-1	424	1170
Wsc06A-2	360	1266
Wsc06A-3	328	1326
Wsc06B-1	325	1332
Wsc09D-1	292	1409
Wsc09D-2	256	1513
Wsc09F-1	290	1414
Wsc09F-2	302	1384
Wsc12A-1	381	1231
Wsc12A-2	363	1260
Wsc12A-3	359	1267
Wsc12A-4	375	1241
Wsc12A-5	330	1322
Wsc12B-1	376	1239
Wsc12B-2	425	1168
Wsc12B-3	361	1264
Wsc12B-4	415	1182
Wsc17B-1	453	1134
Wsc17B-2	471	1114
Wsc17B-3	460	1126
Wsc17B-4	430	1162

Sample-Point #	Zn content (ppm)	T (Celcius)
Wsc22A-1	339	1304
Wsc22A-2	305	1377
Wsc22A-3	298	1394
Wsc22A-4	298	1394
Wsc29G-1	261	1497
Wsc29G-2	295	1401
Wsc29G-3	286	1424
Wsc29G-4	338	1306
Wsc31B-1	375	1241
Wsc31B-2	374	1242
Wsc37A-1	329	1324
Wsc37A-2	434	1157
Wsc37A-3	354	1276
Wsc37A-4	377	1237
Wsc37A-5	356	1273
Wsc37D-1	384	1226
Wsc37D-2	334	1314
Wsc37D-3	284	1430
Wsc37E-1	243	1558
Wsc38D-1	516	1069
Wsc38D-2	452	1135
Wsc38G-1	385	1225
Wsc38G-2	269	1472
Wsc38G-3	333	1316
Wsc38G-4	340	1302
Wsc39D-1	343	1296
Wsc39D-2	301	1386
Wsc39D-3	363	1260
Wsc39C-1	371	1247
Wsc39C-2	378	1236
Wsc39C-3	336	1310
Wsc40D-1	338	1306
Wsc40D-2	293	1406
Wsc40D-3	249	1537
Wsc40D-4	271	1466
Wsc41C-1	386	1223
Wsc41C-2	422	1172
Wsc41C-3	352	1280
Wsc41D-1	286	1424
Wsc41D-2	385	1225
Wsc41D-3	367	1254
Wsc41D-4	339	1304
Wsc41B-1	308	1370
Wsc41B-2	340	1302
Wsc41B-3	278	1446

Sample-Point #	Zn content (ppm)	T (Celcius)
Wsc41E-1	290	1414
Wsc41E-2	353	1278
Wsc41E-3	312	1361
Wsc41I-1	249	1537
Wsc41I-2	345	1293
Wsc41G-1	445	1144
Wsc41G-2	420	1175
Wsc41G-3	372	1245
Wsc41G-4	447	1141
Wsc41N-1	440	1150
Wsc41M-1	317	1349
Wsc41M-2	367	1254
Wsc41M-3	449	1139
Wsc41M-4	337	1308
Wsc43B-1	431	1161
Wsc43B-2	459	1127
Wsc43B-3	353	1278
Wsc43C-1	398	1205
Wsc48E-1	301	1386
Wsc48E-2	349	1285
Wsc48C-1	292	1409
Wsc48C-2	294	1404
Wsc50A-1	517	1068
Wsc50A-2	423	1171
Wsc50A-3	311	1363
Wsc50A-4	612	993
Wsc50B-1	301	1386
Wsc50B-2	300	1389
Wsc52E-1	418	1178
Wsc52E-2	381	1231
Wsc52E-3	417	1179
Wsc52B-1	367	1254
Wsc52B-2	365	1257
Wsc52B-3	364	1259
Wsc52C-1	323	1337
Wsc52C-2	343	1296
Wsc52C-3	311	1363
Wsc56F-1	436	1155
Wsc56F-2	359	1267
Wsc56F-3	337	1308

Analyses collected with beam current of 100 nA, accelerating voltage of 20 kV, and count time of 100 s; Precision ±40 ppm

Appendix F: Replicate analyses for olivine microinclusions in fibrous diamonds from Wawa

Sample	W15A-1	W15A-2	W15A-3	W15A-4	Avg	W15A Original
Orientation	**0°**	**90°**	**180°**	**270°**		
SiO_2	37.56	38.16	37.20	38.70		39.70
Al_2O_3	0.19	0.20	0.26	0.41		0.11
Cr_2O_3	0.80	0.11	1.53	0.32		0.58
FeO	11.10	8.39	15.12	9.60		10.98
MnO	0.09	0.17		0.10		0.12
MgO	49.93	52.55	45.54	50.48		48.15
CaO	0.05		0.07			
NiO	0.29	0.43	0.28	0.38		0.35
Total	100.00	100.00	100.00	100.00		100.00
Initial Total	65.42	66.86	41.26	64.93		93.82
Si	0.936	0.939	0.945	0.954	0.943	0.983
Al	0.006	0.006	0.008	0.012	0.008	0.003
Cr	0.016	0.002	0.031	0.006	0.014	0.011
Fe	0.231	0.173	0.321	0.198	0.231	0.227
Mn	0.002	0.003		0.002	0.003	0.003
Mg	1.855	1.927	1.724	1.856	1.841	1.776
Ca	0.001		0.002		0.002	
Ni	0.006	0.008	0.006	0.008	0.007	0.007
Total	3.053	3.058	3.036	3.036	3.046	3.010
Mg#	88.92	91.78	84.30	90.36	88.84	88.66

Blank cells are below detection limits

Sample	W15B-1	W15B-2	W15B-3	W15B-4	Avg	W15B Original
Orientation	**0°**	**90°**	**180°**	**270°**		
SiO_2	48.12	40.58	37.96	42.26		45.80
Al_2O_3						
Cr_2O_3						
FeO	3.35	3.41	3.06	3.19		3.72
MnO	0.12	0.12	0.21	0.20		0.10
MgO	48.22	55.60	58.65	54.07		50.07
CaO						
NiO	0.19	0.28	0.12	0.28		0.31
Total	100.00	100.00	100.00	100.00		100.00
Initial Total	68.91	67.19	67.03	67.96		91.02
Si	1.124	0.971	0.914	1.005	1.003	1.080
Al						
Cr						
Fe	0.065	0.068	0.062	0.063	0.065	0.073
Mn	0.002	0.003	0.004	0.004	0.003	0.002
Mg	1.680	1.983	2.105	1.917	1.921	1.760
Ca						
Ni	0.003	0.005	0.002	0.005	0.004	0.006
Total	2.876	3.029	3.086	2.995	2.997	2.920
Mg#	96.25	96.67	97.16	96.79	96.72	96.00

Blank cells are below detection limits

Sample	W52C-1	W52C-2	W52C-3	W52C-4	Avg	W52C Original
Orientation	**0°**	**90°**	**180°**	**270°**		
SiO_2	43.58	46.72	39.47	39.67		35.89
Al_2O_3	0.04	0.05	0.09	0.15		0.06
Cr_2O_3		0.05		0.06		0.07
FeO	7.12	5.48	6.49	5.32		8.43
MnO	0.12	0.11	0.20	0.12		0.13
MgO	48.74	47.19	53.34	54.36		55.10
CaO	0.06		0.06			
NiO	0.34	0.39	0.35	0.32		0.33
Total	100.00	100.00	100.00	100.00		100.00
Initial Total	85.06	78.84	48.71	63.11		85.50
Si	1.048	1.106	0.959	0.959	1.018	0.889
Al	0.001	0.001	0.003	0.004	0.002	0.002
Cr		0.001		0.001	0.001	0.001
Fe	0.143	0.109	0.132	0.107	0.123	0.175
Mn	0.002	0.002	0.004	0.002	0.003	0.003
Mg	1.748	1.666	1.933	1.958	1.826	2.034
Ca	0.002		0.001		0.001	
Ni	0.007	0.007	0.007	0.006	0.007	0.006
Total	2.951	2.893	3.039	3.039	2.980	3.110
Mg#	92.42	93.88	93.61	94.80	93.68	92.09

Blank cells are below detection limits

Appendix G: Raw electron microprobe data for fibrous diamond mineral inclusions indicating screening process used for accuracy of analyses

Wawa Garnet: 24 accepted, 17 rejected

Red Text = Rejected analysis

All three criteria within ±0.05
All three criteria within ±0.10
All three criteria within ±0.20

Raw Probe Data

Normalized

Label	Mineral Phase	SiO_2	TiO_2	Al_2O_3	Cr_2O_3	FeO	MnO	MgO	CaO	Na_2O	NiO	Total	SiO_2	TiO_2	Al_2O_3	Cr_2O_3	FeO	MnO	MgO	CaO	Na_2O	NiO	Total
W6M-1	grt	17.13		7.39	2.81	2.92	0.21	7.52	2.62			40.60	42.20		18.21	6.91	7.20	0.50	18.53	6.45			100.00
W6N-1	grt	13.19		6.46	2.45	2.22	0.15	6.67	1.93			33.08	39.88		19.52	7.42	6.72	0.45	20.17	5.83			100.00
W6O-1	grt	12.20		5.56	1.72	1.66	0.14	5.27	1.62			28.21	43.30		19.75	6.09	5.91	0.50	18.69	5.76			100.00
W6P-1	grt	19.98		8.89	3.74	3.58	0.25	9.33	3.26			49.04	40.77		18.13	7.62	7.30	0.51	19.02	6.64			100.00
W6Q-1	grt	18.43		7.98	3.90	3.61	0.20	8.44	3.23			45.80	40.26		17.42	8.51	7.88	0.44	18.45	7.05			100.00
W6R-1	grt	13.19		6.25	2.07	2.76	0.06	4.73	1.41	0.17		30.64	43.05		20.39	6.75	9.02	0.19	15.44	4.61	0.55		100.00
W6S-1	grt	21.81		6.50	3.83	3.75	0.26	8.39	4.82	0.68		50.04	43.59		12.99	7.66	7.49	0.51	16.76	9.63	1.36		100.00
W6T-1	grt	25.61		10.15	5.36	3.39	0.15	10.67	5.42	0.27		60.99	41.98		16.63	8.78	5.55	0.24	17.49	8.88	0.45		100.00
W6U-1	grt	20.30		8.81	3.38	3.56	0.21	8.59	3.04			47.91	42.38		18.40	7.06	7.44	0.45	17.94	6.35			100.00
W6W-1	grt	24.65		11.72	3.52	3.91	0.21	11.87	3.31	0.06		59.25	41.61		19.78	5.94	6.60	0.35	20.04	5.58	0.11		100.00
W6X-1	grt	21.57		7.01	2.16	2.74	0.15	8.02	4.11	0.20		45.97	46.93		15.26	4.71	5.96	0.33	17.45	8.94	0.44		100.00
W6Y-1	grt	25.81		11.78	4.32	3.98	0.27	12.33	3.76			62.24	41.47		18.93	6.94	6.39	0.43	19.80	6.03			100.00
W6BB-1	grt	20.38		7.89	2.15	3.92	0.36	8.60	3.39	0.08		46.78	43.57		16.88	4.60	8.38	0.77	18.39	7.25	0.17		100.00
W6CC-1	grt	15.22		8.49	3.27	3.71	0.15	6.61	2.97	0.15		40.57	37.51		20.94	8.05	9.14	0.37	16.28	7.33	0.37		100.00
W9A-1a	grt	5.84		3.04	1.08	0.80		3.77	0.31	0.34		15.23	38.48		20.03	7.12	5.25	0.00	24.84	2.04	2.24		100.00
W9B-1a	grt	1.03		0.40	0.09	0.16		0.33	0.06			2.11	49.78		19.30	4.18	7.90	0.00	15.89	2.95			100.00
W13A-1	grt	9.27		3.05	3.58	2.08	0.14	3.80	2.21			24.16	38.42		12.62	14.85	8.63	0.60	15.73	9.16			100.00
W13B-1	grt	2.28		1.14	0.82	0.53		0.69	0.89	0.06		6.43	35.46		17.76	12.83	8.31	0.00	10.76	13.93	0.95		100.00
W13C-1	grt	30.55		4.66	0.90	4.02		1.77	2.22	5.56		49.69	61.49		9.38	1.82	8.09	0.00	3.57	4.46	11.19		100.00
W13D-1	grt	8.54		2.54	3.49	1.71	0.08	3.64	2.09	0.07		22.15	38.53		11.48	15.75	7.71	0.38	16.42	9.43	0.30		100.00
W13G-1	grt	7.30		2.02	2.97	1.87	0.09	2.84	2.41	0.50		19.98	36.53		10.09	14.86	9.34	0.44	14.22	12.04	2.49		100.00
W13H-1	grt	1.42		0.51	0.65	1.14		0.76	0.41	0.06		4.94	28.76		10.39	13.06	22.98	0.00	15.42	8.23	1.17		100.00
W13I-1	grt	5.95		1.40	2.96	1.46	0.07	1.61	1.77	0.07		15.29	38.90		9.18	19.33	9.56	0.45	10.53	11.58	0.47		100.00
W13J-1	grt	6.57		1.53	3.34	1.76	0.09	1.84	1.71	0.06		16.90	38.90		9.04	19.79	10.42	0.52	10.89	10.11	0.34		100.00
W13K-1	grt	3.10		0.79	1.17	0.60	0.05	1.00	0.77			7.49	41.38		10.58	15.63	7.97	0.71	13.38	10.34			100.00
W16B-1	grt	13.86		0.25		0.04		0.96	1.13	2.11		18.36	75.53		1.35		0.20		5.22	6.17	11.52		100.00
W16B-2	grt	12.02		0.21				0.69	1.00	1.45		15.37	78.17		1.39				4.52	6.49	9.43		100.00
W16C-1	grt	16.61		4.11	2.61	3.25	0.13	4.49	2.58			33.84	49.18		12.18	7.73	9.63	0.38	13.28	7.63			100.00
W16F-1	grt	19.06		7.89	6.42	3.52	0.14	9.89	2.75			49.73	38.38		15.89	12.92	7.09	0.29	19.91	5.53			100.00
W16M-1	grt	20.20		8.19	5.95	4.71	0.25	8.88	3.98			52.16	38.73		15.70	11.41	9.03	0.48	17.03	7.63			100.00
W16N-1	grt	33.78		14.73	9.01	6.06	0.36	17.07	4.68			85.73	39.42		17.19	10.52	7.07	0.41	19.93	5.46			100.00
W16G-1	grt	23.21		8.67	5.78	3.90	0.23	9.94	3.61			55.38	41.94		15.66	10.44	7.05	0.42	17.96	6.53			100.00
W16H-1	grt	17.16		6.95	4.02	3.06	0.15	7.52	2.22			41.10	41.77		16.91	9.79	7.46	0.37	18.29	5.41			100.00
W16I-1	grt	8.48		5.18	3.51	2.36	0.13	3.93	1.54	0.37		25.51	33.26		20.31	13.74	9.26	0.50	15.42	6.05	1.45		100.00
W16J-1	grt	18.05		8.12	4.73	3.28	0.16	8.45	2.53	0.05		45.36	39.79		17.89	10.42	7.23	0.35	18.62	5.57	0.11		100.00
W16K-1	grt	8.30		3.15	2.11	1.45		3.94	1.53	0.14		20.67	40.23		15.29	10.21	7.05		19.11	7.41	0.69		100.00
W16L-1	grt	34.51		13.06	8.40	5.54	0.28	16.59	6.01	0.23		84.60	40.79		15.43	9.92	6.55	0.33	19.61	7.10	0.27		100.00
W41A-1	grt	9.38		5.31		3.95	0.12	2.76	2.31			23.87	39.36		22.30		16.57	0.50	11.56	9.71			100.00
W41B-1	grt	8.94		4.90		3.47	0.07	2.54	2.00	0.12		22.05	40.55		22.24		15.75	0.32	11.53	9.06	0.55		100.00
W53C-1a	grt	32.94		15.92	8.73	9.71	0.46	17.62	2.53	0.07		87.97	37.44		18.10	9.92	11.03	0.52	20.02	2.88	0.08		100.00
W53D-1a	grt	36.24		16.86	8.50	7.52	0.30	18.34	5.82	0.14		93.73	38.66		17.99	9.07	8.02	0.32	19.57	6.21	0.15		100.00

		3.000 <±0.05										8.000 <±0.05	3.000 <±0.05
		3.000 <±0.10										8.000 <±0.10	3.000 <±0.10
		3.000 <±0.20										8.000 <±0.20	3.000 <±0.20
Label	Mineral Phase	Si	Ti	Al	Cr	Fe	Mn	Mg	Ca	Na	Ni	Total	Mg+Fe+Ca
W6M-1	grt	3.055		1.553	0.395	0.436	0.031	2.000	0.500			7.971	2.936
W6N-1	grt	2.894		1.669	0.425	0.408	0.028	2.182	0.453			8.059	3.043
W6O-1	grt	3.091		1.661	0.344	0.352	0.030	1.989	0.441			7.907	2.782
W6P-1	grt	2.971		1.557	0.439	0.445	0.031	2.067	0.519			8.030	3.031
W6Q-1	grt	2.956		1.508	0.494	0.484	0.027	2.019	0.555			8.043	3.057
W6R-1	grt	3.106		1.733	0.385	0.544	0.012	1.661	0.356	0.077		7.874	2.561
W6S-1	grt	3.218		1.130	0.447	0.462	0.032	1.845	0.762	0.195		8.091	3.069
W6T-1	grt	3.060		1.429	0.506	0.338	0.015	1.900	0.693	0.063		8.004	2.932
W6U-1	grt	3.067		1.570	0.404	0.450	0.027	1.936	0.492			7.946	2.878
W6W-1	grt	2.990		1.675	0.337	0.397	0.021	2.146	0.430	0.015		8.011	2.973
W6X-1	grt	3.358		1.287	0.266	0.357	0.020	1.862	0.685	0.061		7.895	2.904
W6Y-1	grt	2.992		1.610	0.396	0.386	0.026	2.130	0.466			8.005	2.982
W6BB-1	grt	3.160		1.443	0.264	0.508	0.047	1.989	0.563	0.024		7.998	3.061
W6CC-1	grt	2.778		1.827	0.472	0.566	0.023	1.798	0.582	0.054		8.099	2.946
W9A-1a	grt	2.772		1.700	0.406	0.316		2.667	0.157	0.313		8.332	3.140
W9B-1a	grt	3.472		1.586	0.230	0.461		1.651	0.221			7.620	2.333
W13A-1	grt	2.923		1.131	0.893	0.549	0.038	1.784	0.746			8.065	3.079
W13B-1	grt	2.721		1.606	0.779	0.533		1.231	1.145	0.141		8.157	2.910
W13C-1	grt	4.356		0.783	0.102	0.479		0.377	0.338	1.537		7.971	1.194
W13D-1	grt	2.933		1.030	0.948	0.491	0.024	1.863	0.769	0.044		8.101	3.122
W13G-1	grt	2.861		0.931	0.920	0.612	0.029	1.660	1.010	0.379		8.402	3.282
W13H-1	grt	2.404		1.023	0.864	1.607		1.922	0.737	0.189		8.746	4.266
W13I-1	grt	3.033		0.844	1.192	0.623	0.030	1.224	0.967	0.072		7.985	2.815
W13J-1	grt	3.035		0.831	1.221	0.680	0.034	1.267	0.845	0.051		7.964	2.792
W13K-1	grt	3.137		0.945	0.937	0.505	0.046	1.512	0.840			7.922	2.858
W16B-1	grt	5.058		0.107		0.011		0.522	0.442	1.496		7.636	0.975
W16B-2	grt	5.165		0.108				0.445	0.459	1.208		7.386	0.904
W16C-1	grt	3.568		1.041	0.443	0.584	0.023	1.437	0.593			7.690	2.614
W16F-1	grt	2.844		1.388	0.757	0.439	0.018	2.199	0.439			8.084	3.077
W16M-1	grt	2.900		1.385	0.676	0.565	0.030	1.901	0.612			8.069	3.078
W16N-1	grt	2.893		1.487	0.610	0.434	0.026	2.180	0.429			8.059	3.043
W16G-1	grt	3.070		1.351	0.604	0.432	0.026	1.960	0.512			7.953	2.903
W16H-1	grt	3.044		1.453	0.564	0.454	0.023	1.987	0.422			7.948	2.864
W16I-1	grt	2.530		1.821	0.826	0.589	0.032	1.748	0.493	0.214		8.254	2.830
W16J-1	grt	2.916		1.545	0.604	0.443	0.022	2.035	0.438	0.016		8.018	2.915
W16K-1	grt	2.969		1.330	0.596	0.435		2.103	0.586	0.099		8.118	3.123
W16L-1	grt	2.994		1.335	0.576	0.402	0.020	2.146	0.558	0.039		8.070	3.106
W41A-1	grt	2.951		1.970		1.039	0.032	1.292	0.780			8.064	3.111
W41B-1	grt	3.017		1.950		0.980	0.020	1.278	0.723	0.079		8.047	2.981
W53C-1a	grt	2.785		1.587	0.583	0.686	0.033	2.221	0.229	0.012		8.136	3.136
W53D-1a	grt	2.849		1.563	0.528	0.494	0.020	2.150	0.491	0.021		8.116	3.135

Wawa Olivine: 25 accepted, 24 rejected
*Replicate averaged analysis for W15A replaced accepted analysis in table, and

Rejected due to CaO > 0.50 wt%
Red Text = Rejected analysis

Both criteria within ±0.05
Both criteria within ±0.10

Raw Probe Data

Normalized

Label	Mineral Phase	SiO_2	TiO_2	Al_2O_3	Cr_2O_3	FeO	MnO	MgO	CaO	Na_2O	NiO	Total	SiO_2	TiO_2	Al_2O_3	Cr_2O_3	FeO	MnO	MgO	CaO	Na_2O	NiO	Total
W5A-1a	ol	0.66				0.08		0.67				1.43	46.86		0.00	0.00	5.58	0.00	47.55	0.00		0.00	100.0
W5A-1b	ol	0.62				0.10		0.61				1.37	46.93		0.00	0.00	7.18	0.00	45.88	0.00		0.00	100.0
W6A-1	ol	1.91				0.28		2.07				4.31	44.87		0.00	0.00	6.54	0.00	48.59	0.00		0.00	100.0
W6B-1	ol	3.80				0.76		5.02	0.03			9.65	39.55		0.00	0.00	7.92	0.00	52.25	0.28		0.00	100.0
W6E-1	ol	14.26			0.03	2.31		17.91			0.12	34.70	41.16		0.00	0.09	6.68	0.00	51.71	0.00		0.35	100.0
W6F-1	ol	2.31				0.37		2.70				5.40	42.92		0.00	0.00	6.86	0.00	50.22	0.00		0.00	100.0
W6G-1	ol	29.41		0.06		4.72	0.08	37.21			0.30	71.82	40.97		0.09	0.00	6.57	0.11	51.84	0.00		0.42	100.0
W6H-1	ol	3.92				0.70		4.30				8.97	43.91		0.00	0.00	7.86	0.00	48.23	0.00		0.00	100.0
W6I-1	ol	20.52		0.04		3.38		25.08			0.17	49.25	41.72		0.08	0.00	6.87	0.00	50.99	0.00		0.34	100.0
W6J-1	ol	18.17				3.10	0.07	23.26			0.16	44.82	40.59		0.00	0.00	6.93	0.16	51.97	0.00		0.35	100.0
W6K-1	ol	6.74				1.31		8.99				17.12	39.54		0.00	0.00	7.68	0.00	52.78	0.00		0.00	100.0
W6L-1	ol	20.87		0.05		3.87		25.85	0.04		0.19	50.91	41.03		0.10	0.00	7.61	0.00	50.82	0.07		0.37	100.0
W6V-1	ol	22.80				3.18	0.06	27.33			0.15	53.54	42.60		0.00	0.00	5.94	0.12	51.06	0.00		0.28	100.0
W6Z-1	ol	20.74		0.04		3.40	0.08	26.82	0.07		0.15	51.32	40.43		0.09	0.00	6.63	0.15	52.28	0.13		0.30	100.0
W6AA-1	ol	17.84				3.32		23.78	0.07		0.19	45.25	39.47		0.00	0.00	7.34	0.00	52.62	0.15		0.42	100.0
W13F-1	ol	27.86		0.67	0.07	4.31	0.11	33.19	0.09		0.20	66.50	41.90		1.00	0.10	6.48	0.16	49.91	0.13		0.30	100.0
W15A-1a	ol	37.24		0.10	0.55	10.30	0.11	45.16			0.33	93.82	39.70		0.11	0.58	10.98	0.12	48.15	0.00		0.35	100.0
W15B-2a	ol	41.67				3.39	0.09	45.56			0.28	91.02	45.80		0.00	0.00	3.72	0.10	50.07	0.00		0.31	100.0
W16A-1	ol	13.97		0.01		0.96		16.12	0.36		0.11	31.59	44.29		0.05	0.00	3.04	0.00	51.14	1.13		0.35	100.0
W16D-1	ol	14.84		0.14	0.04	2.51		20.16			0.09	37.81	39.28		0.38	0.10	6.65	0.00	53.36	0.00		0.23	100.0
W16E-1	ol	17.14		0.04		2.29		22.52	0.05		0.18	42.28	40.59		0.10	0.00	5.42	0.00	53.32	0.13		0.43	100.0
W17A-1	ol	22.61		0.04		1.79	0.11	28.63			0.15	53.37	42.39		0.08	0.00	3.36	0.21	53.67	0.00		0.28	100.0
W17B-1	ol	10.99		0.05	0.04	1.70	0.05	12.70			0.12	25.66	42.84		0.19	0.15	6.62	0.19	49.52	0.00		0.48	100.0
W17C-1	ol	24.36		0.04		3.94	0.11	28.95	0.12		0.23	57.75	42.18		0.07	0.00	6.83	0.19	50.14	0.20		0.40	100.0
W17D-1	ol	24.95				1.27		29.55			0.08	55.94	44.68		0.00	0.00	2.27	0.00	52.91	0.00		0.14	100.0
W17E-1	ol	25.53		0.05		3.15	0.09	33.00	0.03		0.16	62.03	41.17		0.08	0.00	5.08	0.15	53.20	0.06		0.26	100.0
W17F-1	ol	18.89		0.11		3.23	0.06	28.34	0.04		0.19	50.86	37.15		0.22	0.00	6.34	0.11	55.71	0.08		0.38	100.0
W40A-1	ol	15.11				2.10	0.02	12.28	0.10		0.08	29.72	50.90		0.00	0.00	7.06	0.06	41.36	0.34		0.28	100.0
W40B-1	ol	28.49				3.55	0.09	24.85	0.06		0.15	57.24	49.81		0.00	0.00	6.21	0.16	43.45	0.11		0.27	100.0
W40C-1	ol	18.93		0.04		3.45		19.19	0.03		0.18	41.86	45.26		0.09	0.00	8.25	0.00	45.90	0.07		0.43	100.0
W40E-1	ol	11.22				1.63		13.08	0.05		0.09	26.07	43.06		0.00	0.00	6.24	0.00	50.18	0.18		0.34	100.0
W40F-1	ol	21.24				2.53	0.08	25.74			0.20	49.81	42.66		0.00	0.00	5.07	0.16	51.71	0.00		0.40	100.0
W40G-1	ol	19.18				2.92		19.34			0.16	41.65	46.10		0.00	0.00	7.02	0.00	46.50	0.00		0.38	100.0
W40H-1	ol	9.11				0.95		8.58	0.05		0.13	18.88	48.42		0.00	0.00	5.03	0.00	45.58	0.26		0.72	100.0
W40I-1	ol	30.17				3.75	0.11	34.51			0.23	68.80	43.87		0.00	0.00	5.45	0.16	50.19	0.00		0.33	100.0
W48B-1	ol	19.82		0.30		3.21	0.08	46.00	0.69		0.26	70.35	28.18		0.42	0.00	4.56	0.11	65.39	0.98		0.36	100.0
W52A-1	ol	29.52				4.74	0.09	35.26	0.06		0.23	69.94	42.23		0.00	0.00	6.78	0.12	50.45	0.09		0.33	100.0
W52B-1	ol	20.77				1.91	0.10	27.97			0.16	50.93	40.80		0.00	0.00	3.75	0.20	54.95	0.00		0.31	100.0
W52C-1	ol	30.68		0.05	0.06	7.21	0.11	47.09			0.28	85.50	35.89		0.06	0.07	8.43	0.13	55.10	0.00		0.33	100.0
W52D-1	ol	9.87				1.92		13.95			0.14	25.91	38.14		0.00	0.00	7.42	0.00	53.91	0.00		0.53	100.0
W52E-1	ol	19.96		0.25	0.05	12.60	0.06	28.27			0.27	61.49	32.48		0.41	0.09	20.50	0.10	45.99	0.00		0.44	100.0
W52F-1	ol	27.52			0.06	5.08	0.09	39.54	0.04		0.28	72.63	37.91		0.00	0.08	6.99	0.13	54.46	0.05		0.38	100.0
W52G-1	ol	22.96		0.16		3.11	0.08	35.95	0.06		0.24	62.55	36.71		0.25	0.00	4.98	0.12	57.47	0.09		0.38	100.0
W52H-1	ol	23.29		0.06		4.17		32.54	0.03		0.24	60.38	38.60		0.10	0.00	6.91	0.00	53.93	0.05		0.40	100.0
W53A-1a	ol	25.32		0.13	0.06	4.34	0.08	35.80	0.04		0.26	66.04	38.35		0.19	0.08	6.58	0.13	54.21	0.06		0.40	100.0
W53B-1a	ol	9.66		0.07		1.88		12.06	0.26		0.13	24.12	40.13		0.31	0.00	7.81	0.00	50.13	1.07		0.55	100.0
W53B-1b	ol	9.94		0.07		1.51		12.10	0.38		0.12	24.17	41.21		0.28	0.00	6.24	0.00	50.19	1.58		0.49	100.0
W53E-1a	ol	10.42				0.78		13.88	1.80		0.07	27.00	38.68		0.00	0.00	2.89	0.00	51.52	6.67		0.24	100.0
W53F-1a	ol	18.50				1.78		21.80			0.17	42.31	43.79		0.00	0.00	4.21	0.00	51.60	0.00		0.41	100.0

												3.000 <±0.05 3.000 <±0.10		2.000 <±0.05 2.000 <±0.10
Label	Mineral Phase	Si	Ti	Al	Cr	Fe	Mn	Mg	Ca	Na	Ni	Total	MG#	Mg+Fe
W5A-1a	ol	1.107		0.000	0.000	0.110	0.000	1.675	0.000		0.000	2.893	93.82	1.785
W5A-1b	ol	1.116		0.000	0.000	0.143	0.000	1.626	0.000		0.000	2.884	91.93	1.769
W8A-1	ol	1.070		0.000	0.000	0.130	0.000	1.729	0.000		0.000	2.930	92.98	1.859
W6B-1	ol	0.965		0.000	0.000	0.162	0.000	1.901	0.007		0.000	3.035	92.16	2.063
W6E-1	ol	0.996		0.000	0.002	0.135	0.000	1.864	0.000		0.007	3.004	93.24	1.999
W6F-1	ol	1.031		0.000	0.000	0.138	0.000	1.799	0.000		0.000	2.969	92.88	1.937
W6G-1	ol	0.991		0.002	0.000	0.133	0.002	1.870	0.000		0.008	3.007	93.36	2.003
W6H-1	ol	1.056		0.000	0.000	0.158	0.000	1.729	0.000		0.000	2.944	91.63	1.888
W6I-1	ol	1.008		0.002	0.000	0.139	0.000	1.836	0.000		0.007	2.991	92.97	1.975
W6J-1	ol	0.985		0.000	0.000	0.141	0.003	1.880	0.000		0.007	3.015	93.04	2.020
W6K-1	ol	0.963		0.000	0.000	0.156	0.000	1.917	0.000		0.000	3.037	92.46	2.073
W6L-1	ol	0.996		0.003	0.000	0.154	0.000	1.840	0.002		0.007	3.002	92.25	1.994
W6V-1	ol	1.023		0.000	0.000	0.119	0.002	1.828	0.000		0.005	2.977	93.88	1.947
W6Z-1	ol	0.980		0.002	0.000	0.134	0.003	1.889	0.003		0.006	3.019	93.36	2.024
W6AA-1	ol	0.963		0.000	0.000	0.150	0.000	1.913	0.004		0.008	3.037	92.75	2.063
W13F-1	ol	1.009		0.029	0.002	0.131	0.003	1.792	0.003		0.006	2.975	93.21	1.923
W15A-1a	ol	0.983		0.003	0.011	0.227	0.003	1.776	0.000		0.007	3.010	88.66	2.004
W15B-2a	ol	1.080		0.000	0.000	0.073	0.002	1.760	0.000		0.006	2.920	96.00	1.833
W16A-1	ol	1.049		0.001	0.000	0.060	0.000	1.805	0.029		0.007	2.951	96.77	1.865
W16D-1	ol	0.954		0.011	0.002	0.135	0.000	1.933	0.000		0.005	3.039	93.47	2.068
W16E-1	ol	0.979		0.003	0.000	0.109	0.000	1.917	0.003		0.008	3.020	94.60	2.026
W17A-1	ol	1.008		0.002	0.000	0.067	0.004	1.903	0.000		0.005	2.990	96.61	1.970
W17B-1	ol	1.032		0.005	0.003	0.133	0.004	1.778	0.000		0.009	2.964	93.02	1.911
W17C-1	ol	1.019		0.002	0.000	0.138	0.004	1.805	0.005		0.008	2.980	92.91	1.943
W17D-1	ol	1.050		0.000	0.000	0.045	0.000	1.853	0.000		0.003	2.950	97.65	1.898
W17E-1	ol	0.989		0.002	0.000	0.102	0.003	1.906	0.001		0.005	3.009	94.92	2.008
W17F-1	ol	0.909		0.006	0.000	0.130	0.002	2.032	0.002		0.007	3.088	94.00	2.161
W40A-1	ol	1.198		0.000	0.000	0.139	0.001	1.451	0.009		0.005	2.802	91.26	1.590
W40B-1	ol	1.172		0.000	0.000	0.122	0.003	1.524	0.003		0.005	2.828	92.58	1.646
W40C-1	ol	1.088		0.003	0.000	0.166	0.000	1.645	0.002		0.008	2.911	90.84	1.810
W40E-1	ol	1.034		0.000	0.000	0.125	0.000	1.796	0.005		0.006	2.966	93.48	1.921
W40F-1	ol	1.021		0.000	0.000	0.102	0.003	1.845	0.000		0.008	2.979	94.78	1.947
W40G-1	ol	1.100		0.000	0.000	0.140	0.000	1.653	0.000		0.007	2.900	92.20	1.793
W40H-1	ol	1.140		0.000	0.000	0.099	0.000	1.600	0.007		0.014	2.860	94.17	1.699
W40I-1	ol	1.047		0.000	0.000	0.109	0.003	1.787	0.000		0.006	2.953	94.26	1.895
W48B-1	ol	0.705		0.012	0.000	0.096	0.002	2.440	0.026		0.007	3.289	96.23	2.535
W52A-1	ol	1.019		0.000	0.000	0.137	0.003	1.814	0.002		0.006	2.981	92.99	1.951
W52B-1	ol	0.977		0.000	0.000	0.075	0.004	1.961	0.000		0.006	3.023	96.32	2.036
W52C-1	ol	0.889		0.002	0.001	0.175	0.003	2.034	0.000		0.006	3.110	92.09	2.209
W52D-1	ol	0.934		0.000	0.000	0.152	0.000	1.969	0.000		0.010	3.066	92.84	2.121
W52E-1	ol	0.855		0.013	0.002	0.451	0.002	1.805	0.000		0.009	3.138	80.00	2.256
W52F-1	ol	0.928		0.000	0.002	0.143	0.003	1.987	0.001		0.007	3.071	93.28	2.130
W52G-1	ol	0.894		0.007	0.000	0.101	0.003	2.087	0.002		0.007	3.102	95.37	2.189
W52H-1	ol	0.942		0.003	0.000	0.141	0.000	1.962	0.001		0.008	3.057	93.29	2.103
W53A-1a	ol	0.936		0.005	0.002	0.134	0.003	1.972	0.002		0.008	3.061	93.63	2.106
W53B-1a	ol	0.981		0.009	0.000	0.160	0.000	1.827	0.028		0.011	3.015	91.97	1.986
W53B-1b	ol	0.999		0.008	0.000	0.127	0.000	1.813	0.041		0.010	2.997	93.48	1.940
W53E-1a	ol	0.944		0.000	0.000	0.059	0.000	1.874	0.174		0.005	3.056	96.95	1.933
W53F-1a	ol	1.040		0.000	0.000	0.084	0.000	1.828	0.000		0.008	2.960	95.63	1.911

Diavik Olivine: 13 accepted, 9 rejected

Rejected due to CaO > 0.50 wt%
Red Text = Rejected analysis

Both criteria within ±0.05
Both criteria within ±0.10

Raw Probe Data

Label	Mineral Phase	SiO_2	TiO_2	Al_2O_3	Cr_2O_3	FeO	MnO	MgO	CaO	Na_2O	NiO	Total
Dvk1C-1	ol	9.07		0.33		0.67		11.55				21.63
Dvk9A-1	ol	36.16				6.01		48.36			0.33	90.96
Dvk9B-1	ol	16.89				2.90	0.06	18.36			0.09	38.33
Dvk9C-1	ol	8.12				1.20		11.25				20.67
Dvk9D-1	ol	8.12				1.00		9.85	0.12			19.17
Dvk9E-1	ol	9.06				1.69		12.69			0.08	23.55
Dvk9F-1	ol	26.34		0.07	0.04	5.64	0.08	36.12			0.26	68.57
Dvk9H-1	ol	20.61				3.51		25.64	0.07		0.16	50.03
Dvk9I-1	ol	18.22				3.60	0.06	24.20			0.16	46.27
Dvk9J-1	ol	20.94		0.09		3.56		26.33	0.03		0.18	51.18
Dvk12B-1	ol	23.42		0.81		7.12	0.15	33.57	0.14			65.21
Dvk13A-1	ol	23.56		0.09		4.23	0.09	25.55	0.85		0.21	54.59
Dvk14F-1	ol	25.55				4.21		32.88	0.04		0.17	62.93
Dvk14G-1	ol	20.28			0.04	4.03		26.09			0.14	50.65
Dvk14H-1	ol	18.27		0.11		3.02		22.20	1.53		0.13	45.31
Dvk15B-1	ol	31.43		1.23		8.08	0.13	40.15	0.18			81.22
Dvk15D-1	ol	26.55		0.89		7.83	0.16	37.95	0.22			73.65
Dvk23D-1	ol	18.34		0.07		5.15	0.10	22.36	0.09		0.14	46.27
Dvk23H-1	ol	26.73		1.26		5.87	0.07	21.67	8.18		0.12	63.92
Dvk23E-1	ol	17.02		0.33	0.24	6.16		19.59	0.30		0.20	43.88
Dvk23F-1	ol	10.39		0.09	0.05	1.63		12.82	0.10		0.07	25.16
Dvk23G-1	ol	16.35		0.03		3.64		21.43			0.19	41.69

Normalized

Label	SiO_2	TiO_2	Al_2O_3	Cr_2O_3	FeO	MnO	MgO	CaO	Na_2O	NiO	Tot
Dvk1C-1	41.94		1.52	0.00	3.11	0.00	53.43	0.00		0.00	100
Dvk9A-1	39.80		0.00	0.00	6.62	0.00	53.22	0.00		0.37	100
Dvk9B-1	44.10		0.00	0.00	7.57	0.15	47.94	0.00		0.25	100
Dvk9C-1	39.49		0.00	0.00	5.82	0.00	54.69	0.00		0.00	100
Dvk9D-1	42.54		0.00	0.00	5.23	0.00	51.63	0.61		0.00	100
Dvk9E-1	38.52		0.00	0.00	7.20	0.00	53.95	0.00		0.33	100
Dvk9F-1	38.43		0.10	0.06	8.23	0.12	52.68	0.00		0.38	100
Dvk9H-1	41.23		0.00	0.00	7.02	0.00	51.28	0.14		0.33	100
Dvk9I-1	39.40		0.00	0.00	7.79	0.13	52.33	0.00		0.34	100
Dvk9J-1	40.95		0.17	0.00	6.96	0.00	51.49	0.06		0.36	100
Dvk12B-1	35.91		1.25	0.00	10.91	0.22	51.49	0.21		0.00	100
Dvk13A-1	43.16		0.17	0.00	7.75	0.16	46.81	1.56		0.39	100
Dvk14F-1	40.65		0.00	0.00	6.70	0.00	52.30	0.07		0.28	100
Dvk14G-1	40.11		0.00	0.08	7.96	0.00	51.58	0.00		0.28	100
Dvk14H-1	40.35		0.24	0.00	6.67	0.00	49.06	3.39		0.29	100
Dvk15B-1	38.71		1.52	0.00	9.95	0.16	49.44	0.23		0.00	100
Dvk15D-1	36.06		1.21	0.00	10.64	0.21	51.56	0.30		0.00	100
Dvk23D-1	39.65		0.15	0.00	11.15	0.23	48.35	0.18		0.29	100
Dvk23H-1	41.83		1.97	0.00	9.19	0.11	33.92	12.80		0.19	100
Dvk23E-1	38.82		0.74	0.55	14.05	0.00	44.69	0.69		0.46	100
Dvk23F-1	41.31		0.37	0.18	6.49	0.00	50.98	0.40		0.27	100
Dvk23G-1	39.28		0.07	0.00	8.73	0.00	51.47	0.00		0.46	100

3.000 <±0.05
3.000 <±0.10

2.000 <±0.05
2.000 <±0.10

Label	Mineral Phase	Si	Ti	Al	Cr	Fe	Mn	Mg	Ca	Na	Ni	Total	MG#	Mg+Fe
Dvk1C-1	ol	0.994		0.042	0.000	0.062	0.000	1.887	0.000		0.000	2.985	96.84	1.949
Dvk9A-1	ol	0.966		0.000	0.000	0.134	0.000	1.926	0.000		0.007	3.034	93.48	2.061
Dvk9B-1	ol	1.061		0.000	0.000	0.152	0.003	1.719	0.000		0.005	2.939	91.87	1.871
Dvk9C-1	ol	0.955		0.000	0.000	0.118	0.000	1.972	0.000		0.000	3.045	94.36	2.090
Dvk9D-1	ol	1.018		0.000	0.000	0.105	0.000	1.843	0.016		0.000	2.982	94.63	1.948
Dvk9E-1	ol	0.941		0.000	0.000	0.147	0.000	1.965	0.000		0.006	3.059	93.03	2.112
Dvk9F-1	ol	0.943		0.003	0.001	0.169	0.002	1.928	0.000		0.007	3.055	91.94	2.097
Dvk9H-1	ol	0.998		0.000	0.000	0.142	0.000	1.851	0.004		0.006	3.002	92.87	1.993
Dvk9I-1	ol	0.963		0.000	0.000	0.159	0.003	1.906	0.000		0.007	3.037	92.29	2.065
Dvk9J-1	ol	0.992		0.005	0.000	0.141	0.000	1.859	0.002		0.007	3.006	92.95	2.000
Dvk12B-1	ol	0.896		0.037	0.000	0.228	0.005	1.915	0.006		0.000	3.086	89.38	2.143
Dvk13A-1	ol	1.05		0.00	0.00	0.16	0.00	1.69	0.04		0.008	2.951	91.50	1.849
Dvk14F-1	ol	0.98		0.00	0.00	0.14	0.00	1.89	0.00		0.005	3.016	93.30	2.024
Dvk14G-1	ol	0.98		0.00	0.00	0.16	0.00	1.87	0.00		0.005	3.022	92.03	2.037
Dvk14H-1	ol	0.99		0.01	0.00	0.14	0.00	1.79	0.09		0.006	3.011	92.91	1.923
Dvk15B-1	ol	0.95		0.04	0.00	0.20	0.00	1.81	0.01		0.000	3.025	89.86	2.019
Dvk15D-1	ol	0.90		0.04	0.00	0.22	0.00	1.92	0.01		0.000	3.084	89.63	2.137
Dvk23D-1	ol	0.98		0.00	0.00	0.23	0.00	1.78	0.00		0.006	3.016	88.55	2.015
Dvk23H-1	ol	1.05		0.06	0.00	0.19	0.00	1.27	0.34		0.004	2.921	86.81	1.462
Dvk23E-1	ol	0.98		0.02	0.01	0.30	0.00	1.68	0.02		0.009	3.007	85.01	1.971
Dvk23F-1	ol	1.00		0.01	0.00	0.13	0.00	1.84	0.01		0.005	2.995	93.34	1.967
Dvk23G-1	ol	0.96		0.00	0.00	0.18	0.00	1.88	0.00		0.009	3.036	91.31	2.061